NBSIR 74-611 (R)

NBS Space Processing Research

E. Passaglia, R. L. Parker

Institute for Materials Research
National Bureau of Standards
Washington, D. C. 20234
Phone: (301) 921-2961

Novemb

Annual
For the
NASA (

Parker, R. L., Space processing program of the National Bureau of Standards. Paper in Materials Sciences in Space with Application to Space Processing. Vol. 52. Progress in Astronautics and Aeronautics. L. Steg, Ed., pp. 423-435 (American Institute of Aeronautics and Astronautics, New York, NY 1977).

U. S. DEPARTMENT OF COMMERCE
NATIONAL BUREAU OF STANDARDS

NBSIR 74-611

NBS SPACE PROCESSING RESEARCH

E. Passaglia, R. L. Parker

Institute for Materials Research
National Bureau of Standards
Washington, D. C. 20234
Phone: (301) 921-2961

November 1974

Annual Report
For the Period 1 November 1973 - 31 October 1974
NASA Contract W-13,475, Mod. 3

This reports was prepared by the National Bureau of Standards under Contract W-13,475, Mod. 3 - NBS Space Processing Research, for the Advanced Missions Program of the National Aeronautics and Space Administration.

U. S. DEPARTMENT OF COMMERCE, Frederick B. Dent, Secretary

NATIONAL BUREAU OF STANDARDS, Richard W. Roberts, Director

Table of Contents

National Bureau of Standards
Space Processing Research

Summary

This report describes NBS work for NASA in support of NASA's Space Processing Program covering the period November 1, 1973 to October 31, 1974. The objectives of the NBS program are to perform ground-based studies (and, where appropriate, space-based studies) of those aspects of space that could possibly provide a unique environment for making materials more perfect or more pure. The approach taken deals primarily with experimental and theoretical studies of the possible effects of the absence of gravitational forces on those materials preparation processes where the presence of gravity may be important in reducing perfection or purity. The materials preparation processes studied comprise six tasks in the areas of crystal growth, purification and chemical processing, and the preparation of composites. There is an additional seventh task on consulting support.

The results obtained for each task are given in detailed summaries in the body of the report. Briefly, in Task 1 - Crystal Perfection in Czochralski Growth - several crystallographic effects have been examined and found to be crucial factors in determining the ultimate level of perfection in copper crystals; very highly perfect crystals have been grown and evidence presented that gravity is the origin of possible slip dislocations during crystal growth on earth. In Task 2 - Evaporative Preparation of Ultra-High Purity Materials - experimental tests of the evaporative purification calculations have been started, initially on levitated liquid Mo, with some significant reduction of metallic impurities. In Task 3 - Vacuum Effects in the Preparation of Composite Materials - the characterization of composites consisting of reinforcements of silicon carbide, tungsten, bare pyrolytic graphite and

sapphire, each in an aluminum matrix, was carried out by optical and scanning electron microscopy. In Task 4 - Melt Shape in Weightless Crystal Growth - simulated low-g studies of liquid water zones on ice cylinders have shown that in the absence of a temperature gradient, the stable configuration is one in which the ice cylinder passes entirely through the liquid water zone. In Task 5 - Vapor Transport Synthesis and Crystal Growth of Oxides - mercurous chloride was transported at very high rates and this system may be suitable for the Apollo-Soyuz Test program. In Task 6 - Surface Traction and other Surface Phenomena - the enhancement of evaporative purification rates by capillary convection was studied by a Green's function method. In Task 7 - Consulting Support - a rather wide range of meetings, consultation, talks and other interaction with NASA and NASA contractors has taken place.

From these results at NBS, as well as from the Skylab results on space processing, the benefits of the space environment on a wide range of materials preparation and processing techniques are becoming apparent. Better crystals are, or can be, obtained in certain cases. The possibility of higher purities looks quite good. While more work is clearly needed, the program is beginning to bear fruit.

Task 1

Crystal Perfection in Czochralski Growth

M. Kuriyama, W. J. Boettinger
H. E. Burdette and R. M. Eaton

Metallurgy Division
Institute for Materials Research

Summary

As a continuation and expansion of our previous work (NASA Contract W-13,475 #3 task 1), an intensive study has been performed to seek optimum solidification parameters for the production of sizable, highly perfect copper crystals by Czochralski growth. In this report, the objective has been widened to include crystallographic effects as opposed to the fluid flow effect, per se. The crystal perfection has been assessed as in the previous report by nondestructive methods of x-ray diffraction, such as Borrmann anomalous transmission and rocking curve measurements by double crystal spectrometry.

This report completes the work on the preparation of sizable, highly perfect single crystals of copper. Many interesting results about the crystal growth processes and the resultant crystal perfection have been obtained. From these results, the following conclusion has been drawn. With other factors held constant, an optimum range of growth conditions, characterized by the rotational speeds of the seed and the melt, can be definitely chosen, which improves the crystal perfection to a certain level. It has been found, however, that more crucial factors in determining the ultimate level of perfection are:

1. the crystal perfection in seed crystal and thus the importance of the bottle-necking,

2. a particular crystallographic choice of the growth direction (the <100> direction is most preferable as the growth direction), and

3. the immobilization of possible dislocations in the growth process.

In particular, the last factor is quite interesting in view of possible space experiments. This factor can, perhaps, be altered or eliminated in the growth process of copper in space. Discussions have been made in detail on this subject, based upon our observations made on the earth. Further study of the crystallographic effects of factors 2. and 3. on the resultant crystalline perfection are strongly recommended.

Introduction

Motivated by man's access to space, one conceived an idea that metal crystals can be melt-grown in space free of dislocations. One reasoned this idea, based on the lack of gravity in space and, in turn, the lack of thermal convection in the melt. Thermal convection, induced by gravity acting on density differences in the melt, would be believed to influence the quality of resultant crystals grown on earth.

However, no one could assert with a certainty that the quality of crystals, or better the degree of crystal perfection, was related to crystal growth conditions. One lacked a systematic study on their relationship. The documentation of the growth conditions for the preparation of dislocation-free metal crystals was earnestly needed before one could even attempt the possibility of manufacturing perfect metal crystals in space.

In previous reports,* we documented the crystal imperfections in sizable copper single crystals grown under various growth conditions by the Czochralski technique. Emphasis was placed on the following aspects:

a. reproducibility of crystal perfection for given growth conditions,

b. "bottle-necking" effects in the process of crystal growth,

c. annealing effects after sample crystals were prepared in a disc form.

Results obtained in these previous works seem to indicate that there is a general trend towards a reproducible relationship between crystal perfection and growth conditions. For a practical reason, the growth conditions are described in terms of directly controllable process parameters, such as the

---

* The previous reports will, hereafter, be referred to as Report I (Government Order H-84832A, National Aeronautics and Space Administration; NBS Report 10873) and Report II (Contract W-13,475 No. 1 - NBS Materials Science and Manufacturing in Space Research, for the Advanced Mission Program of the N.A.S.A.; NBS report NBSIR 73-402)

rotational speed of the seed and of the melt.

As a continuation and an expansion of our previous works, optimum solidification parameters for the production of highly perfect copper crystals by Czochralski growth are sought in this report, including an additional aspect

d. the effect of seed orientations,

along with the documentation of crystal imperfections under various growth conditions. Aspect d is added as an independent parameter so that the genuine fluid flow conditions in the melt may be separated from other physical conditions.

In this report, a vital part of the research is, again, the non-destructive assessment of crystal perfection by x-ray dynamical diffraction. Further development has, therefore, been continued on high resolution x-ray diffraction methods for the characterization of sizable metal crystals.

At the end of this report, a conclusion will be drawn not only from the present work, but also from the previous works documented in Reports I and II. Therefore, this report can be considered as a concluding report on the growth conditions for the production of large, highly perfect copper crystals by Czochralski growth.

Experimental Procedures

The details of the crystal-growth procedures and the assessment of crystal perfection by x-ray dynamical diffraction have been described in Report I and a previous paper.[1] In this report, only changes and improvements are discussed, along with a brief description of the x-ray techniques.

Large copper single crystals were grown by the Czochralski technique from single crystal seeds in a vacuum furnace. The pulling speed was 0.10 cm min^{-1}

In Reports I and II, we have determined that no improvement of crystal perfection is made by reducing the speed to values as low as 0.01 cm min^{-1}. The melt and seed were rotated around a common axis with various speeds as described later. Copper of 99.999% purity was used as the melt charge. Crystal boules were grown with initial narrowing of the boule diameter at one region, thus forming a "bottle-neck". The grown crystals were usually about 6 cm long with diameters between 1.5 and 3.0 cm and with a bottle-neck diameter of less than 1 mm.

On removing the grown boules from the furnace, the waxing technique was used as described in Report II. The boules were sliced into discs with an acid saw. At least three slices were obtained from each boule. We designed and constructed an improved version of an acid saw (Fig. 1). This saw is capable of slicing seven discs simultaneously in a much shorter period of time (approximately less than 8 hours) than the time required by a previous saw (approximately more than 78 hours). The effect of the new saw on the resultant perfection of crystal discs was confirmed by an x-ray test to be nil. The discs were polished on an acid polishing wheel as described in Report I.

The thickness of the copper discs was determined by the x-ray anomalous transmission effect as described in Report I, II and a previous paper.[1] For the assessment of the perfection of sample crystals, two different x-ray optical arrangments were employed, namely, an asymmetrical crystallographic topographic camera (ACT) and a high-resolution double-crystal scanning diffractometer (SCAD).[1] The quality of the beam in SCAD was the same as that given in Report II and previous papers.[1,2]

An x-ray image intensifying tube has been introduced in the ACT system with the collaboration of Professor R. E. Green, Jr. of The Johns Hopkins

University. This image tube has made it possible to assess the quality of perfection of the sample crystals almost instantaneously. Not only the surface diffraction topograph, but also the transmission topograph of samples are visible on the image tube. This greatly facilitates the alignment of crystals for the maximum coverage.

Experimental Results

1. Fluid Flow Conditions

As in the previous reports, the fluid flow conditions in the melt during crystal growth are classified into groups by different sets of values of the principle variables, angular velocity of crucible and seed rotation, as listed in Table I. Although individual values of the variables differ from those in previous reports, the group number represents, as a rule, almost the identical physical condition in the melt. By interchanging the values of y (seed rotation) and z (crucible rotation), we obtain $\Delta = y - z$ with opposite signs. Based on the results in Reports I and II and the results in the present work, there appears to be no significant difference in the resultant crystal perfection due to the difference in the sign of Δ. Therefore, we do not discriminate fluid flow conditions from each other when the sign of Δ is changed by interchanging the values of y and z.

In Reports I and II, the orientation of seed crystals was selected so that the growth axis was approximately 20° from both <111> and <110>. One of several reasons for this particular selection was to minimize crystallographic effects, if any, on the study of the crystal growth processes from the melt. This was desirable because the primary question raised had been the effects of fluid flow on the quality of crystalline perfection. In the lowest approximation, fluid flow effects would be resulted from a continuum

medium rather than a crystalline medium that might play a critical role in the real solidification processes.

Since Reports I and II contain sufficient data on the growth conditions, per se, it is desirable in this report to study crystallographic effects on crystal growth, and to determine which of the two factors - fluid flow or crystallography - is more critical to the resultant crystalline perfection. For this purpose, we have grown crystals from well-oriented single crystal seeds; the crystals grown in the <111> direction of the seed crystals are specified by the number 2 as the first digit of their sample number, like 254301, and the crystals grown in the <100> direction of the seed crystals by the digit 4. The crystals grown under the conditions outlined in previous reports have sample numbers starting with 0.

2. Spectroscopic Data

As in Report II, spectroscopic data - namely, rocking curve widths - alone supply adequate information regarding the degree of crystal perfection in sample crystals. The value of each rocking curve width was measured as the full width of half maximum (FWHM) of each rocking curve, or spectral profile. The profiles were obtained in both transmission and surface reflection geometries. The crystals were considered to be more perfect, the smaller the observed width. Typical rocking curves obtained in both geometries are shown in Fig. 2.

In Table II, we list the values of rocking curve widths for all the samples of the 0-series, 2-series (111 - orientation) and 4-series (100 - orientation) examined in this year's work, along with the values of y, z and Δ for the growth conditions. Rocking curve widths observed in the

transmission geometry for crystals of the same degree of perfection vary with the crystal thickness. In most crystals, the perfection is not uniform throughout the crystal. In the 0-series crystals, the local variation of rocking curves was as much as that reported in Report II. In contrast, the crystals of the 2- and 4-series did not display as large a variation as did those of the 0-series. The rocking curve widths listed in Table II are the values averaged over the crystals. In this table, some of annealed crystals are included for completeness; their sample numbers are distinguished from the sample numbers for as-grown crystals by a letter A.

It was found in Report II on the 0-series that growth conditions I and III are equally good for the production of highly perfect crystals. This has led us to speculate that the value of Δ is more critical to the resultant perfection than the individual values of y and z. To check this speculation, growth condition VI has been added, in which the value of Δ is kept almost the same as I and III, but the values of y and z are greatly changed. As seen in table II, this speculation appears to be proved for the crystals of the 0-series. In general, the present data are in good agreement with the results obtained in Report I and II not only for the 0-series, but also for the other series of crystals. Growth condition V, in which the seed is rotated in the opposite direction to the crucible, again produced crystals of low quality from which the rocking curve showed a multi-peak structure as in Report II.

As far as the rocking curve widths are concerned, it is apparent that growth condition III should be chosen as an optimum growth condition for highly perfect crystals, regardless of the seed orientations. However, growth conditions VI and I are almost as favorable. This is most easily seen in the

values of the surface reflection rocking curve widths, but is also seen in the transmission rocking curve widths when the effect of crystal thickness is considered. The rocking curve width in the surface reflection geometry for sample #458302 under growth condition III is larger than those widths under other growth conditions. However, this contradiction can be accounted for by the thinness of the crystal which makes the crystal vulnerable to strains. In fact, the narrow width observed in the transmission geometry supports the fact that the crystal is, indeed, more perfect than the others.

Another interesting result can be found in Table II, when the rocking curve widths are compared with each other within the same growth condition. As a rule, the crystals grown in <100> direction (4-series) show narrower widths than the crystals of other series. The exception (#461302) found in growth condition VI can be explained by the thinness of the crystal, using the same argument as described above for #458302. If comparisons are made only among the rocking curve widths from the 4 series crystals under different growth conditions, it appears that growth conditions I, II, III and VI are equally effective in producing highly perfect crystals of the <100> orientation.

3. X-ray Topographical Results

The rocking curve measurements, by themselves, doubtless provide adequate information on the degree of crystal perfection as a functional of growth condition, as shown above. These measurements, however, are not convincing to many due to the lack of a visual image of the locations, distributions and shapes of crystalline imperfections. We will therefore present here the results of topographic observations made by the ACT system. In view of their higher resolution, topographs taken by the SCAD system will be used, whenever necessary, to confirm or resolve subtle differences among the ACT results.

Since, for lack of space, we cannot present all the topographs here, we will describe the qualities of the crystals as-grown under various growth conditions, based on their topographs.

Examples of the topographs are shown in Figs. 3a and b* in both the $2\bar{2}0$ surface reflection and the $11\bar{1}$ transmission geometry from an as-grown crystal. As seen in these topographs, the entire volume of the crystals usually participates in diffraction simultaneously to form a diffraction topograph, regardless of the diffraction geometry. This condition implies in the present ACT system that the possible misorientation over the entire area of the crystal should be much less than 30 second of arc.

A. The crystals of the 0-series

The topographs obtained from the 0-series crystals reproduces the identical details of imperfections observed in Report II. As we speculated and confirmed by the rocking curve measurements, the crystals grown under growth condition VI also showed the Lomer-Cottrell locking structure as clearly as the crystals grown under growth condition III, as described in Report II. The observation of Lomer-Cottrell dislocations in as-grown copper single crystals has been reported in detail in a previous paper.[2] Furthermore, it is confirmed in this report that the crystals grown under growth condition II also showed evidence of Lomer-Cottrell dislocations, although they were, in most cases, less distinct.

B. The crystals of the 2-series

Next, we turn to the x-ray diffraction topographs obtained from the crystals grown in the <111> direction. The crystals grown under growth

---

* The topograph enlargements are composites as a result of microscope limitations during enlargement, and partly as a result of successful growth of large crystals surpassing the anticipated size of the beam.

conditions I, II, III and VI all showed a distinct Lomer-Cottrell locking arrangement, although the image-visibility of these dislocations appears to be dependent on the crystal thickness. Fig. 3b shows the topograph obtained from a rather thick crystal, in contrast with the typical transmission topograph of Lomer-Cottrell dislocations in a thin crystal which was shown in Report II and in a previous paper.[2] Fig. 3c shows the SCAD transmission topograph at a higher resolution where Lomer-Cottrell dislocations are well demonstrated. The growth conditions in which the value of Δ is large produced the crystals of poor quality. The topographs of such crystals clearly show a mosaic structure, or more accurately, coherent domains surrounded by extremely low angle grain boundaries. These topographs have almost the same features as those topographs shown in Figs. 4a and b.

C. The crystals of the 4-series

Here we describe the topographs obtained from the crystals grown in the <100> direction. All the surface diffraction topographs of the crystals grown under growth conditions I, III and VI are similar to the surface topograph shown in Fig. 3a. The transmission topographs from these crystals clearly show the Lomer-Cottrell dislocation arrangements as seen in the other series of crystals. The crystals grown under growth condition II show a somewhat different feature in their diffraction topographs, as shown in Fig. 5a and b. The origin of these scattered dotted structures has not been explained satisfactorily. These structures have been reported by Fehmer and Uelhoff[3,4] in a copper crystal grown by the Czochralski technique. A detailed study of this structure is currently in progress. Fig. 5c shows this structure in the SCAD surface topograph with a higher resolution. The growth conditions, IV and V, produced the crystals having multi-coherent domains, as seen in the

other series of crystals. However, there remains a definite distinction between their topographs and topographs of other series grown under these growth conditions. Unlike the other series of crystals in which the anomalous transmission effect is disrupted so heavily, the 4-series crystals grown under conditions IV and V show the anomalous transmission effect, as shown in Fig. 4b. In the transmission topograph, the crystals even show the formation of Lomer-Cottrell locks in individual domains. This fact implies that the crystals of the 4-series have much higher degrees of perfection, even under growth conditions IV and V, than the crystals of the other series.

Typical surface and transmission topographs taken by the SCAD system are shown in Figs. 6a and b, where scratches, sometimes unavoidable during the chemical polishing process, are also seen along with dislocations and other defects. Examples of surface and transmission topographs taken by the ACT system from annealed crystals are shown in Figs. 7a and b. Fig. 7c shows the part of the surface topograph, taken by the SCAD system, where no dislocations are visible.

Conclusion and Discussion

During the past three years, we have performed an extensive study on the crystal growth of copper single crystals by the Czochralski technique, with emphasis on the documentation of the resultant crystal perfection. The total number of crystal boules grown, including those used for seed crystals, reached 102. From them, 117 discs were examined by the two sophisticated two-crystal x-ray spectrometer systems which were developed uniquely in our laboratory. To perform this task in the most effective manner, an extensive knowledge of x-ray dynamical diffraction was utilized. The development of our ACT (asymmetrical crystal topography) system has made it possible to

collect the photographic (topographic) data from a large number of sample discs in both the surface reflection and the transmission modes with maximum efficiency and precision. Quantitative data, such as the rocking curve widths, have also been collected at various locations of each sample with great accuracy. One shortcoming, however, is found in the intensity of x-rays generated by our x-ray tubes and generator. Although an image intensifying system has been added to the ACT system, the weak intensity problems from our x-ray generator have not been eliminated.

In this report, we intend to draw some conclusions on the effect of growth conditions on the crystalline perfection in copper single crystals grown by the Czochralski technique. First of all, we have to emphasize the fact that the same degree of crystal perfection can be reproduced repeatedly under given growth conditions as shown in Reports I and II as well as in this report. This reproducibility, at least, makes it possible and even sensible to have conducted some experiments determining whether or not there is indeed a correlation between the crystalline perfection and the controllable growth parameters for the melt. In other words, were it not for this reproducibility, our experiments would have been meaningless. As we demonstrated in this report, we had predicted from the previous results in Reports I and II that a new growth condition, namely VI, should produce as good a crystal as the other conditions I and III did, and we confirmed successfully that prediction. This implies that our collected data are meaningful enough to analyse the validity of the relationship between those two quantities. It can be concluded, as far as the growth condition is concerned, that an optimum growth condition for the preparation of highly perfect copper crystals is, as a rule, characterized by the small value of Δ

(the difference between the speeds of the seed and the melt). The directions of the seed and melt rotations should be in the same direction for this optimum condition. It has been proven that growth conditions with large Δ's produce crystals of poor quality that exhibit several coherent but independent (judged from their well defined boundaries) domains.

The optimum growth condition certainly is significant in the growth of the 0-series crystals. In the growth of the 2-series crystals (grown in the 111 direction), this optimum condition still has some significance, although the difference in the crystal perfection becomes more subtle when growth condition II is compared with, for example, VI. It can even be said that, for the crystals of the 4-series grown in the <100> direction, the growth conditions do not have great influence on the resultant perfection, as seen in Table II. It is, however, fair to conclude that there is a general range of growth conditions which improves crystal perfection to a certain level, regardless of their growth directions - the range being specified by the small value of Δ.

A more crucial factor influencing the ultimate level of crystal perfection has been found in the bottle-necking effect, or rather the original perfection in seed crystals. It is indispensable in the production of sizable perfect crystals to use a highly perfect crystal as a seed and to reduce the chances of introducing further dislocations with initial narrowing the boule diameter at one region.

Annealing does not improve crystal perfection to a large extent, unless as-grown crystals have been already highly perfect, or have had particular arrangements of crystal imperfections such as Lomer-Cottrell locks discussed in Report II and in a previous paper. In general, prolonged annealing tends to

introduce dislocations from the crystal edge and develop pile-ups of dislocations, thus creating extremely low angle boundaries.

A significant result in this report is the observation of crystallographic effects. Dominance of the growth direction on the ultimate level of crystalline perfection obviously cannot be ignored, as described in a previous section. Another effect related to crystallography is slightly more delicate; as seen in Figs. 3 and 5, some particular sets of dislocation arrangements are usually observed in the best crystals, and these arrangements are strongly dependent on the crystal structure of materials, as discussed in a previous paper.[2] The Lomer-Cottrell locks are perhaps unlikely to form, for example, in the body-centered cubic crystal. The structure observed in Fig. 5 is very likely related to the types of dislocations originally developed in the process of solidification, although careful studies have not as yet been completed.

As we discussed in Report II and a previous paper,[2] the formation of dislocation structures, such as Lomer-Cottrell locking, plays a decisive role in the preparation of sizable, highly perfect copper crystals. The crystals grown under optimum growth conditions have the overall high degree of perfection, as judged from their display of the prominent Borrman anomalous transmission effect. All the regions in the interior of the crystals, therefore, are likely to have similar properties with respect to each other. If the formation of a Lomer-Cottrell dislocation is energetically favorable at one place, then there is no doubt that dislocations of a similar type would occur through the same process everywhere inside the bulk crystal.

In fact, when a slice of the as-grown crystal showed the arrangements of Lomer-Cottrell dislocations over its entire volume, as shown in Fig. 3,

the degree of crystal perfection was equally high for any part of the crystal boule of about 6 cm long. In contrast, some as-grown crystals which did not show the Lomer-Cottrell locks showed an extremely high degree of perfection in one portion of the boule, but did not show the same high quality of perfection in other parts of the boule. Most of these crystals tended to develop low-angle grain boundaries somewhere along the length of the boule. This tendency indicates that the formation of particular sets of interacting dislocations makes dislocations immobile, thus aids to produce a sizable, highly perfect crystal. If wide-spread slip occurs or if many dislocations form randomly, then the locking would not take place and the dislocations would still be mobile, and would affect the subsequently grown part of the crystal, resulting in a less perfect crystal.

It is likely that dislocations are generated in the growth process. They will either disappear by slip through the crystal, or remain randomly in the crystal at obstructions. During crystal growth on the earth, crystals are grown in the field of gravity. Gravity exerts a body force on crystals and can produce slip in the crystals at high temperatures during their growth process. Especially when the crystal is being pulled, the weight of the crystal may produce a sufficient shear stress, resulting in slip. Unless the slip goes through the entire crystal, dislocations are likely to remain in the crystal and be subject to further motion. If they are sessile, they won't move, and they will prevent further slip from occurring. On the earth, it is easier to make dislocations form a certain arrangment, as we demonstrated, than to make all the dislocations move out of the crystals.

Compared with the crystals grown in other directions, the crystals of the 4-series grown in the <100> direction have the largest number (8) of slip

systems ({111} planes, <110> directions) available and the maximum shear stress is produced by the crystal weight on these slip systems. It is thought that this physical condition will lead quite easily to the formation of Lomer-Cottrell locks and hence crystals of high perfection. These crystallographic arguments, including the fact that 4-series crystals show the best degree of perfection, support the hypothesis that gravity is the origin of possible slip during crystal growth.

In conclusion, it cannot be denied in the preparation of sizable, highly perfect copper sizable single crystals that a certain range of growth condition offers an optimum set of directly controllable parameters for the fluid flow in the melt. This range is more critically limited by the value of the difference of the rotation speeds of the seed and the melt than by the individual values of speeds. It is, however, found that more crucial factors in determining the ultimate level of perfection are 1) the crystal perfection in seed crystals and the control of inheritance of seed imperfections (the bottle-necking), 2) the crystallographic orientation of the growth direction, and 3) the immobilization of possible dislocations in the growth process. The <100> direction appears to be most favorable for perfection in crystals. The crystals could probably have been made perfect by the choice of the proper growth direction, if no gravity had acted on the crystals. The observed dislocation numbers in the copper crystals that were grown in the past are as low as 5 dislocation per cm^2. In some annealed crystals, major parts of the crystal volume display no dislocations at all, although a few dislocations can be seen near the edge of the crystals.

Based upon the results and conclusions of this report, it is extremely desirable to further study the crystallographic effects, in particular, by

use of a face-centered cubic metal other than copper. These crystallographic effects should also be studied in the absence of gravity. From an academic point of view, many interesting observations, such as the structure shown in Fig. 5, and the annealing effect, should be studied in detail.

References

1. M. Kuriyama, J.G. Early and H.E. Burdette, Proc. of AIAA 12th Aerospace Sciences Meeting (1974) Paper No. 74-204. This paper is attached to this report as Appendix I.

2. M. Kuriyama, J.G. Early and H.E. Burdette, Journal Appl. Crystallography (1974) 7. This paper is also attached to this report as Appendix II.

3. H. Fehmer and W. Uelhoff, Journal Cryst. Growth 13/14 (1972) 257.

4. E. Kappler, W. Uelhoff, H. Fehmer and F. Abbink, "Herstellung von Kupfereinkristallen Kleiner Verzetungsdichte" Westdeutscher Verlag, Opladen (1971).

Table I Fluid Flow Conditions

Group Number	Seed Rotation (y)	Crucible Rotation (x)	Difference ($\Delta = y - x$)
I	- 5.0	- 4.4	- 0.6
	+ 5.0	+ 4.4	+ 0.6
II	+10.0	+ 6.0	4.0
	+10.0	+ 5.0	+ 5.0
	-10.0	- 5.0	- 5.0
III	-20.0	-19.6	- 4.0
	+20.0	+19.6	+ 4.0
	+20.0	+20.6	- 0.6
IV	+20.0	+10.0	+10.0
	+20.0	+20.6	+ 0.6
V	+ 5.0	- 5.0	+10.0
	- 5.0	+ 5.0	-10.0
VI	+10.8	+10.0	+ 0.8
	-10.0	-10.0	+ 0.8
	-10.8	-10.0	- 0.8

Rotation speed is in units of rotation per minute.

Table II X-ray Spectroscopic Data

Group Number	Crystal Slice Number	Seed Rotation (y)	Crucible Rotation (x)	Difference ($\Delta = y - x$)	Thickness (L) mm	(220) Surface FWHM- sec. of arc	(111) Transmission FWHM- sec. of arc	μL
I	252301	- 5.0	- 4.4	- 0.6	unobtainable	33.0	8.5	---
I	453301	+ 5.0	+ 4.4	+ 0.6	0.8092	29.0	11.0	44.60
I	453302	+ 5.0	+ 4.4	+ 0.6	1.0235	33.0	9.0	56.42
II	040401	+10.0	+ 6.0	+ 4.0	0.3294	36.0	13.0	18.16
II	040402	+10.0	+ 6.0	+ 4.0	0.9212	33.0	10.5	50.78
II	040402A	+10.0	+ 6.0	+ 4.0	0.9212	27.0	8.0	50.78
II	254301	+10.0	+ 5.0	+ 5.0	unobtainable	40.0	33.0	---
II	456301	-10.0	- 5.0	- 5.0	0.6269	29.0	8.5	34.55
II	456302	-10.0	- 5.0	- 5.0	0.2558	28.0	9.0	14.10
III	042301	+20.0	+20.6	- 0.6	0.6557	29.5	12.5	36.14
III	255301	+20.0	+19.6	+ 0.4	0.3070	27.0	10.25	16.92
III	255302	+20.0	+19.6	+ 0.4	0.5	ACT topographs only		27.56
III	269301	+20.0	+20.6	- 0.6	0.5566	29.0	13.0	30.68
III	269302	+20.0	+20.6	- 0.6	0.5	ACT topographs only		27.56
III	458301	-20.0	-19.6	- 0.4	0.6654	25.0	9.5	36.68
III	458302	-20.0	-19.6	- 0.4	0.1471	31.5	10.0	8.11
IV	257301	+20.0	+10.0	+10.0	unobtainable	40.5	not observed	---
IV	459302	+20.0	+10.0	+10.0	0.5	58.0	not observed	27.56
V	260302	- 5.0	+ 5.0	-10.0	0.8253	51.5	15.5	45.49
V	262302	- 5.0	+ 5.0	-10.0	0.5	ACT topographs only		27.56
V	463402	+ 5.0	- 5.0	+10.0	---	multigrain	multigrain	---
V	463402	+ 5.0	- 5.0	+10.0	not observed	ACT topographs only		---
VI	043301	+10.8	+10.0	+ 0.8	0.6140	33.0	10.0	33.84
VI	043303	+10.8	+10.0	+ 0.8	0.3390	38.0	11.0	18.69
VI	043303A	+10.8	+10.0	+ 0.8	0.3390	27.0	12.0	18.69
VI	049202	-10.0	-10.8	+ 0.8	0.8476	30.5	10.0	46.72
VI	246301	-10.8	-10.0	- 0.8	0.5309	63.5	multiple peaked	92.26
VI	246302	-10.8	-10.0	- 0.8	0.5820	40.0	15.5	32.08
VI	246303	-10.8	-10.0	- 0.8	0.6717	29.5	11.0	37.02
VI	250301	-10.0	-10.8	+ 0.8	0.8891	29.5	9.0	49.00
VI	250302	-10.0	-10.8	+ 0.8	0.8444	26.0	11.0	46.54
VI	250302A	-10.0	-10.8	+ 0.8	0.8444	27.0	9.3	46.54
VI	461301	+10.0	+10.4	- 0.4	0.2558	33.0	10.5	14.10
VI	461302	+10.0	+10.4	- 0.4	0.3199	33.5	10.5	17.63

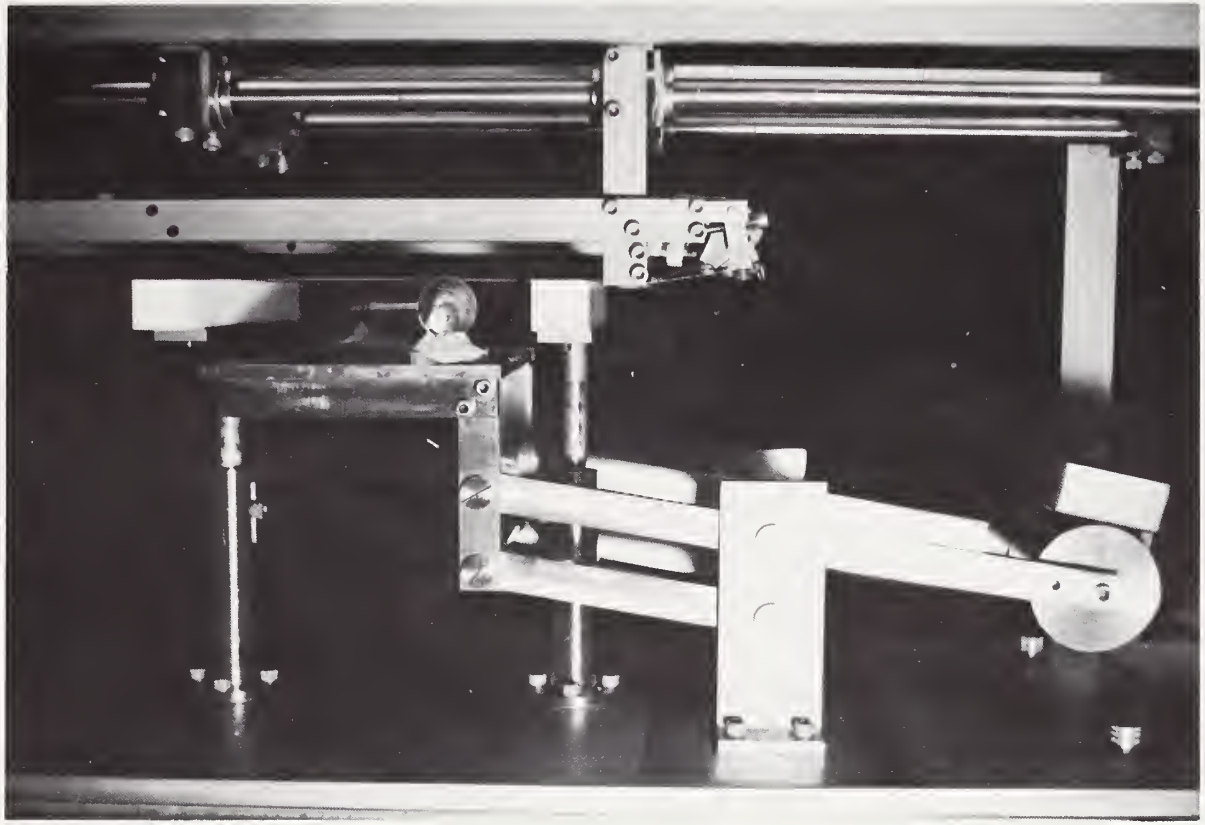

Fig. 1 Photograph of new acid saw.

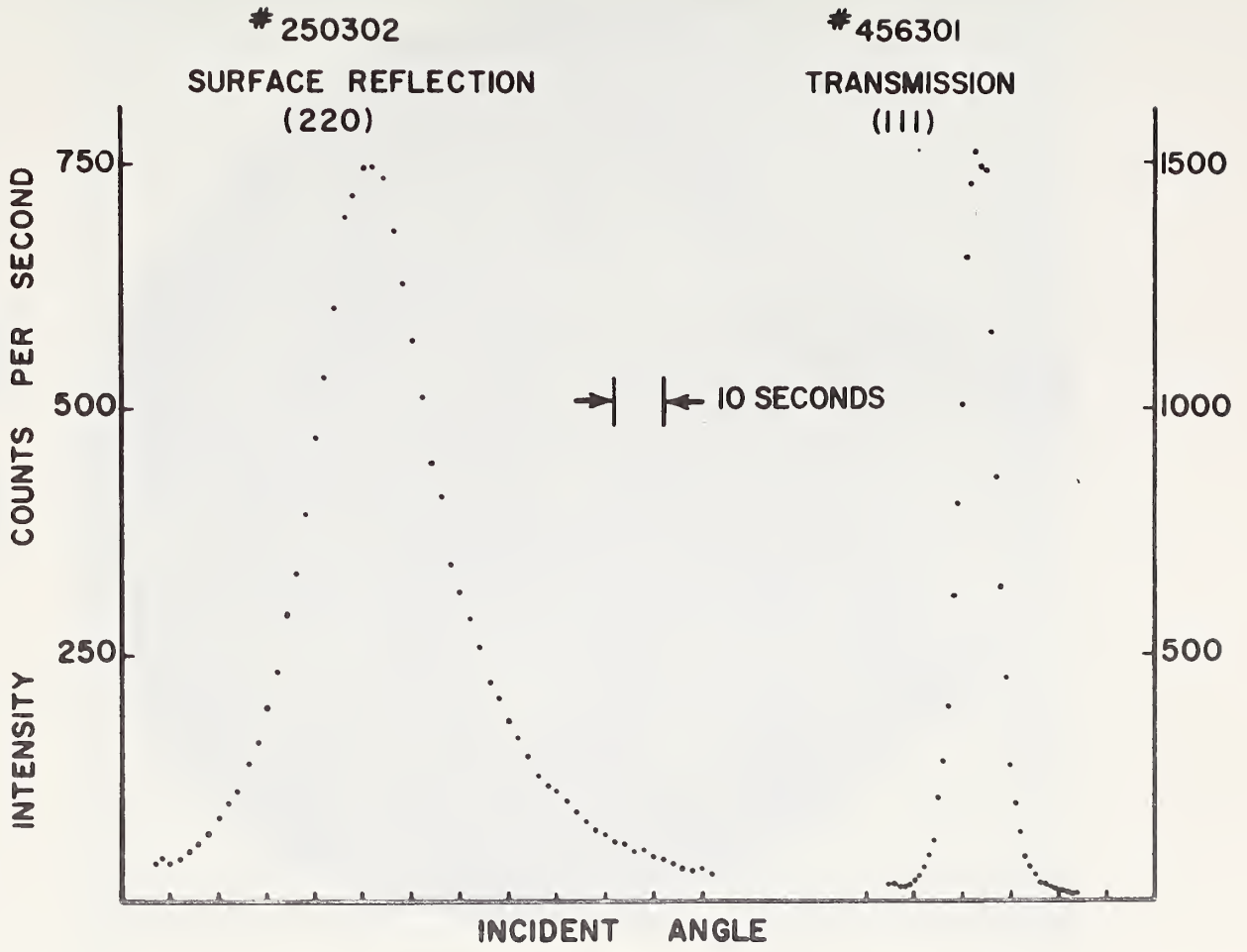

Fig. 2 Typical rocking curves obtained in reflection and transmission geometries.

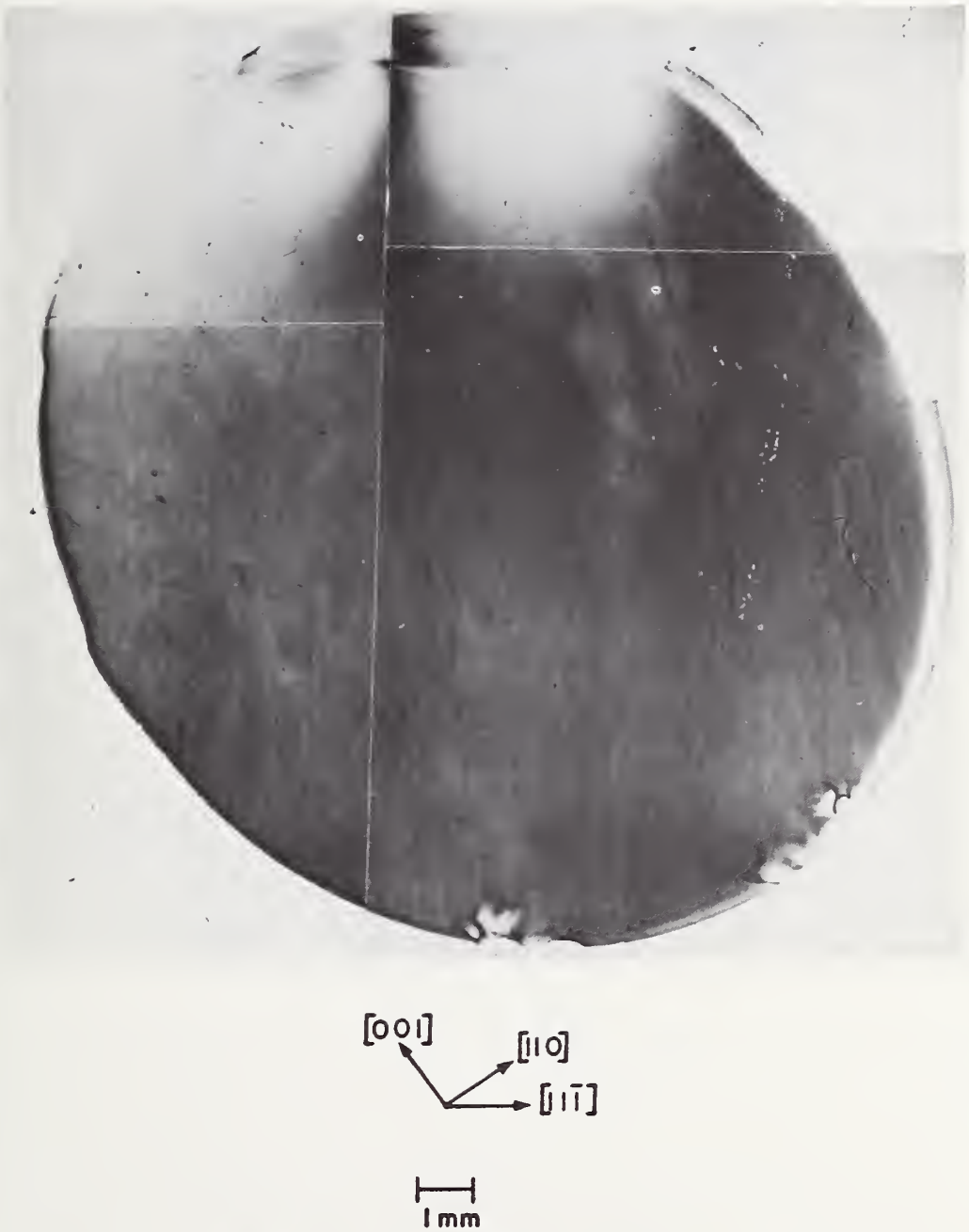

Fig. 3a ACT $2\bar{2}0$ reflection topograph
of as-grown cropper crystal #255301.

Fig. 3b ACT 11$\bar{1}$ transmission topograph of as-grown copper crystal #250302.

Fig. 3c SCAD 11$\bar{1}$ transmission topograph of as-grown copper crystal #255301.

Fig. 4a ACT $2\bar{2}0$ reflection topograph of as-grown copper crystal #459302.

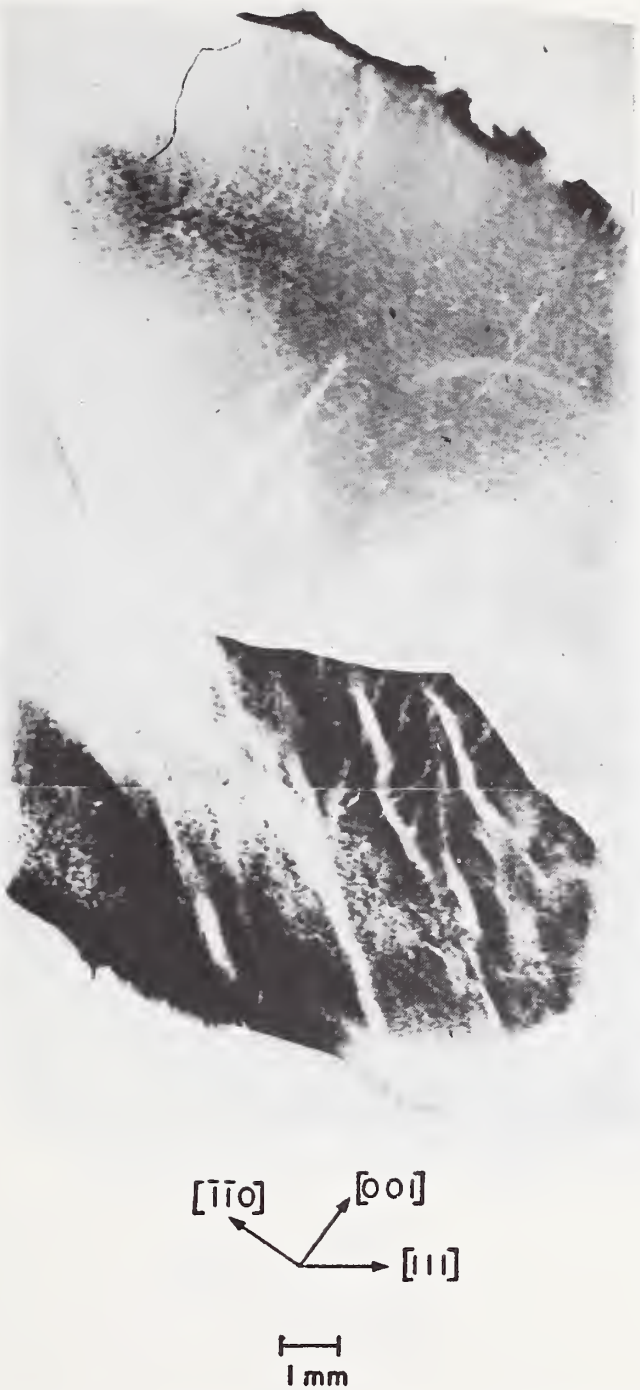

Fig. 4b ACT 111 transmission topograph of as-grown copper crystal #459302.

Fig. 5a ACT 2$\bar{2}$0 reflection topograph
of as-grown copper crystal #456302.

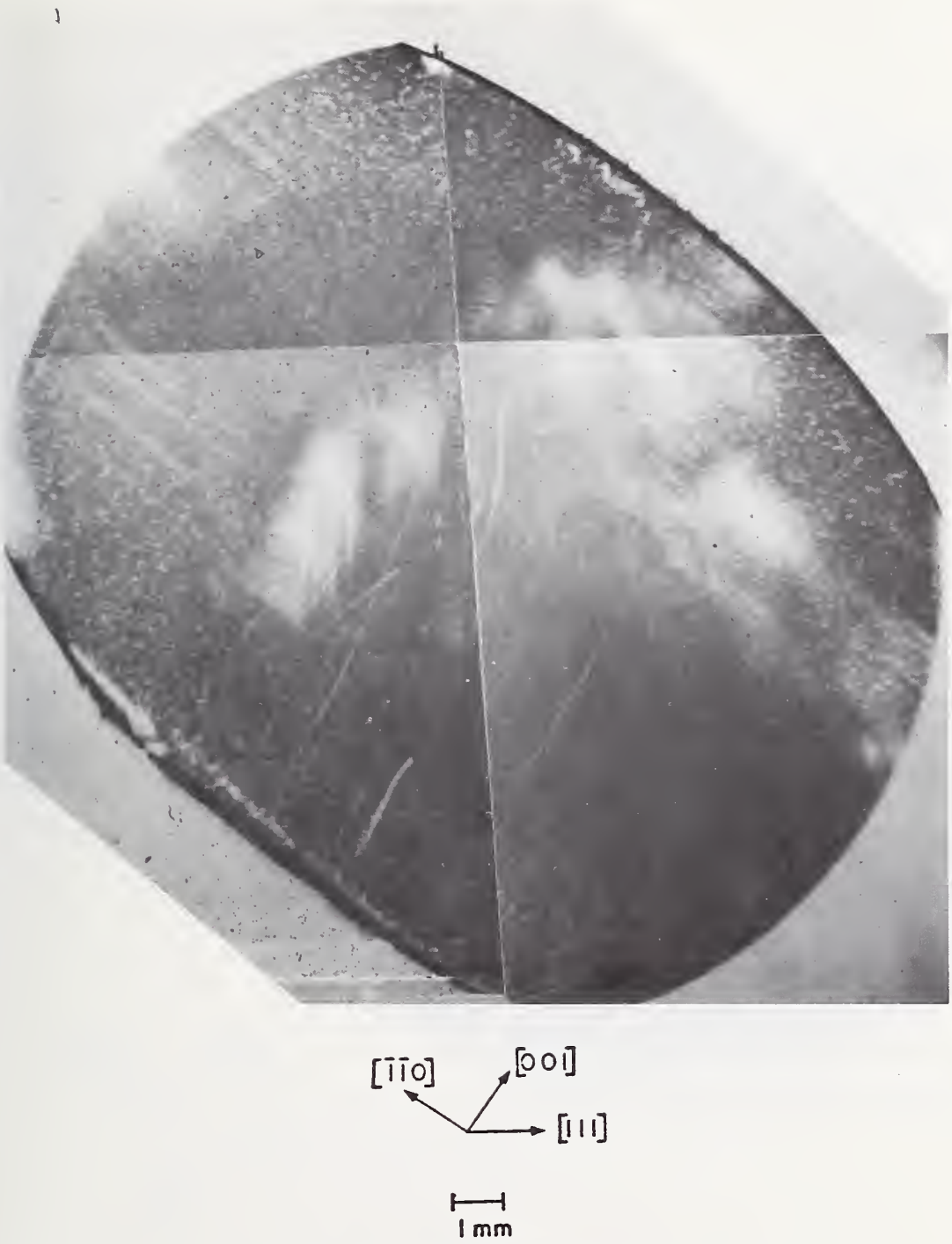

Fig. 5b ACT 111 transmission topograph of as-grown copper crystal #456301.

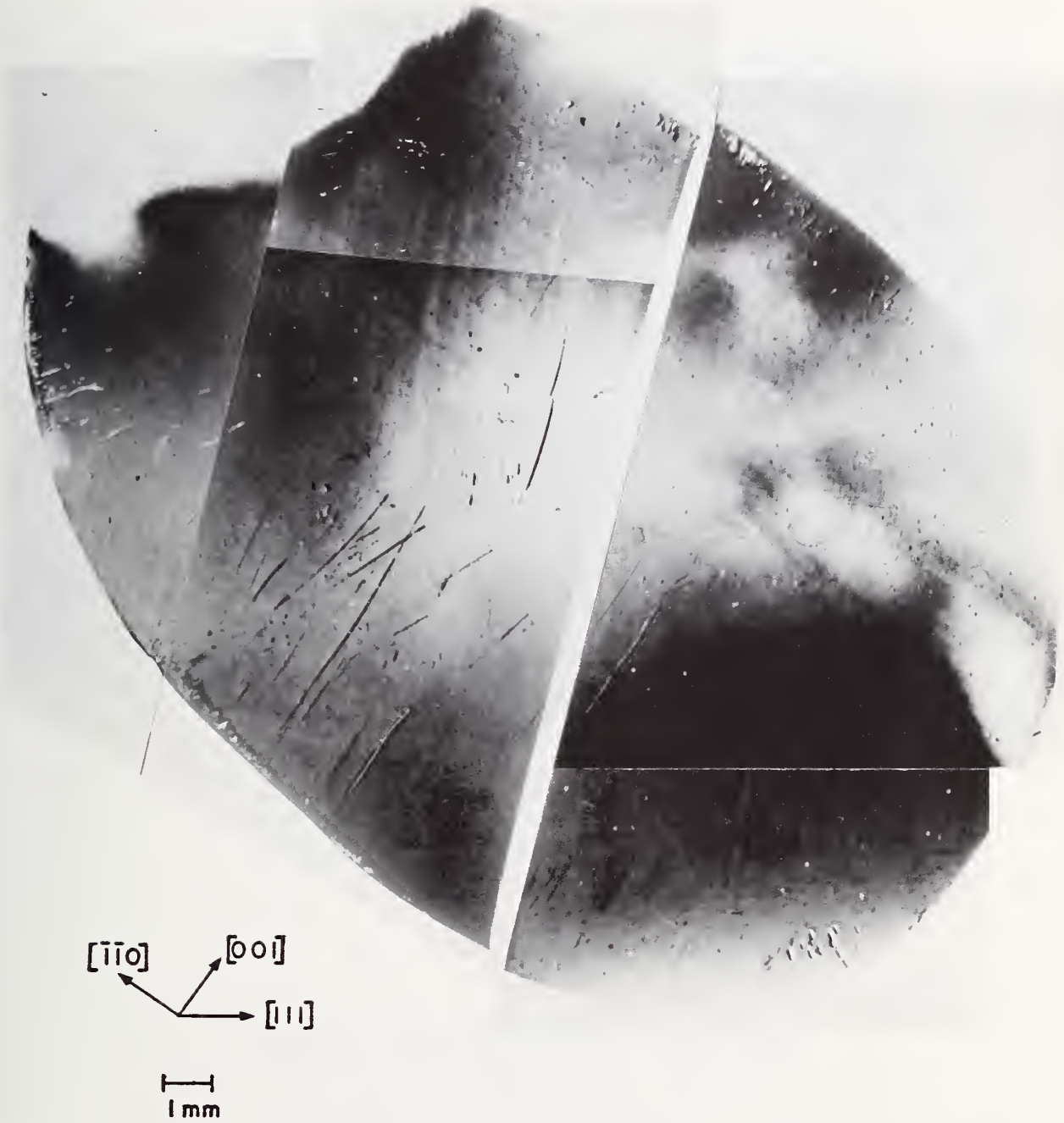

Fig. 5c SCAD $2\bar{2}0$ reflection topograph of as-grown copper crystal #456301.

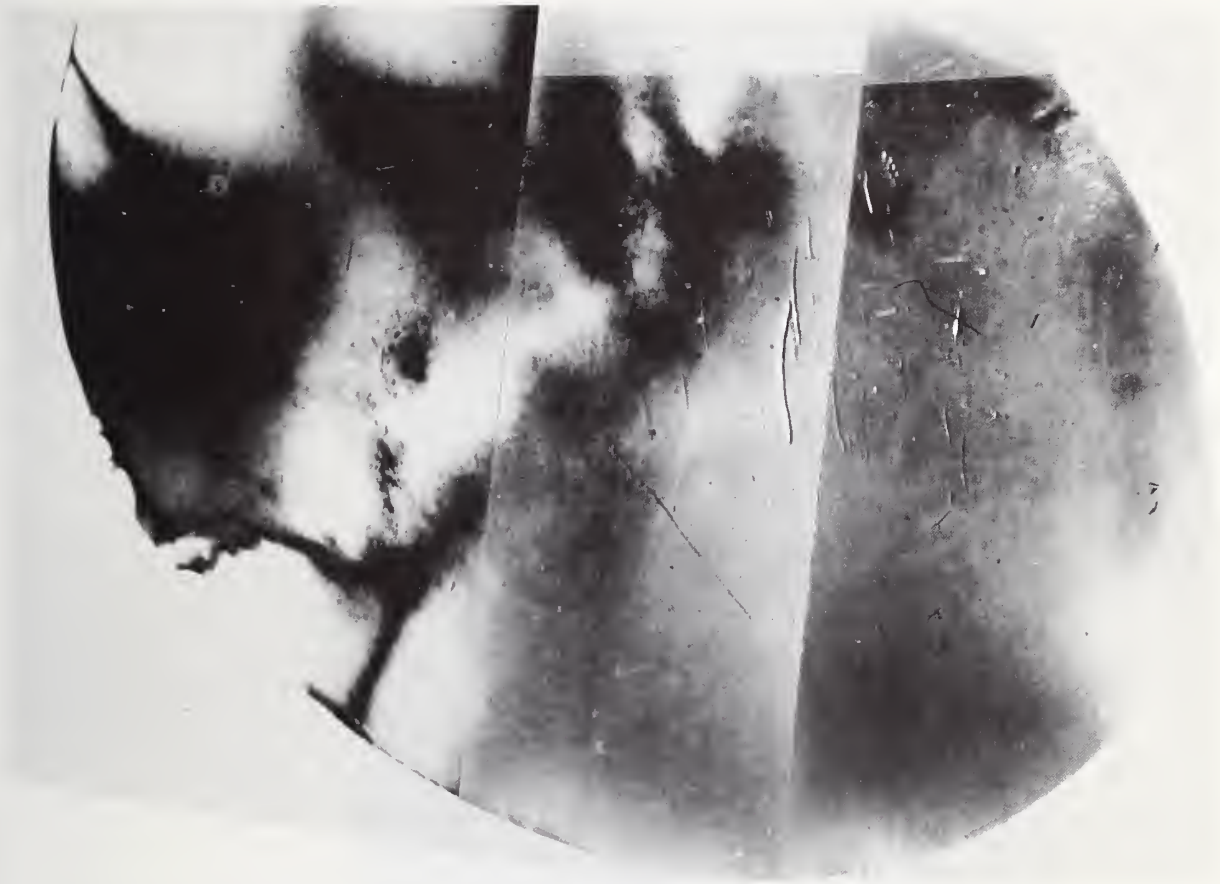

Fig. 6a SCAD $2\bar{2}0$ reflection topograph of as-grown copper crystal #458301.

Fig. 6b SCAD 111 transmission topograph of as-grown copper crystal #458301.

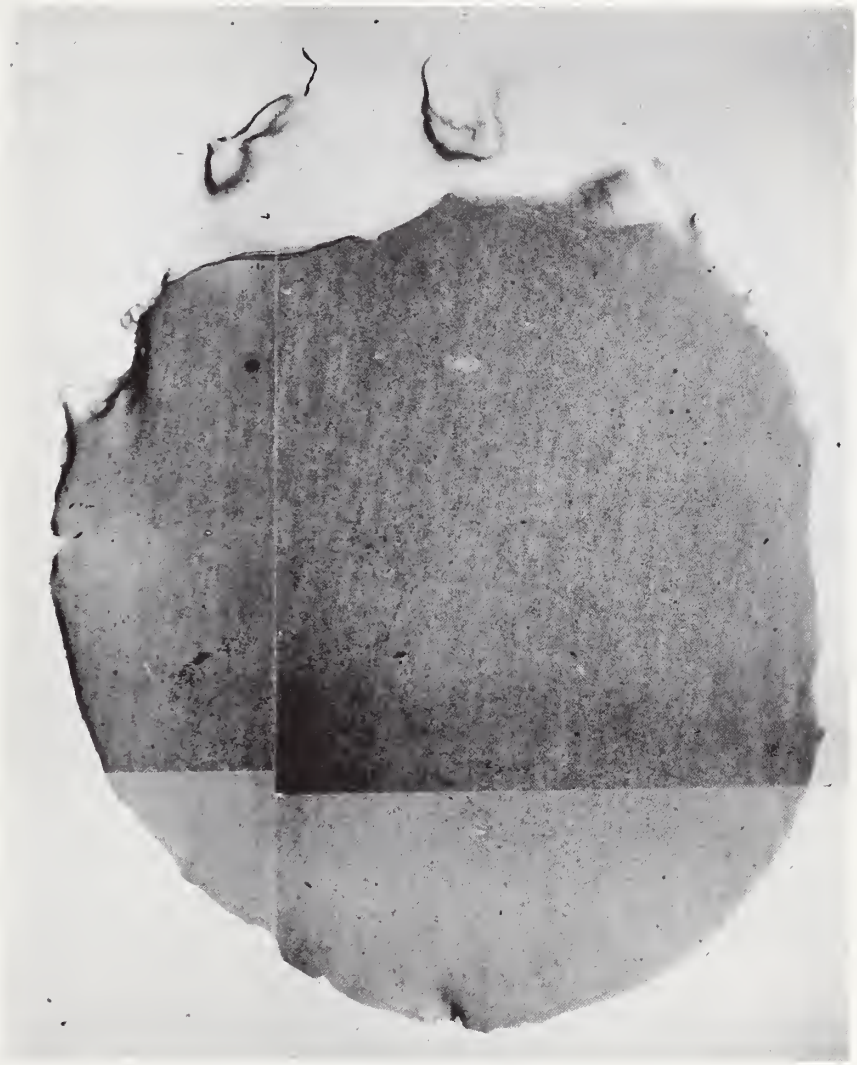

Fig. 7a ACT $2\bar{2}0$ reflection topograph of annealed copper crystal #040402A.

Fig. 7b ACT 11$\bar{1}$ transmission topograph of annealed copper crystal #250302A.

Fig. 7c SCAD $2\bar{2}0$ reflection topograph of annealed copper crystal #040402A.

Appendix I

FLUID FLOW EFFECTS ON CRYSTALLINE PERFECTION†

M. Kuriyama, J. G. Early and H. E. Burdette
Institute for Materials Research
National Bureau of Standards
Washington, D. C. 20234

Abstract

In the absence of gravity, thermal convection, i.e., convection induced by gravity acting on density differences in the melt, would be expected to be negligible. Fluid flow in the melt, including thermal convection, probably affects the perfection of crystals grown from the melt. At present, the relationship between crystal growth conditions, in particular, fluid flow conditions, and the degree of crystal perfection has not been well established for metals. It is, therefore, highly desirable to document the perfection of crystals grown from the melt in terms of directly controllable process parameters, before one even begins to analyse the fluid flow conditions in the melt in terms of thermodynamical variables. In this paper, optimum solidification parameters for the production of highly perfect copper crystals by Czochralski growth are sought along with the documentation of crystal imperfections under various growth conditions. A vital part of research of this type is the assessment of crystal perfection. X-ray techniques which do not in their application produce defects and which allow the characterization of imperfections in single crystals are chosen to assess crystal perfection. The properties of crystals grown from the melt are anticipated to vary over a large range, since the growth conditions, especially the fluid flow conditions, are deliberately changed. The x-ray techniques employed ranged from ordinary Laue photography through Borrmann topography to double-crystal scanning diffractometry, thus allowing crystals with a wide variation in perfection to be studied. As a set of controllable solidification parameters, the rotation of the seed and of the melt and the diameter of the bottle-neck are chosen. X-ray diffraction topographs are analysed along with the data obtained from rocking curve measurements. Tables of growth conditions and quantitative data of rocking curve widths are presented.

I. Introduction

Other investigators have reported the growing of metal single crystals containing regions which are totally dislocation-free.(1)-(6) However, it has not generally been possible to grow sizable metal crystals free of dislocations. In contrast, semiconducting materials, such as Si and Ge, have been grown from the melt phase, free of dislocations. The principle mechanism for the dislocation generation in these crystals has been studied extensively.(7)-(11) The difficulty in growing highly perfect metal crystals may be attributed to their low dislocation energy and high dislocation mobility, compared with those factors for semiconducting crystals. Imperfections can be produced by impurity particles present in the melt which may originate in the container used to hold the melt, or the imperfections may already exist in the seed crystal and thus easily propagate into the growing crystal.

In addition to these defect sources, one certainly cannot neglect sources related to thermal conditions. Among these, the presence of thermal convection and other fluid flow phenomena in the melt may affect the solidification process resulting in the build-up of inhomogeneous strain fields sufficiently large to cause dislocations to multiply. Since thermal convection is induced predominantly by gravity acting on density differences in the melt, it is usually impossible to completely control fluid flow, especially convection, during crystal growth on the earth's surface.

At the present time, the relationship between the crystal growth conditions and the degree of crystal perfection has not been systematically studied for metals. The primary objective of this paper, therefore, deals with a documentation of the resultant crystal perfection under various growth conditions with emphasis being placed on the following aspects: a. reproducibility of crystal perfection for given growth conditions, b. "bottle-necking" effects in the processes of crystal growth, c. annealing effects after sample crystals are prepared in a disc form.
In studying crystal perfection as a functional of fluid flow, it is necessary first to establish the fact that there is, indeed, such a relation. It must be determined whether or not the variations of crystal perfection are caused by fluid flow conditions, per se, or by other factors, such as the perfection of seed crystals and the procedures of handling grown crystals. For this reason, aspects b and c are included in this study, although analysing the results in aspect a alone seems sufficient to define the optimum fluid flow conditions in the melt for the present purpose.

In this research, one must examine the crystal imperfections in the interior of crystals in sufficient detail without disturbing the already existing imperfections. X-ray dynamical diffraction by a crystal is known to be very sensitive to inhomogeneous strain distributions inside the crystal. In nearly perfect single crystals, the dynamical diffraction effect often produces well resolved contrasts in intensity distributions around single dislocations: this technique is known as x-ray diffraction topography. When the crystal is less perfect, the diffraction topographs usually become more complex. However, this technique is still useful to detect and analyse bulk strains. One shortcoming of x-ray topography lies in its inability to describe the crystal imperfections quantitatively. When x-rays are diffracted by a crystal, all the information on irregular arrangements of atoms is contained in the diffracted x-rays: the intensity distributions and the angular broadening of the diffracted beams can provide quantitative data on the crystal imperfections. Double crystal diffractometry can

† Supported by the Advanced Missions Program of the National Aeronautics and Space Administration

be used to extract quantitative data from the diffracted x-ray beams along with x-ray topography. We, therefore, utilize the dynamical diffraction effect for the characterization of the perfection of the crystals.

II. Crystal Growth Procedures

Since Young and Savage(3) succeeded in preparing copper single crystals of very low dislocation density, investigations of metal single crystal growth have been carried out with copper more often than with other metals. We, therefore, chose to study copper so that the previous information on the growing conditions and the degree of the crystal perfection could be utilized. Unlike previous workers, we grow crystals of reasonably large size (1.5 cm ~ 3.0 cm in diameter compared with previous crystal sizes of 0.1 cm ~ 1.5 cm). The reasons for this are that 1) historically, it has been difficult to grow such large crystals free of dislocations, 2) in our experiments we substantially change the conditions of fluid flow, deviating from the conditions in which most previous crystals of low dislocation density have been grown, and 3) sizable single crystals are more useful for industrial purpose.

In order to grow perfect crystals, it is necessary to minimize any possibility of introducing imperfections during the process of crystal growth. If one can grow crystals without containers, one would expect less perturbation to the crystals. This has been verified by Kappler et al.(5) A technique which enables single crystals to be grown without touching a crucible is known as the Czochralski technique.(12) The material in the crucible is heated in a vacuum slightly above the melting temperature. Then a small single crystal (seed) is immersed in the melt and subsequently withdrawn at a slow rate. The melt adhering to the seed solidifies immediately above the melt surface as it is being pulled upward. A schematic diagram of the Czochralski apparatus is shown in Fig. 1, where the principle variables defining the growth conditions are denoted by x (pulling speed), y (seed rotation) and z (crucible rotation). The pulling speed is generally between 0.013 cm/min. and 0.1 cm/min., which is slow enough to minimize the rate of the latent heat input at the interface. The pulling speed does not cause as significant a change in diameter, except for crystals having a very small bottle-neck diameter (~ 0.05 cm), as does the temperature of the melt. When the crystal initially grows with a very small bottle-neck diameter, the pulling speed affects the diameter of the growing part significantly until the bottle-neck region completely clears the top of the furnace.

Crystals are grown from single crystal seeds, and copper of 99.999% purity is used as the melt charge. The orientation of the seed crystal is selected so that the growth axis lies in the neighborhood of the direction deviated about 20° from both <111> and <110>. The reason for this particular selection is based on the considerations of diffraction conditions with respect to the possible directions of the Burgers vector in the copper crystal. A disc shape crystal having (110) planes as its faces is most convenient, so that the three strongest diffracting planes, (111), (002) and

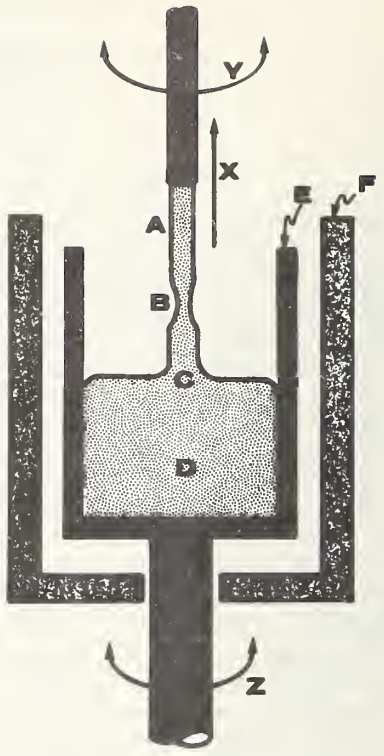

Fig. 1 Schematic of Czochralski apparatus A-seed; B-bottle-neck; C-solid/liquid interface region; D-melt; E-crucible; F-heater; X-pulling direction; Y-seed rotation; Z-crucible rotation

(220), can be used in transmission geometry. If the crystal is grown in the <110> direction, diffraction using these two planes cannot reveal dislocations associated with the growth direction. (The growth direction lies in a slip plane.) Since the growth direction is a unique direction, it is unwise to lose any information concerning those dislocations (or a slip system (111) <110>).

Crystal boules are grown by initially narrowing the diameter at one region of the boule. Narrowing the crystal diameter (the bottle-neck) is produced by increasing the temperature of the melt. The boules are sliced into discs by an acid saw,(13) and the discs are polished on an acid polishing wheel using a saturated solution of $CuCl_2$ in HCl.(13) At least three slices of sample crystals were cut from different regions of each boule. One of the slices after being polished was annealed at 1000°C for three days in a hydrogen (dew point = -90°F) flow furnace.

III. Assessment of Crystal Perfection

Theory of X-ray diffraction in imperfect crystals

One of the limiting factors for research of this type is the ability to determine the properties of crystal imperfections in sufficient detail. Careful chemical etching can reveal defect structures in high resolution, but these defects are revealed only on the crystal surface. By contrast, x-ray diffraction provides a unique and powerful tool for the investigation of these defects in the interiors of crystals. It is also

known that ordinary x-rays are non-destructive to most materials. Although the relatively simple kinematic diffraction theory is almost adequate for the investigations of defects in ordinary imperfect crystals, a complete and detailed description of diffraction phenomena requires the more rigorous theory - dynamical theory of diffraction. This is particularly important in the study of nearly perfect crystals where dynamical effects provide extremely sensitive probes for investigating the imperfections. There have been theoretical difficulties in the application of the well-known Ewald and Laue dynamical theory(14)(15) to imperfect crystals, since this dynamical theory is valid only for perfect crystals. However, a generalized dynamical theory of diffraction has been formulated to be readily applicable to real crystals containing imperfections(16)(17).

The basic idea of employing x-ray diffraction techniques to a study of crystal imperfections lies in the fact that an x-ray Laue spot has a fine structure in it and this fine structure is closely related to imperfections in crystals. The recent advanced techniques, such as x-ray topography, can magnify at high resolution a Laue spot from a large portion of a crystal. In the x-ray topographs obtained from an imperfect crystal, one observes black and white images superimposed on a background. For a thin crystal where the product of the linear absorption coefficient μ and the crystal thickness L is less than 1, defects may appear as black (in the photographic negative; stronger intensity) images accompanied by a faint anomalous transmission (or diffraction) beam trace. For intermediate thickness where $1 < \mu L < 10$, the topographs show primarily white images. Black images sometimes appear as well as black-white contrast images. Usually one should expect complicated patterns for these cases. For a thick crystal ($\mu L > 10$), the Borrmann (anomalous transmission) effect(18) becomes dominant and is accompanied by white images of good contrast. Black images or non-uniform intensity distribution may still be observed in the topographs. When a crystal is nearly perfect, the topograph clearly shows the images of individual dislocations. The above qualitative description of images is based on casual observation of topographs. More complicated patterns including interference effects, etc. are also observed.

According to a generalized dynamical theory,(17) the scattering amplitude of an imperfect crystal is given by

$$\langle k'R' \mid S \mid kR\rangle = \sum_i F_k^{(i)} \exp[i\{\alpha_i + K_z - U(H)\}\cdot L] + \sum\sum_{(i\neq j)} W(H)\, F_{K-H} \exp[i(\beta_j + K_z)\, L], \qquad (3\text{-}1)$$

where k and k' are the incoming and the outgoing momentum (wave-vector) of x-rays, R and R' are the positions on the crystal surfaces where the x-rays are coming in and out, respectively, L is the crystal thickness, and H is the reciprocal lattice vector perpendicular to the diffracting plane. This expression is derived for a single Bragg diffraction condition where $|k'| \sim |k+H| \sim |k|$. The quantity F is the dynamical amplitude of the transmitted (K=0) or the Bragg-diffracted (K=H) x-ray beam obtained in the usual dynamical theory for a perfect crystal, where the polarizability should be corrected by the distortion factor. The solutions of the dispersion equations for the incoming beam and the outgoing beams are given by α and β, respectively. The detailed descriptions of physical quantities involved are not discussed here since it is beyond the scope of this paper. However, Eq. (3-1) is helpful to understand topographic images.

The quantities, U(H) and W(H), are related to the crystal imperfections under a certain region irradiated by the incident beam. When the crystal is perfect, these quantities become zero, giving ideal dynamical diffraction

$$\langle kR \mid S \mid k'R'\rangle = \sum_i F_k^{(i)} \exp[i(\alpha_i + K_z)\, L]. \qquad (3\text{-}2)$$

When the crystal becomes really imperfect, the scattering amplitude reduces to

$$\langle kR \mid S \mid k'R'\rangle = \sum_{(i\neq j)} W(H)\, F_{K-H}^{(i)} \exp[i(\beta_j + K_z], \qquad (3\text{-}3)$$

giving the kinematical scattering amplitude. In this case, W(H) F becomes equal to the x-ray structure factor. The first term of Eq. (3-1) is, therefore, considered as the dynamical diffraction term caused mainly by the diffraction mechanism similar to the dynamical diffraction in a perfect crystal. The second term is a new additional diffraction mechanism due to the presence of crystal imperfections. This effect is also the result of dynamical diffraction, although in the imperfect crystal limit it yields the kinematical result given by Eq. (3-3).

In the first term of Eq. (3-1), the imaginary part of α - U(H) can be thought of as the effective absorption coefficient under the diffraction condition. This quantity is given by

$$\mu^{(i)}\ \text{eff} = \mathrm{Im}\,[\alpha_i - U(H)] = \mu[1+(-1)^i \frac{1}{\sqrt{\epsilon^2+1}} \frac{\mathrm{Im}[v(H)]}{\mathrm{Im}[v(0)]}\, e^{-M(H)}], \qquad (3\text{-}4)$$

where ϵ is the parameter indicating a deviation from the Bragg condition, v(H) and v(0) are the 0-th and H-th Fourier transform of the polarizability. The ratio, Im v(H)/Im v(0), generally is very close to one. M(H) is the distortion correction factor relating to the second moment of the strain distribution in the crystal portion irradiated by the x-ray beam. In a perfect crystal, M(H) is equal to zero, making μ eff (corresponding the i=1 mode) almost zero. This is the phenomena known as the Borrmann anomalous transmission effect(18) in which the transmitted and the diffracted beams suffer negligible absorption. When the crystal is not perfect, M(H) increases, creating higher effective absorption. Since M(H) is also a function of position of imperfections, the effective absorption coefficient becomes larger at the imperfection sites. This is the primary reason why one can see the image of imperfections clearly in the Borrmann topographs.

The second term is usually responsible for black-white contrasts of imperfections seen in topographs. This term contains almost complete information on the properties of imperfections, and describes the phenomenon previously known as secondary extinction.(17) Unlike the first term, where the contrast is independent of incident angle, this second term shows that the contrast of dislocation images changes from a black-white one to a white-black one, depending on the incident angle or, in other words, the sign of the strain

field gradient. This is also experimentally known as a complementary relation of images: the topographic contrast formed by the (hkℓ) and $(\bar{h}\bar{k}\bar{\ell})$ reflections is reversed or complementary. Another important fact concerning the diffraction effects in topography is that a local strain distribution, such as a dislocation line and isolated imperfections, appear in topographs as a local image at the supposedly corresponding region, although the image is sometimes clearly resolved or sometimes slightly blurred. The reason why most imperfections form as a local image is due mainly to the Borrmann diffraction mechanism. In topography, a beam of a limited size, or an extremely well collimated beam is used as the incident beam. According to x-ray diffraction optics,(16)(17) the diffracted (or transmitted) beam given by the first term of Eq. (3-1) comes out of the exit face of the crystal at the place where the diffracting plane meets the exist surface, as shown in Fig. 2. If an imperfection is located in this path, the disruption of the Borrmann effect takes place to produce the image of the imperfection, due to the change of the effective absorption coefficient. The scattering mechanism for the second term in Eq. (3-1) is, however, slightly different from the above optics, thus creating blurred images of imperfections.

The schematic illustration of the image formation is shown in Fig. 3, where the incident beam sweeps the surface of the crystal. In this figure, the diffracted intensity is plotted: (a) corresponds to the intensity due to the first term of Eq. (3-1), and (b) to that due to the second term. When the first term is dominant, one can have a typical Borrmann topograph due to the mechanism (a) in this figure. Otherwise one usually observes the superposition of the cases (a) and (b).

Experimental apparatus for diffraction

For the characterization of the perfection of sample crystals, we use two different x-ray optical alignments, namely an asymmetrical topographic camera and a high resolution double crystal spectrometer. The former, which will be called ATC hereafter, was designed in order to enable us to survey a large number of sample crytals effectively in a shorter time period than that required for ordinary topography. Although this was accomplished at the expense of high resolution, the quality of topographs from the ATC remained just as good as in ordinary x-ray topography. (It was one of the requirements for this design to maintain such high quality in the topographs.) In the ATC, the first crystal is a silicon crystal whose surface makes an angle of 13.5° with the (111) diffracting plane. The incident x-ray beam falls on the crystal surface almost parallel to it, and the (111) diffracted beam appears with a size of 1.7 cm x 2.5 cm, being sufficiently large enough to cover the entire area of sample crystals. Care must be taken with the first crystal so that it would not superimpose its own surface structure on topographs of the structure of the sample crystal. This requirement often induces an unavoidable lack of ideal high resolution in the ATC. The schematic diagram of the ATC is shown in Fig. 4. Topographs are taken from the sample crystal (Cu) both in transmission geometry, where the (111) diffraction of copper is used, and in reflection geometry, where the (220) diffraction is used.

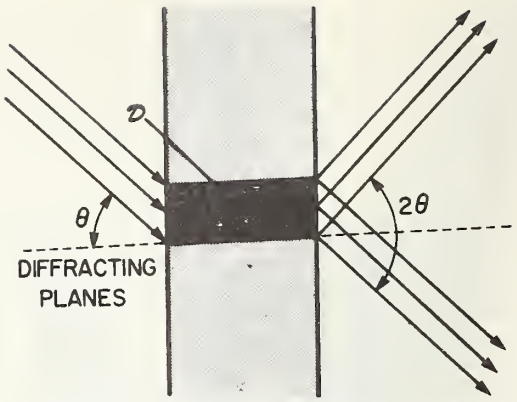

Fig. 2 Schematic of Borrmann diffraction geometry

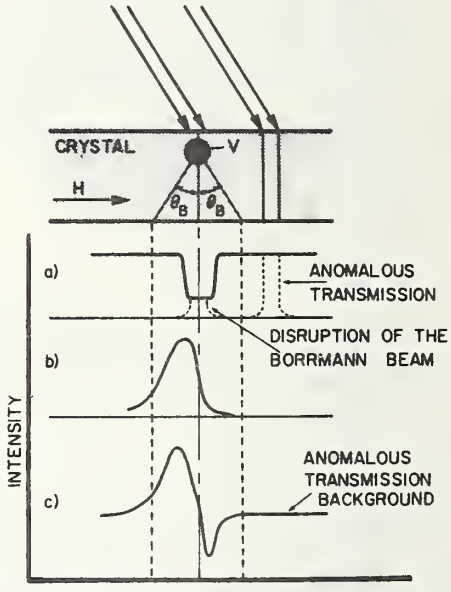

Fig. 3 Schematic of image formation mechanism and origin of contrast effects

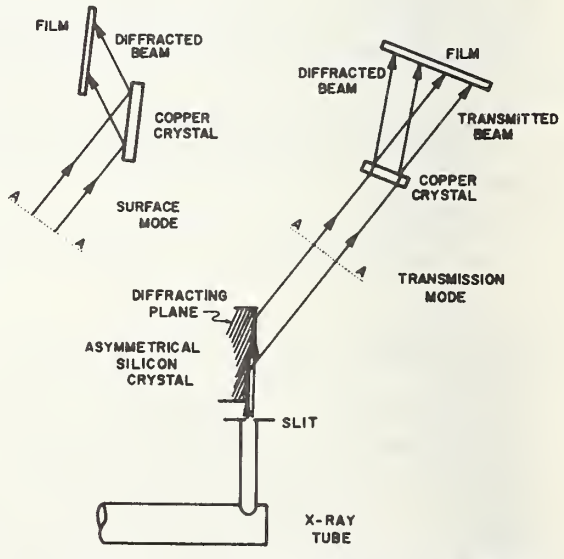

Fig. 4 Schematic of the asymmetrical topographic camera (ATC) illustrating both surface reflection and transmission modes

To obtain diffraction rocking curves and high resolution topographs at various locations on the sample crystals, the high resolution double crystal spectrometer (hereafter called the spectrometer) has been used with a scanning stage mounted on it. The schematic diagram of the spectrometer is shown in Fig. 5 where the first crystal is only shown in reflection geometry. A silicon crystal of disc shape whose surface is a (110) crystallographic plane has been chosen as the first crystal to obtain a well collimated monochromatic beam from the (220) Bragg diffraction both in reflection and transmission geometry. Between the x-ray source of a point focus x-ray tube and the first crystal, a horizontal slit of 6 mm and a vertical slit of 0.3 mm have been inserted. When the first crystal is in reflection geometry, two vertical slits of 0.15 mm and 0.10 mm, respectively, are placed a distance of 3 cm apart from each other before the second crystal. When the first crystal is in transmission geometry, no slits are inserted.

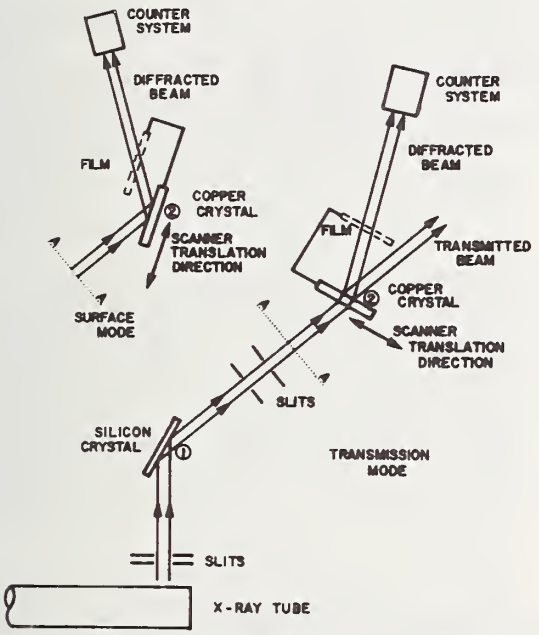

Fig. 5 Schematic of high resolution double crystal spectrometer with scanning capability illustrating both surface reflection and transmission modes

The quality of the beam was checked by measuring the rocking curves of a dislocation free germanium crystal which was placed at the second crystal position. The full width at half maximum (FWHM) of the rocking curve from the (220) germanium diffraction was determined to be 12.8 seconds of arc in the Si (220) surface/Ge (220) surface mode and 15.5 seconds of arc in the Si (220) transmission/Ge (220) surface mode, using Cu Kα radiation. For topography, exposure times range between 24 hours and 100 hours of transmission, and between 2 and 24 hours for reflection. The ATC requires much shorter exposure times than the scanning spectrometer. These topographs are recorded on Ilford L-4 nuclear plates with an emulsion thickness of 50 μm.

In this work, it is also necessary to measure with sufficient accuracy the thickness of crystal discs without touching them since the rocking curve width in transmission becomes narrower for the same degree of perfection, when the crystal disc becomes thicker. Also, the thickness data are used in the determination of dislocation densities to estimate the volume of the crystal portion where the dislocations are counted on the transmission topographs. We measure the crystal thickness by use of the Borrmann (anomalous transmission) effect of x-ray dynamical diffraction. The thickness is calculated from the following equation:

$$D = (L_0 - L_S)/\tan\theta, \qquad (3\text{-}5)$$

where θ is the Bragg angle, and L_0 and L_S are the positions of the beam traces. In the present work, the slit placed in the x-ray beam before the crystal is 0.01 cm wide. A photograph of a nuclear plate used for the determination of thickness is shown in Fig. 6, where the (111) Bragg diffraction was used with Cu $K\alpha_1$ radiation.

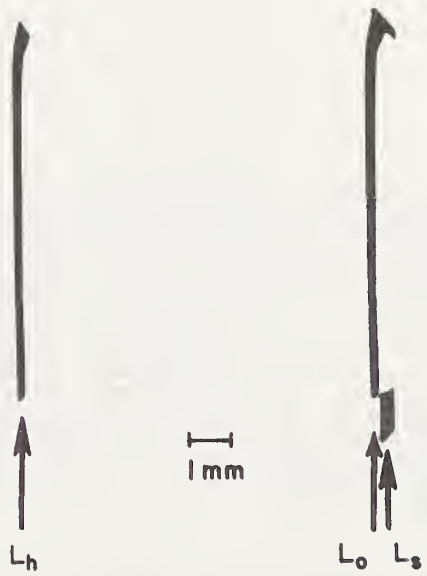

Fig. 6 Photograph used for thickness determination

Table I Fluid Flow Conditions

Group Number	Crucible Rotation (Y)	Seed Rotation (z)	Difference (Δ = Y - Z)
I	-5.4 rpm	-6.0 rpm	+0.6 rpm
II	+6.0 rpm	+10.0 rpm	-4.0 rpm
III	-20.6 rpm	-20.0 rpm	-0.6 rpm
IV	+30.0 rpm	+20.0 rpm	+10.0 rpm
V	-6.6 rpm	+6.0 rpm	-12.6 rpm

VI Experimental Results

Fluid Flow Conditions

The fluid flow conditions in the melt during crystal growth are classified into groups by different sets of values of the principle variables, angular velocity of crucible and seed rotation, as

Table II X-ray spectroscopic data

Growth Condition	Neck Diameter mm	Crystal Slice Number	Post Growth Treatment	Thickness mm	(220) Surface Reflection FWHM Seconds of Arc	(111) Transmission FWHM Seconds of Arc	Perfection Ranking		μL
							Surface	Transmission	
I	1.4	023302	As Grown	0.40	70	α_1 α_2 not resolved	7	--	22.05
I	1.4	023303	Annealed	0.40	70	α_1 α_2 not resolved	7A	--	22.05
I	<1	024301	As Grown	0.6580	35	18	2	3	36.27
I	2	025303	As Grown	0.5883	35	14	2	1	32.43
I	2	025302	Annealed	0.3488	29	14	1A	4A	19.23
I	1.2	035302	As Grown	0.50	47	Not Observed	5	7	27.56
I	1.2	035301	Annealed	0.7549	36	11	5A	2A	41.60
I	~1	036301	As Grown	0.2463	35	20	2	4	13.58
I	~1	036303	Annealed	0.3838	32	12	3A	3A	21.15
II	1	026301	As Grown	0.5502	46	17	4	2	30.33
II	1	026302	Annealed	0.5629	33	11	4A	2A	31.03
II	4	027303	As Grown	0.2550	50	Multiple Peaks	6	5	14.06
II	4	027301	Annealed	0.1791	40	15	6A	5A	9.87
III	<1	028303	As Grown	0.8934	32	14	1	1	49.24
III	<1	028301	Annealed	0.7989	37	10	2A	1A	44.03
III	>2	030302	As Grown	0.40	43	Multiple Peaks	3	5	22.05
III	>2	030303	Annealed	0.4638	31	12	2A	3A	25.56
III	~1	037303	As Grown	0.1439	35	17	2	2	7.93
III	~1	037302	Annealed	0.7101	31	11	2A	2A	39.14
IV	Polycrystalline Boule								
V	3	034303	As Grown	0.25	Multiple Grains				
V	3	034301	Annealed	0.20	Multiple Grains				

listed in Table I. By interchanging the values of y and z, we obtain Δ with opposite signs. There appears to be no significant difference in the resultant crystal perfection due to the difference in the sign of Δ. Therefore, we do not discriminate fluid flow conditions from each other when the sign of Δ is changed by interchanging the values of y and z. In addition, we have introduced another parameter indicating the diameter of the bottle-necks grown during the crystal growth process. There are always at least two different bottle-neck diameters chosen in each group; one is very narrow, usually less than 1 mm and the other between 2 mm and 4 mm.

Spectroscopic Data

In Table II, we list the values of rocking curve widths (FWHM) observed in both transmission and surface reflection geometry for all the growth conditions, including annealing. The crystal is considered to be more perfect, the smaller the observed width. The crystals are ranked, as shown in the eighth and ninth columns, in increasing order of their widths. The annealed crystals are ranked separately with the letter A accompanied by their rank. The ranks based on the transmission data should be judged along with the value of μL, because, even with the same degree of perfection, thicker crystals show narrower widths.

In most crystals, the perfection is not uniform throughout the crystal. Rocking curves taken at different locations from the same crystal are shown in Fig. 7, where the (111) diffraction is set in transmission geometry (μL ~ 25). In this figure, the horizontal axis represents a decreasing glancing angle to the right. The little humps on the right side of the individual profiles correspond to the Bragg diffraction due to Cu $K\alpha_2$ radiation. The separation of the α_1 and α_2 peaks in the Si (220)/Cu (111) non-parallel ($1\bar{1}$) setting is -20.8 second of arc, which is the difference between the separation of α_1 and α_2 due to Si (220) and that due to the Cu (111) diffraction.

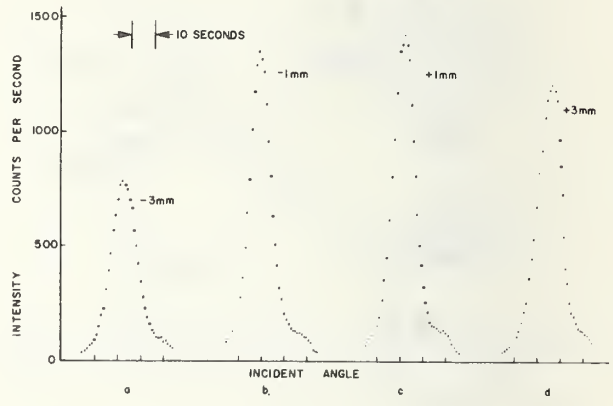

Fig. 7 Diffraction rocking curves taken in transmission geometry for crystal #030303 at various locations on the crystal

Typical rocking curve profiles are shown in Fig. 8 and 9 for various crystals. In Fig. 8, the curves were obtained in both transmission and surface reflection geometry of the copper crystal with the first crystal, Si (220), in transmission geometry. The horizontal axis represents an increasing glancing angle to the right. The smaller peaks correspond to the α_2 diffraction: the separation in the reflection geometry is calculated to be +163.0 seconds of arc. Fig. 9 shows the rocking curve profiles from a crystal of good quality (#037303) and a typical rocking curve from a crystal of poor perfection (#035302). The latter crystal did not produce observable anomalous transmission. These profiles were obtained with the first crystal, Si (220), in surface reflection geometry.

X-Ray Topographs of the Grown Crystals

As mentioned previously, diffraction topographs were taken by two different x-ray

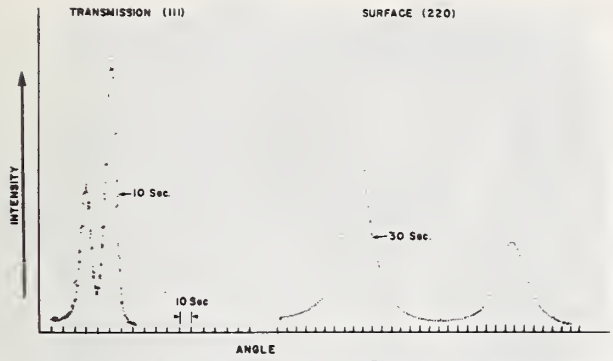

Fig. 8 Diffraction rocking curves in both surface reflection and transmission geometry for crystal #026302. In this alignment, both copper $K\alpha_1$ and $K\alpha_2$ radiation components are present with the smaller peak due to $K\alpha_2$

alignments, the ATC and the scanning spectrometer. The topographs taken by the ATC usually gave the entire view of the sample crystals, unless the crystal size was larger than the size of the x-ray beam. Examples of the topographs are shown in Figs. 10a and b in both the reflection and the transmission geometry from an as-grown crystal. Since for lack of space we cannot show all the topographs here, we shall describe the qualities of the crystals as-grown under various growth conditions, based on their topographs.

The crystals grown under Growth Condition I with a narrow neck generally produced surface topographs (obtained by a surface Bragg diffraction) almost as good as those shown in Fig. 10a, but with a continuous distribution of darkness (excess intensity) areas which we call "strain contours". The transmission topographs (taken in transmission geometry) indicated, however, much poorer quality in those crystals, showing the anomalous transmission only in about 50% of the total area.

In contrast, the crystals grown in Growth Condition I with a wider neck showed much poorer quality in their surface topographs, in which not only the strain contours, but many lines of imperfections appeared. These crystals usually did not produce good transmission topographs.

The crystals grown in Growth Condition II were of a quality similar to those grown in Growth Condition I with larger necks. The surface topographs showed many strain contours and often the topograph images did not cover the entire exposed area of the crystals. The transmission topographs were broken up into many areas, indicating that the perfect crystal areas were very much limited to small local regions. These results were consistent in this growth condition, regardless of their bottle-neck diameters.

The crystals grown in Growth Condition III with a narrow neck generally displayed the highest quality of perfection. Fig. 10a and b are examples of the topographs from the crystals grown in this condition. The surface topographs showed far fewer crater-type images than those taken from crystals grown under other growth conditions. The number of visible dislocations in the surface topo-

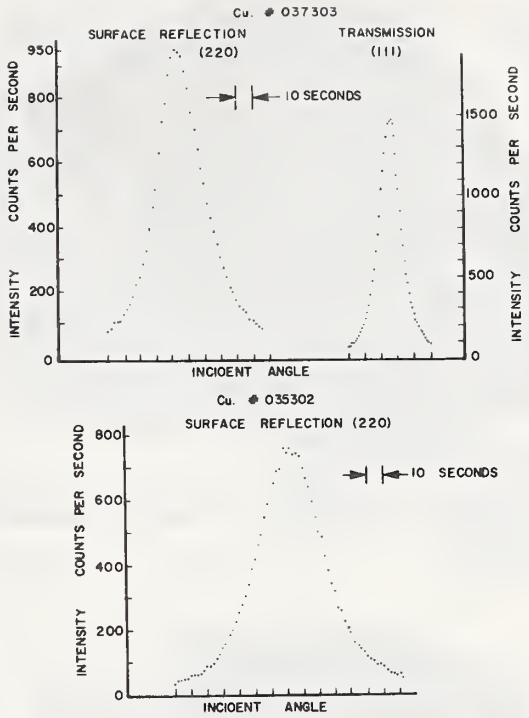

Fig. 9 Diffraction rocking curves taken from a typically good crystal (#037303) in both surface reflection and transmission geometry and a typically poor crystal (#035302) in surface reflection

graphs are found to range between 11 and 100 dislocations per cm^2 for the crystals as-grown in this condition. The transmission topographs, however, reveal more imperfections in the interior of the crystals, as shown in Fig. 10b. One of the common features in the transmission topographs from these crystals is shown in Fig. 11, although this crystal happened to show this feature in a somewhat exaggerated fashion. In this topograph, many lines run normal to the <111> direction. The Bragg diffraction in this case is (111). Also, additional lines, though less visible, run normal to the $\langle\bar{1}11\rangle$ direction. In addition, there appear black and white bands parallel to the <110> direction. Those lines are caused by extended dislocations associated with a stacking fault, running almost parallel to the $\langle 10\bar{1}\rangle$ direction. The lines probably represent Lomer-Cottrell locking of the interacting dislocations.(19)(20)

The crystals grown in this condition but with a large neck diameter generally produced topographs of almost the same quality of perfection as the crystals grown in Growth Condition I with a large bottle-neck. The transmission topographs consisted of several regions, indicating that there were few highly perfect regions throughout the crystals. The crystals grown in Growth Condition IV could not be investigated by x-ray topography, as they were not single crystals.

Under the Growth Condition V, regardless of the bottle-neck diameter, the crystals displayed typical mosaic structures, as shown in Fig. 12. No transmission topographs were produced.

Now we turn to the annealing effects. As

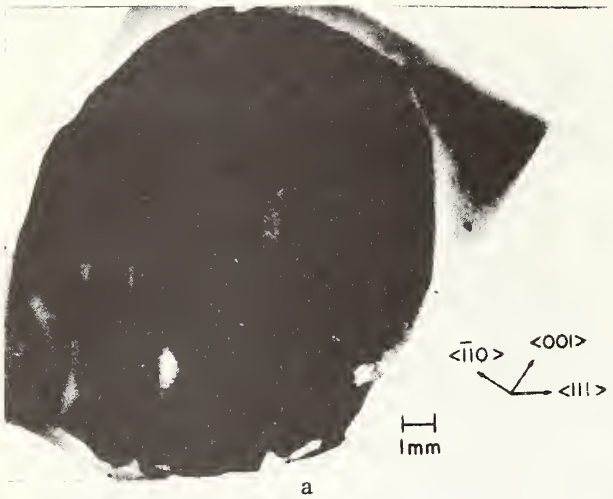

a

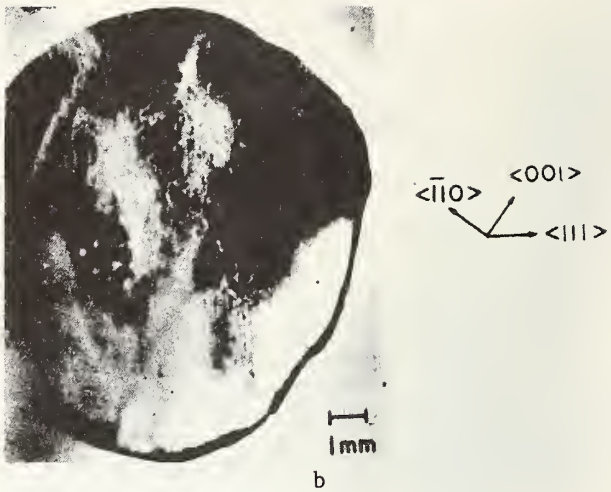

b

Fig. 10 ATC topographs of as-grown crystal #028303, growth condition III
a. (220) surface reflection composite topograph b. (111) transmission topograph

Many of the topograph enlargements are composite photographs resulting from microscope limitations during enlargement.

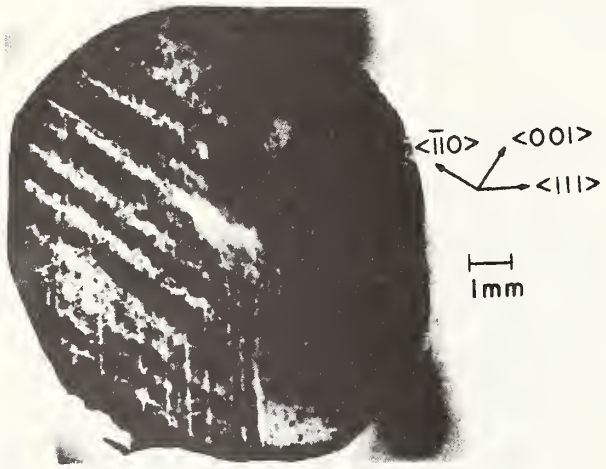

Fig. 11 ATC transmission topograph of as-grown crystal #037303, growth condition III

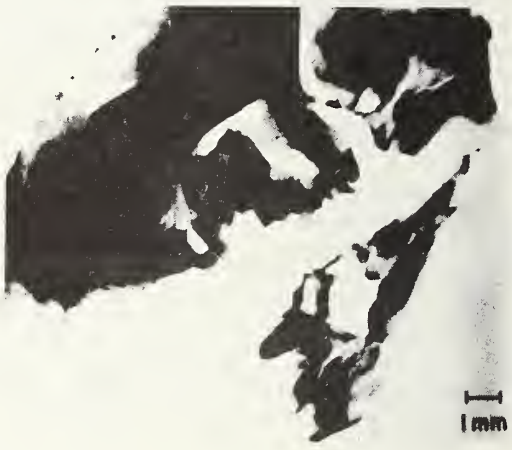

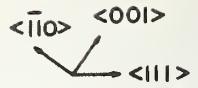

Fig. 12 ATC surface reflection composite topograph of as-grown crystal #034303, growth condition V

indicated in Table II, at least one crystal from the boules in each growth condition was annealed. The surface topograph from an annealed crystal of Growth Condition V is just as bad as Fig. 12, indicating that the mosaic structure was not affected by annealing. The annealed crystals of Growth Condition II showed polygonization, which usually resulted in the formation of several subgrains.

All the topographs taken from the annealed crystals in Growth Conditions I and III showed an equally high degree of perfection in both surface and transmission geometry. The resultant degree of perfection was almost independent of the bottle-neck diameters. Examples of the surface and transmission topographs are shown in Fig. 13a and b of Growth Condition III. As seen in the transmission topographs, the Lomer-Cottrell locks of dislocations disappeared and dislocation net works appeared rather randomly.

The number of dislocations counted on the surface topographs for these annealed crystals was less than 23 dislocations per cm^2, the smallest number observed was 7 disl./cm^2. The dislocation densities can be obtained from the transmission topographs which show the dislocations in the interior of the crystals. In this case, the dislocation density is equal to the number of dislocations multiplied by the length of each dislocation divided by the volume where the dislocations are counted. The average number of dislocations thus obtained was 15 dislocations per cm^2. The smallest number was 12.8 dislocations per cm^2. In these annealed crystals, there were always subgrain boundaries observed, which were, of course, considered to be piled-up dislocations, but were not included in the count of individual dislocations. The subgrain boundaries would have eventually been driven out of the crystals, if we had annealed the crystals for a longer period of time. In the transmission topograph taken on the scanning spectrometer, the details of the dislocation networks are clearly visible. A few examples of enlarged topographs taken by the spectrometer are shown in Fig. 14 a and b, representing a highly

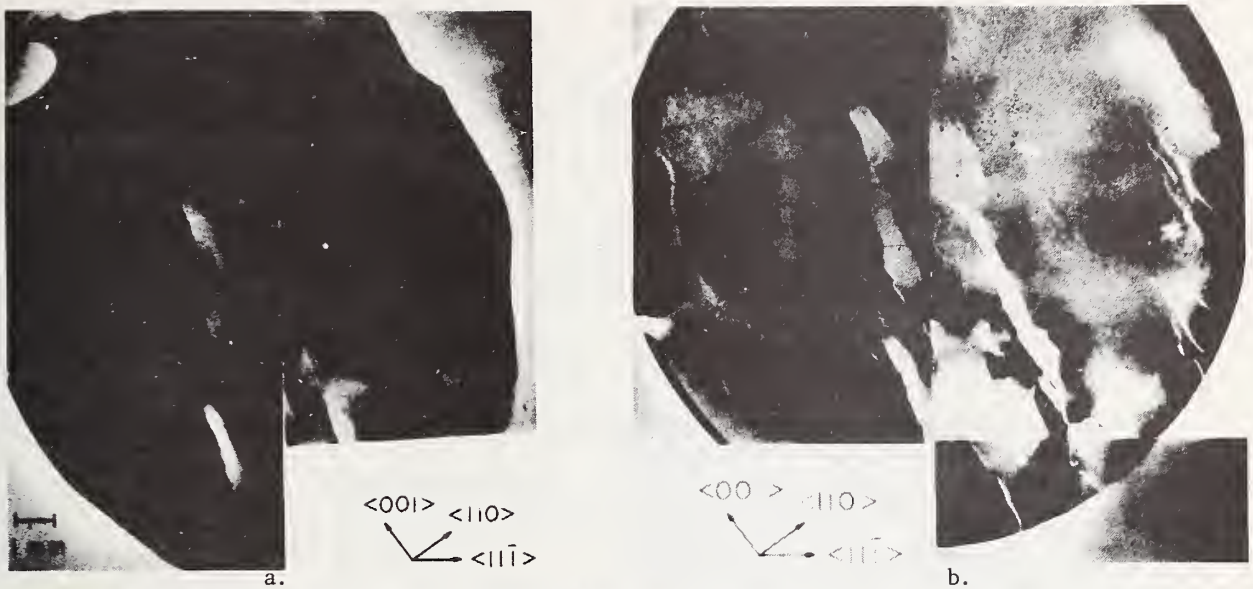

a. b.

Fig. 13 Scanning spectrometer topographs of annealed crystal #025302
a. (220) surface reflection composite topograph b. (111) transmission composite topograph

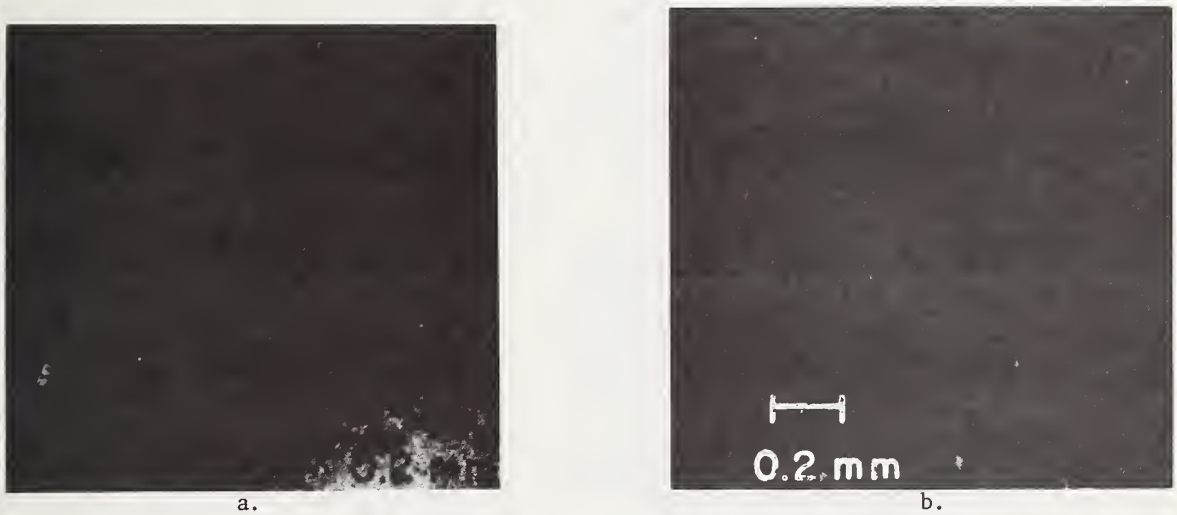

a. b.

Fig. 14 Enlarged regions of scanning spectrometer topographs
a. highly perfect region b. highly dislocated region

perfect region and a highly dislocated region, respectively.

V. Conclusion and Discussion

Before concluding this paper, we would like to emphasize one of our principles followed in conducting the present work. At present, many people believe that growing perfect crystals is still an art where personal skills play significant roles. Although we do not object to this view, and often agree with it based on our experience, we have attempted to eliminate such art from the present work. This attitude probably resulted in producing crystals less perfect than they could be. However, we see significance in establishing reproducibility of the resultant crystal perfection as a functional of growth conditions, rather than a functional of the "art" part of crystal growth technology. In the present work, we grew crystals as routinely as possible, with the least amount of human control. Once the variables were set, we did not attempt to modify these variables in response to local perturbations which occurred from time to time during growth. During the growth process, we were tempted more than once to correct the diameter by changing temperatures or to increase the pulling or rotation speed when the melt surface started vibrating occassionally. However, we made none of these corrections.

The spectroscopic data indicated that Growth Condition III generally produced crystals of higher perfection, along with crystals produced under Growth Condition I with narrow necks. These results are in good agreement with the observations of the x-ray topographs. The topographs obtained by the scanning spectrometer further helped to distinquish the subtle differences in crystals grown under conditions I and III. Those topographs indicated that Growth Condition III with narrow

bottle-necks usually produced crystals of better quality than Condition I. The other growth conditions are clearly inferior to Conditions I and III. It is, therefore, concluded that Growth Condition III is most optimum for growing a single crystal of high perfection, when the bottle-neck is made less than one millimeter in diameter.

If one anneals crystals, Growth Conditions I and III with narrow bottle-necks result in almost the same degree of crystal perfection. However, crystals grown in the other conditions did not show much improvement in quality as a result of annealing. It is, therefore, further concluded that annealing becomes most effective only when the grown crystals are already highly perfect.

In the optimum growth condition, the density of dislocations can be as low as 11 dislocations per cm^2 for "as-grown" crystals, and as low as 7 dislocations per cm^2 for annealed crystals. The lowest dislocation density measured from the transmission topographs was 12.8 dislocations/cm^2 which is in good agreement with the dislocation densities determined from surface topographs.

As an initial approach to the study of fluid flow effects in the melt on metal crystal growth, we have placed emphasis on the documentation of the resultant crystal perfection under various fluid flow conditions. The fluid flow conditions have been described by several directly controllable process parameters. It is obvious at this stage that these parameters are not yet connected to the more sophisticated basic physical quantities as the thermodynamical variables which directly characterize the state of fluid flow. There is, however, no unperturbing method of directly measuring physical quantities of fluid flow while crystals of high perfection are being grown. Any disturbance of the melt destroys or drastically changes the resultant perfection of grown crystals. Once the relation between crystal perfection and fluid flow conditions as given by the process parameters is established, one can characterize by other direct methods the fluid flow motion under a given set of the process parameters, regardless of the consequences on the crystal perfection of grown crystals.

1. S. Howe and C. Elbaum, Phil. Mag. 6 (1961) 1227.
2. S.H. McFairlane and C. Elbaum, Appl. Phys. Letters I (1965) 43.
3. F.W. Young and J.R. Savage, J. Appl. Phys. 35 (1964) 1917.
4. H. Fehmer and W. Uelhoff, J. Sci. Instrum. 2 (1969) 771.
5. E. Kappler, W. Uelhopp, H. Fehmer and F. Abbink, "Herstellung von Kupereinkristallen kleiner Versetungsdichte" Forschungsberichte des Landes Nordrhein-Westfalen Nr. 2181, Westdeutcher Verlag, Opladen.
6. C.H. Sworn and T.E. Brown, J. Cryst. Growth 15 (1972) 195.
7. W.C. Dash, J. Appl. Phys. 30 (1959) 459.
8. E. Billing, Proc. Roy. Soc. (London) A235 (1956) 37.
9. P. Penning, Philips Res. Repts. 13 (1958) 79.
10. J.C. Brice, J. Crystal Growth 2 (1968) 395.
11. A. Steinemann and V. Zimmerli, J. Phys. Chem. Solids. Suppl. 1, (1967) 81.
12. J.Z. Czochralski, Phys. Chem. 92 (1917) 219.
13. F.W. Young and T.R. Wilson, Rev. Sci. Instru. 32 (1961) 559.
14. P.P. Ewald, Ann. Physik 49 (1916) 1 and 117; 54 (1917) 519.
15. M.v. Laue: Erg. exakt. Naturw. 9 (1931) 133.
16. M. Ashkin and M. Kuriyama, J. Phys. Soc. Japan 21 (1966) 1549.
17. M. Kuriyama, J. Phys. Soc. Japan 23 (1967) 1369, Acta Cryst. A25 (1969) 682; Zs. Naturforschung 28a (1973) 622.
18. G. Borrmann, Phys. Z. 42 (1941) 157, Z. Phys. 127 (1950) 297.
19. W.M. Lomer, Phil. Mag. 42, (1951) 1327.
20. A.H. Cottrell, Phil. Mag. 43, (1952) 645.

Appendix II

J. Appl. Cryst. (1974) Vol. 7

An Immobile Dislocation Arrangement in As-grown Copper Single Crystals Observed by X-ray Topography

by

Masao Kuriyama, James G. Early and Harold E. Burdette

Institute for Materials Research
National Bureau of Standards
Washington, D. C. 20234, U.S.A.

Abstract

X-ray diffraction topography using transmission geometry has revealed an interesting array of extremely straight and narrow long line images in sizable copper single crystals grown under particular growth conditions by the Czochralski technique. These images are analyzed and elucidated by a model of Lomer-Cottrell dislocations. The formation of these sessile dislocations usually aids the growth of large copper crystals of high perfection. The high-degree of perfection over the entire volume of the crystals accounts for such macroscopic arrangements of Lomer-Cottrell dislocations which have not previously been observed by electron microscopic techniques.

1. Introduction

There have been several reports on growing metal single crystals containing regions which are totally dislocation-free (Howe and Elbaum, 1961; McFarlane and Elbaum, 1965). In particular, copper crystals of high perfection have been prepared and studied in detail by Young and Savage (1964) and Fehmer and Uelhoff (1969). More recently, Sworn and Brown (1972), followed by Tanner (1972), have demonstrated that copper crystals, although small in diameter, could be grown free of dislocations by initially narrowing the crystal diameter at one region of the boule.*

Even with these studies, however, the documentation of the growth conditions for the preparation of dislocation-free metal crystals still is far from complete, unlike in the case of semiconducting crystals (Billig, 1956; Penning, 1958; Brice, 1968; Dash, 1959; Steinemann and Zimmerli, 1967). Continued efforts are still needed to establish reproducible growth conditions for the production of large, highly perfect metal crystals. As one such effort Kuriyama, Early and Burdette (1974) have recently studied the relationship between fluid flow conditions and the degree of crystal perfection during the growth of large, highly perfect copper crystals by the Czochralski technique. In this study, x-ray diffraction topography has revealed that one particular growth condition results in many extremely straight dislocation lines in the crystals. These lines run across almost the entire diameter of the crystal, and lie in a crystallographic set of three possible slip planes for the face-centered cubic crystal. Interestingly, these lines can also be

---

* The reader should keep in mind always that the term "dislocation free" is always dependent on the technique used to detect the dislocations.

observed with good contrast in the topographs when this particular set of slip planes is chosen as diffracting planes. Consequently, these dislocation lines cannot be identified simply as ordinary edge or screw dislocations. The purpose of this paper deals with an identification of those extremely straight line structures observed in these as-grown copper crystals.

2. Experimental Procedures

The details of the crystal growth procedures and the assessment of crystal perfection by x-ray dynamical diffraction have been described in a previous paper (Kuriyama, Early and Burdette, 1974). In the present paper, we shall only describe the experimental conditions relevant to the present work. Large copper single crystals were grown from single crystal seeds in a vacuum furnace by the Czochralski technique. The pulling speed was between 0.013 cm/min. and 0.100 cm/min. The melt and seed were rotated around a common axis in the same direction with speeds ranging from 5 rpm to 20 rpm; the relative speed of rotation was 0.6 rpm. Copper of 99.999% purity was used as the melt charge. Crystal boules were grown by initially narrowing the boule diameter at one region, thus forming a bottle-neck. The grown crystals were about 6 cm long with diameters between 1.5 cm and 3.0 cm and with a bottle-neck diameter of 0.5 mm. The boules were sliced into discs by an acid saw and the discs were polished on an acid polishing wheel in the same manner as Young and Wilson (1961). The discs have $(1\bar{1}0)$ planes as their parallel faces, so that the four strongest diffracting planes, (111), $(11\bar{1})$, (002) and (220), can be used in transmission geometry.

For the assessment of the perfection of sample crystals, we employed two different x-ray optical arrangements, namely an asymmetrical crystal topographic camera and a high resolution double crystal scanning diffractometer.

The former, which will be hereafter called asymmetrical crystal topography (ACT), is equipped with a monochromator made from a silicon crystal whose surface makes an angle of 13.5° with the (111) diffracting plane for Cu Kα radiation. The incident x-ray beam falls on the silicon crystal surface almost parallel to it, and the (111) diffracted beam appears with a size of 1.7 cm x 2.5 cm, sufficiently large to cover the entire area of the sample copper crystals. In the latter arrangement, which will in the future be called the scanning diffractometer (SCAD), a scanning device is attached to a high resolution double crystal diffractometer so that the well collimated narrow beam can scan with high resolution the entire crystal. This enables us to obtain the profiles and widths of rocking curves at any location in the crystal. The quality of the beam in SCAD was checked by measuring the rocking curves of a dislocation free germanium crystal which was placed at the second crystal position. The full width at half maximum (FWHM) of the rocking curve from the (220) germanium diffraction was determined to be 12.8 seconds of arc in the Si (220) surface/Ge (220) surface mode and 15.5 seconds of arc in the Si (220) transmission/Ge (220) surface mode, using Cu Kα radiation. This silicon crystal was used as the first crystal or monochromator in either transmission or reflection geometry to obtain the rocking curves and scanning topographs from sample copper crystals.

The thickness of the copper discs was determined by the anomalous transmission effect (Kuriyama, Early and Burdette, 1974) as shown in Fig. 1. The thickness can be geometrically related to the distance between the images L_o and L_s. The thinnest disc was 0.1439 mm thick and the thickest was 0.8934 mm thick. The product of the ordinary linear absorption coefficient and thickness thus ranged from 7.93 to 49.24 for Cu Kα radiation.

3. Rocking Curve Widths and Topographs

The rocking curves were obtained from the copper discs by the $(2\bar{2}0)$ diffraction in the reflection geometry and the (111), $(\bar{1}\bar{1}\bar{1})$, $(11\bar{1})$, and (002) in the transmission geometry. For as-grown crystals, the peak intensity of the rocking curves varied up to 30% at different locations in the crystal. The width of the curves, however, did not vary as much. The values (FWHM) of the rocking curve widths, averaged over the crystals, are 34 seconds of arc for the $(2\bar{2}0)$ surface reflection, and 14, 13 and 12 seconds of arc, respectively for the (111) and $(\bar{1}\bar{1}\bar{1})$, $(11\bar{1})$ and (002) diffraction in the transmission geometry.* Typical profiles of the rocking curves are shown in Fig. 2 for these diffracting planes.

Fig. 3 shows a topograph taken by the ACT in the reflection geometry of the $(2\bar{2}0)$ diffraction.** This represents the usual surface reflection topograph taken from the crystals grown under the conditions described in section 2. An example of the transmission topographs also taken by the ACT is shown in Fig. 4, where the (002) diffraction was used. The crystal used for this topograph was determined by the anomalous transmission effect to be 0.1439 mm thick. This topograph illustrates the common features in the transmission topographs from the crystals grown under the present growth condition. In this topograph, many lines run normal to the $[11\bar{1}]$ direction, while another set of lines runs normal to the [111] direction. In addition, there appear black and white bands parallel to the [110] direction. As indicated in Fig. 4, the first set of lines is denoted by set I, the second by set II, and the set of bands by set III.

---

* The rocking curve width in the transmission geometry varies as the crystal thickness changes. The values reported here are obtained from a crystal of $\mu L = 7.93$.

** Several of the topograph enlargements are composite photographs resulting from microscope limitations during enlargement.

The transmission topographs obtained from the (111), $(11\bar{1})$, (002) and (220) diffractions are reproduced in Fig. 5a, b, c and d, respectively. It is observed in these topographs that the image contrast of the sets, I and II, depends on the diffracting planes used. The experimental results from these topographs can be summarized as follows:

1) The lines in the sets, I and II, are extremely straight, narrow, and discontinuous, running almost across the entire crystal.
2) The lines in set I lie in the $(11\bar{1})$ plane; when the images of these lines are projected on the $(1\bar{1}0)$ plane, the plane of the topographs, they run parallel to the [112] direction.
3) The lines in set II lie in the (111) plane; when the images of these lines are projected on the $(1\bar{1}0)$ plane, the plane of the topographs, they run parallel to the $[11\bar{2}]$ direction.
4) In the $(11\bar{1})$ diffraction, the lines in set I have better contrast than those in set II. In the (111) diffraction, the relation of contrast is reversed. In the (002) and (220) diffraction conditions, both set I and II appear to have equal contrast.
5) Set III consists of black and white bands running in the [110] direction.

In this paper, we confine ourselves to the identification of sets I and II.

4. A sessile dislocation arrangement

In dynamical diffraction, the image contrast due to crystal imperfections is determined by the factor $\{1 - \exp[i\underset{\sim}{H} \cdot \underset{\sim}{u}(\underset{\sim}{r})]$, where $\underset{\sim}{H}$ is a reciprocal lattice vector in a reference perfect crystal and $\underset{\sim}{u}(\underset{\sim}{r})$ is an atomic displacement vector at a position $\underset{\sim}{r}$ inside the crystal (Kuriyama, 1967; 1969). In the first order approximation for almost perfect crystals, this factor may be replaced by $\partial \{\underset{\sim}{H} \cdot \underset{\sim}{u}(\underset{\sim}{r})\}/\partial\sigma_K$, where σ_K is a coordinate along the x-ray

propagation direction (Kuriyama, 1970; 1972; 1973). There are two propagation directions in a single Bragg diffraction; one is the transmitted direction ($\underset{\sim}{K} = \underset{\sim}{0}$) and the other the Bragg diffracted direction ($\underset{\sim}{K} = \underset{\sim}{H}$). In x-ray diffraction topography, the principal concern is not with quantitative information on the imperfections, but rather, the qualitative visual impact given by the imperfections through such information as their locations, shapes and distributions. In a crude approximation which is suitable for qualitative topography, the local contrast condition may be replaced by a simpler factor $\underset{\sim}{H} \cdot \underset{\sim}{u}(\underset{\sim}{r})$ or $\underset{\sim}{H} \cdot \underset{\sim}{b}$, where $\underset{\sim}{b}$ is the Burgers vector of a dislocation. It should be, of course, noted even in this crude approximation that $\underset{\sim}{u}(\underset{\sim}{r})$ is not parallel to $\underset{\sim}{b}$. However, the crude contrast factor, $\underset{\sim}{H} \cdot \underset{\sim}{b}$, is convenient for practical purposes.

This contrast condition first eliminates the possibility that the lines in sets I and II are glissile dislocations of a pure screw or pure edge character. Such dislocations lie in a slip plane, and their Burgers vectors also lie in this plane. When this slip plane is used as a diffracting plane, there will not be image contrast for these dislocations. In contrast with this prediction, the lines are clearly visible in the topographs under these particular diffraction conditions, as the summarized results indicate. Results 2 and 3 state that these lines lie in the (111) slip planes and the $(1\bar{1}\bar{1})$ slip planes, respectively for set II and set I. Let us first assume that these line images are caused by dislocations. The formation of the clear images under the particular diffraction conditions implies that the Burgers vectors, or more correctly those significant atomic displacements associated with the dislocations, do not lie in the dislocation slip planes. Along with

result 1, this strongly suggests that the dislocations observed in the topographs could be dislocations interacting with each other to form immobile lines of dislocations i.e. Lomer-Cottrell locks (Lomer, 1951; Cottrell, 1952).

In a face-centered cubic crystal, the possible interactions of dislocations on two intersecting slip planes have been studied extensively (for example, Cottrell, 1964; Hirth and Lothe, 1968). Let us consider set II as an example. Result 3 demands that the lines of dislocations should be either in the $[0\bar{1}1]$ direction or in the $[\bar{1}01]$ direction. The possible lock direction $[\bar{1}10]$ would not be visible in the topographs, because this direction is perpendicular to the $[11\bar{2}]$ direction in which the observed line images of set II run in the plane of the topographic images. In order to produce the locks in the direction of $[0\bar{1}1]$, the two intersecting slip planes have to be (111) and $(1\bar{1}\bar{1})$. For the locks in the direction of $[\bar{1}01]$, the (111) and $(\bar{1}1\bar{1})$ planes are involved. There are three possible directions of the Burgers vectors in each slip plane. These three dislocations in a slip plane can therefore interact with three possible dislocations in the other intersecting slip plane. After consideration of (i) which pairs of dislocations can be energetically stable, (ii) which of the stable pairs can glide afterwards, and (iii) which form annihilated screw disloactions, only two pairs are found which can form a sessile dislocation line that runs parallel to a given locking direction. Both pairs result in the same Burgers vector which lies in neither of the original slip planes. For the $[0\bar{1}1]$ locking direction, the resultant Burgers vector is (1/2) [011]. We denote this Lomer-Cottrell lock as

type II A. For the dislocation locked in the $[\bar{1}01]$ direction, the resultant Burgers vector is given by (1/2) [101]. This lock is denoted as type II B. In a similar fashion, we find for set I the following Lomer-Cottrell locks; IA runs parallel to the [011] direction with the Burgers vector (1/2) $[01\bar{1}]$, and IB runs in the [101] direction with the Burgers vector (1/2) $[\bar{1}01]$.

Next we apply the approximate contrast conditions for these possible locks to the diffraction conditions used. The results are shown in Table I. As mentioned previously, the contrast condition resulting in $\underset{\sim}{H} \cdot \underset{\sim}{b} = 0$ simply means that the image contrast under such a diffraction condition is inferior to the contrast under different diffraction conditions. These results are in a good agreement with the observed results 3 and 4. Since all the dislocation lines of these locks make an angle of about 30° with the $(1\bar{1}0)$ plane, they should terminate on the crystal surface. To confirm this, topographs were taken in high resolution by the SCAD under the $(2\bar{2}0)$ diffraction condition in the reflection geometry. As shown in Fig. 6, we observe that the dislocation images on the surface topograph are indeed aligned, though short in their length, in the exactly same way as predicted. In Fig. 6, the images of the terminating dislocations of set II run in the vertical direction perpendicular to the [111] direction.

In addition, the high resolution topographs were taken by the SCAD in the transmission geometry for the (111), $(11\bar{1})$, and (002) diffraction. As shown in Fig. 7, the line images of sets I and II are indeed very narrow. We thus conclude that the assumption of Lomer-Cottrell locks elucidates all the results listed in section 3 with the exception of result 5.

5. Discussion

Lomer-Cottrell dislocations have been found in face-centered cubic crystals by electron transmission microscopy (Whelan, 1958; Mader, Seeger

and Thieringer, 1963). They appear, however, as a rather isolated local event in the entire crystal. The length of the dislocations are short. Unlike the observations in electron transmission microscopy, the Lomer-Cottrell dislocations observed in the present paper have occurred almost throughout the entire crystal, and their length is on a macroscopic scale. The difference between the electron microscopic and the x-ray topographic observations can be attributed to the following facts. First, the crystals used for x-ray topography are bulk (1.5 cm in diameter and almost 1 mm thick) compared with the thin-films used for electron transmission microscopy. Next, due to the over-all high degree of perfection in the bulk crystals (judged from their display of the prominent Borrmann anomalous transmission effect), all the regions in the interior of the crystals are likely to have similar properties with respect to each other. If the formation of a Lomer-Cottrell dislocation is energetically favorable at one place, there is no doubt that dislocations of a similar type would occur everywhere inside the crystal. This phenomenon is very unlikely to occur in thin films, since the perfection of these thin films is not as high over the entire film as these crystals used for x-ray anomalous transmission topography. The simultaneous use of x-ray topography with a simple metal crystal of high perfection has, for the first time, made it possible to observe the extensive arrays of Lomer-Cottrell dislocations on a macroscopic scale over the entire volume of the crystals.

There are a few additional comments worthy of note concerning the growing of sizable perfect copper single crystals. When a slice of the as-grown crystal show the arrangements of Lomer-Cottrell dislocations over its entire volume, as shown above, the degree of crystal perfection is equally high for any part of the crystal boule of about 6 cm long.

In contrast, some as-grown crystals grown under different growth conditions frequently show a high degree of perfection in one portion of the boule, but not necessarily the same quality of perfection in other parts of the boule. Most of these crystals tend to develop low angle grain boundaries somewhere along the length of the boule. This fact may indicate that a particular growth condition aids dislocation interactions to form immobile Lomer-Cottrell locks. When this phenomenon takes place, the resultant crystal becomes highly perfect. If widespread slip occurs or if many dislocations form randomly, as in the case of the other growth conditions, then the locking would not take place and the dislocations would still be mobile and affect the subsequently grown part of the crystal, resulting in a less perfect crystal.

The work reported herein was partially sponsored by the Advanced Missions Program of The National Aeronautics and Space Administration under Contract W-13,475 No. 1. The authors wish to express their thanks to Dr. Roland de Wit and Dr. A. W. Ruff of the Metallurgy Division, National Bureau of Standards for their discussion.

References

1. Billig, E. (1956) Proc. Roy. Soc. (London) A 235 37-55.

2. Brice, J.C. (1968) J. Cryst. Growth 2 395-401.

3. Cottrell, A.H. (1952) Phil. Mag. 43 645-647.

4. Cottrell, A.H. (1964) "Theory of Crystal Dislocations" Gordon and Breach, New York.

5. Dash, W.C. (1959) J. Appl. Phys. 30 459-474.

6. Fehmer, H. and Uelhoff, W. (1969) J. Sci. Instrum. 2 771-775.

7. Hirth, J.P. and Lothe, J. (1968) "Theory of Dislocations" McGraw-Hill, New York.

8. Howe, S. and Elbaum, C. (1961) Phil. Mag. 6 1227-1240.

9. Kuriyama, M., Early, J.G. and Burdette, H.E. (1974) Proc. of AIAA 12th Aerospace Sciences Meeting, Paper No. 74-204.

10. Kuriyama, M. (1967) J. Phys. Soc. Japan 23 1369-1379.

11. Kuriyama, M. (1969) Acta Cryst. A 25 682-693.

12. Kuriyama, M. (1970) Acta Cryst. A 26 56-59.

13. Kuriyama, M. (1972) Acta Cryst. A 28 588-593.

14. Kuriyama, M. (1973) Zs. f. Naturforsch. 28a 622-626.

15. Lomer, W.M. (1951) Phil. Mag. 42 1327-1331.

16. Mader, S., Seeger, A. and Thieringer, H. (1963) J. Appl. Phys. 34 3376-3386.

17. McFarlane, S.H., and Elbaum, C. (1965) Appl. Phys. Letters 1 43-44.

18. Penning, P. (1958) Philips Res. Repts. 13 79-97.

19. Steinemann, A. and Zimmerli, V. (1967) J. Phys. Chem. Solids, Suppl. 1, 81-87.

20. Sworn, C.H. and Brown, T.E. (1972) J. Cryst. Growth 15 195-203.

21. Tanner, B.K. (1972) J. Cryst. Growth 16 86-87.

22. Whelan, M.J. (1958) Proc. Roy. Soc. A 249 114-137.

23. Young, F.W. and Savage, J.R. (1964) J. Appl. Phys. 35 1917-1924.

Table I

Contrast Factor for possible Lomer-Cottrell Locks

	Directions		Contrast Factor			
Type of Locks	Line	Burgers Vector	(111)	$(11\bar{1})$	(002)	(220)
I A	[011]	$[01\bar{1}]$	0	$\sqrt{\frac{2}{3}}$	$\frac{1}{\sqrt{2}}$	$\frac{1}{2}$
I B	[101]	$[\bar{1}01]$	0	$\sqrt{\frac{2}{3}}$	$\frac{1}{\sqrt{2}}$	$\frac{1}{2}$
II A	$[0\bar{1}1]$	[011]	$\sqrt{\frac{2}{3}}$	0	$\frac{1}{\sqrt{2}}$	$\frac{1}{2}$
II B	$[\bar{1}01]$	[101]	$\sqrt{\frac{2}{3}}$	0	$\frac{1}{\sqrt{2}}$	$\frac{1}{2}$

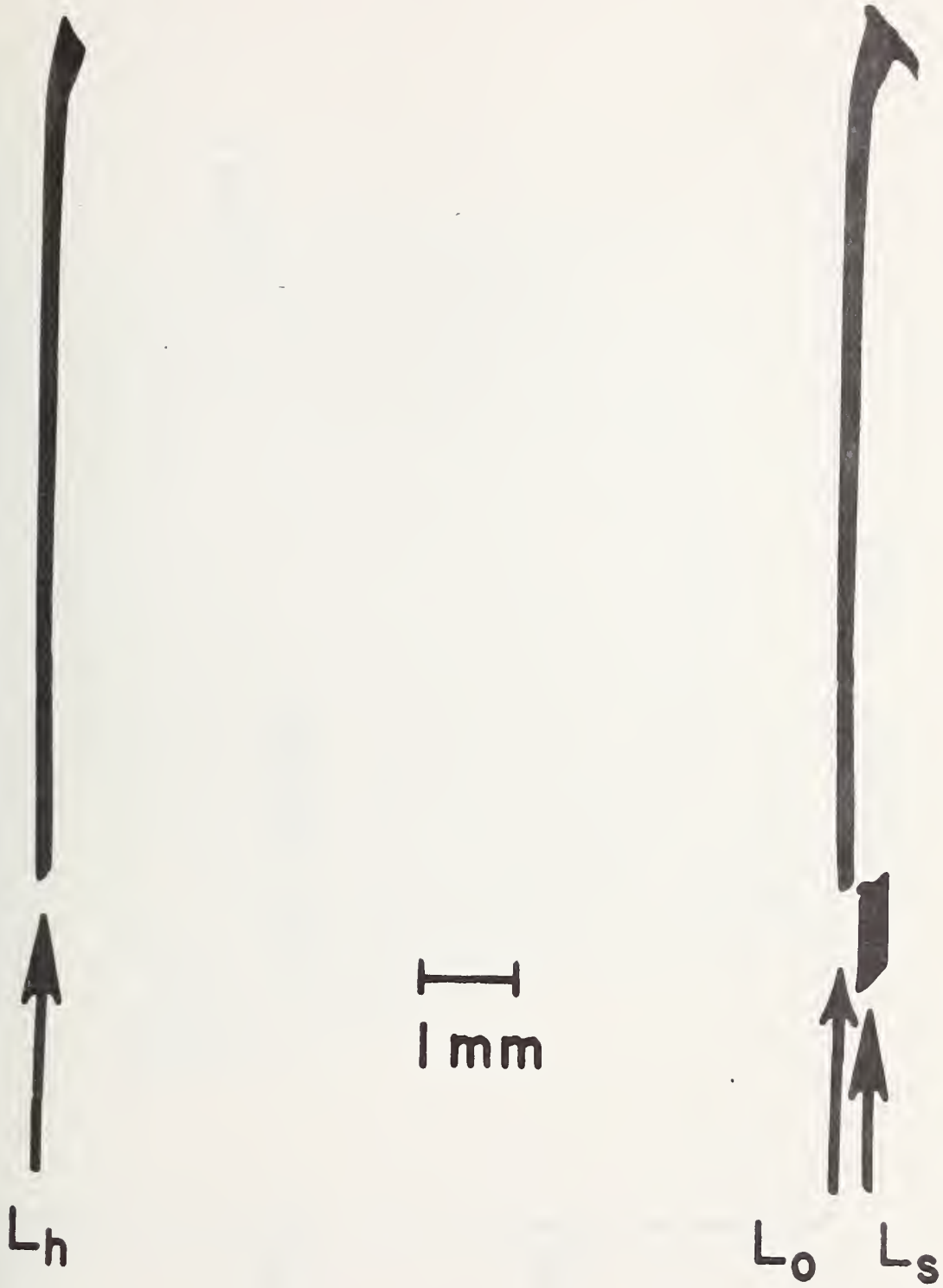

Fig. 1 Photograph illustrating the Borrman anomalous transmission effect in a copper crystal grown under the conditions described in the text. The photograph indicates the parameters used to determine the crystal thickness. L_o and L_h are the beam images diffracted in the transmitted and the Bragg diffracted direction, respectively. L_s is the image of a part of the line-shaped incident beam.

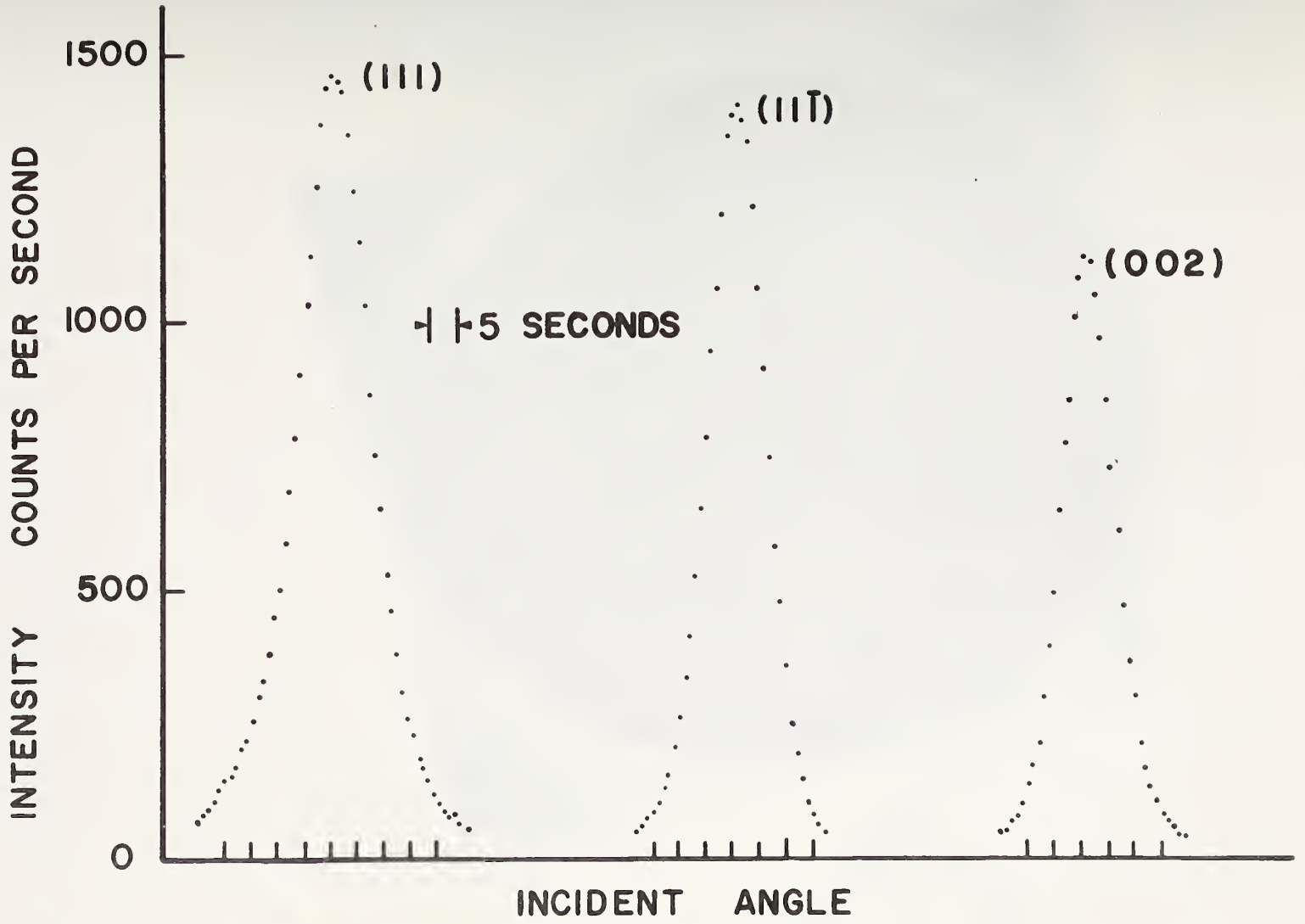

Fig. 2 Rocking curves for the (111), (11$\bar{1}$) and (002) diffraction in the transmission geometry.

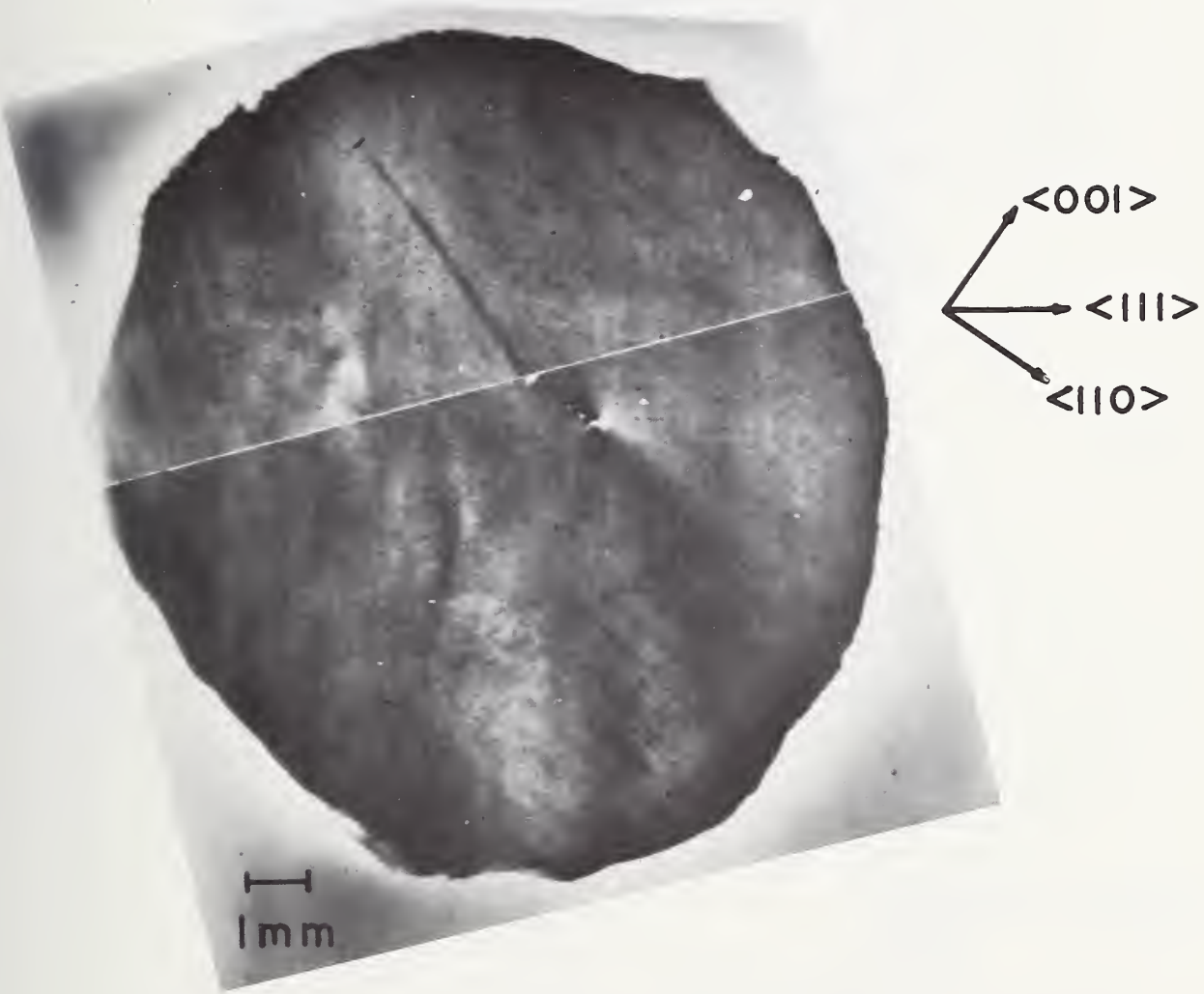

Fig. 3 ACT topograph of the $(2\bar{2}0)$ diffraction in the reflection geometry.

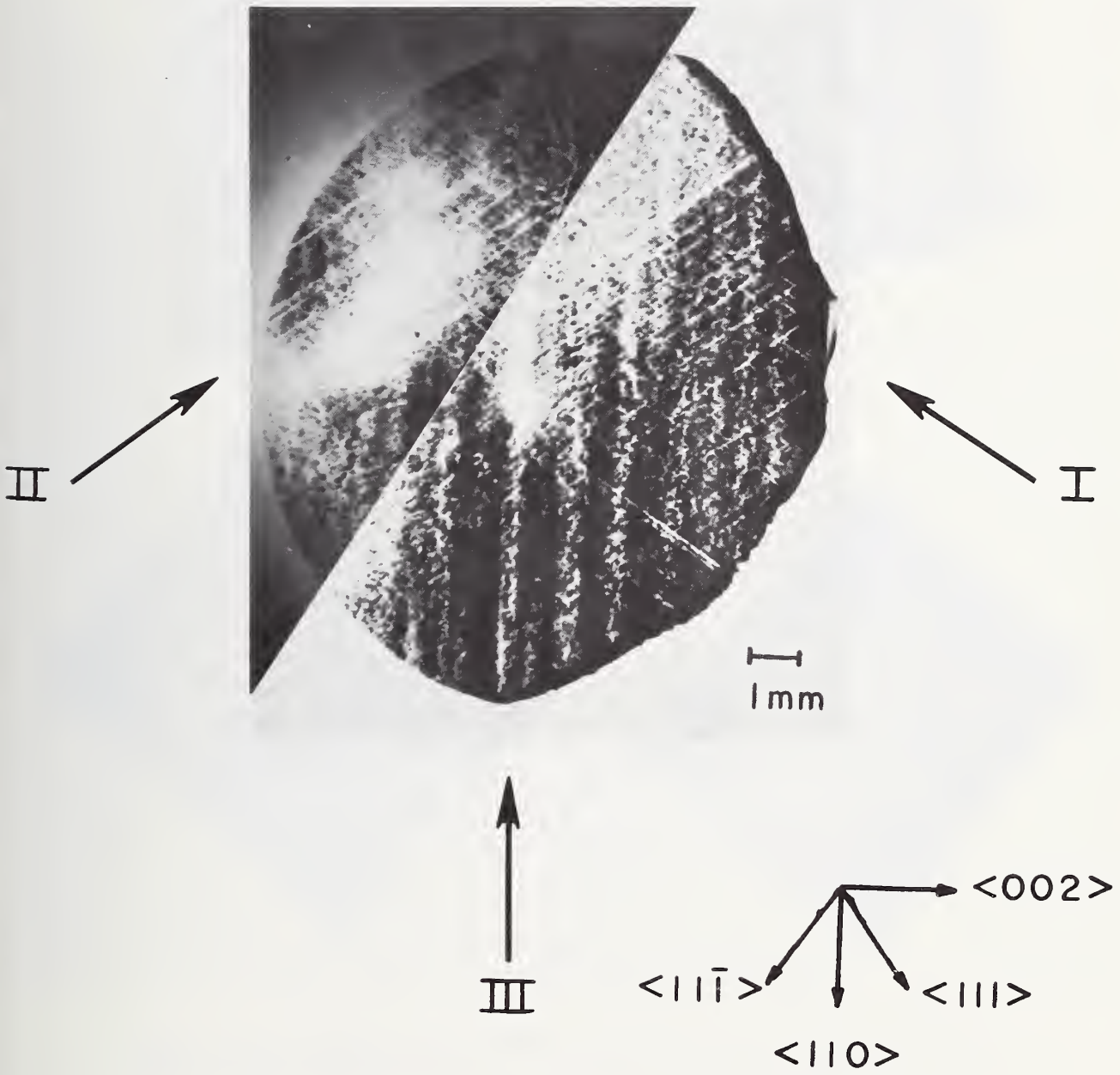

Fig. 4 ACT topograph of the (002) diffraction in transmission geometry. Three sets of images are indicated with the arrows indicating the direction parallel to the line images of each set.

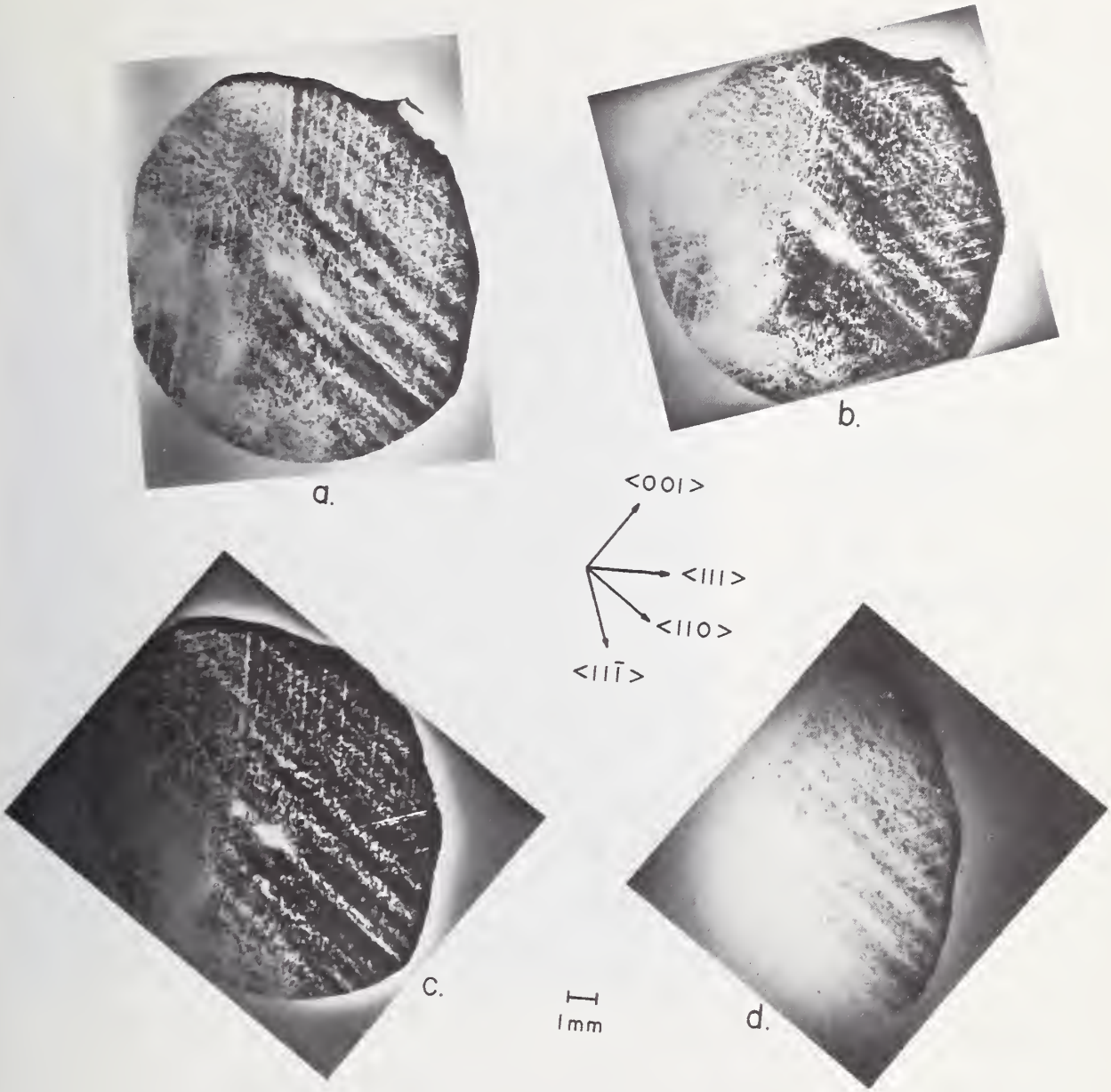

Fig. 5a ACT transmission topographs obtained from different diffracting planes. (111) diffraction.

Fig. 5b ACT transmission topographs obtained from different diffracting planes. ($11\bar{1}$) diffraction.

Fig. 5c ACT transmission topographs obtained from different diffracting planes. (002) diffraction.

Fig. 5d ACT transmission topographs obtained from different diffracting planes. (220) diffraction.

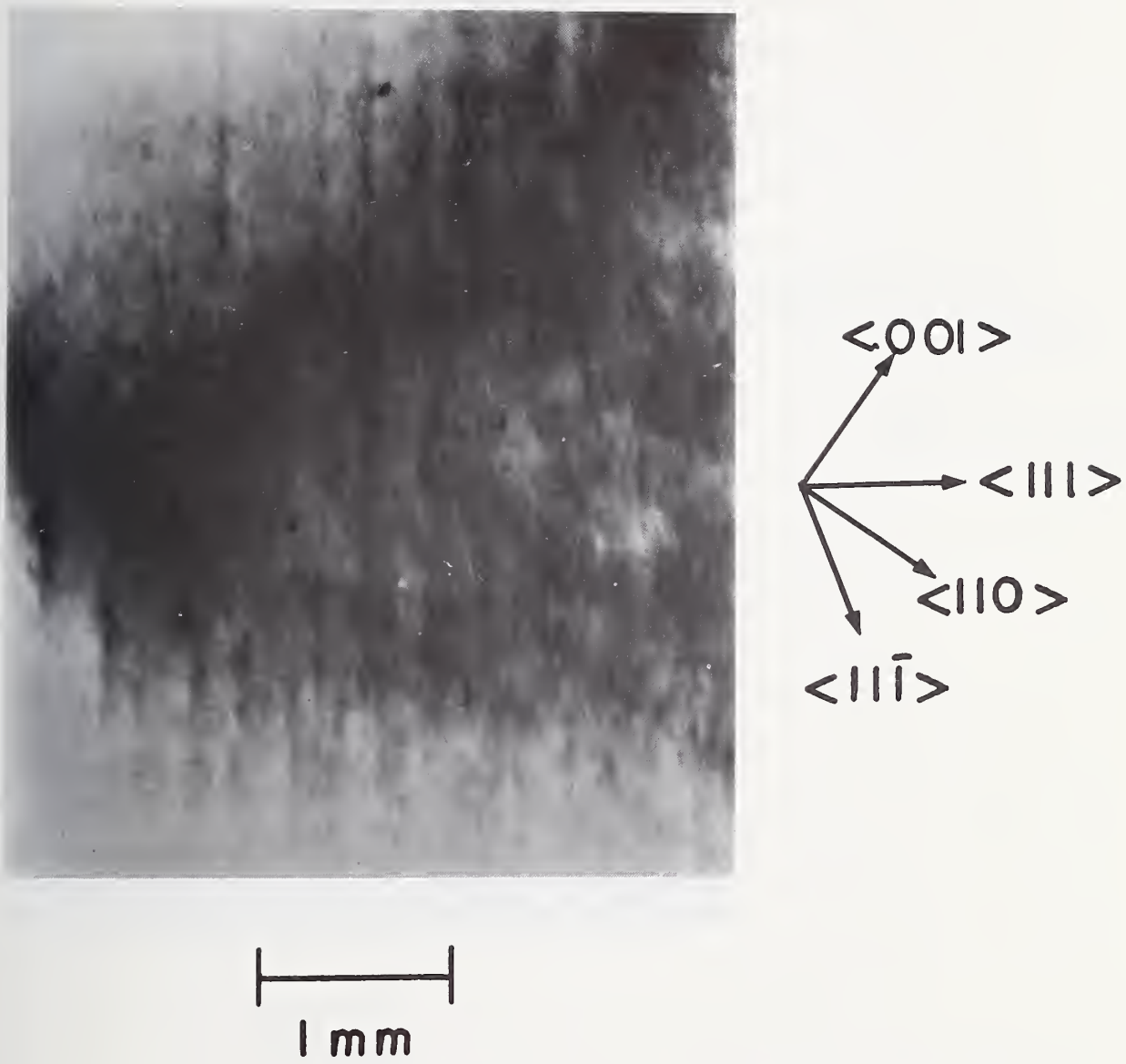

Fig. 6 SCAD topographs taken in the reflection geometry. This magnified topograph of the ($2\bar{2}0$) surface diffraction shows the images of dislocations terminating on the surface. Although short in length, they are aligned in the same direction as observed in Fig. 4.

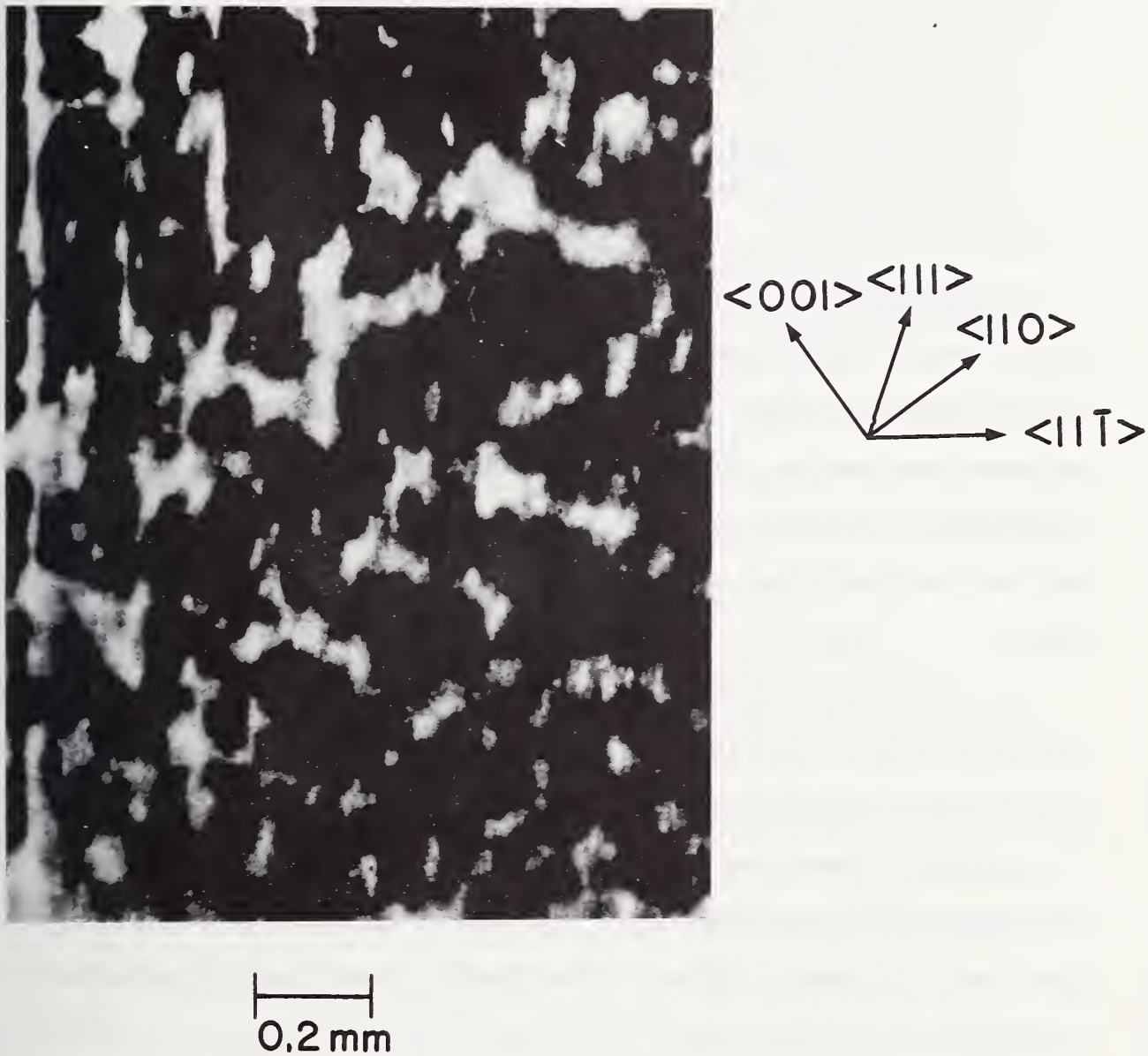

Fig. 7 SCAD transmission topograph. This magnified topograph of the (11$\bar{1}$) diffraction illustrates that the line images of sets I and II are very narrow.

Task 2

Evaporative Preparation of Ultra-High Purity Materials

R. C. Paule
Inorganic Materials Division

W. J. Boettinger and F. S. Biancaniello
Metallurgy Division

Institute for Materials Research

Summary

Techniques for the ultrapurification of materials by high temperature evaporation of volatile contaminants have been developed with emphasis on containerless processing. Calculations of multicomponent evaporative processes have previously indicated that high degrees of purification can be obtained for selected systems. The calculations and computer programs have now been simplified, and diagnostics and internal checks have been added.

An experimental examination of the evaporative purification calculations has been started. An RF induction levitation system has been developed to generate data on purification rates and initial experiments on Molybdenum are reported. A modulated beam mass spectrometric facility has been built to continuously measure evaporative purification processes as a function of time. Both of these facilities will be used for a detailed evaluation of the purification calculations.

Introduction

This Task involves the development of techniques for the ultrapurification of refractory ceramics and metals by high temperature evaporation of volatile contaminants. The zero-gravity environment of space will be used to allow the containerless melting and evaporation of relatively large samples, and to provide high vacuum. Last year's efforts (NASA Contract W-13,475 #1)[1] were largely devoted to the development of calculations to predict evaporative purification rates and to indicate promising chemical systems for further investigation. This has now been followed by more detailed investigations into the basis of evaporative purifications.

The calculations, which have indicated highly successful evaporative purifications, are based on a number of assumptions. While these assumptions are quite reasonable, they still must be critically evaluated. The calculational assumptions are that:

(a) all significant vapor species have been considered,

(b) the thermodynamic constants are correct,

(c) ideal solution behavior is obtained,

(d) the evaporation coefficients are unity or near unity, and

(e) there is adequate mixing of the melt to avoid formation of concentration gradients during the evaporative purification.

Assumptions a through d are being critically examined under this Task. Assumption e is being examined separately under Task #6 of this contract (Surface Traction and Other Surface Pehnomena).

Real chemical systems are expected to have minor deviations from the above assumptions. Such minor deviations are relatively unimportant and can be accounted for. We must, however, be sure that there are no gross

deviations that will be detrimental to the purification process.

We have now embarked on an extensive experimental program to further examine our calculated results. Our experimentation has taken two paths. First, we have used RF induction coils to levitate and melt metal samples (primarily Mo), and by initial and final chemical analyses to measure evaporative purification rates. Data collected from such experiments will be used to test the calculations for overall accuracy for small samples which were truly processed without a container. Secondly, we have designed and constructed a modulated beam mass spectrometric facility to continuously measure species evaporating from a molten sessile drop (initially Al_2O_3). Such experiments will provide detailed analysis of the specific assumptions of the calculations mentioned above.

Work has also continued toward the simplification of the evaporative purification calculations, and to make the computer programing easier for others to use.

Our overall goals are to conveniently and accurately predict purification rates and ultimate purifications. This includes a description of the complex chemistry normally found in real purification systems. It is also our goal to accurately predict optimum materials and conditions for purification.

Levitation Experiments

Electromagnetic levitation with an RF induction coil is one of the best techniques available to study the evaporative purification of metals and alloys. Contamination by containers or unmelted or unheated parts of the sample is absent. Samples are rapidly heated to temperature. Liquid samples are stirred by the magnetic field and a relatively large surface to volume ratio is available for evaporation.

The state of the art of levitation melting has been reviewed by several authors.[2,3,4] The principle of electromagnetic levitation involves the creation of a spatial minimum of the magnetic field produced by a suitably designed radio frequency induction coil. This field induces eddy currents in a small metal sample placed in this field. The interaction of these eddy currents and the magnetic field cause a force to be exerted on the sample which will suspend it freely inside the levitation coil. These induced eddy currents also heat the sample. Because both the heating and the lifting are controlled by the strength of the magnetic field, it is not usually possible to control the lifting and heating independently. Hence, if one establishes a magnetic field which will adequately levitate the sample there is usually no independent control over the temperature. The temperature of the sample will adjust to some value determined by the power input to the sample and the heat lost by the sample.

Many metals and alloys have been levitation melted successfully in inert atmospheres with few problems. However in the past, a vacuum environment has posed severe limitations on the usefulness of levitation melting for quantitative studies of evaporative purification. Under vacuum conditions, many metals vaporize excessively. Metals with sufficiently high vapor pressures are often either difficult to melt or once melted tend to drip from the bottom of the levitated charge. In addition, arcing between the sample and the coil or between adjacent coil turns has often limited the performance of electromagnetic levitation in vacuum. The purpose of the initial phase of this research was to determine whether these problems could be overcome at least for some materials so that meaningful purification experiments can be performed using electromagnetic levitation.

Levitation System - The basic equipment system used in this research was a commercial levitation melting facility which is part of the Metallurgy Division Specimen Preparation Laboratory. Briefly, it consists of the following: a 450 KHz, 20 kW radio frequency generator with an air core 12:3 transformer to improve generator and levitation coil impedance matching; a coaxial power feed through a vacuum collar; a levitation coil which will be described later; and a vacuum chamber with supporting vacuum system capable of a vacuum of 4×10^{-5} Pa (3×10^{-7} torr). Photographs of the system are shown in Fig. 1a and 1b.

Choice of metals to be studied and the design of a suitable levitation coil were the first tasks undertaken. In previous work (in our laboratory) using conventional funnel shaped coils (Fig. 2a), it was determined that 4 gm samples of the metals Mo and Nb could be easily levitated but could not be easily melted. In addition, these metals were good candidates for evaporative purification with expected eliminations of many metallic impurities and also of interstitial oxygen.[5] Efforts were directed toward designing a levitation coil which would increase the power input to the sample, and hence permit these metals to be melted and held at temperatures just over their melting points.

Many of the conventional levitation coils reported in the literature have been designed on the basis of alloy preparation. They have large diameter windings on the top so that specimens can be easily dropped into the coil with tongs without venting the vacuum system. They also have a lot of space in the interior of the coil compared to the sample size so that oscillating specimens do not hit the coil. According to a report by Hulsey,[6] these coils have rather low coil gradients (gradient of the magnetic field

per unit coil current along the axis of the coil). Hulsey's experimental data on the power (P_ω) developed in a levitated sample as a function of the square of the coil current times the square of the coil gradient for various coil designs are shown in Fig. 3. Hulsey indicates that conventional coils (low coil gradients) typically operate in the region of the curve with negative slope and have relatively low power input to the sample. That conventional coils operate in this region of the curve is supported by the observation reported in the literature that the temperature of a levitated sample can be raised by lowering the coil current. It is obvious that much more power can be developed in a levitated sample in a coil with a high coil gradient.

Following this suggestion, a levitation coil was designed with as high a coil gradient as was feasible. This levitation coil has identical opposing sections (wound in the opposite sense) consisting of three turns each with as small a diameter as was practical for a 4.5 gm sample (sphere of radius 5 mm). This coil is shown in Fig. 2b. It is wound with 3.175 mm diameter copper tubing with 0.5 mm wall thickness. Using this coil it was possible to levitate and melt Nb and Mo at stable temperatures just over their melting points for up to five minutes.

It was found to be mandatory to omit a refractory coating on the coils and to clean them carefully after each levitation run to prevent arcing of the coils.

The size of the sample was found to be very critical to the success of the levitation melting. This is not surprising because with this coil design the magnetic field changes drastically over the diameter of the sample. Molybdenum samples greater than 5 gm would drip from the bottom during levitation and samples less than 4 gm would not melt.

It should be noted that with this coil samples could be levitated while remaining solid and then be melted by increasing the coil current. This indicates that the coil gradient of this coil is large enough to be operating on the part of Hulsey's curve (Fig. 3) which has positive slope. As mentioned earlier, this gives increased power efficiency.

Evaporative purification of Mo - Molybdenum samples nominally 4.5 gm were cut from a single rod of diameter 8.4 mm. Two samples from different parts of the rod were retained for chemical analysis. Purification experiments were performed in both the liquid and solid state using the electromagnetic levitation system just described and are summarized in Table 1.

For a solid state purification experiment, a conventional coil design was used (Fig. 2a). A sample was dropped into the coil with the power on with tongs operated from outside the vacuum system. Samples processed in this manner were heated to a maximum temperature estimated to be about 2500° ±100°C in about one minute. These samples were held at temperature for the times shown in Table 1 and were dropped into cold copper molds by cutting the power.

For a liquid state purification experiment the new coil design previously discussed was used (Fig. 2b). A sample was placed in the levitation coil and turned so that it rested directly on the lower turns of the coil. The system was evacuated and with the power control set to a maximum, the RF generator was turned on. Samples processed in this manner were immediately levitated, became completely molten in one minute, and were estimated to be heated to maximum temperatures just over the melting point (2623°C). The fact that samples were molten was determined by visual

Table 1 - Summary of Evaporative Purification Experiments of Molybdenum

	Specimen No.	Initial Mass	Initial Vacuum		Time at Temp.	Analysis (ppm by weight)																		
	-	gm	Pa	torr	min	Fe	Sn	Si	W	Cr	Cu	K	Al	Ca	Ta	As	Mn	Sb	Nb	Zr	V	Ge	Ga	O
Initial	I1	-	-	-	-	20	20	10	10	5	5	2	2	0.5	0.5	0.5	0.5	0.2	<0.2	0.2	0.1	0.05	0.05	-
	I2	-	-	-	-	20	10	10	5	2	2	2	1	0.5	0.5	0.2	0.5	0.1	<0.2	<0.2	0.1	<0.05	0.1	5
Solid State	S1	3.9626	$4x10^{-5}$	$3x10^{-7}$	1	10	5	5	10	5	1	2	0.2	0.5	0.2	1	1	0.05	<0.2	<0.2	0.1	0.1	<0.02	5
	S2	4.0715	$9x10^{-5}$	$7x10^{-7}$	5	10	5	5	10	1	0.5	0.5	0.05	0.2	0.2	0.1	0.2	0.05	<0.2	<0.2	0.05	0.2	<0.02	8
	S3	4.0175	$3x10^{-4}$	$2x10^{-6}$	30	10	20	5	10	5	2	2	0.5	0.5	0.5	0.2	0.5	0.2	<0.2	0.5	0.1	0.05	0.05	-
Liquid State	L1	4.9322	$4x10^{-4}$	$3x10^{-6}$	1	2	0.2	1	10	0.5	2	1	0.5	0.1	0.2	<0.02	<0.02	0.05	<0.2	<0.2	<0.02	<0.05	<0.02	8
	L2	4.8142	$1x10^{-4}$	$1x10^{-6}$	2	0.5	0.2	0.2	10	0.1	2	0.2	20	0.1	0.1	0.05	<0.02	0.05	20	<0.2	<0.02	<0.05	<0.02	5
	L3	4.5133	$7x10^{-5}$	$5x10^{-7}$	2	0.5	0.1	0.2	10	0.1	2	0.5	0.1	0.05	0.1	0.1	<0.02	0.02	<0.2	<0.2	<0.02	<0.05	<0.02	11
	L4	4.5075	$1x10^{-4}$	$1x10^{-6}$	3	50	10	2	10	10	20	1	5	0.5	0.1	0.2	0.5	0.05	2	<0.2	0.2	<0.05	<0.02	10
	L5	4.5126	$3x10^{-4}$	$2x10^{-6}$	5	5	0.2	0.2	50	0.5	2	<0.1	0.2	0.5	0.5	<0.02	0.05	0.02	<0.2	.5	<0.02	<0.05	0.02	-
	L6	4.5172	$4x10^{-5}$	$3x10^{-7}$	5	1	<0.1	0.2	10	0.05	1	0.2	<0.05	0.02	<0.1	0.05	<0.02	<0.02	<0.2	<0.2	<0.02	<0.05	<0.02	8
	L7	4.4745	$4x10^{-5}$	$3x10^{-7}$	5	1	0.1	0.2	5	0.1	2	0.2	0.5	0.02	0.2	<0.02	<0.02	0.05	<0.2	<0.2	<0.02	<0.05	<0.02	4

observation of the shape change of the samples. Accurate measurements of the temperature have not yet been made. The samples were held molten for the times shown in Table 1 and were cast into cold copper molds by cutting the power.

Samples were chemically analyzed by a commercial firm using spark source mass spectroscopy for the metallic impurities and inert gas fusion analysis for the oxygen impurity. Accuracy claimed by the firm is a factor of 2 for the metallic impurities and ± 3 ppm for the oxygen impurity. Data for all detected metallic impurities are given in Table 1 for the various experiments performed. Exceptions are the metals Ti, Mg, Na, Cd, and Co whose analyses were subject to interference. Data for the oxygen content are also given for all but three experiments for which analysis was not performed.

The data for sample L4 would appear to be completely erroneous and at the present time, no explanation is available. The other liquid state purification samples show purifications of 95% of Fe, Sn, Si, and others. The solid state purification samples did not exhibit such purifications due to the lack of mixing. Within the different groups of these preliminary experiments - solid state or liquid state - there appears to be little correlation between impurity level and time. It is quite possible that the scatter in the data has obscured this correlation. An important part of future work on this subject will be to determine the source of this scatter.

Within the experimental accuracy of the chemical analysis, the oxygen level of processed samples is essentially unchanged. The starting level of the oxygen impurity is so low that the amount of oxygen present in processed samples is probably determined by the partial pressures of the residual gases in the vacuum system. Further experiments will attempt to monitor these

partial pressures and to perform experiments with initially higher levels of oxygen.

Successful levitation has only been accomplished in the last stages of this year's work. Hence a detailed analysis of the purifications has not been performed for this report. Significant purifications of metallic impurities have been obtained using electromagnetic levitation and further work will emphasize the generation of reproducible data so that evaporation rates can be obtained.

A New Mass Spectrometric Facility

A new modulated beam quadrupole mass spectrometric (M.S.) facility is being developed to continuously observe evaporative purification processes as a function of time. A high sensitivity modulated beam mass spectrometer is needed to allow the detailed investigation of the specific assumptions used in the purification calculations. Our new M.S. facility is now nearly completed. All designs for the system have been completed, all parts obtained, and the vast majority of the system assembled. The system is shown in Figures 4 and 5. A summary listing the current state of the system components is given below.

Component	Designed	Parts Obtained	Assembled
Vacuum pumps, valves and traps	X	X	X
Vacuum envelope and frame	X	X	X
Electronic and vacuum safety protect system	X	X	X
Bake-out and LN refill system	X	X	
Oscilloscope sweep drive	X	X	X
M.S. electronic consoles	X	X	X
M.S. head (mass filter)	X	X	X
Chopper (beam modulator)	X	X	
Chopper drive and electronics	X	X	X
Furnace	X	X	

Several points regarding the design of the M.S. system are worthy of note. The vacuum enclosure is designed such that the low pressures of non-condensable background gases will be the same in the furnace and in the mass filter regions. The conventional diaphragm between these two regions has been eliminated. This should help minimize background signals when using the modulated beam detection system. If for any reason this innovation is not satisfactory, a diaphragm can be easily inserted between the two flanged regions. The vacuum enclosure can then be differentially pumped in the conventional manner.

The large tube stainless steel vacuum enclosure is designed for rapid and efficient pumping, and is fully bakable. Low pressures of the order of 10^{-6} Pa (10^{-8} Torr) will be routinely attainable. The frame for the system has been kept to a minimum to allow easy access.

Except for the molecular beam aperture, the furnace is surrounded by an optically dense, but vacuum pumpable, water cooled jacket. The jacket, plus the use of a very small tungsten filament furnace should minimize outgassing problems due to heat build-up in the system.

The quadrupole mass filter has been positioned to the uppermost portion of the vacuum chamber so as to allow a maximum separation between the mass filter and the molecular beam chopper. This was accomplished by offsetting the mass filter on its flange and by use of an eccentric conical expansion section in the vacuum wall. The large separation between the mass filter and the chopper is needed to obtain an adequate drift time and phase shift of the chopped molecular beam. Examination of phase shift information allows one to identify the neutral evaporating species in the molecular beam.

Measurements of phase shifts differentiate between parent and fragment ions which are formed in the M.S. ion source.

The use of a modulated (chopped) beam detection system is advantageous in that it allows one to ignore unmodulated signals coming from background gases in the mass spectrometer. By minimizing the effect of background gases, modulated beam detection allows a greater sensitivity to the evaporating species which are of interest.

As indicated by the table above, assembly of the mass spectrometric facility is nearly complete. We are currently testing the vacuum system and making preliminary checks on the electronics.

Initial mass spectrometric measurements will be made on the evaporating species coming from a sessile drop of molten Al_2O_3. Recent calculations by A. L. Dragoo, under Task #6 of this contract, have indicated that molten Al_2O_3 at 2500 K should exhibit good Marangoni mixing. The melt circulation time is calculated to be ~10 seconds when using a temperature gradient of only 1 K/cm. Al_2O_3 should be one of the candidate materials considered for future space purifications.

Evaporative Purification Calculations

Our computer programs for the evaporative purification calculations are considered to be working research tools. We have accordingly modified and improved the programs as follows: (1) programing and symbolism have been greatly simplified, (2) extensive program notes have been added as well as information on requirements of the input data, and (3) checks have been added for satisfaction of stoichiometric and equilibrium constant relationships, and diagnostic notices are printed if these relationships are not satisfied. With the exception of the thermodynamic data, the programs now check the

input data for correctness. A subtle partial redundance in the input data allows the programs to do this.

We have received and complied with a request for aid from Dr. Franklin F. Y. Wang, Department of Material Science at the State University of New York at Stony Brook. Dr. Wang, a NASA subcontractor through the Jet Propulsion Laboratory, requested that we send him a copy of the computer program for our vacuum evaporative purification calculations. We have sent him the program, along with test data and results, and have given assistance in the establishment of the program at Stony Brook. Dr. Wang plans to examine the purification of SiO_2 containing B_2O_3 impurity. We will be collaborating in this work.

We have also received a request for assistance from Gerald Wouch of General Electric Space Sciences Laboratory. General Electric, a NASA contractor, is interested in the evaporative purification of tungsten. Wouch will be obtaining analytical chemical analyses of initial and final impurity concentrations in tungsten samples which have been given different evaporative purification treatments. We have agreed, when this information is available, to use our computer programs and calculations to look at the results. This should be of interest both from the viewpoint of examining the experimental results and the theoretical calculations.

Reports

A talk and paper entitled, Ultrapure Materials: Containerless Evaporation and the Roles of Diffusion and Marangoni Convection, was presented at the AIAA 12th Aerospace Sciences Meeting in Washington, D.C. A preprint of the paper is included in Appendix I of this project report. The paper is being submitted for the symposium publication.

The paper entitled, Calculation of Complex Equilibria Involving Vaporization into Vacuum, has been accepted for publication in the December 1974 issue of High Temperature Science. A preprint of this paper was included in last year's Annual Report.

Status and Conclusions

An electromagnetic levitation system has been developed to perform quantative evaporative purification experiments. Significant containerless purification of Molybdenum has been obtained using this system. A modulated beam mass spectrometric facility has been built to examine the specific assumptions involved in the purification calculations. Both of these experimental facilities will be used to further examine purification rates and evolve optimum conditions and materials. Programing of the evaporative purification calculations has been simplified and improved.

References

1. R.C. Paule, NBSIR 73-402, 33 (1973).

2. W.A. Peifer, J. Metals, 17, 487 (1965).

3. G. Comenetz and J.C.R. Kelly, Jr., "Containment of Hot Matter", in High-Temperature Materials and Technology, I.E. Cambell and E.M. Sherwood, Ed., 600, John Wiley & Sons, New York (1967).

4. R.F. Bunshah, "Melting, Casting, and Distillation Techniques", in Techniques of Materials Preparation and Handling, R.F. Bunshah, Ed., 801, John Wiley & Sons, New York (1968).

5. L. Brewer and G.M. Rosenblatt, Trans. Met. Soc. AIME., 224, 1268 (1962).

6. W.J. Hulsey, AEC Rept. Y-1413, (1963).

7. B. Harris and A.E. Jenkins, J. Sci. Instr., 36, 238 (1959).

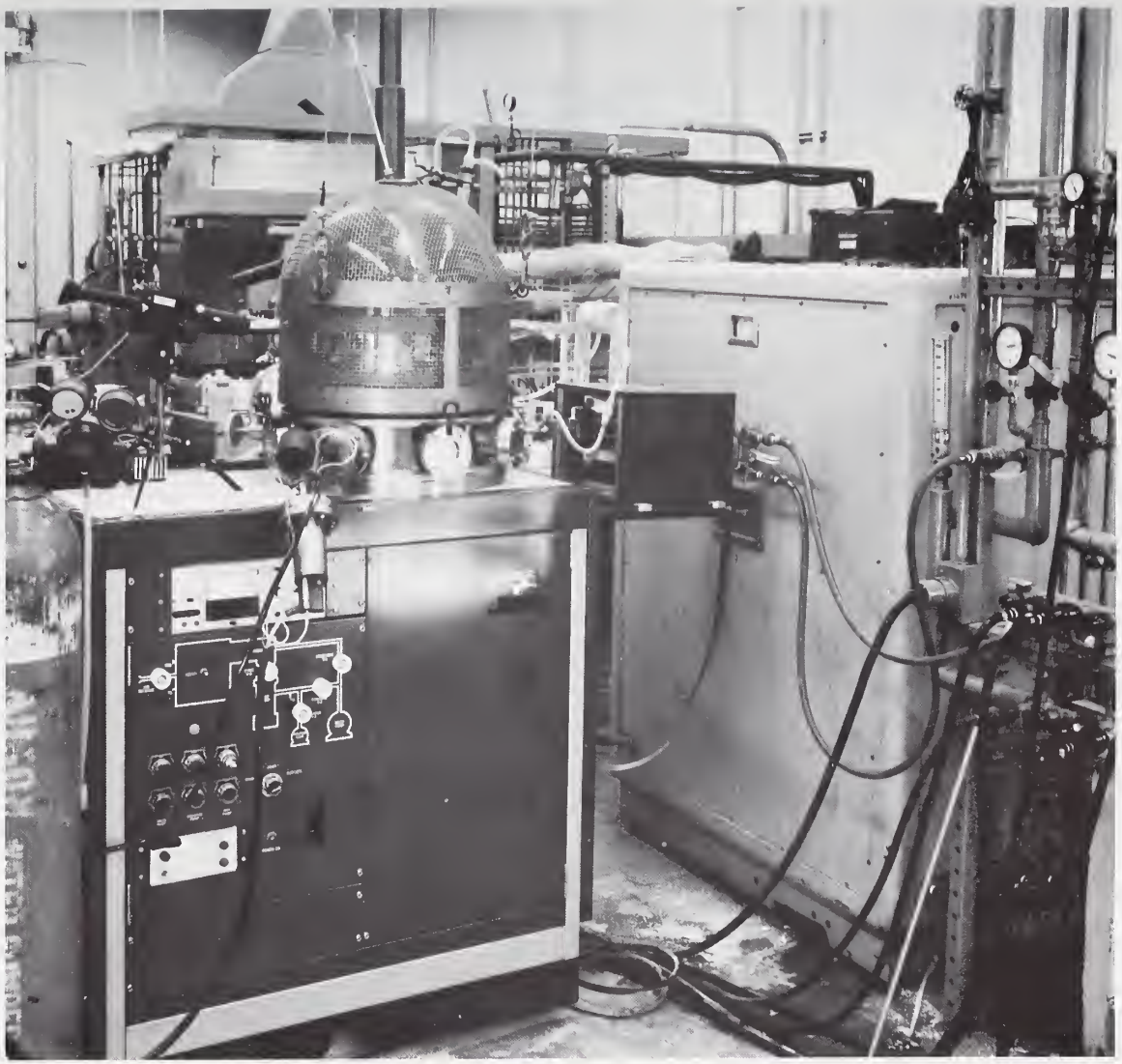

Fig. 1a Photograph of levitation system showing RF generator, 12:3 transformer, vacuum chamber, and supporting vacuum system.

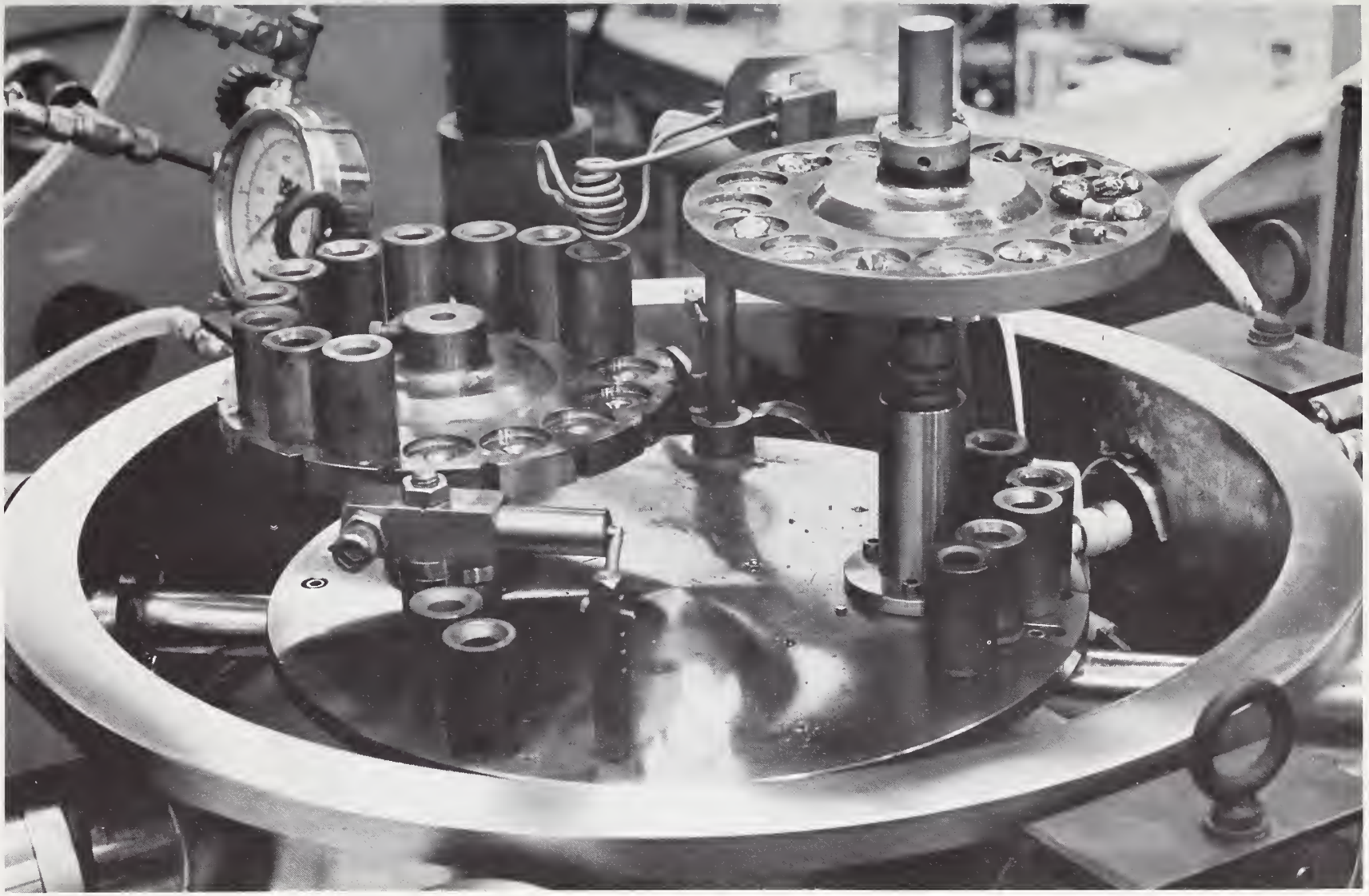

Fig. 1b Photograph of interior of vacuum chamber showing levitation coil, specimen tray and copper molds.

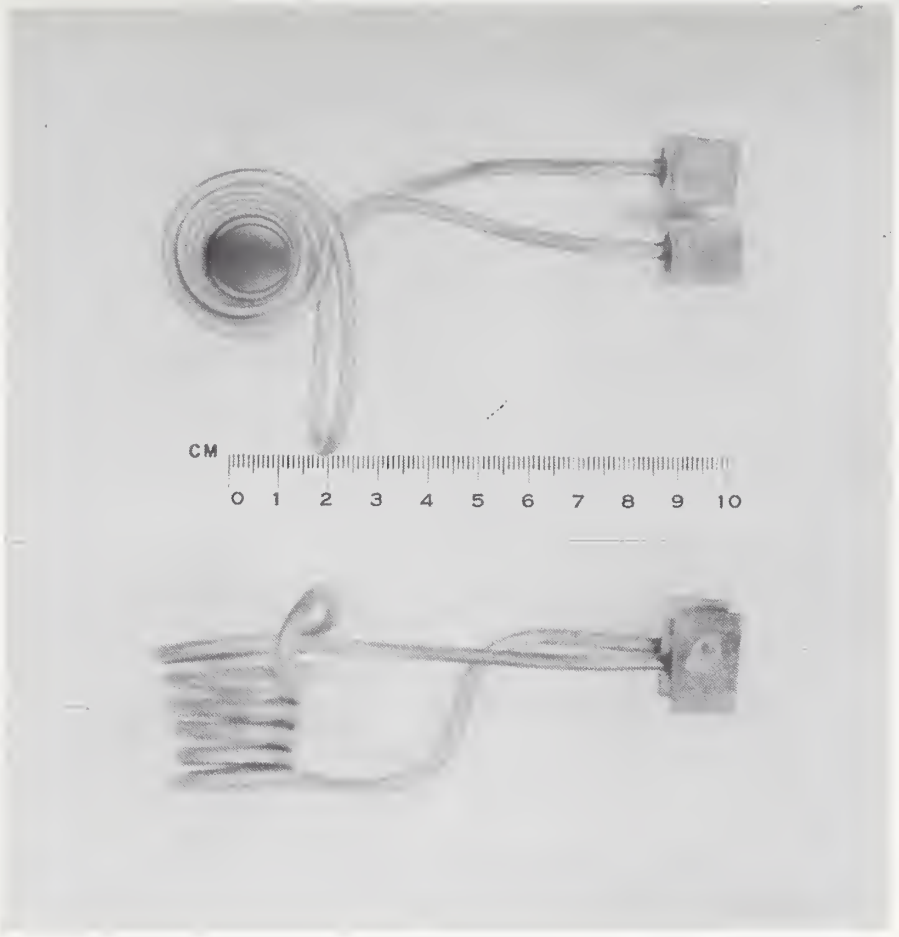

Fig. 2a Photographs of top and side view of a conventional levitation coil and the coil used for solid state evaporative purification experiments of Mo.

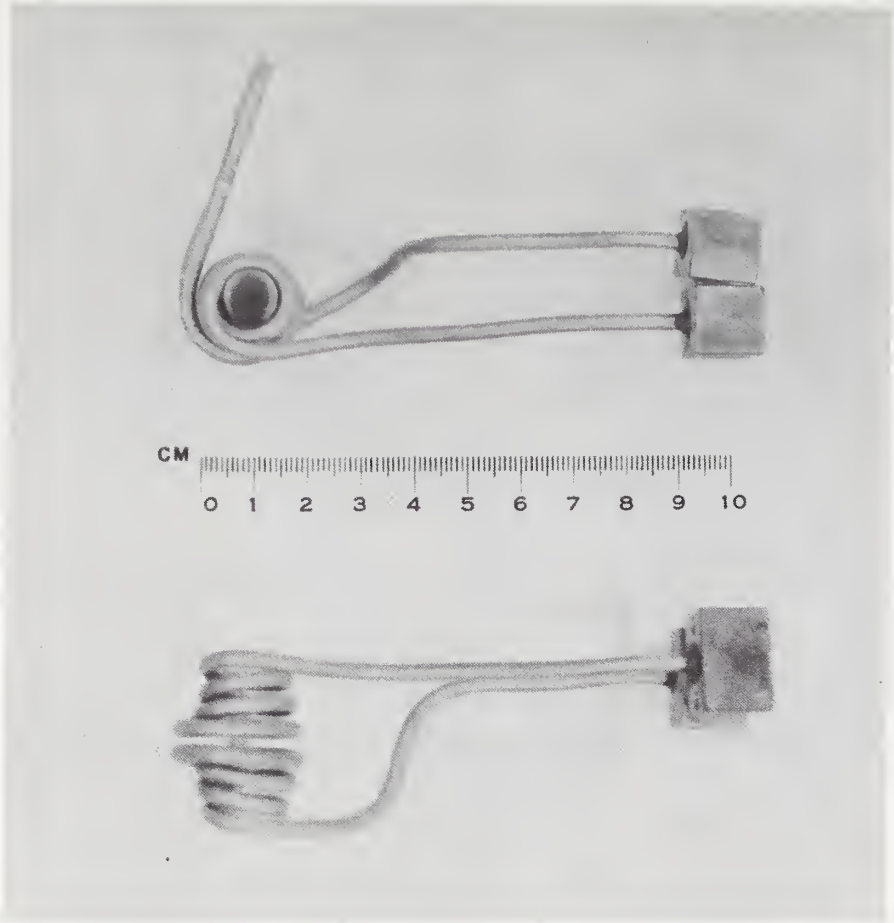

Fig. 2b Photographs of top and side view of the levitation coil designed for liquid state evaporative purification experiments on Mo.

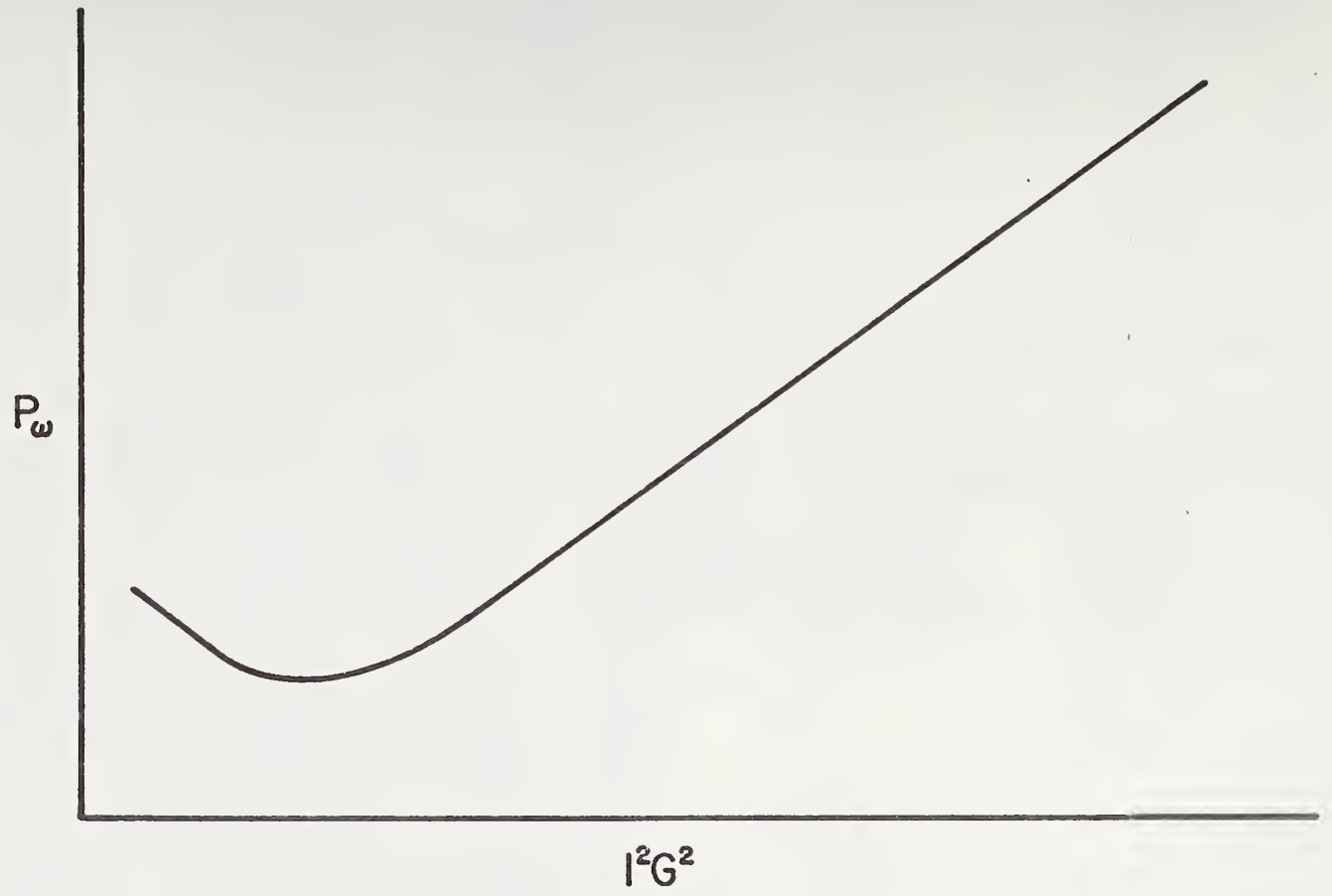

Fig. 3 Schematic plot of experimental data[6] on the power (P_ω) developed in a sample levitated in a R.F. coil as a function of the square of the coil current times the square of the coil gradient (I^2G^2).

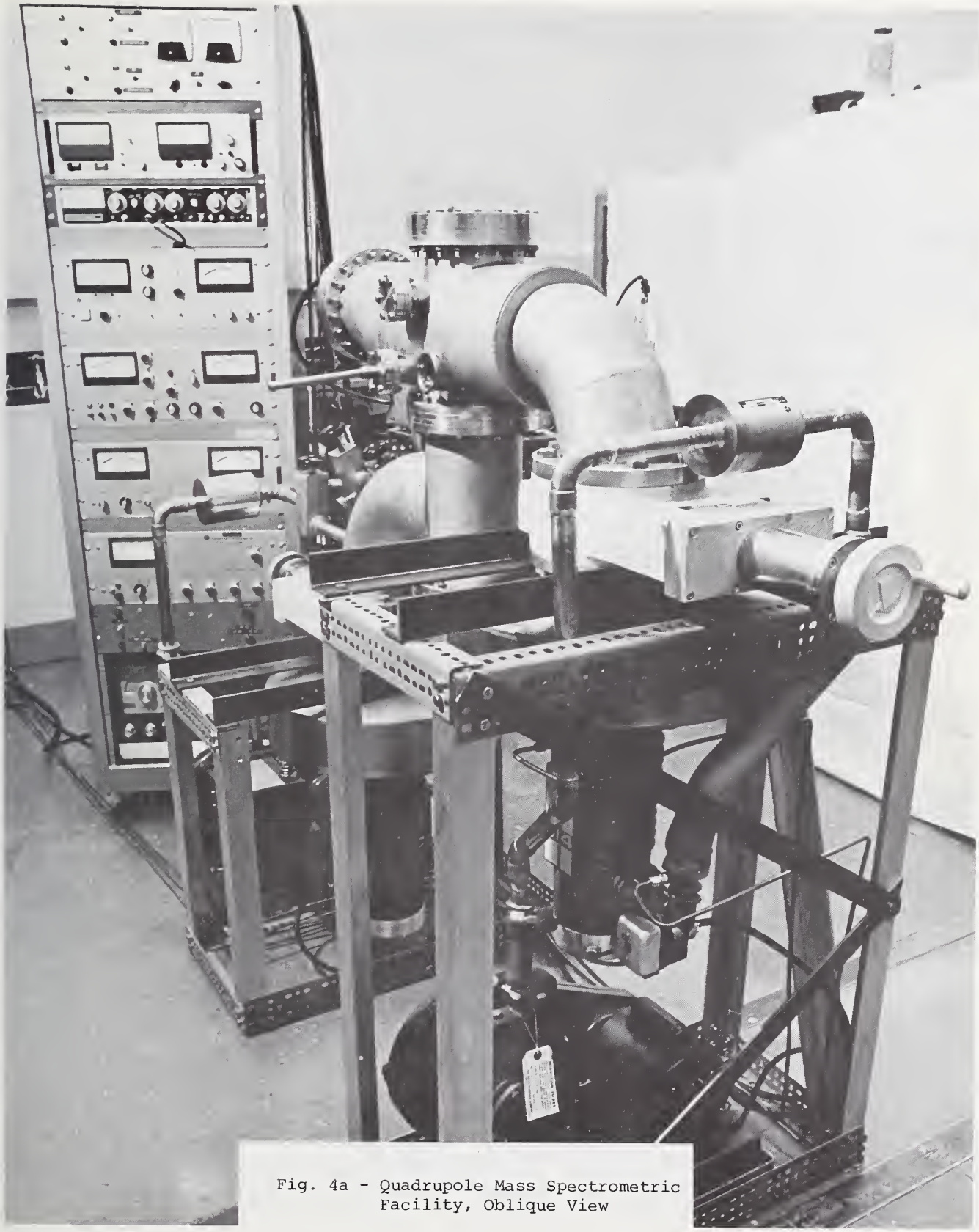

Fig. 4a - Quadrupole Mass Spectrometric Facility, Oblique View

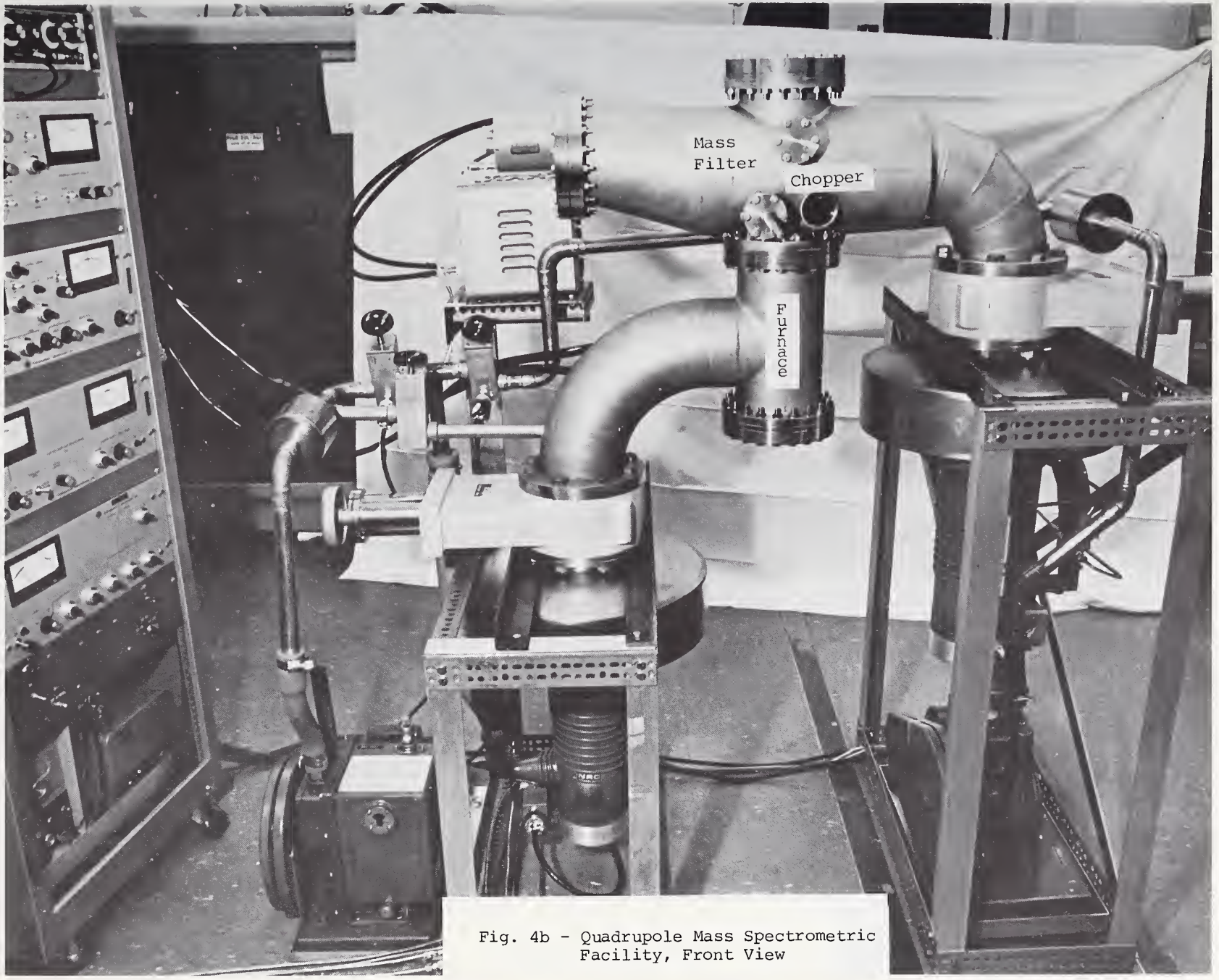

Fig. 4b - Quadrupole Mass Spectrometric Facility, Front View

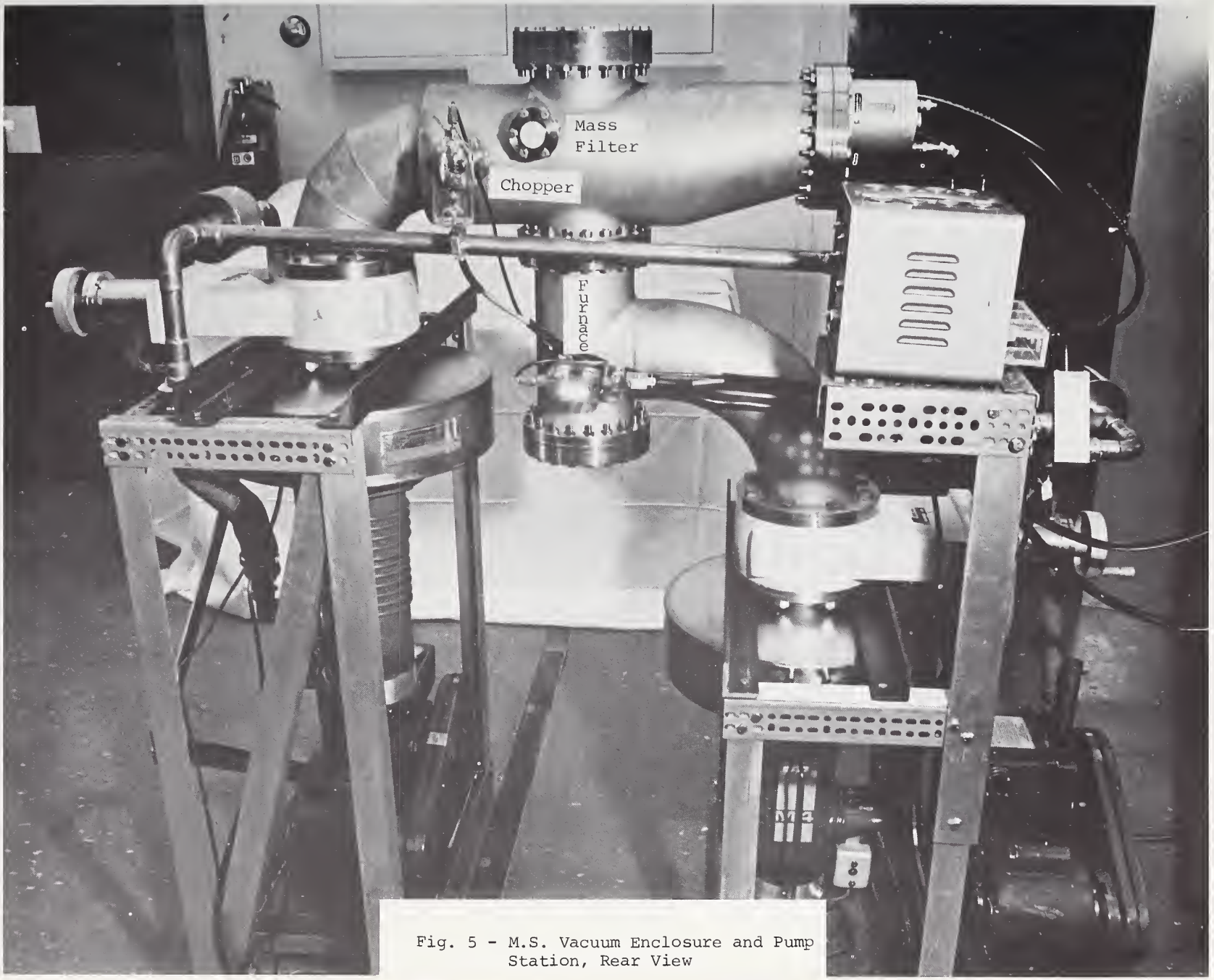

Fig. 5 - M.S. Vacuum Enclosure and Pump Station, Rear View

Appendix I

ULTRAPURE MATERIALS: CONTAINERLESS EVAPORATION AND THE ROLES OF DIFFUSION AND MARANGONI CONVECTION†

Alan L. Dragoo and Robert C. Paule
Institute for Materials Research
National Bureau of Standards
Washington, D. C. 20234

Abstract

Contamination from containers is a major problem in preparing ultrapure refractory materials. Space with its zero gravity and its high vacuum offers an opportunity for containerless purification of these materials. The evaporation of impurities from a melt will involve many complex chemical equilibria. Thermodynamic calculations have been modified to describe these equilibria when impurities in the melt evaporate into vacuum. The contributions of diffusion and Marangoni convection to mass transfer rates in the bulk liquid have been estimated. Calculations for the evaporative purification of molten alumina are given.

I. Introduction

Hot containers used in the production and purification of refractory materials are a common source of contamination. Space with its zero gravity and its high vacuum offers an opportunity for containerless purification of refractories.

The distillation of volatile impurities from a melt is one means of purification. In this paper, we will describe a technique for estimating distillation rates. This technique begins with a phenomenological expression for the magnitude, J_i, of the evaporative flux of component i from the melt. That is,

$$J_i = \alpha_i c_i \ , \qquad (1)$$

where α_i is the rate parameter and c_i is the molar concentration at the surface of the melt. Eq. (1) can be rewritten in terms of the mole fraction x_i by using the relation $c_i = c_{tot} x_i$, where c_{tot} is the sum of the concentrations of all components of the melt. The rate parameter α_i depends upon the chemical environment in the vicinity of the surface of the melt.

Complex chemical equilibria occur within an evaporating refractory since numerous minor impurities are present and since the high temperatures employed enhance the reaction rates. The general formalism for the calculation of complex equilibria previously was modified by one of us[1] to describe evaporative purification. Four classes of evaporation problems were investigated. The evaporating gases were considered under conditions of (1) constant pressure, (2) constant volume, (3) vacuum, and (4) partial vacuum with a low-pressure of an oxidizing or reducing gas. The two conditions (3) and (4) are of particular interest since they allow for the greatest isolation of the sample and the least chance of sample contamination by the container.

The purification rate of a melt is maximized when the melt is well stirred. The stirring process brings impurities to the surface where they can be expelled from the system by vaporization. A well-stirred melt also offers the mathematically simplest condition for the calculation of the mole fraction of each component in the liquid at selected times. If a plot of mole fraction of a component against time is made for a short duration, we can obtain an effective rate parameter α_i for that component. When the elapsed time is large, we generally find that the rate parameter is a function of time. The results of the calculation of the mole fractions at given times will be the subject of the first portion of this paper.

An actual melt may not be well-stirred in which case the rate of purification will be less than in the "ideal" melt described in the previous paragraph. In addition to the transport of material by convection which also occurs in the well-stirred melt, the nonhomogeneous concentrations in the actual melt will give rise to diffusion. Thus, the mole fraction x_i of component i at the surface will depend upon its rate of evaporation and upon its rate of transport to the surface by both convection and diffusion in the melt.

Our solution of the convective diffusion-evaporation problem for the concentration of any one of the constituents of the melt will be discussed in the second part of this paper. In this problem, convection will be assumed to be driven by surface traction, commonly known as the Marangoni effect. The effective rate parameters for evaporation which are required in the convective diffusion problem will be obtained from the results of the complex equilibria calculations described in the first part of this paper. The use of the effective rate parameters will allow us to treat the melt as a binary system in which only one of the components is volatile.

II. Calculations of Complex Equilibria

There are many articles in the literature dealing with the calculation of complex equilibria.[2-8] These calculations which involve computer programming cannot be used to solve our problem without extensive modifications. We have therefore developed our own equations and computer

† Financial support was provided by NASA under contract W-13,475 # 1.

programs for solving the problem of vaporization into vacuum. Modifications and adaptations were made to Kandiner and Brinkley's[2] general formalism for the calculation of complex equilibria. In simplest terms, their formalism involves the use of a series of mass balance equations for the independent species of the system and a series of equilibrium constant equations for the dependent species. The equilibrium constant equations, in turn, involve relationships between the masses, the pressures and the activities of the various species. To describe the evaporation of a melt into vacuum we have modified the formalism using the Knudsen equation and the ideal solution theory. The calculational approach is quite general and allows for relatively easy and direct modifications to describe a variety of situations of practical interest.

III. Results

Our calculations show that good evaporative purification of refractories in vacuum may be obtained. Table I shows the results of calculations for Al_2O_3 evaporative purification in vacuum at 2400 K, where 10 ppm (mole basis) FeO and 10 ppm SiO_2 impurities are initially present. Row 2 of the table shows that the rate of Al_2O_3 loss is very low, while rows 3 and 4 show that FeO and SiO_2 are rapidly lost from the melt. The FeO and SiO_2 concentrations are approximately halved after only one second. The remaining 12 species in the table, under the heading "Moles of Species Present," represent the moles of gases vaporized during each time interval (0-0.005 seconds, 0.005-0.25 seconds, 0.25-0.50 seconds, etc.). Finally the instantaneous pressures of all species are reported at the bottom of the table. It is evident that the calculations yield considerable information. The computer results, as indicated by this table, are obtained from the solution of each problem.

High rates of purification can result in a depletion of impurities at the surface and concentration gradients can occur. Homogeniety of the final melt, however, is highly desired. This can be accomplished by slowing the purification rates to allow time for better mixing. The slower rates of purification also allow time for better control of the experiment.

Table I. Vacuum Evaporation of Al_2O_3 + 10 ppm FeO and 10 ppm SiO_2 (2400 K)

Moles of Species Present					
Elapsed Time, seconds	.005	.250	.500	.750	1.000
Liquids					
Al_2O_3	1.0000E+00	1.0000E+00	9.9999E-01	9.9999E-01	9.9999E-01
FeO	9.9821E-06	9.1660E-06	8.3941E-06	7.6801E-06	7.0209E-06
SiO_2	9.9667E-06	8.5491E-06	7.2988E-06	6.2214E-06	5.2953E-06
Gases					
O	1.8199E-07	8.7991E-06	8.8694E-06	8.7728E-06	8.6875E-06
O_2	6.1007E-09	2.9106E-07	2.8981E-07	2.8354E-07	2.7805E-07
Al	8.9146E-08	4.4565E-06	4.6317E-06	4.7084E-06	4.7779E-06
AlO	1.2000E-08	5.9193E-07	6.0772E-07	6.1106E-07	6.1405E-07
AlO_2	6.6628E-10	3.2430E-08	3.2890E-08	3.2711E-08	3.2551E-08
Al_2O	1.8579E-09	9.3499E-08	9.7772E-08	9.9937E-08	1.0191E-07
Al_2O_2	1.0292E-11	5.1107E-10	5.2792E-10	5.3374E-10	5.3897E-10
Fe	1.7815E-08	8.1233E-07	7.6845E-07	7.1083E-07	6.5620E-07
FeO	8.2998E-11	3.7345E-09	3.4897E-09	3.1929E-09	2.9189E-09
Si	2.2587E-13	9.7506E-12	8.7050E-12	7.5844E-12	6.5827E-12
SiO	3.3262E-08	1.4168E-06	1.2495E-06	1.0768E-06	9.2550E-07
SiO_2	2.0138E-11	8.4641E-10	7.3738E-10	6.2853E-10	5.3498E-10
Pressure of Species Present (Atm)					
Gases					
O	3.5140E-06	3.4673E-06	3.4252E-06	3.3879E-06	3.3549E-06
O_2	1.6659E-07	1.6220E-07	1.5828E-07	1.5485E-07	1.5186E-07
Al	2.2352E-06	2.2804E-06	2.3227E-06	2.3612E-06	2.3960E-06
AlO	3.7976E-07	3.8230E-07	3.8465E-07	3.8676E-07	3.8866E-07
AlO_2	2.4700E-08	2.4536E-08	2.4386E-08	2.4253E-08	2.4135E-08
Al_2O	7.5013E-08	7.7043E-08	7.8953E-08	8.0701E-08	8.2292E-08
Al_2O_2	4.6061E-10	4.6680E-10	4.7255E-10	4.7775E-10	4.8244E-10
Fe	6.4267E-07	5.9806E-07	5.5444E-07	5.1287E-07	4.7346E-07
FeO	3.3961E-09	3.1185E-09	2.8559E-09	2.6129E-09	2.3887E-09
Si	5.7788E-12	5.0910E-12	4.4542E-12	3.8808E-12	3.3683E-12
SiO	1.0661E-06	9.2679E-07	8.0100E-07	6.9028E-07	5.9330E-07
SiO_2	7.5356E-10	6.4638E-10	5.5185E-10	4.7039E-10	4.0037E-10

Table II. Vacuum Evaporation of Al_2O_3 + 10 ppm CaO (2400 K)

Moles of Species Present				
Elapsed Time, seconds	0.005	20.00	40.00	60.00
Liquids				
Al_2O_3	1.0000E+00	9.9975E-01	9.9950E-01	9.9925E-01
CaO	9.9998E-06	9.2986E-06	8.6465E-06	8.0401E-06
Gases				
O	1.6143E-07	6.4560E-04	6.4548E-04	6.4535E-04
O_2	4.8005E-09	1.9197E-05	1.9193E-05	1.9189E-05
Ca	1.8850E-10	7.0120E-07	6.5210E-07	6.0643E-07
Al	1.0670E-07	4.2676E-04	4.2671E-04	4.2665E-04
AlO	1.2741E-08	5.0957E-05	5.0949E-05	5.0941E-05
AlO_2	6.2753E-10	2.5097E-06	2.5092E-06	2.5088E-06
Al_2O	2.3611E-09	9.4435E-06	9.4424E-06	9.4413E-06
Al_2O_2	1.1602E-11	4.6402E-08	4.6396E-08	4.6389E-08
Pressure of Species Present (Atm)				
Gases				
O	3.1171E-06	3.1170E-06	3.1169E-06	3.1168E-06
O_2	1.3109E-07	1.3108E-07	1.3107E-07	1.3106E-07
Ca	5.7606E-09	5.3581E-09	4.9838E-09	4.6355E-09
Al	2.6754E-06	2.6756E-06	2.6757E-06	2.6758E-06
AlO	4.0321E-07	4.0322E-07	4.0323E-07	4.0323E-07
AlO_2	2.3264E-08	2.3264E-08	2.3263E-08	2.3263E-08
Al_2O	9.5332E-08	9.5338E-08	9.5343E-08	9.5348E-08
Al_2O_2	5.1926E-10	5.1927E-10	5.1929E-10	5.1930E-10

Table III. Evaporation of Al_2O_3 + 10 ppm CaO, Vacuum + 10^{-5} Atm Oxygen (2400 K)

Moles of Species Present				
Elapsed Time, seconds	0.005	60.00	120.00	180.00
Liquids				
Al_2O_3	1.0000E+00	9.9984E-01	9.9967E-01	9.9951E-01
CaO	9.9999E-06	9.3413E-06	8.7259E-06	8.1511E-06
Gases				
Ca	5.8757E-11	6.5868E-07	6.1532E-07	5.7482E-07
Al	1.8569E-08	2.2281E-04	2.2278E-04	2.2276E-04
AlO	7.1134E-09	8.5352E-05	8.5343E-05	8.5333E-05
AlO_2	1.1240E-09	1.3486E-05	1.3485E-05	1.3483E-05
Al_2O	2.2941E-10	2.7526E-06	2.7523E-06	2.7520E-06
Al_2O_2	3.6165E-12	4.3393E-08	4.3388E-08	4.3384E-08
Pressure of Species Present (Atm)				
Gases				
O	1.0000E-05	1.0000E-05	1.0000E-05	1.0000E-05
O_2	1.3491E-06	1.3491E-06	1.3491E-06	1.3491E-06
Ca	1.7956E-09	1.6776E-09	1.5674E-09	1.4644E-09
Al	4.6560E-07	4.6560E-07	4.6560E-07	4.6560E-07
AlO	2.2512E-07	2.2512E-07	2.2512E-07	2.2512E-07
AlO_2	4.1669E-08	4.1669E-08	4.1669E-08	4.1669E-08
Al_2O	9.2626E-09	9.2626E-09	9.2626E-09	9.2626E-09
Al_2O_2	1.6186E-10	1.6186E-10	1.6186E-10	1.6186E-10

Better experimental control would be particularly important if one wished to produce doped materials through selective vaporization processes. The subject of controlled doping, however, will not be discussed in this paper.

Slower purification of Al_2O_3 can be obtained by exposing the melt to a low ambient oxygen pressure. The pressure can be kept low enough to maintain vacuum (Knudsen) flow conditions and yet can be high enough to shift chemical equilibria and slow the vaporization rates. Tables II and III list results for the evaporative purification of Al_2O_3 containing 10 ppm CaO. Table II is for the "pure" vacuum case and Table III is for a "vacuum" containing 10^{-5} atm oxygen. The higher oxygen pressures shown in Table III shift the equilibrium away from the reduced vapor species Ca(g) by the reaction $Ca(g)+O(g)\rightarrow CaO(l)$. This causes slower rates of purification. Figure 1 shows the rate of CaO removal both for the case of "self-developed" oxygen (Table II) and for the case of P_0 equal to 10^{-5} atm (Table III).

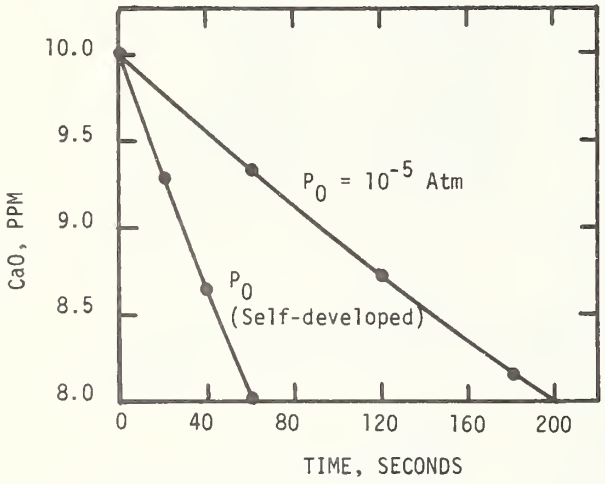

Fig. 1 CaO Vaporization from Al_2O_3 at 2400 K.

In making calculations of complex chemical equilibria one must be sure to include all significant chemical species involved in the system. Similarily one must use care in the selection of correct thermodynamic data to represent the chemical equilibrium constants. Ignoring these factors may result in grossly incorrect answers. The use of adequate chemical species and correct input data, however, can yield a wealth of information and can allow the proper choice of oxidizing or reducing conditions to achieve desired vaporization (purification) goals. The ultimate choice of evaporation conditions will include the combined solutions of the "ideal" complex equilibria evaporation problem and the convective diffusion problem.

IV. Convective Diffusion and Evaporation

A. Description of the Process

Stirring in a levitated melt must be accomplished remotely. We will consider here one possible way of doing this--that of convection driven by surface traction, that is, by surface tension gradients. An imbalance of forces along the surface of the liquid can arise, first, from surface temperature gradients in which case the resulting fluid flow is called "thermal capillary convection." Secondly, these imbalanced surface forces can arise from surface concentration gradients in which case the flow is called "solutal capillary convection." In addition, the surface traction may deform the levitated melt somewhat away from a spherical shape; however, for the discussion here, the melt will be thought of as having a nearly spherical configuration.

The relationships between the various aspects of the convective mass transfer problem are depicted in Figure 2. A non-uniform surface temperature gives rise directly to thermal capillary convection and indirectly to solutal capillary convection through the surface concentration gradients produced by the non-uniform evaporation. The non-uniform evaporation also causes the diffusion to depend upon direction. In addition to being non-uniform, the diffusion-evaporation phenomenon is complicated in other ways.

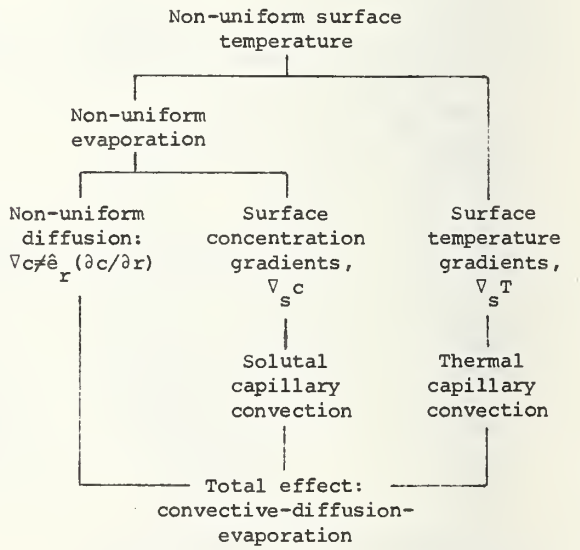

Fig. 2 The Relationship of the Components of the Convective-Diffusion-Evaporation Process in a Non-uniformly Heated Drop.

The two convective processes do not necessarily act in concert, but may oppose one another. For example, thermal capillary movement near the surface most often flows from the vicinity of a hot surface region toward that of a cold surface region because the surface tension for most materials decreases with increasing temperature. Solutal capillary flow will tend either to reinforce or to cancel the thermal capillary flow depending on the variation of the surface tension with concentration.

The total circulation within a convection cell--regardless of whether it is driven by thermal or solutal forces--must be considered in estimating the convective contribution to the evaporation rate. Not only is the convective mass transport from the interior toward the surface important, but also the spreading of the liquid over the surface must be considered.

B. A Convective Diffusion Problem

1. Formulation of the Problem

We have formulated a model of a convective diffusion process which arises when a linear temperature gradient is imposed along the z-axis of a spherical drop. The model is simplified further by the added assumption of steady, non-convective heat transfer. The temperature distribution in the drop is

$$T = T_o + T_1 r\cdot\cos\theta \ . \qquad (2)$$

Following the scheme of Figure 2, we first consider the convective velocity components. For the thermal capillary convection, we adapt the solutions of Young, et al[9] who calculated the circulation of a bubble rising in a vertical temperature gradient. The velocity field components in a drop are

$$u_r^T = (U^T/R^2)(R^2-r^2)\cos\theta \qquad (3a)$$

$$u_\theta^T = -(U^T/R^2)(R^2-2r^2)\sin\theta \ , \qquad (3b)$$

where the radius of the drop is R and the characteristic speed is U^T. This speed is

$$U^T = -(\gamma_T T_1 R/3\mu) ,$$

where $\gamma_T = (\partial\gamma/\partial T)_o$ is the temperature coefficient of the surface tension and μ is the coefficient of the viscosity.

Since the concentrations and the concentration gradients are time-dependent, the components of the solutal capillary velocity field will also be time-dependent. Formulas for these components can be derived after the manner of Miller and Scriven's[10] treatment of an oscillating droplet. Their work must be modified to include the surface traction terms in the boundary conditions. The derivation is lengthy and neither it nor the results will be given here, but two observations will be made. First, the velocity components are proportional to the surface concentration gradient. Second, the velocity components possess a time-dependence of the form $\exp(-\beta t)$ as does the surface concentration gradient. The first observation suggests that when impurity concentrations are less than a few ppm and the temperature gradient is large, which can be the case for molten alumina, solutal capillary convection can be ignored. The second observation suggests that the solutal convective term in the convective diffusion equation will decay exponentially, so that it rapidly becomes even less significant as time elapses. Solutal capillary convection has been ignored, then, in our estimates for molten alumina.

Having introduced the two convective processes, we turn now to the third branch of Figure 2--the non-uniform evaporation. The boundary conditions for the dynamical problem are greatly simplified by the incorporation of all chemical effects into the rate parameter α. However, the temperature dependence of α is considered explicitly by the approximation

$$\alpha(T) = \alpha_o + \alpha_1 T_1 R\cdot\cos\theta \ . \qquad (4)$$

Since we restrict the temperature field, the velocity field and the rate parameter to terms of order $\cos\theta$, or $\sin\theta$, we restrict the convective diffusion equation, the boundary conditions and the concentration to these same functions of θ. We write the concentration as

$$c(r,\theta,t) = c_1(r,t) - c_2(r,t)\cos\theta \ . \qquad (5)$$

By choosing this form for the concentration, the convective diffusion equation can be split into two equations,

$$\frac{\partial c_1}{\partial t} = \frac{D}{r^2}\frac{\partial}{\partial r}\left(r^2\frac{\partial c_1}{\partial r}\right) + \frac{1}{3}f_r\frac{\partial c_2}{\partial r} - \frac{2}{3}f_\theta\frac{c_2}{r} \qquad (6a)$$

$$\frac{\partial c_2}{\partial t} = \frac{D}{r^2}\frac{\partial}{\partial r}\left(r^2\frac{\partial c_2}{\partial r}\right) - 2Dc_2 + f_r\frac{\partial c_1}{\partial r} \ , \qquad (6b)$$

where

$$f_r = (U^T/R^2)(R^2-r^2) \qquad (7a)$$

$$f_\theta = -(U^T/R^2)(R^2-2r^2) \qquad (7b)$$

and D is the diffusion coefficient. Likewise, the evaporation equations become

$$-D\frac{\partial c_1}{\partial r} = \alpha_o c_1 - \frac{1}{3}\alpha_1 T_1 R c_2 \qquad (8a)$$

$$-D\frac{\partial c_2}{\partial r} = \alpha_o c_2 - \alpha_1 T_1 R c_1 \ . \qquad (8b)$$

Equations (8a) and (8b) are evaluated at r = R.

2. Description of the Solution

The convective diffusion equations (6a) and (6b) were integrated using the method of Green's functions[11] to obtain solutions for c_1 and c_2. The very complicated results[12] consist of sums over infinite series of terms. Some of the terms contain integrals which cannot be performed easily or which yield very cumbersome expressions. Moreover, the solutions for c_1 and c_2 are coupled as are the differential equations from which they were obtained. Nevertheless, certain features of the solutions of c_1 and c_2 can be distinguished.

First, the result for c_1 can be separated into three parts as

$$c_1 = c_{1D} + c'_{1D} + c_{1U}. \qquad (9)$$

Proceeding from left, c_{1D} is the solution to the pure diffusion problem which is treated by Crank,[13] section 6.34. The next part, c'_{1D} is a correction to the diffusion problem due to the non-uniform evaporation. Since the effect of non-uniform evaporation in this problem is to create an asymmetric concentration distribution and since c_{1D} is part of the symmetric term c_1, it represents a second-order, symmetric correction to the diffusion problem and can be ignored. The convective flow also tends to make the concentration distribution asymmetric, so that we take c_{1U} to be a negligible symmetric correction.

Although c_2 could also be split into three parts, the pure-diffusion part vanishes due to the assumption of an uniform concentration at the initial time t = 0. Thus,

$$c_2 = c_{2D} + c_{2U}\ , \qquad (10)$$

where c_{2D} contains the contribution of the non-uniform evaporation to the diffusion problem and c_{2U} is the convective diffusion part. Equation (10) is coupled to (9) through c_{2U}. However, since $c_1 \approx c_{1D}$, the solution for c_{1D}--which is known--can be used to find c_{2U}. Unfortunately, the result is extremely complicated and, therefore, is not easily used to estimate the evaporation rates. Care must be exercised in the development of further approximations to c_{2U} to avoid approximations which are non-analytic at the surface.

The total rate of evaporation is

$$V_{tot} = 4\pi R^2 \alpha_o [c_1 - (\alpha_1 T_1 R/3\alpha_o) c_2] \qquad (11)$$

$$= V_{1D} + V_{2D} + V_{2U}\ ,$$

where c_1 and c_2 are evaluated at r = R. We compare V_{2D} and V_{2U} to V_{1D} by estimating the ratios V_{2D}/V_{1D} and V_{2U}/V_{1D}. That is, we estimate the relative enhancement of the evaporation rate and not the absolute rate.

Since the solution for c_{2D} resembles that for c_{1D} at r = R, an approximation can be obtained for c_{1D}, which is

$$c_{2D}(R,t) \approx (\alpha_1 T_1 R^2/2\pi D)(Dt/R^2)\ c_{1D}(R,t). \qquad (12)$$

A very approximate estimate of $c_{2U}(R,t)$ was attempted using the Green's function result. The result is

$$|c_{2U}(R,t)| \approx |(\alpha_o^2 \gamma_T T_1 R^4/6\pi^4 \mu D^3)(Dt/R^2) c_{1D}(R,t)|. \qquad (13)$$

Substituting (12) and (13) into (11), we obtain

$$V_{tot} \approx 4\pi R^2 \alpha_o c_{1D}(R,t)[1-(\alpha_1^2 T_1^2 R^3/6\pi\alpha_o D)(Dt/R^2) + (\alpha_o \alpha_1 \gamma_T T_1^2 R^5/18\pi^4 \mu D^3)(Dt/R^2)]. \qquad (14)$$

The choice of sign for condition (13) and, hence, for the convective term in (14) is based on the assumption that the most important contribution of the convective flow lies in its bringing impurity-enriched liquid from the interior to the surface. If, instead, its major function were that of smoothing out the concentration differences along the surface in such a way as to reduce the surface concentration, it could reduce the rate of evaporation.

3. Estimates of the Evaporation Rates

The data used in these estimates is given in Table IV. The rate parameters, α_c and α_1, were computed for the vacuum evaporation of an initial concentration of 10 ppm of CaO in molten alumina by means of the complex equilibria analysis described in Section III. The density ρ and the viscosity μ have been measured by Bates, et al[14] at the two temperatures, 2400 and 2600 K, that we have considered here. "Reasonable" values were assumed for the temperature coefficient of surface tension, γ_T, and the diffusion coefficient, D. Experimentally measured values of γ_T for the molten salts[15] are in the range of -0.01 to -0.1 dyn/cm/K for many salts. Diffusion coefficients for many liquid systems are of the order of 1×10^{-5} cm^2/s. Our values for these two quantities are enclosed in parentheses to indicate that they are order-of-magnitude estimates.

Estimates of the rates are given in Table V. The relative rates have been computed for two temperature gradients. At the lower gradient of 1 K/cm, the convective enhancement of the diffusion-controlled evaporation rate is small for evaporation times of practical importance. However, a large gradient, on the order of 100 K/cm, might yield an appreciable enhancement of the evaporation rate. Such gradients would probably cause many non-linear effects in the melt, so that our estimates are less certain for the larger gradients.

Table IV. Parameters for the Estimation of Evaporation Rates

	Units	2400 K	2600 K	Ref.
$3\alpha_o/R$	s^{-1}	0.00338	0.01225	This work
$3\alpha_1/R$	s^{-1}/K	4.44×10^{-5}	4.44×10^{-5}	" "
D	cm^2/s	(1×10^{-5})	(1×10^{-5})	
	mm^2/s	(1×10^{-3})	(1×10^{-3})	
γ_T	dyn/cm/K	(-0.1)	(-0.1)	
	N/m/K	(-1×10^{-4})	(-1×10^{-4})	
μ	cp	110	62	14
	Pa·S	.11	.062	
ρ	g/cm^3	2.584	2.330	14
	kg/m^3	2584	2330	
R (1 mol Al_2O_3)	cm	2.1	2.2	
	mm	21	22	
U^{T*}	cm/s	0.064	0.12	
	mm/s	0.64	1.2	

*U^T evaluated for a temperature gradient of 1K/cm.

Table V. Estimated Magnitudes of Various Contributions to the Evaporation Rate for CaO from Molten Alumina

	Temp Gradient K/cm	2400 K	2600 K
$\lvert v_{2D}/v_{1D} \rvert$	1	5×10^{-8}	1×10^{-8}
	100	5×10^{-4}	1×10^{-4}
$\lvert v_{2U}/v_{1D} \rvert$	1	0.4 t	3 t
	100	4000 t	3×10^4 t

*Times t in seconds. Estimates are for times less than 1×10^3 s.

Surface traction forces are weak forces relative to the buoyant force on earth and convective flows generated by them can be damped significantly if the viscosity of the liquid is high. Thermal capillary enhanced stirring in molten alumina will occur if a large temperature gradient is used to overcome the moderately high viscosity--60 to 100 cp--of the melt. A liquid with a viscosity on the order of 1 cp, however, could have ratios of V_{2U}/V_{1D} which would be about 100 times greater than those given in Table V. Such a low viscosity liquid could exhibit a noticeable enhancement of the evaporation rate by surface traction driven convection even at gradients as low as 1K/cm.

V. Conclusions and Future Work

The phenomenological description of an evaporation rate as the product of a rate parameter and a surface concentration allows the separation of the computation of the evaporation rate into two more manageable problems:

- the computation of the rate parameter from the analysis of the complex chemical equilibria,
- the solution of the convective diffusion problem.

These computations have been illustrated here by the evaporative purification of molten alumina.

A very rough estimate of the enhancement of the evaporation rate by thermal capillary convection was calculated for CaO in an alumina melt. With alumina, significant enhancement by capillary convection may be attained when a large temperature gradient--on the order of 100 K/cm--is used. With liquids having low viscosities of about 1 cp, however, significant enhancement will occur even for small temperature gradients of 1 K/cm.

To date, we have studied the complex equilibria by means of the calculations described here. Mass spectrometric observations of the evaporative process are planned in order to experimentally check the chemical calculations. The experimental data will also provide information about departures from the solution ideally assumed in the calculations. In addition to alumina, other materials will be examined mass spectrometrically.

References

1. Paule, R. C., Calculation of Complex Equilibria Involving Vaporization into Vacuum, to be published.
2. Kandiner, H. J. and Brinkley, S. R., Ind. Eng. Chem. 42, 850 (1950).
3. White, W. B., Johnson, S. M., and Dantzig, G. B., J. Chem. Phys. 28, 751 (1958).
4. Gordon, S. and McBride, B. J., NASA, SP-273 (1971).
5. Feldmann, H. F., Simons, W. H. and Bienstock, D., U. S. Bur. of Mines, RI-7257 (1969).
6. Zeleznik, F. J. and Gordon, S., Ind. Eng. Chem. 60, 27 (1968).
7. Van Zeggeren, F. and Storey, S. H., The Computation of Chemical Equilibria, Cambridge University Press, 1970.
8. Klein, M., Physical Chemistry, Vol 1/Thermodynamics, Chapter 7, edited by Eyring, H. E., Jost, W. and Henderson, D., Academic Press, New York, 1971.
9. Young, N. D., Goldstein, J. S. and Block, M. J., J. Fluid Mech. 6, 350 (1959).
10. Miller, C. A. and Scriven, L. E., J. Fluid Mech. 32, 417 (1968).
11. Morse, P. M. and Feshbach, H., Methods of Theoretical Physics, McGraw-Hill Book Co., Inc. (New York, 1953), Chapter 7.
12. Dragoo, A. L., to be published.
13. Crank, J., The Mathematics of Diffusion, Oxford University Press (London, 1956).
14. Bates, J. L., McNeilly, C. E. and J. J. Rasmussen, "Properties of Molten Ceramics," in Ceramics in Severe Environments, ed. by Kriegel, W. W. and Palmour, H., III, Plenum Press (New York, 1971).
15. Janz, G. J., Lakshminarayanan, G. R., Tomkins, R. P. T. and Wong, J., Section 2. Surface Tension Data in Molten Salts, Vol. 2, NSRDS-NBS 28, Nat. Stand. Ref. Data Ser., Nat. Bur. Stand. (U.S.)(August 1969).

Task 3

Vacuum Effects in the Preparation of Composite Materials

H. Yakowitz

Metallurgy Division
Institute for Materials Research

Summary

Characterization of composites consisting of reinforcements of silicon carbide, tungsten, bare pyrolytic graphite and sapphire each in an aluminum matrix was carried out by optical and scanning electron microscopy. Electron probe microanalysis techniques were also utilized. These composites were prepared in an oxygen-free vacuum under Contract NAS 8-29620. The most promising composite of the group appears to be the sapphire-aluminum followed by the graphite-aluminum.

A new means to deduce local strains near the matrix-reinforcement interface is being explored. The method consists of using optical diffraction of electron channelling patterns to monitor the effects of strain. This report shows the validity of the method as well as initial results.

Signal processing equipment for the scanning electron microscope was fabricated in order to better observe the matrix-reinforcement interface. This equipment permits us to obtain the first and second time derivatives of the signal as well as their absolute values. The equipment is relatively inexpensive; circuit diagrams are included in this report.

Introduction

A major objective of this work is to measure strains in the vicinity of the matrix-reinforcement interface in composite materials. One possible means to achieve this end is to prepare selected area electron channelling patterns in the scanning electron microscope. Then if these patterns can be correlated with strains, a map of the strains near the interface can be prepared. Obtaining the electron channelling patterns is usually straightforward. However, assessing the amount of strain in the region from which the channelling pattern originates is not at all straightforward.

Originally, divergent beam (Kossel) microdiffraction was going to be used to provide quantitative strain correlation with the electron channelling patterns. This method proved less than satisfactory for a variety of reasons including the impossibility of obtaining satisfactory Kossel patterns without tilting the specimen in the scanning electron microscope. Such tilting seriously degrades the electron channelling pattern. Hence, Kossel and electron channelling patterns could not be prepared simultaneously, the result being that the Kossel method could not be used as originally anticipated.

Therefore, a different method of assessing strains from electron channelling patterns had to be developed. The method chosen is to use a tapered tensile bar strained a known amount as a calibration source. Electron channelling patterns can then be prepared and the strain determined. Optical diffraction is being used to assess the changes in the electron channelling pattern as a function of strain.

The strain correlation represents the main thrust of the work for the year. In addition, signal processing equipment for the scanning electron microscope was fabricated in order to better observe the matrix-reinforcement interface.

Finally, several composite materials supplied by Mr. I. C. Yates of the Marshall Space Flight Center were examined and characterized. These consisted of aluminum matrices with various reinforcers; the specimens were prepared by Convair Aerospace Division of General Dynamics under Contract NAS 8-29620.

Tapered Tensile Bar Approach

The idea for using the tapered tensile bar for electron channelling pattern studies was devised by Davidson [1]. The original idea was derived from a method used to relate etch pit density to macroscopic strain in Fe-3 1/4% Si transformer steel [2].

The specimen was designed for use with an Instron straining machine and is shown schematically in Fig. 1. Both aluminum and nickel were selected as materials to carry out the strain calibration and correlation. Aluminum was chosen because of its desirable properties as a matrix for composites: (1) Relatively low processing temperature, (2) Good wetting characteristics, (3) Susceptibility to controlled oxidation so as to permit density controlled composites, (4) Availability, and (5) Cost. Nickel was chosen because it rates well on items (2), (4), and (5) above and does not require a prohibitively high processing temperature. Density control with a nickel matrix may, however, be a problem. In both cases, nickel and aluminum, commercially pure polycrystalline stock was used to prepare the tapered tensile bars since material of this purity and type will almost certainly be used for any large-scale manufacturing of composites.

The aluminum bars were strained to a nominal value of 1.2% after being annealed for 61 hours at 525°C.

Strain was then determined along the bar, a grid having been placed on the surface and measured before and after deformation. The shape of the strain

versus position on the bar curve is shown in Fig. 2. Based on Davidson's determination of the degradation of electron channelling patterns as a function of strain, this strain characteristic is entirely satisfactory for the desired correlation [1].

The bar was then annealed, this time for 92 hours at 525°C, to promote grain growth. A grid was placed on the surface by a photochemical process. This was necessary since no surface strains can be tolerated from scribing a grid. The bar was then electropolished to its final form; the grid was not destroyed by polishing in a solution of 5% perchloric acid in ethanol for five minutes at 50 volts, 0.2 amps and a temperature of -70°C.

Electron channelling patterns of a number of grains in the bar were then prepared; these represent the "unstrained condition." These patterns are shown in Fig. 3. Each is sharp and characteristic of well-annealed unstrained material.

The way in which changes in these patterns arising from strains can be assessed must now be considered. Davidson has used the human eye which is fairly sensitive to comparisons of overall pattern contrast and distortion, widths of high and low index channelling lines and the absence of high order lines [1]. Davidson claims a relative accuracy of "at least 1%" for the eye. This method also utilizes the information from the whole electron channelling pattern.

One can assess, somewhat more quantitatively, line breadths by monitoring the signal electronically along a line. Figure 4 taken from last year's report [3] shows the effect of rolling strain on the line profile. This method has a disadvantage in that only a portion of the electron channelling pattern is monitored.

A method which uses the whole electron channelling pattern is the optical transform method. Here the optical diffraction pattern or transform of the

electron channelling pattern is taken. Changes is the electron channelling pattern affect the optical transform. Hence, the aim is to obtain and evaluate optical transforms of electron channelling patterns.

Optical Transforms

The optical bench used to generate optical transforms is shown schematically in Fig. 5. Since laser light is used, the system exhibits the property known as spatial coherence, i.e., the illumination consists of a spatial distribution of complex-valued amplitude [4].

The Fourier transform of a complex function $\tilde{g}$ of two independent variables, x and y, can be called $F\{\tilde{g}\}$ and defined by

$$F\{\tilde{g}\} = \int_{-\infty}^{+\infty}\int \tilde{g}(x,y)\ \exp\ [-i2\pi(f_x x + f_y y)]dxdy$$

Hence, $F\{\tilde{g}\}$ is a complex-valued function of two independent variables f_x and f_y, referred to as frequencies. Similarly the inverse Fourier transform of a function $\tilde{G}(f_x,f_y)$ can be called $F^{-1}\{\tilde{G}\}$ and defined by

$$F^{-1}\{\tilde{G}\} = \int_{-\infty}^{+\infty}\int \tilde{G}(f_x,f_y)\ \exp\ [i2\pi(f_x x + f_y y)]df_x df_y$$

Now, the assertion is made that the system represented in Fig. 5 is a linear system, and its properties can be described by linear systems theory. This simply means that the response of the sample, in this case a transparency of an electron channelling pattern, to several stimuli acting simultaneously is identically equal to the sum of the responses that each of the component stimuli would produce individually. Thus, if a stimulus is decomposed into a linear combination of elementary stimuli, each of which produces a known response of convenient form, then by the property of linearity, the total response can be determined as a corresponding linear combination of the

the responses to the elementary stimuli. Fourier analysis provides a basic means of performing one such decomposition. For example, consider the inverse-transform relationship

$$g(t) = \int_{-\infty}^{+\infty} \tilde{G}(f) \exp(i2\pi ft)df$$

which expresses the time function, g, in terms of its frequency spectrum. This expression represents a decomposition of the function g(t) into a linear combination, in this case, an integral, of elementary functions each having the specific form $\exp(i2\pi ft)$. Therefore, the complex number $\tilde{G}(f)$ is just a weighting factor which must be applied to the elementary function of frequency, f, in order to synthesize the desired g(t).

In an entirely similar way, the two-dimensional Fourier transform may be regarded as a decomposition of a function $\tilde{g}(x,y)$ into a linear combination of elementary functions having the form $\exp[i2\pi(f_x x + f_y y)]$. Such functions have a number of interesting properties, e.g., for any particular frequency pair (f_x,f_y), the corresponding elementary function has zero phase alone lines described by

$$y = -\frac{f_x}{f_y} x + \frac{n}{f_y}$$

where n is any integer. Figure (6) shows that this elementary function can be regarded as being directed in the xy plane at some angle θ, with respect to the x-axis, given by

$$\theta = \tan^{-1} \frac{f_y}{f_x}$$

Furthermore, the distance between zero-phase lines, known as the spatial period, is given by

$$L = \frac{1}{(f_x^{\,2} + f_y^{\,2})^{1/2}}$$

Hence, the Fourier spectrum $\tilde{G}$ of a function $\tilde{g}$ is a description of the weighting factors that must be applied to each elementary function in order to synthesize the desired $\tilde{g}$. However, in the case of the analysis of electron channelling patterns, the pattern represents the function $\tilde{g}$. The patterns possess varying degrees of sharpness as a function of strain in the specimen or other factors such as a coating on the specimen [3].

Therefore, the form of the optical diffraction pattern is expected to change as the electron channelling pattern sharpness changes. Loss of sharpness can lead to loss of high frequency components. In analogy to the simple example represented in Fig. 6, the frequencies f_x and f_y would be altered; and hence, the values of θ and L would be expected to change concomitantly.

The strain calibration thus consists of preparing optical transforms from each of the electron channelling patterns taken from the grains in the annealed, unstrained tapered tensile bar. Then, after straining, new electron channelling patterns are prepared and their optical transforms recorded. If the electron channelling pattern alters due to the applied strain, then the optical transform is also expected to alter. With the aid of Fig. 2, the strain as a function of position in the tapered tensile bar is known. Hence, the end result is a set of electron channelling patterns and their corresponding optical transforms for both the unstrained and strained states. The optical transform method utilizes the whole electron channelling pattern and is unbiased. The experiment consists of preparing the electron channelling pattern from the composite, taking the optical transform and comparing it with the calibration set in order to determine strain as a function of position in the composite.

To test the response of the system, a set of four photographs of a pseudo-electron channelling pattern was prepared. The sharpness of each was successively degraded to produce the set shown in Fig. 7. Then the optical

transform of each was prepared. The pattern produced by Fig. 7a shows sharp spots due to the periodicity of the stipple and the expected symmetry (Fig. 8a). If the central portion of this pattern is enlarged by means of a projector lens, the pattern shown as Fig. 9a results. Figure 7b produced the pattern shown in Fig. 8b without a projector lens. The spot pattern is absent. Use of a projector lens yields the pattern shown in Fig. 9b. Clearly some periodicity remains here. Figures 7c and 7d yielded the patterns shown in Figs. 9c and 9d. The progressive effects are apparent. This simple test set indicates the kinds of effects one can expect to see when real electron channelling patterns are subjected to optical transform techniques.

Figure 10 shows an electron channelling pattern of the <111> pole in niobium as well as its corresponding optical transform. The symmetry elements can be easily seen. Next, an aluminum single crystal was bombarded by argon ions at one end so as to cause local surface damage. Electron channelling patterns and their corresponding optical transforms are shown in Figs. 11 and 12 for the undamaged and damaged portions respectively.

Characterization of NASA Supplied Composite Materials

The materials to be described were prepared by Convair Aerospace Division of General Dynamics under Contract NAS 8-29620. The materials were supplied by Mr. I. C. Yates of Marshall Space Flight Center, NASA monitor for the above contract.

All materials had an aluminum matrix. The reinforcements were respectively (1) SiC in the form of 0.1 mm diameter filaments, (2) Chopped tungsten wires 0.3 mm in diameter, (3) Bare pyrolytic graphite in the form of 0.01 mm diameter fibers and (4) Sapphire (Al_2O_3) filaments about 0.25 mm in diameter.

The composites were prepared in an oxygen-free vacuum. The rationale is that to achieve good bonding, good wetting of the reinforcement by the matrix

is necessary. But wetting truly occurs only in the three-phase, solid-liquid-gas, system. Therefore, in a two-phase system consisting of just solid and liquid, conventional wetting concepts may not apply; and free dispersion (good bonding) can be achieved with any reinforcement. The oxygen-free vacuum was obtained by cycling the vacuum chamber containing mixed aluminum chips and the reinforcement to a pressure of 10^{-3} torr pressurizing with argon and evacuating to 10^{-3} torr several times. Then the sample is heated to 600°C and the evacuation-argon, pressurization-evacuation step repeated once again. The specimen is then heated to 1000°C and manual mixing is carried out followed by slow cooling. Empirically, the 1000°C temperature was established as that which gave the best matrix-reinforcement dispersion and bonding.

The specimens were supplied in their original ingot form. Each specimen was mechanically polished and examined with the optical microscope and with a scanning electron microscope equipped with X-ray microanalysis capabilities.

SiC-Al Specimen

Optical examination revealed material in the matrix grain boundaries, an extensive reaction zone at the SiC-Al interface, the presence of an extraneous phase in the matrix and that the SiC filament from which the reinforcer had been prepared contained a core (Fig. 13). Scanning electron microscope examination shows the SiC to be unevenly dispersed in the matrix and that the extraneous phase seems to have an affinity for the SiC (Fig. 14). The extraneous phase was identified as tungsten bearing by means of the X-ray microanalysis unit attached to the scanning electron microscope. Furthermore, the core material of the SiC was shown to consist of tungsten. The tungsten bearing material in the composite was subjected to quantitative electron microanalysis procedures [5]. Results showed the material to consist of 38% aluminum,

balance tungsten by weight. This corresponds fairly closely to something having the formula Al_4W.

The reaction zones at the SiC-matrix interface are shown in Fig. 15. The SiC has cracked in many places. The matrix exhibits shrinkage pores. Reaction of the SiC with the matrix seems to have proceeded on a non-uniform basis. The extraneous tungsten phase is probably from the tungsten rod used to manually mix the components in vacuo at 1000°C. Even without the extraneous tungsten, it appears that this composite is not entirely satisfactory.

W-Al Specimen

Optical examination shows that the dispersion of the tungsten wires in the aluminum is fairly good. The wires appear to be randomly oriented. (Fig. 16) Optical examination also revealed that the matrix consists of dendritic grains whose boundaries contain a separate phase (Fig. 17).

Scanning electron microscope examination showed the reinforcers to be very irregular in shape and aspect ratio. The separate phase in the grain boundaries appears to be eutectic-like and may well be Al_3W. (Fig. 18) X-ray microanalysis indicates that the aluminum and tungsten had reacted during preparation of the composite. All of the tungsten bearing material contains aluminum. Quantitative electron microanalysis of this material indicates about 42 1/2 percent aluminum by weight, the balance being tungsten. This corresponds to 83.5 atom percent of aluminum or something having a formula Al_5W. Al_5W is reported to be hexagonal in structure with a = 4.902Å and C = 8.857Å [6].

The interface of the reinforcement with the matrix is variable ranging from straight and sharp to regions where local reaction appears to have taken place. (Fig. 19) This variability plus the existence of what is likely to

be a brittle phase throughout the grain boundaries indicates that this particular composite will probably not be suitable for engineering applications.

Graphite-Al Specimen

Both optical and scanning electron microscope examination indicate reaction between the graphite and the matrix; the dispersion appears to be reasonably good (Fig. 20). The amount of reaction which occurred in individual graphite fibers appears to be variable. In some cases a black appearing core remains while in others this core is absent. The size of the core is variable as well. (Fig. 20)

The black core and surrounding grey areas were subjected to quantitative electron microanalysis procedures. The black core contains 29.2% aluminum by weight, balance carbon. This corresponds to 15.5 atom percent aluminum or something approximating AlC_6. The grey region is variable but contains an average 72.3% by weight of aluminum, balance carbon. This corresponds to 53.8 atom percent aluminum and is very likely the well-documented compound Al_4C_3 [7] [8]. It is likely that a composition gradient exists throughout the carbon-bearing material.

This composite may be worth additional effort to obtain mechanical properties tests. Perhaps the time at temperature during fabrication should be lengthened slightly to attempt to react the fiber completely to Al_4C_3.

Sapphire-Al Specimen

The grain boundaries are clean. The dispersion of the sapphire is very poor; all of the reinforcement seems to be at the very edge of the ingot. Probably it floated up and could not be sunk again during the molten stage of fabrication. Tungsten is also present again probably due to the stirring rod.

Figure 21 shows the general aspect of this composite in the region containing the sapphire. Most of the material is sapphire free but has a tungsten-bearing impurity.

The tungsten-bearing impurity was shown by quantitative electron microanalysis techniques to consist of 41.3 percent by weight of aluminum, balance tungsten. This corresponds to 82.6 atom percent of aluminum. Hence, the reaction of tungsten with molten aluminum at 1000°C seems to produce material containing around 80 to 83 atom percent aluminum as shown throughout this study.

In this composite the tungsten bearing material seems to exist both in nodules and in whisker-like needles, whose aspect ratio is roughly 30 to 1. Remarkably, the interface between these needles is straight and very clean at a magnification of 10,000 diameters (Fig. 22). Clearly, this "accidental" tungsten aluminum composite shows more promise than the composite deliberately fabricated of tungsten in aluminum.

In regions where the sapphire is present, the matrix-sapphire interface appears to be excellent. The sapphire filaments appear to exhibit a variable friability. Some are badly fissured while others nearby are completely smooth (Fig. 23). Sapphire is not wetted by aluminum under usual fabrication conditions; however, the fabrication conditions used to make this specimen clearly have resulted in good matrix-reinforcement bonding. More effort to obtain a better dispersion of the sapphire would seem to be in order. If this can be achieved, then the sapphire-aluminum composite should be subjected to a full battery of mechanical properties tests.

In addition, another effort at producing a tungsten-aluminum composite having the aspects illustrated in Fig. 22 probably is worthwhile.

Since the characteristics of the matrix-reinforcement interface are of great interest, the possibility of enhancing the information obtainable from the conventional scanning electron microscope (SEM) by signal processing is attractive. Therefore, some unique signal processing equipment, designed by Mr. C. E. Fiori of NBS, was adapted in prototype form to the SEM. Preliminary tests were so encouraging that we are having a permanent set of the signal processing equipment fabricated for adaption to the SEM. What follows is a description of the equipment, which can be built relatively inexpensively, and the results of the preliminary tests.

The image from an SEM provides the viewer with a representation of a specimen surface in varying shades of grey ranging from black to white on a display cathode ray tube (CRT) or photographic material. The shade of a particular picture point is related to the signal produced by one of the detector systems, which monitor the interaction of the primary beam with the specimen. The detector may respond to primary (back scattered) electrons, secondary electrons, absorbed electrons (specimen current), X-rays, or long wavelength light (cathodoluminescence). The detector signal is amplified to produce a signal suitable to intensity modulate a CRT, which is scanned in synchronism with the primary beam on the specimen to create an image. The characteristics of the SEM signal have been considered elsewhere [9]. The amplification of the detector signal, which we shall refer to as signal processing, takes in its simplest form a direct proportionality between the detector signal and the output signal. In certain circumstances, such a "direct image" contains useful information to an observer: the natural contrast -- the signal ratio, I_1/I_2, between two points of interest -- is sufficient for the human eye to discern. Such a condition is realized when primary electrons are used to form the image from a rough surface; the natural contrast level can be 25%

or more, which can be easily observed by the human eye. However, in many instances the natural contrast is too weak to be easily observed, or at the opposite extreme, the contrast between two regions in the image may be so strong that slight contrast changes within the regions may be invisible to the eye. For these reasons various operators which functionally transform the signal have been developed. The major reason for performing such transformations is to increase the amount of useful information which can be extracted from the specimen. Most SEM s are equipped with two operators -- differential amplification of the signal, usually called the "black level operator," and nonlinear amplification of the signal, referred to as the γ operator. [10]

There are a variety of other operators which can be applied to the signal. In this report three of these additional operators, (1) the first time derivative of the signal, (2) the absolute value of the first time derivative, and (3) the second time derivative are discussed. These operators can enhance fine details from specimens which produce widely varying signal levels within the field of view, can provide apparent vertical or oblique illumination of the specimen, and can produce apparent sharpening of edge details (crispening) in the image.

For this work an amplifier has been constructed which can produce the γ and time dependent signal transformations described above. An additional feature of the amplifier is that it can mix, in any proportion, the direct signal with the derivative signal of interest. For certain image transformations, orthogonal scanning, in which two scans at right angles are superimposed, has been found to be useful. Orthogonal scans with perfect registration are not generally possible with present SEM's. Obtaining accurate registration with analog scan generators is difficult. Therefore, we have constructed a digital scan generator with orthogonal scan capabilities. In addition,

individual coordinates and their respective grey levels are recoverable in computer compatible format from this generator, making possible the eventual use of a digital computer for image processing. The schematic diagrams for this signal processing amplifier and digital scan generator are shown in Fig. 24.

The SEM Recording Process

The image in an SEM is usually observed on a CRT having a long persistence phosphor and recorded photographically on a CRT having a short persistence phosphor. Only photographically recorded images are considered. The brightness range of recorded images is restricted by both the characteristics of the recording film and by the number of statistically valid grey levels which can be distinguished [9]. The exposure density of a film is a logarithmic function of the input signal, progressing from black (no signal or response) to white (full signal or maximum film response). This progression is divided by the eye into a number of grey levels in which a range of input signal produces effectively only one film response or shade of grey. The signal transformations discussed in this paper will only be considered with regard to the photographic image. However, we must recognize that the signal is transformed by the response of both the CRT phosphor and the recording film.

Time Dependent Operators

The SEM operator can choose between (1) low contrast-sensitivity over the entire range of signal intensity or (2) using the black level and γ operators to give high contrast-sensitivity within a restricted range of signal intensity. This choice can be altered by using the first time derivative of the signal, as illustrated in Fig. 25 to modulate the brightness

of the CRT [11]. The first time derivative gives enhanced sensitivity to certain contrast changes at all signal levels. Modulation of the brightness by this derivative signal produces an image in which all areas of constant signal have the same grey level regardless of constant signal intensity. Changes of the signal level produce a variation of brightness. However, pure derivative images produced in SEM's do not give the usual impression of depth, since the static levels of the signal are no longer distinguishable. Furthermore, the time derivative of the signal is not responsive to changes in signal intensity along the scan line. Therefore, contrast boundaries in the original image which do not cross the raster lines do not appear in the derivative image. The derivative signal from a line-type feature, such as an edge, oriented at an angle θ to the scan line will be reduced in intensity by a factor of sin θ from that value when the scan line is perpendicular to the feature. For these reasons, it is usually best to mix in variable proportions, depending on the subject and on the purpose of the image, the original signal with the derivative signal. The major reason for utilizing derivative operators mixed with the original signal is to reduce vast grey level differences and to provide increased contrast in regions of rapidly changing signal level. A basic characteristic of derivative processing is to apparently sharpen edge details in the image; this effect is referred to as "crispening" in television technology [12]. Observers have an overwhelming preference for crisper photographs and thus the derivative processing may be esthetically pleasing [12]. However, crispening must be critically evaluated so that false interpretation of specimen features does not occur. For example, at some magnification where the beam diameter encompasses several picture elements producing an unsharp image, a condition occurs where derivative processing will falsely provide an impression of improved resolution on the micrograph.

An undesirable feature of the time derivative transformation is that the signal-to-noise ratio is always less than that obtainable without the transformation. The derivative operator is extremely sensitive to high frequency components in the total signal spectrum. Since noise in the SEM is always high frequency, the noise is amplified to a greater degree than the signal. This difficulty is of minor importance in many SEM applications, but when the signal-to-noise ratio is inherently small, the derivative operator may not be useful. Another drawback is the case where one wishes to enhance fine details in the presence of rapidly changing high contrast levels. The value of the derivative for sudden signal changes varies widely for the fine details and large signal changes at edges. Saturation must be conceded at these large signal changes to enable fine details to be distributed over the full grey level range. Blooming of the film can be avoided by providing an electronic "clamp" in the derivative circuit to prevent undesirably high signals.

Fig. 26 shows the effects of time differentiation on the image of a simple object, a round hole machined into a thin aluminum disk. Fig. 26a shows the direct image of the hole formed with secondary electrons. The specimen was normal to the primary beam. Shadowing effects occur because of the geometrical relationship of the emissive electron detector and the specimen. Fig. 26b shows the same field imaged with specimen current which provides a uniformly illuminated image. Figs. 26c to h show various time derivatives of the specimen current signal. Fig. 26c shows the first time derivative scanned in the vertical direction only. The anisotropy and information loss caused by this transformation are apparent. The image depends strongly on the orientation of the specimen relative to the scan line; detail parallel to the scan lines is totally lost. The illumination appears to be oblique. Anisotropy in an image is not necessarily undesirable; shadowing in the emissive signal image

enhances the "three-dimensionality" effect. Anisotropy which results from specimen geometry and/or signal collection effects is an inherent feature of the SEM imaging process. Special cases exist in which an isotropic image is produced. However, the artificial anisotropy of the first time derivative represents an undesirable information loss along a line (arrows). Orthogonal scanning, in which two scans at right angles to one another are superimposed, has the effect of rotating the line of information loss in the image, Fig. 26d arrows, and an orientation dependent response is still obtained.

The absolute value of the first time derivative, Fig. 26c, converts all negative derivative signals from the blacker end of the grey scale to the whiter end. Figure 26e shows an image of the hole with the absolute value of the first derivative unidirectionally scanned in the vertical direction; information is again lost. If orthogonal scans are used, Fig. 26f, the entire edge is outlined without information loss. The absolute value of the first derivative is not isotropic, but it is a closer approximation to isotropy. We have found the absolute value operator useful to outline major features when regions with few details are studied. In regions containing much detail, the absolute value image is extremely complicated, making interpretation difficult.

For complicated specimens, the second time derivative, Fig. 26d, can be extremely useful. This operator has the advantage of being isotropic when orthogonal scanning is used, i.e., specimen orientation relative to the scan lines is immaterial. Fig. 26g shows the second derivative image of the hole scanned in one direction -- edge details are apparent but information is again lost parallel to the scan line. Orthogonal scanning with the second derivative, Fig. 26h, produces a uniformly illuminated edge having sharp detail. The illumination is effectively vertical.

While images of simple subjects are useful for illustration, it is informative to show the use of these derivative operators on a typical SEM specimen, e.g., a fracture surface of iron. Figure 27a shows the direct image with the secondary electron signal while Figs. 27b, c, and d show the first time derivative, its absolute value, and the second time derivative with orthogonal scanning respectively. With the first derivative Fig. 27b, the impression of depth is lost, and the edges appear to be obliquely illuminated. With the second derivative, Fig. 27d, the impression of depth is retained due to enhanced sensitivity to fine detail facing the detector, and the edges again appear to be obliquely illuminated. The orthogonally-scanned second derivative is expected to give the appearance of vertical illumination but this condition is not obtained for this specimen with the secondary electron signal. An isotropic operator will not convert an anisotropic direct image to an isotropic image. The absolute value of the first derivative produces a strong outlining effect, Fig. 27c. In Figs. 27e, f, and g the derivatives are mixed in equal proportion with the direct signal. The crispening of edges resulting from the use of the derivative operators and the enhancement of fine details are apparent.

Hopefully, the permanent version of this signal processing equipment will be installed on the SEM in the very near future. Matrix-reinforcement interface characterization utilizing the equipment will then commence.

Conclusions

1. Of the composites prepared under Contract NAS8-29620, aluminum-tungsten, aluminum-sapphire and perhaps aluminum-graphite show promise of being useful in an engineering sense.

2. Optical transforms of electron channelling patterns can be used to assess pattern perfection.

3. The tapered tensile bar coupled with the optical transform technique will provide a means to calibrate electron channelling patterns as a function of strain.

4. Signal processing equipment added to the scanning electron microscope will enable better matrix-reinforcement interface assessment.

References

[1] D. C. Davidson, SEM/74 (O. Johari, ed.) IITRI, Chicago, Ill. (1974) p. 927.

[2] G. T. Hahn, P. N. Mincer and A. R. Rosenfield, Exp. Mech. 11, 248 (1971).

[3] H. Yakowitz and D. E. Newbury in NBS Materials Science and Manufacturing in Space Research (E. Passaglia and R. L. Parker), NBSIR 73-402 (1973) p. 57.

[4] G. W. Stroke, An Introduction to Coherent Optics and Holography, Academic Press, New York (1966).

[5] H. Yakowitz in Practical Scanning Electron Microscopy (J. I. Goldstein and H. Yakowitz, eds.) Plenum Press, New York (1975) Ch. IX, X.

[6] J. Adam and J. B. Rich, Acta Cryst. 8, 349 (1955).

[7] M. von Stackelberg and E. Schnorrenberg, Z. physik. Chem. B27, 37 (1934).

[8] J. H. Cox and L. M. Pidgeon, Can. J. Chem. 41, 1414 (1963).

[9] D. E. Newbury and D. C. Joy, SEM/73 (O. Johari, ed.) IITRI, Chicago, Ill. (1973), p. 151.

[10] C. E. Fiori, H. Yakowitz and D. E. Newbury, SEM/74 (O. Johari, ed.) IITRI, Chicago, Ill. (1974) p. 167.

[11] K. F. J. Heinrich, C. E. Fiori, and H. Yakowitz, Science 167, 1129 (1970).

[12] P. C. Goldmark and J. J. Hollywood, Proc. IRE, 39 (10), 1314 (1951).

Fig. 1 Tapered tensile bar shown actual size.

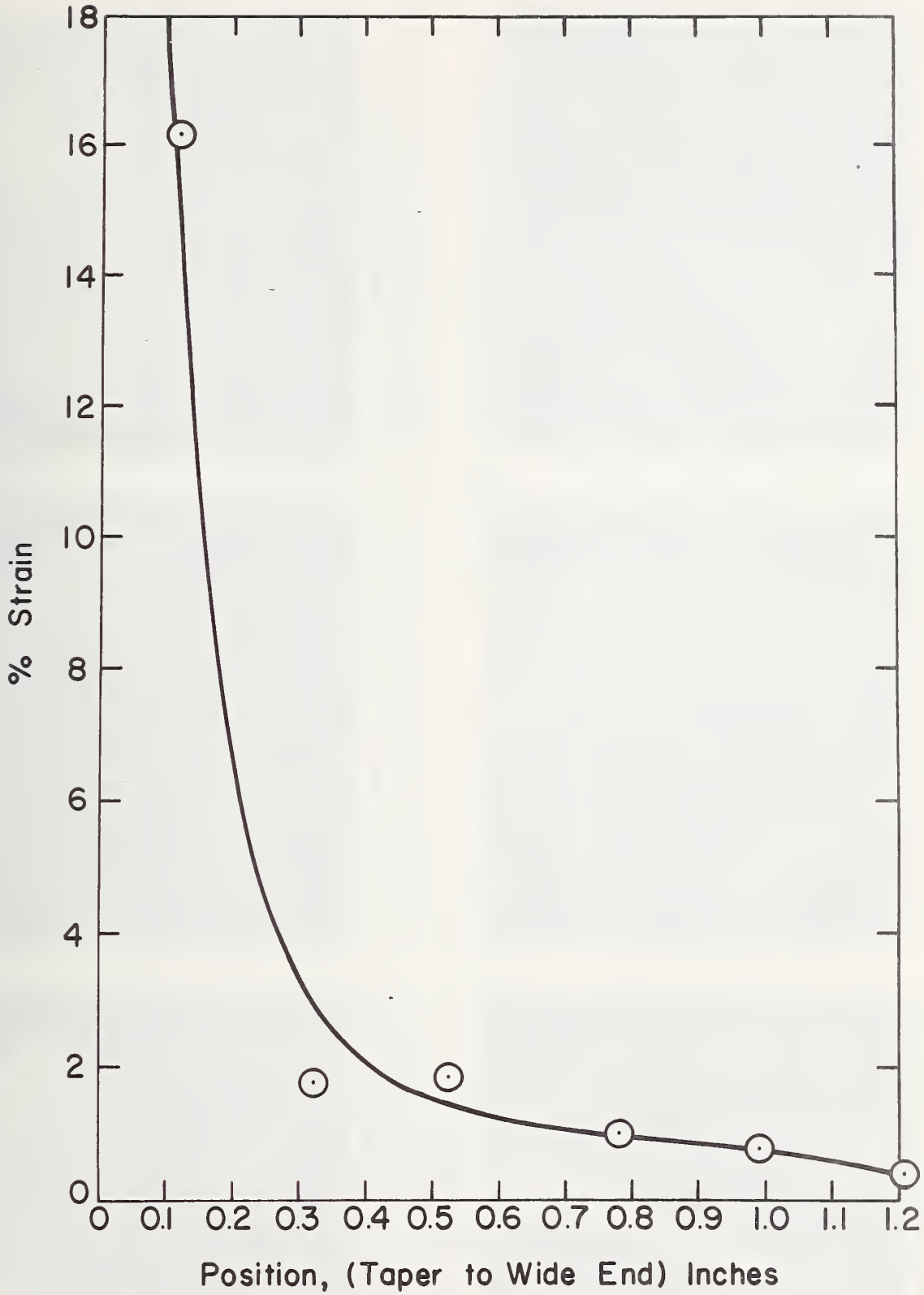

Fig. 2 Actual strain as a function of position in aluminum tapered tensile bar nominally strained 1.2%.

Fig. 3a Electron channelling pattern (ECP) from grain at wide end of annealed tapered tensile bar of Al (30kV, 0.2 μamps).

Fig. 3b Same as Fig. (3a) but proceeding toward narrow end of bar.

Fig. 3c Same as Fig. (3b) but continuing toward narrow end of bar.

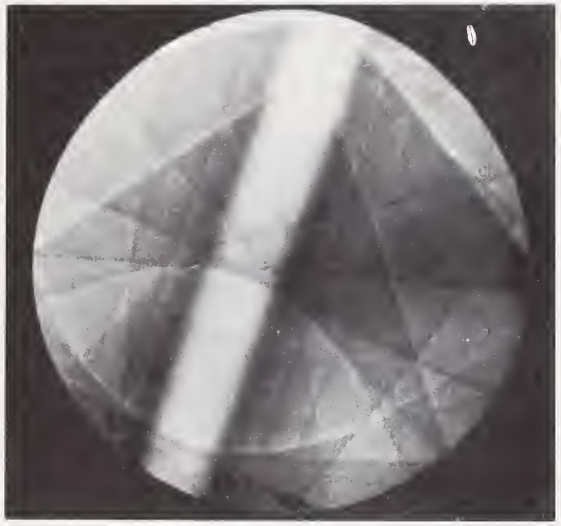

Fig. 3d Same as Fig. (3c) about midway through bar.

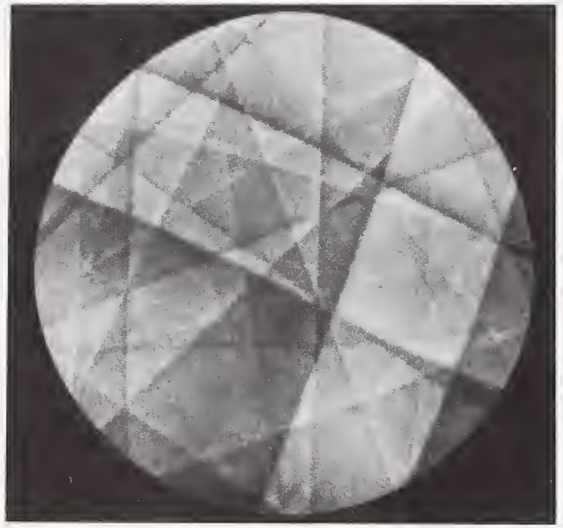

Fig. 3e Same as Fig. (3d) approaching narrow end of bar.

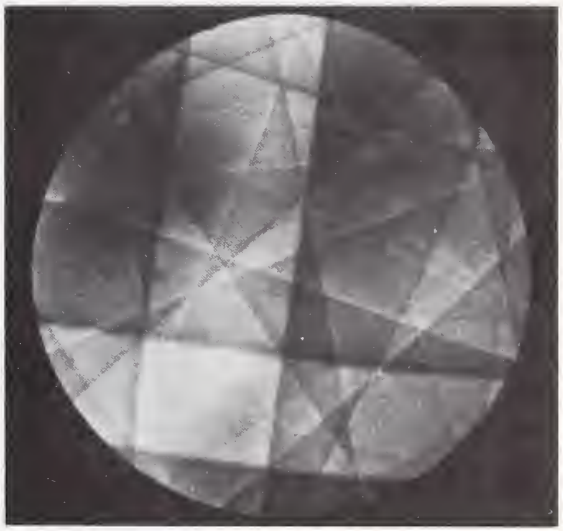

Fig. 3f Same as Fig. (3e) but near narrow neck of bar.

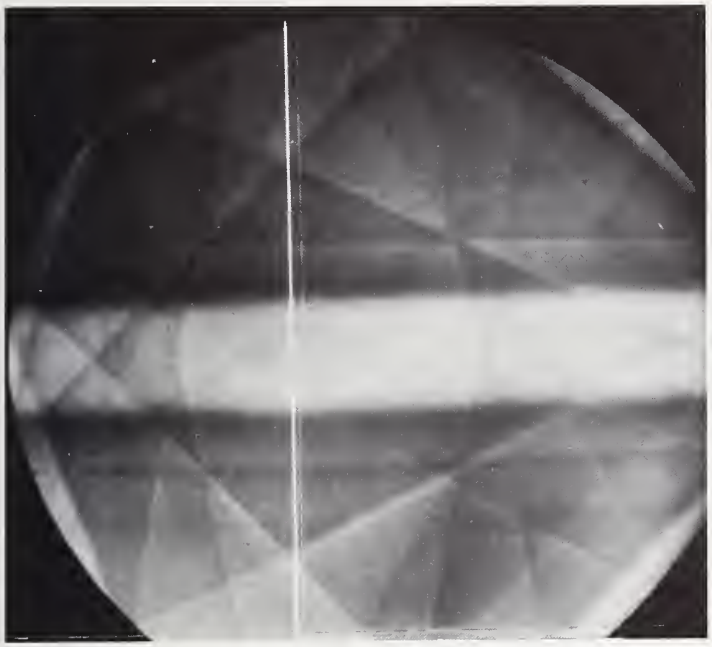

Fig. 4a Electron channelling pattern of annealed electropolished aluminum. Line indicates region from which profile information was taken.

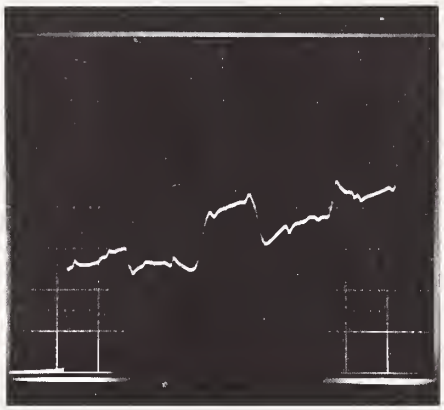

Fig. 4b Intensity profile along line in Fig. 4a. Scale: 2 volts/cm.

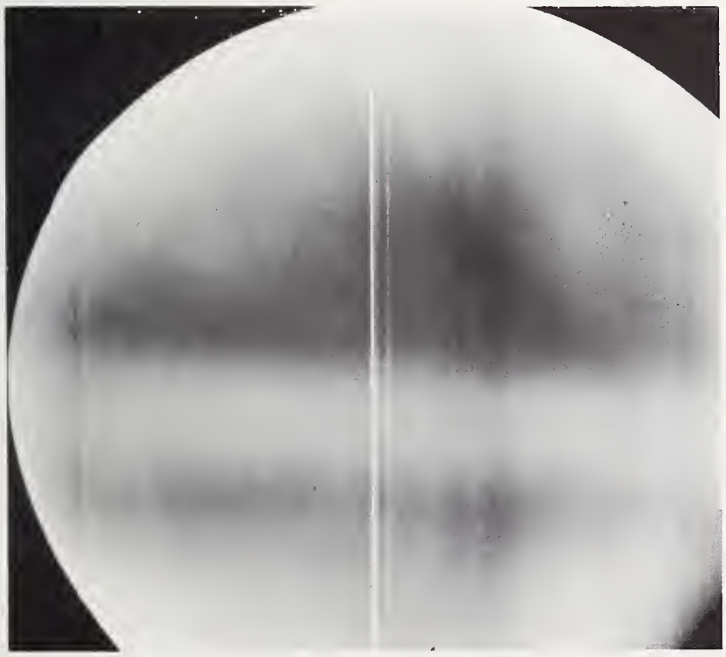

Fig. 4c Electron channelling pattern of aluminum crystal rolled to 5% reduction and then electropolished. Line indicates profile trace position.

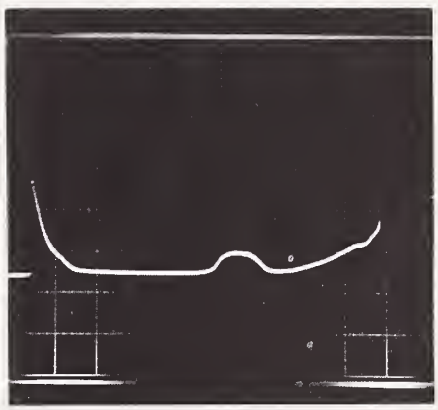

Fig. 4d Intensity profile along line in Fig. (4c). Scale: 2 volts/cm.

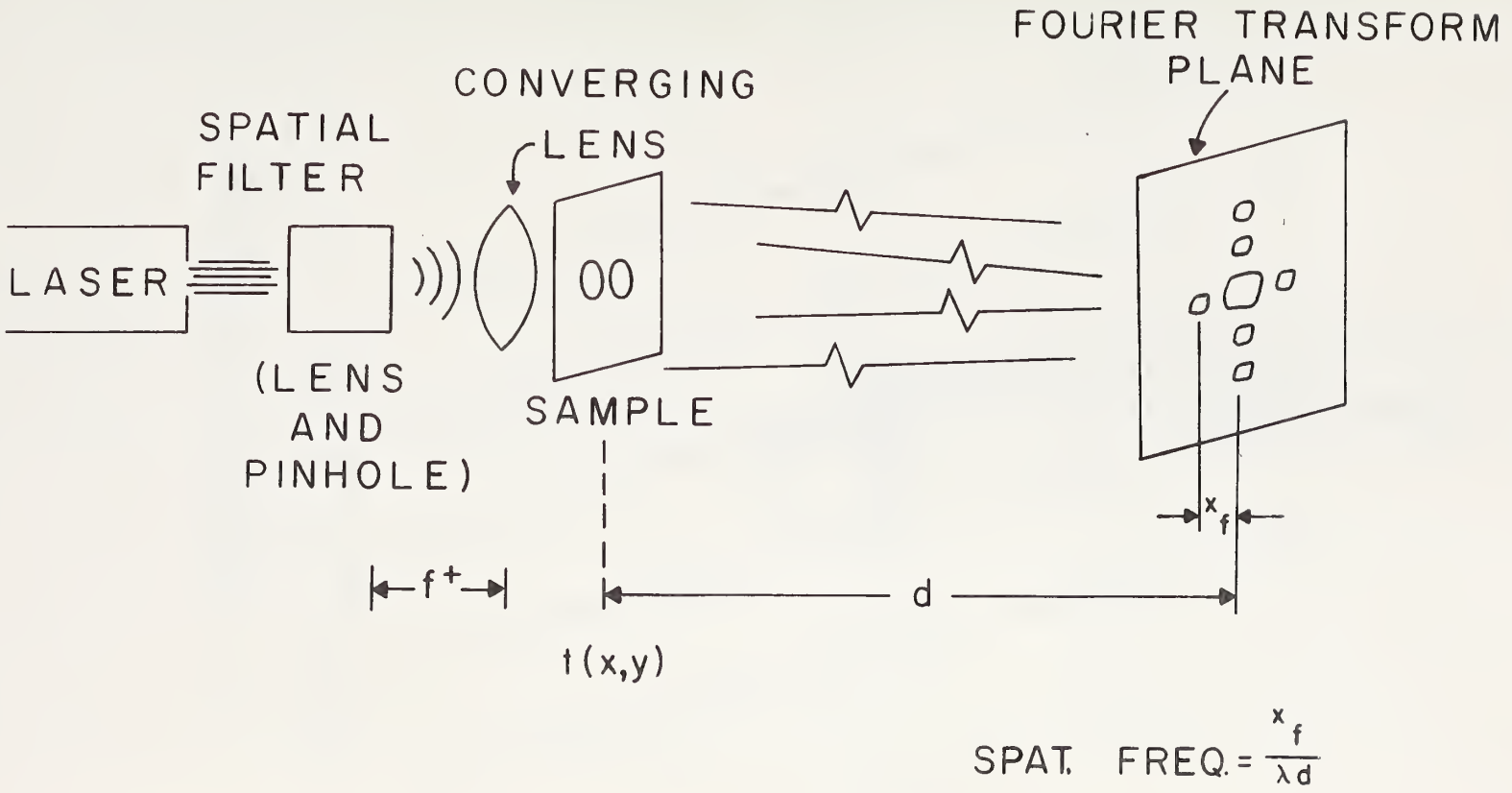

Fig. 5 Schematic view of apparatus used to prepare optical transforms.

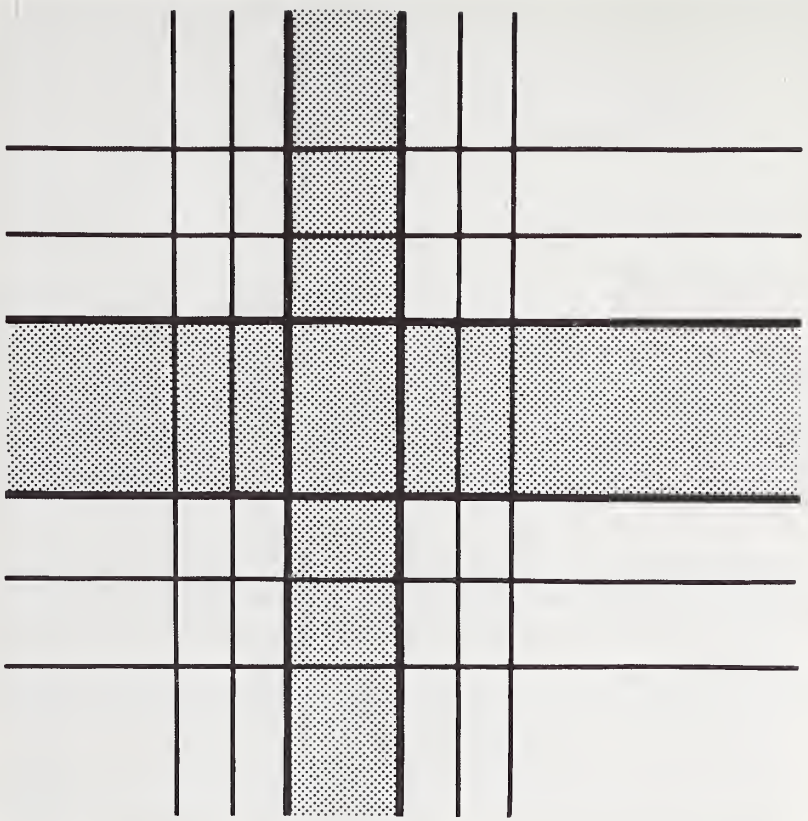

Fig. 7a Pseudo-electron channelling pattern.

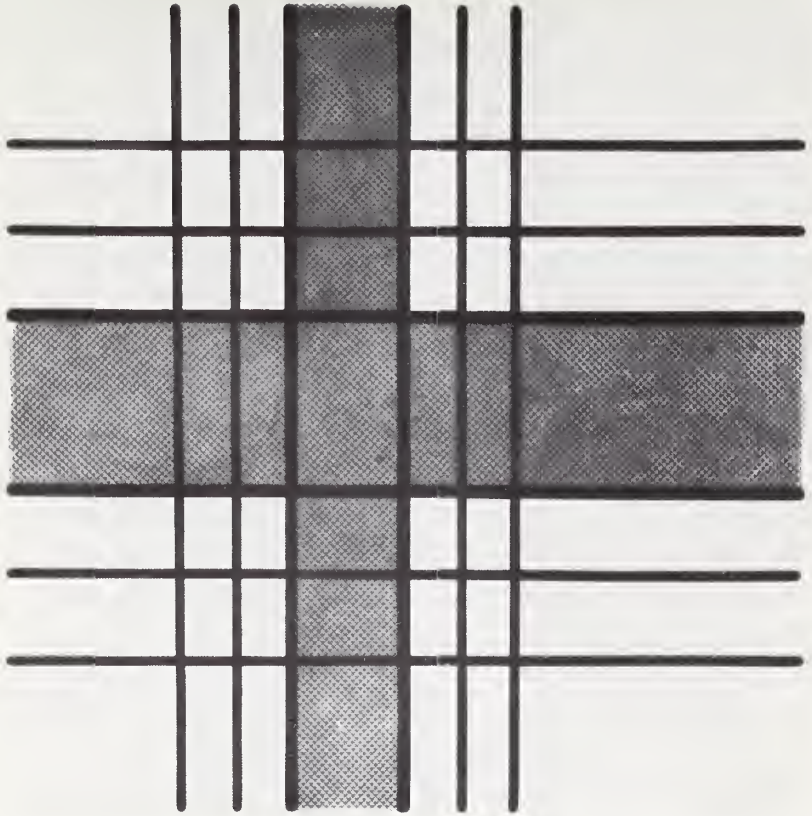

Fig. 7b As Fig. (7a) but slightly out of focus to simulate effects due to strain in a real electron channelling pattern.

Fig. 7c As Fig. (7b) but more blurred.

Fig. 7d As Fig. (7c) but blurred so as to cause absence of some features.

Fig. 8a Optical transform of Fig. (7a) without projector lens. The spot pattern is due to the periodicity in the stipple. The cross is due to the overall pattern symmetry.

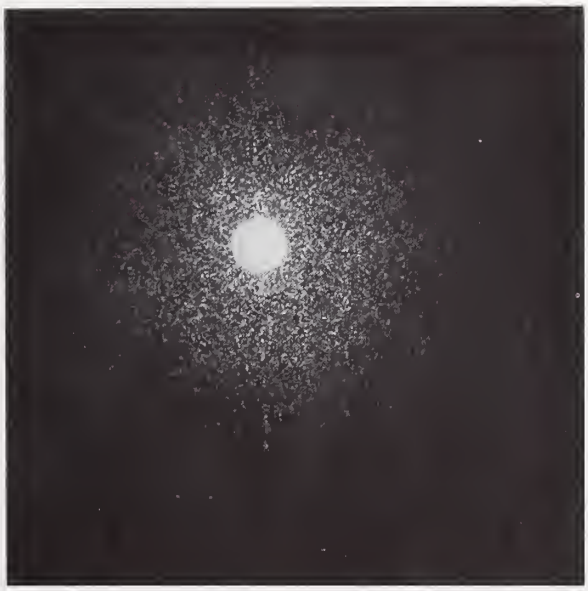

Fig. 8b Optical transform of Fig. (7b) without projector lens. The spot pattern is gone since the stipple pattern is completely blurred.

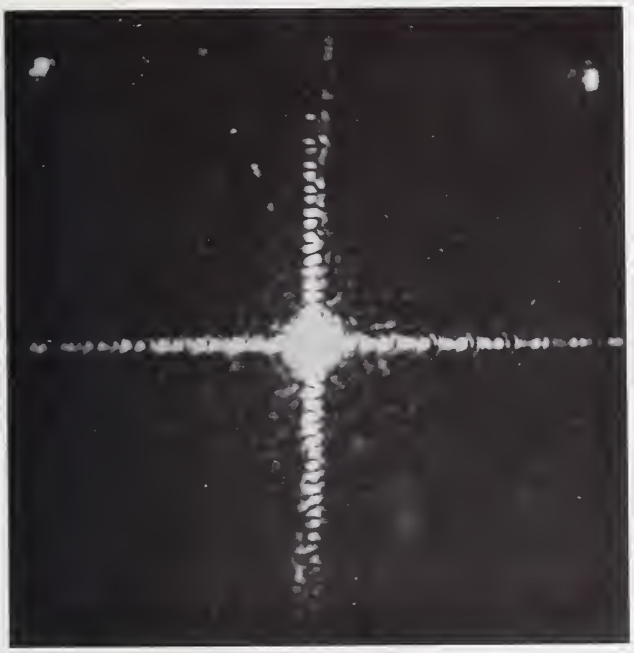

Fig. 9a Optical transform of Fig. (7a) with projector lens. The cross is seen to consist of a number of small spots and has long range.

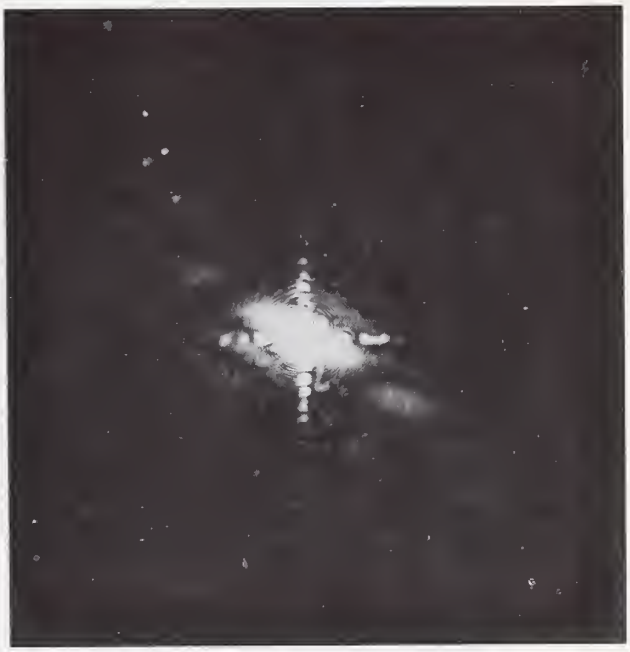

Fig. 9b Optical transform of Fig. (7b) with projector lens. The cross is less well defined than in Fig. (9a).

Fig. 9c Optical transform of Fig. (7c) with projector lens. The cross is poorly defined. Compare with Figs. (9a, b).

Fig. 9d Optical transform of Fig. (7d) with projector lens. The cross is virtually absent. Compare with Figs. (9a, b, c).

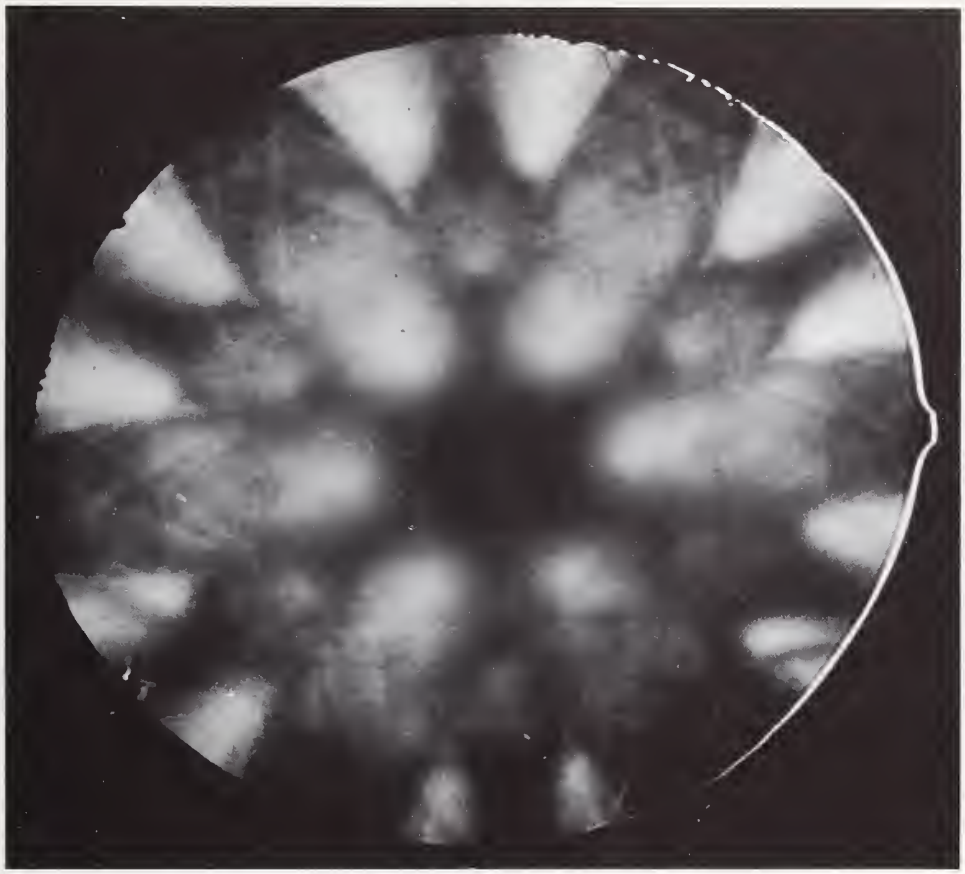

Fig. 10a Electron channelling pattern of the <111> pole of a niobium single crystal.

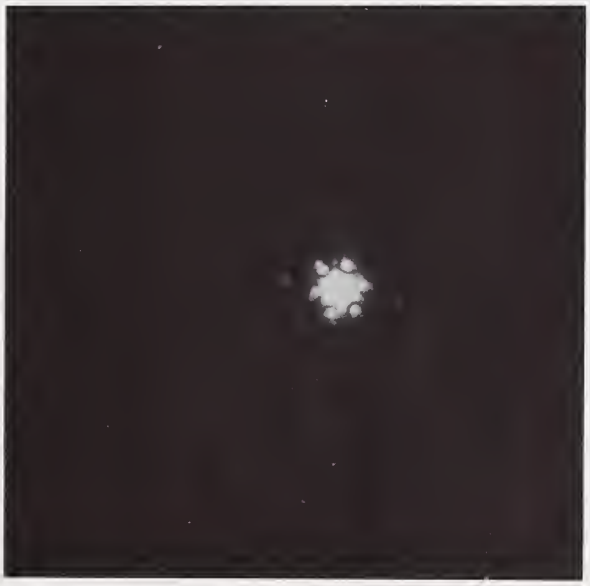

Fig. 10b Optical transform of Fig. (10a) with projector lens. The symmetry elements are apparent.

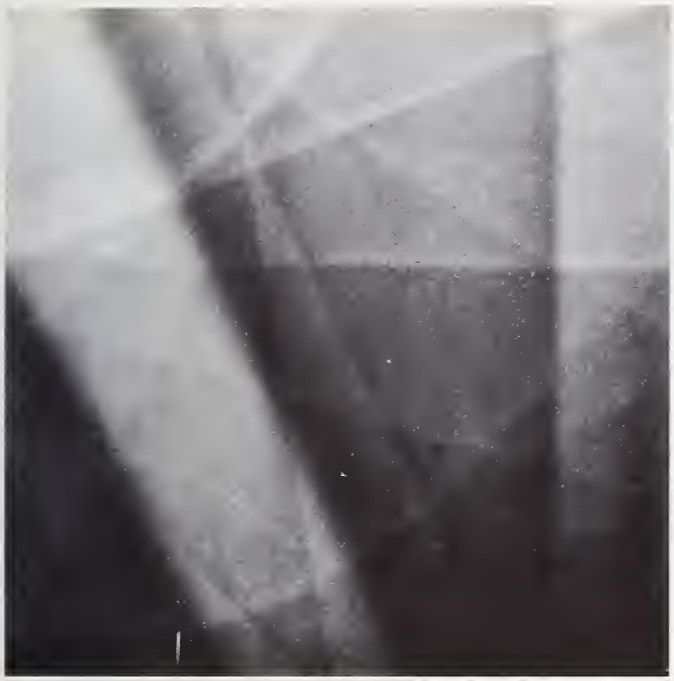

Fig. 11a Electron channelling pattern of annealed electropolished aluminum.

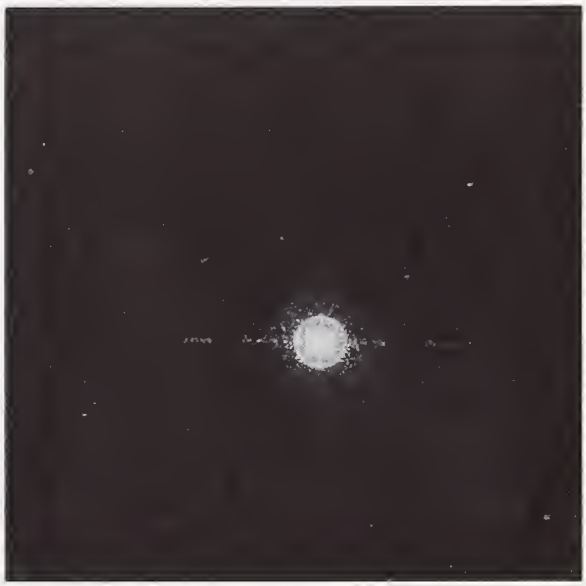

Fig. 11b Optical transform without projector lens of Fig. (11a).

Fig. 12a Electron channelling pattern of deformed aluminum.

Fig. 12b Optical transform, without projector lens, of Fig. (12a). Pattern is considerably less sharp than Fig. (11b).

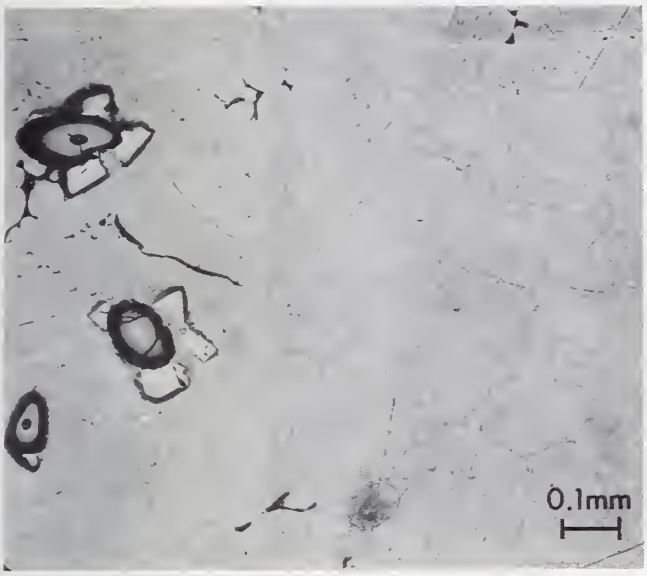

Fig. 13 Optical micrograph showing grain boundary phase, SiC fibers with tungsten core and tungsten impurity in Al matrix - SiC reinforced composite.

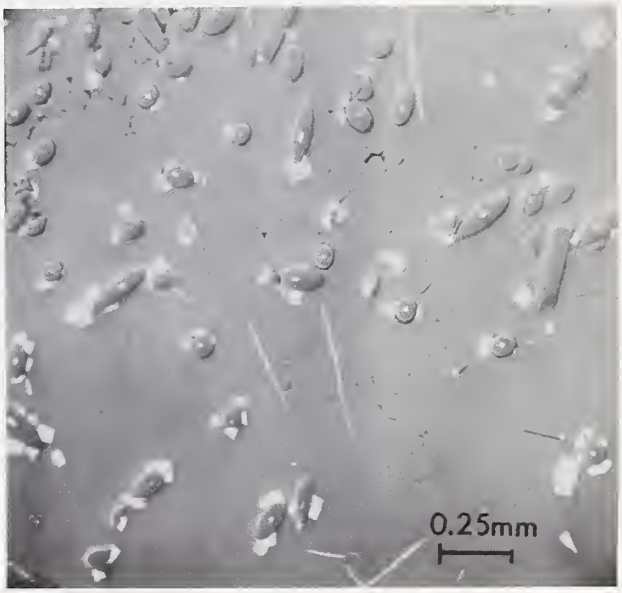

Fig. 14 Scanning electron micrograph (specimen current mode) showing aspect and dispersion of SiC fibers in Al matrix. White regions are W impurity. Note cracks and shrinkage cavities in the matrix.

Fig. 15a Reaction zones at SiC-Al interface. Note cracks in SiC fibers and nonuniformity of reaction zone.

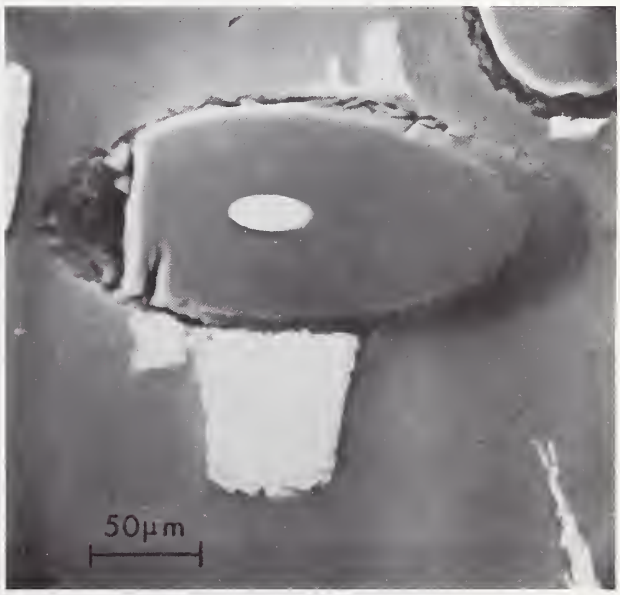

Fig. 15b Detail of reaction zone at SiC-Al interface. White material is Al_4W impurity.

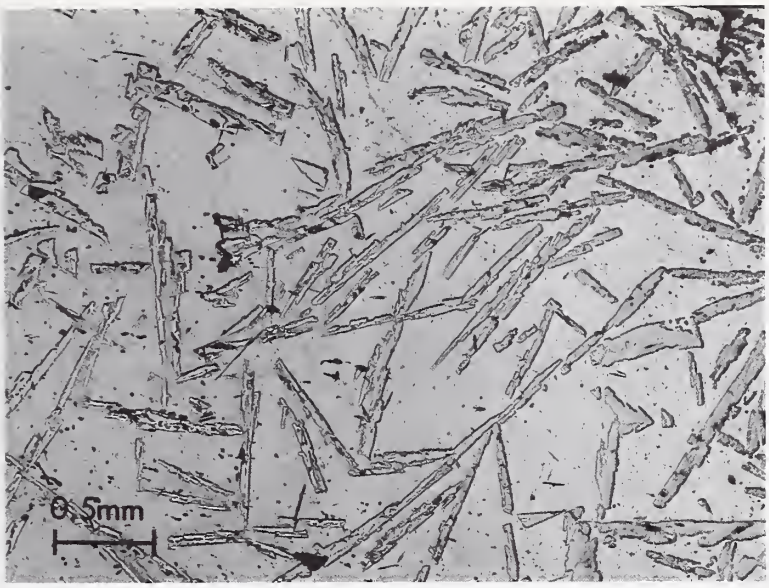

Fig. 16 Aluminum matrix with tungsten wire reinforcement. Optical micrograph shows dispersion of reinforcement and randomness of reinforcer orientation.

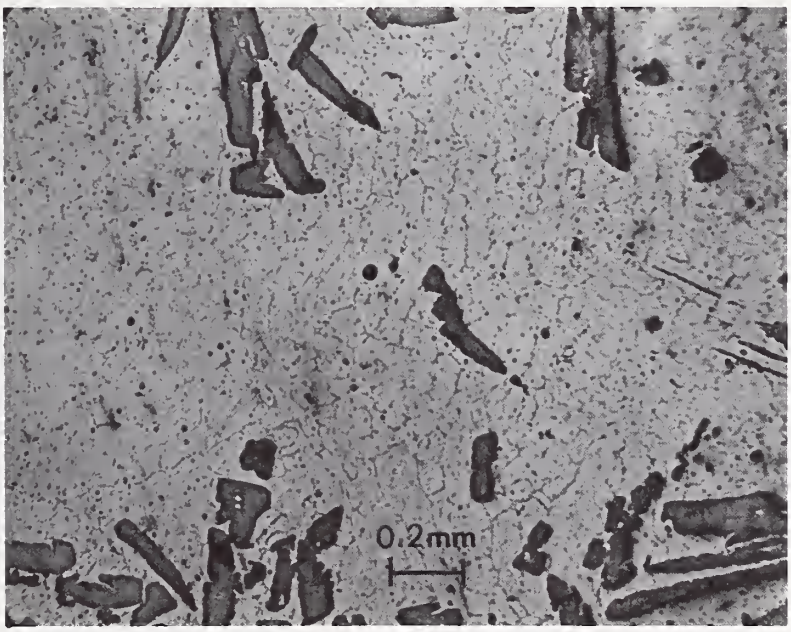

Fig. 17 Optical micrograph showing a grain boundary phase in Al-W composite.

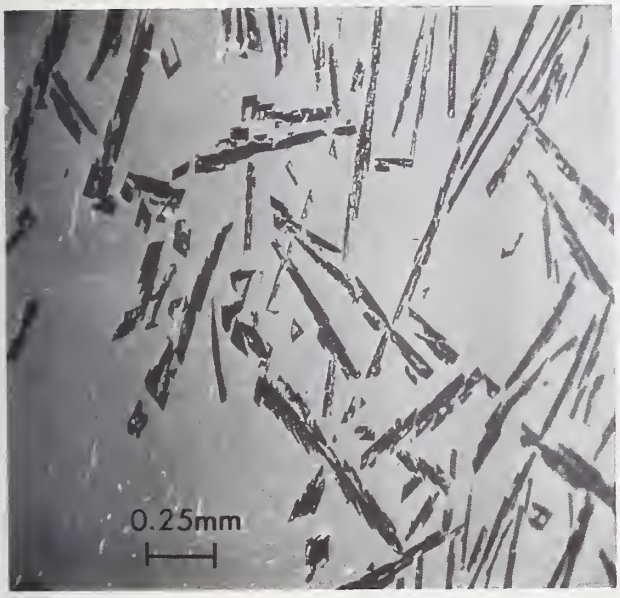

Fig. 18a Scanning electron micrograph showing irregular aspect of reinforcement in Al-W composite.

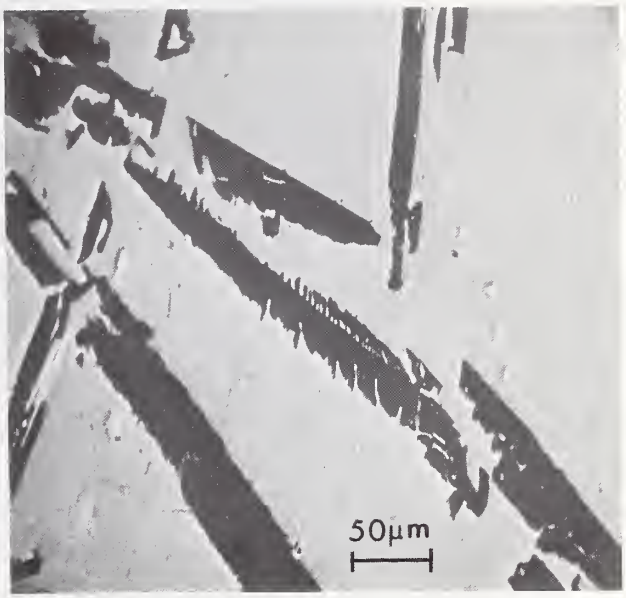

Fig. 18b Scanning electron micrograph showing interfacial attack and the grain boundary phase.

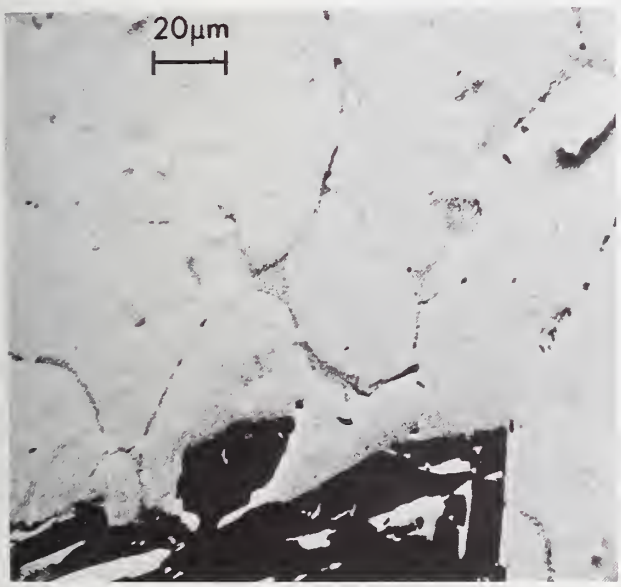

Fig. 18c Scanning electron micrograph showing extent of grain boundary phase.

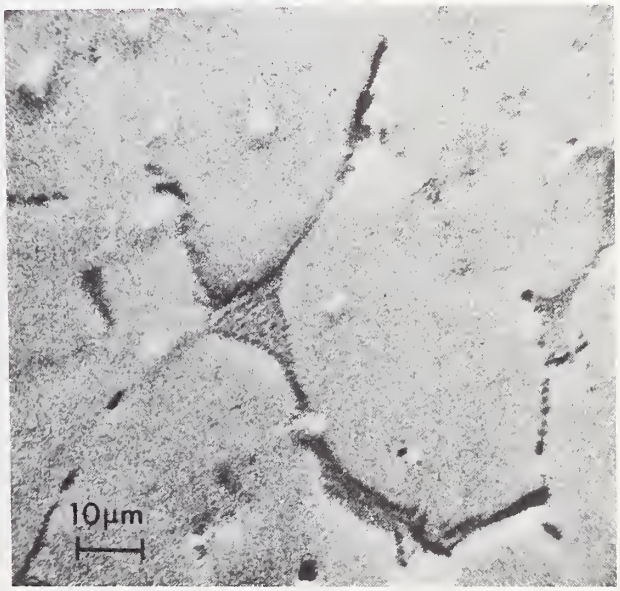

Fig. 18d Grain boundary phase revealed as being eutectic-like material.

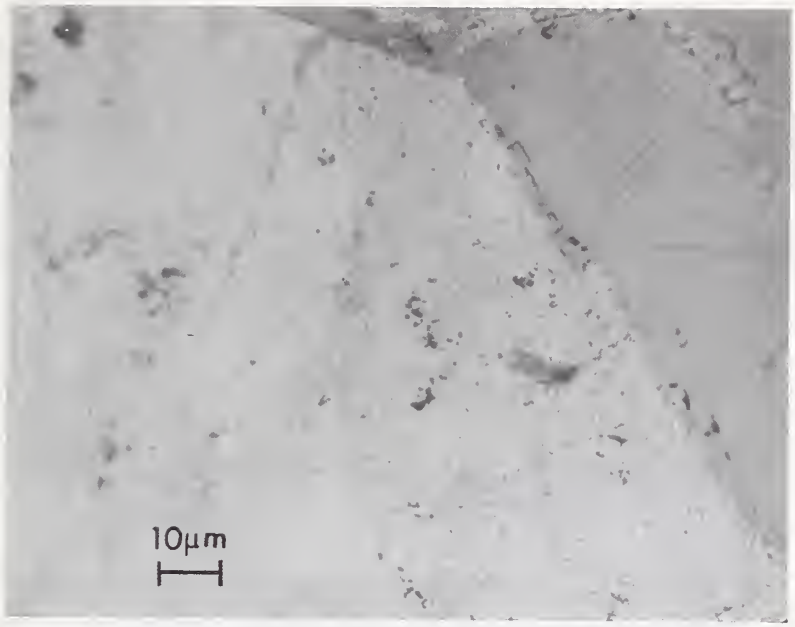

Fig. 19 Optical micrograph showing local reaction at matrix-reinforcement interface in Al-W composite. Reaction product contributes to formation of grain boundary phase.

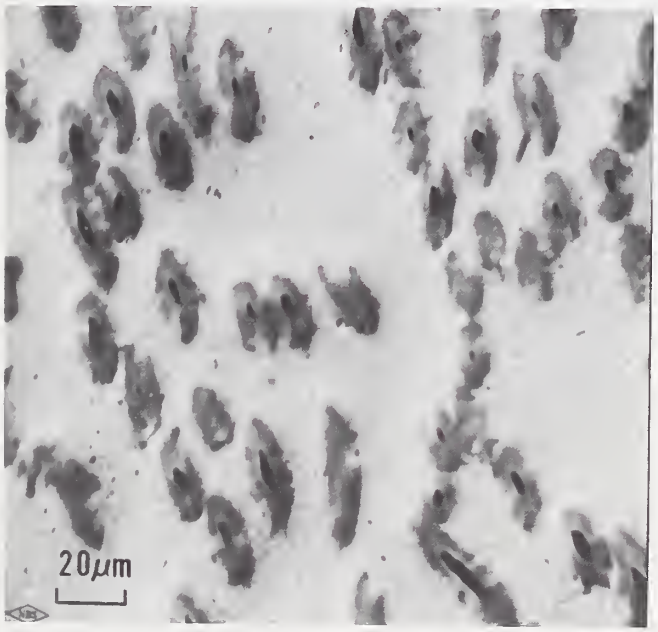

Fig. 20 Scanning electron micrograph of graphite reinforcer-Al matrix composite. Reaction of Al with the graphite has occurred leaving grey (Al_4C_3) regions and some black core (AlC_6) areas.

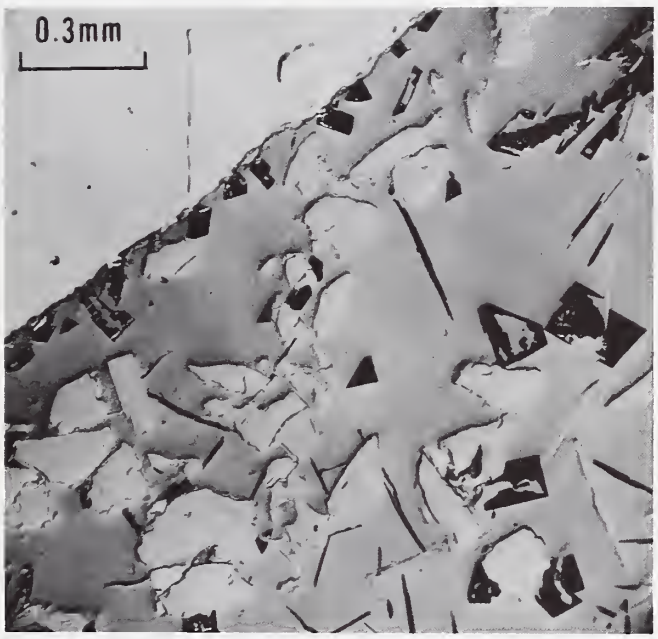

Fig. 21 Scanning electron micrograph of sapphire reinforced Al matrix composite showing agglomeration of sapphire. Black regions are tungsten bearing impurity.

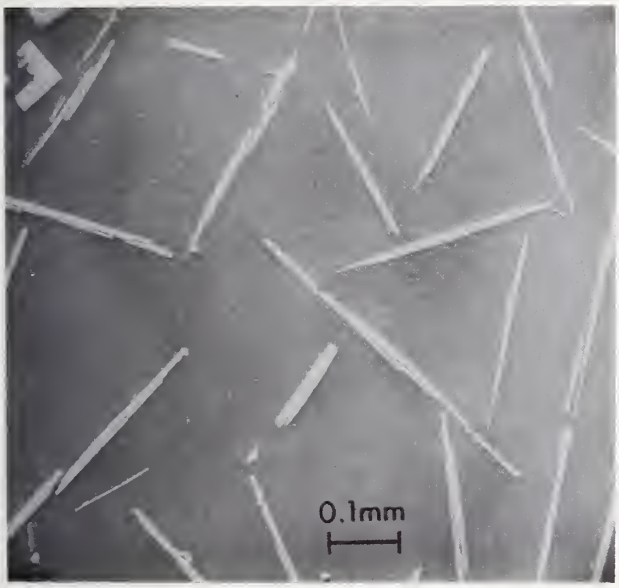

Fig. 22a Sapphire free region of sapphire-Al matrix composite. White needles are tungsten bearing impurity having composition 41.3 wt. pct. Al, balance W.

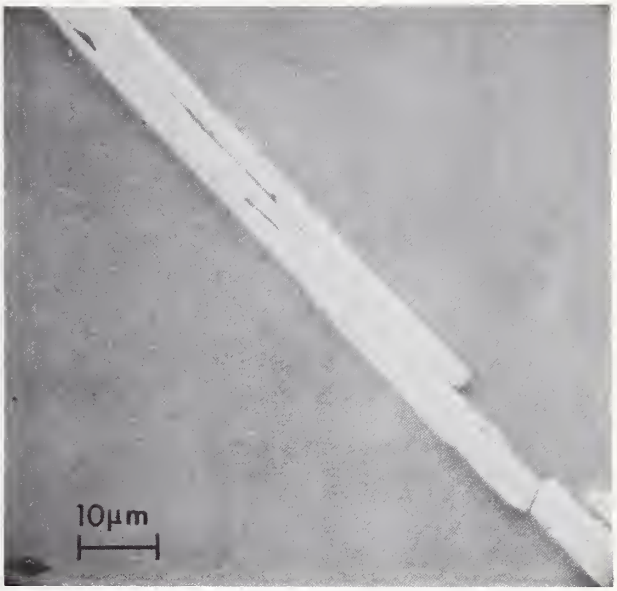

Fig. 22b Detail of W-Al needle in sapphire free region of sapphire-Al matrix composite. Note reaction free interface with matrix.

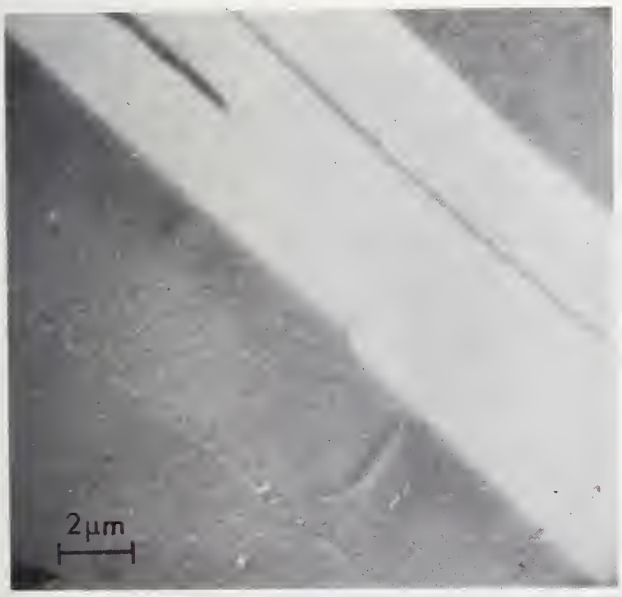

Fig. 22c Interface of W-Al needle. Interface is remarkably clean and sharp.

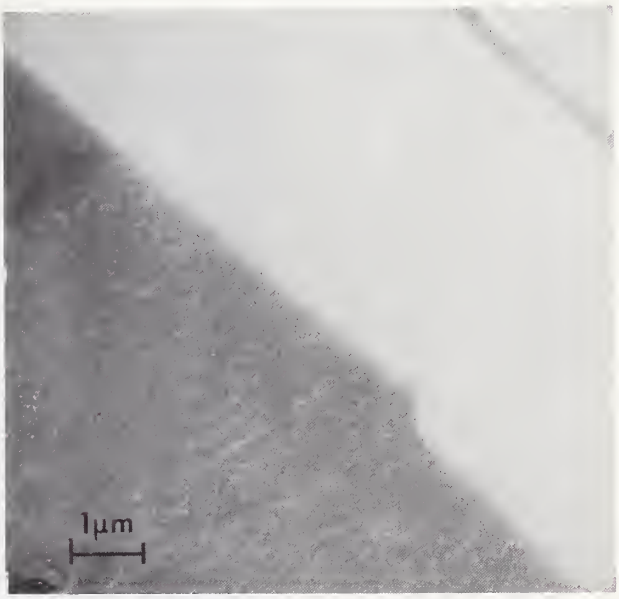

Fig. 22d Interface of W-Al needle showing no visible reaction within 500Å of boundary. Excellent bonding would be predicted for this situation.

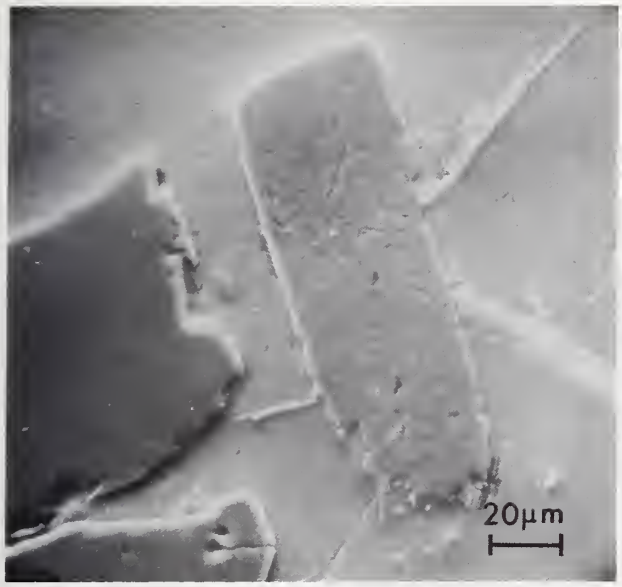

Fig. 23a Sapphire filaments in sapphire-Al matrix composite. Note cracks in case of central feature and absence of cracks in neighboring filaments. White material is W bearing impurity.

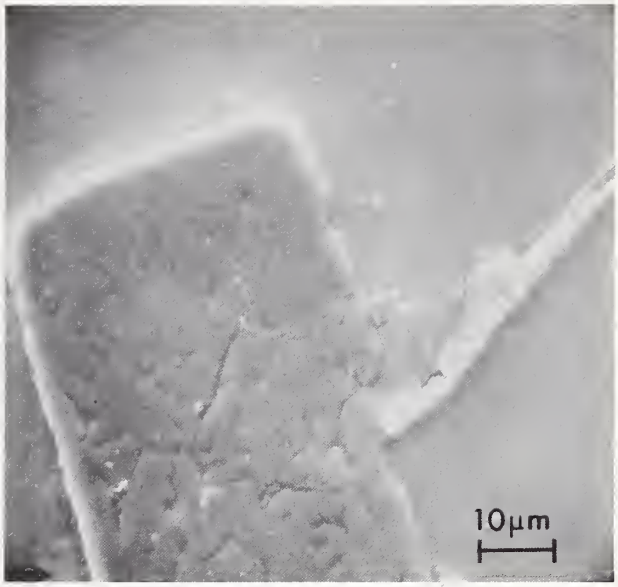

Fig. 23b Same as Fig. (23a) but showing sapphire-Al interface to be reaction zone free.

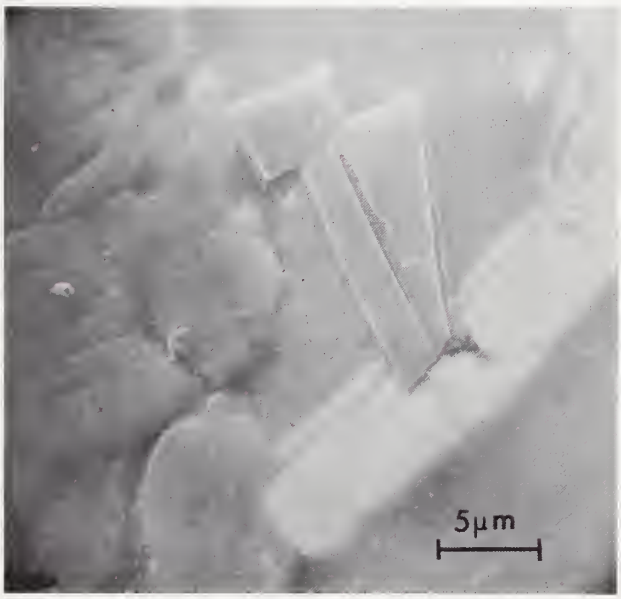

Fig. 23c Same as Fig. (23b) showing clean interface at 1000Å level.

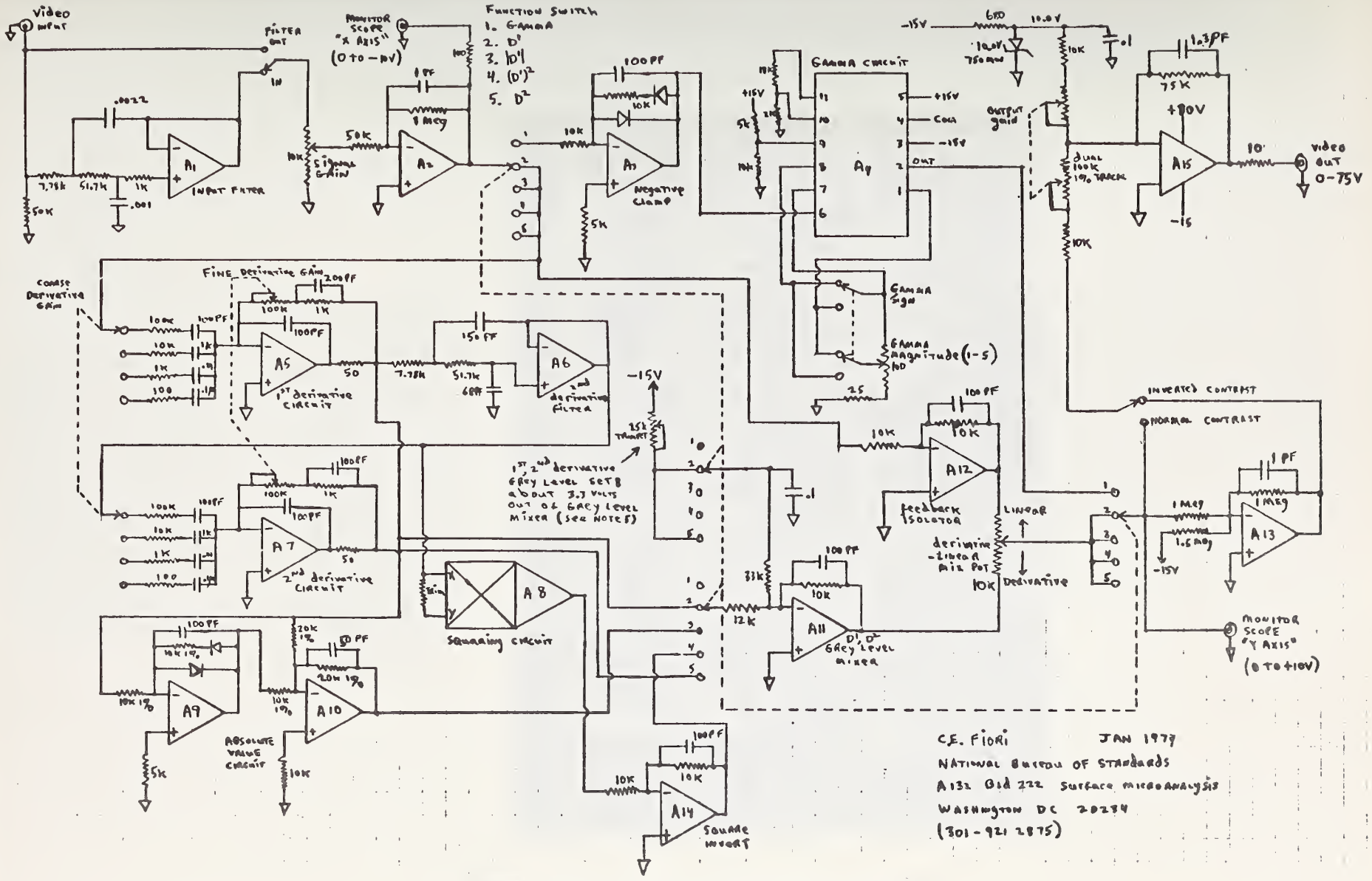

Fig. 24 Schematic diagram of signal processing equipment for scanning electron microscopy.

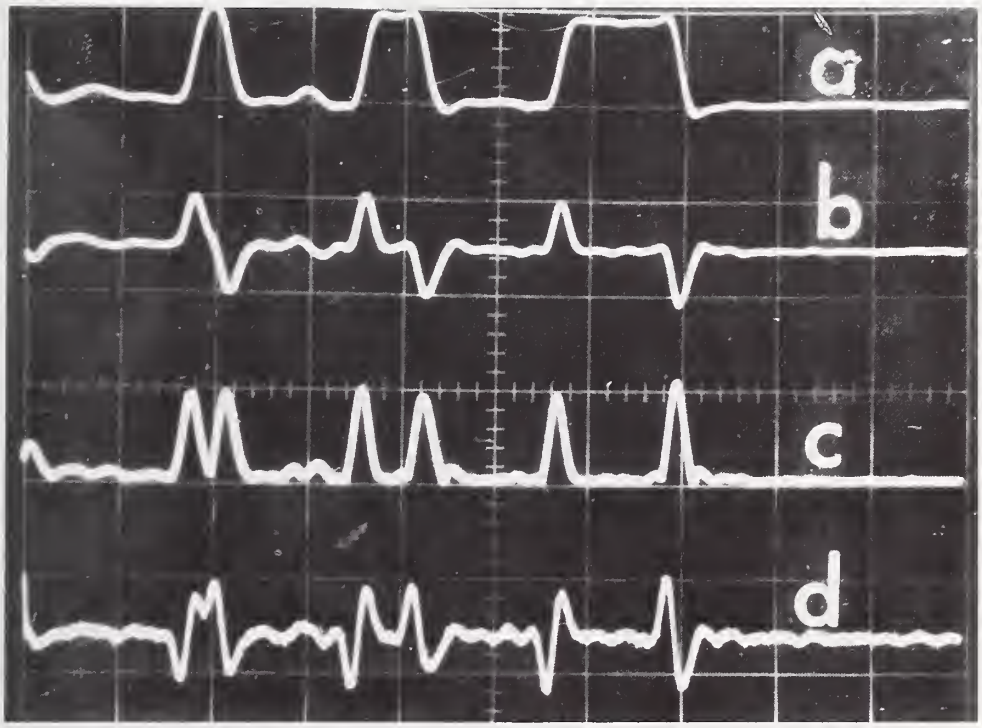

Fig. 25 Effect of derivative operators on signal from typical SEM specimen: (a) Direct emissive signal, (b) First time derivative of signal, (c) Absolute value of first time derivative, (d) Second time derivative (inverted) of signal.

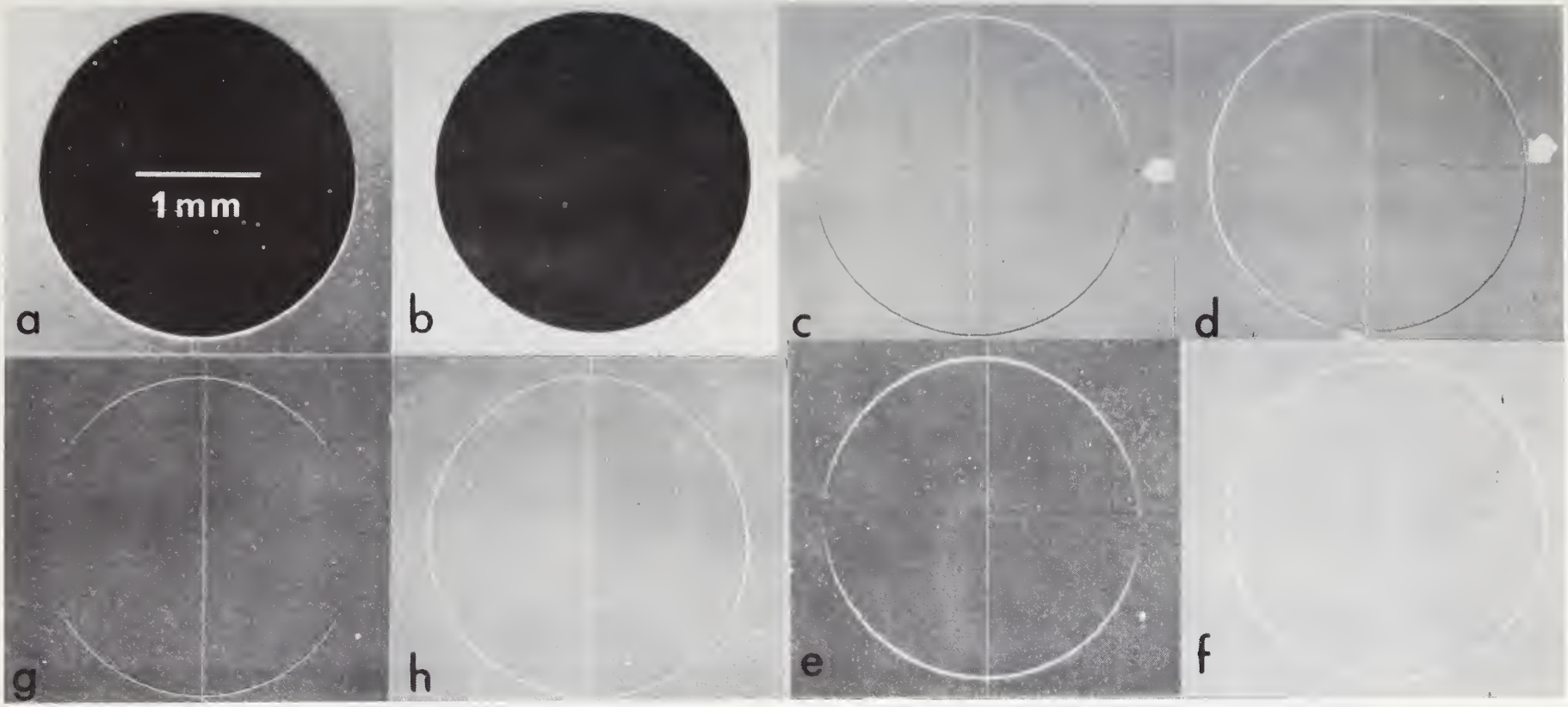

(a) Direct secondary electron image; (b-h) specimen current images.
(b) Direct image, note even edge illumination.
(c) 1st time derivative image scanned unidirectionally; information loss (arrows) and image anisotropy are apparent.
(d) 1st time derivative scanned orthogonally. Line of information loss due to anisotropy is indicated by arrows.
(e) Absolute value of 1st time derivative scanned unidirectionally.
(f) Absolute value of 1st time derivative scanned orthogonally.
(g) 2nd time derivative scanned unidirectionally.
(h) 2nd time derivative scanned orthogonally; note isotropic image and impression of vertical illumination.

Fig. 26 Hole in Al disk; specimen normal to primary beam, 30kV, 5 nA specimen current.

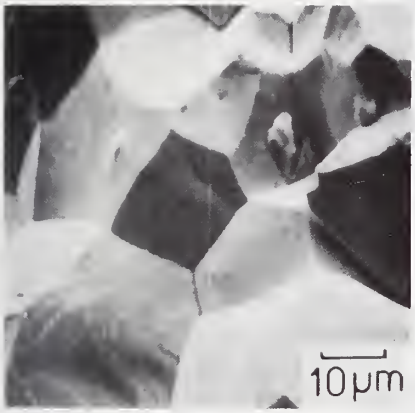

Fig. 27a Secondary electron image of fracture surface of pure iron. No image processing applied, 20kV, 5nA specimen current, specimen tilted 30°.

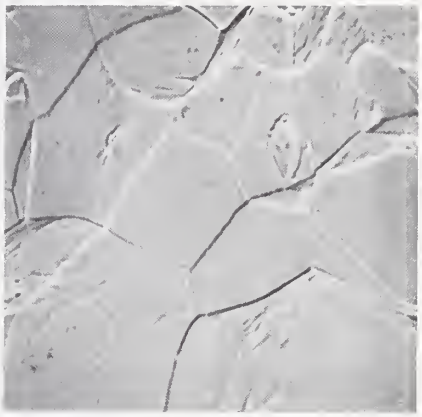

Fig. 27b First time derivative of image in Fig. (27a). Note flattening and apparent oblique illumination. Scanned orthogonally.

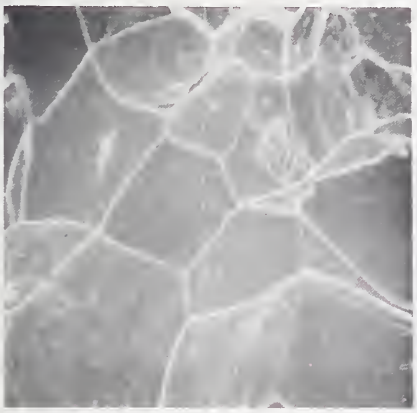

Fig. 27c Absolute value of first time derivative. Note strong outlining of edges. Scanned orthogonally.

Fig. 27d Second time derivative of image of Fig. (27a). Note impression of vertical illumination and less apparent flattening. Scanned orthogonally.

Fig. 27e Same as Fig. (27b) but mixed in equal proportions with direct signals scanned orthogonally; note crispening of image.

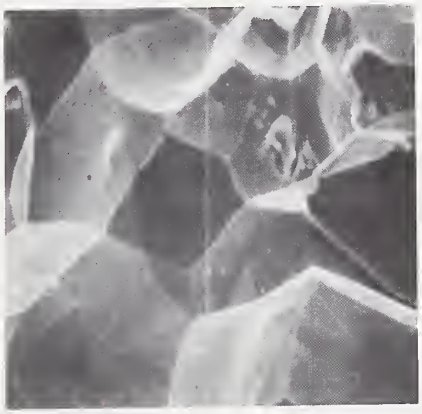

Fig. 27f Same as Fig. (27c) but mixed in equal proportions with direct signal. Scanned orthogonally.

Fig. 27g Same as Fig. (27d) but mixed in equal proportions with direct signal. Scanned orthogonally. Note crispening of image as well as apparent vertical illumination.

Task 4

Melt Shape in Weightless Crystal Growth

S. C. Hardy and S. R. Coriell

Metallurgy Division
Institute for Materials Research

Summary

Experimental investigations of the distribution of water at the end of an ice cylinder in a simulated low gravitational field have yielded different results for isothermal and linear gradient thermal geometries. In the isothermal arrangement, the stable configuration of the ice and water is one in which the cylinder passes entirely through the water zone. In a gradient, however, it is possible to have a cap of water on the end of the cylinder. Theoretical calculations have been carried out on the shape and stability of a vertical rotating liquid zone subject to a weak vertical gravitational field. The first order correction to the zero gravity stability result is obtained.

Introduction

The shape and stability of liquid bodies in zero gravity have been subjects of experimental investigation since the pioneering work of Plateau[1] over a hundred years ago. The quantitative theoretical treatment of these problems is equally old, the basic variational mathematics[2] having been successfully formulated prior to 1900. With the development of space technology, a new interest has arisen in phenomena involving liquids in zero gravity. The particular concern of this project is the shape and stability of the melt during containerless crystal growth in space.

The zero gravity condition has been previously simulated by using immiscible liquids of equal density, soap bubbles, or specimens sufficiently small to make the surface tension forces much larger than the volume forces of gravity. Numerous configurations of liquid and solid surfaces have been studied:[3] (1) zones between solid plates; (2) zones between rings; (3) zones between spheres and (4) pendant drops, and many more complicated arrangements. In addition, the effects of rotation on the shape and stability of the liquid has been investigated[4-6] not only in the laboratory but in space.

With the exception of the recent space experiments by Walter,[7] most of this extensive research has not involved solidification. Furthermore, because of the particular boundary conditions imposed, the analogy with solidification may not be strong. The boundary conditions differ from those appropriate to solidification in two significant respects. First, surface coatings were often used on the solid surfaces to prevent or restrict wetting and eliminate the phenomena known as "capillary run-off". Since crystals generally are wetted by their melts, this clearly does not model solidification. Secondly, the experiments were essentially isothermal whereas solidification generally involves high thermal gradients. Surface tensions are temperature dependent

and, thus, the stability of liquid zones in high temperature gradients may not be the same as in isothermal conditions.

Our experimental research in the past year has been directed to examining the shape of liquid zones in near zero gravity with actual melt-crystal interfaces in contact with the zones. Rather than concentrate on quantitative measurements, we have attempted a variety of qualitative experiments with the intention of doing more detailed work on interesting areas later. We have worked exclusively with water-ice because of convenience and prior experience.

In addition, we have made a study of the variational mathematics used in treating liquid zones. A detailed calculation has been completed applying these techniques to the stability of a cylindrical zone between flat plates in a weak gravitational field and the first order correction to the zero gravity stability criterion has been determined. This calculation is important to our experiments and to experiments in space because zero gravity is never actually attained; it is approximated. Thus, it is essential to understand how small volume forces modify the zero gravity stability criteria.

Experimental Procedures

The technique we have used to simulate zero gravity uses a liquid that is immiscible with water and of nearly the same density as a supporting medium. After trying a number of liquids, we selected a solution of di-n-butyl phthalate and xylene because of availability and adequate solubility at temperatures near 0°C. The solutions are made up in a constant temperature bath at 0°C, the temperature at which we require density balancing. The final density is compared with that of water by forming a small water drop in the solution and watching its motion. This is done using a micrometer syringe and a thin teflon tube inserted into the solution from the top.

Exact density balancing is impossible to achieve when there is a temperature gradient across the water zone; it is very difficult to achieve in isothermal experiments. Therefore, we do not attempt it; rather, we perform identical experiments using solutions with densities higher and lower than that of the water. If the same result is found in both cases, we consider the observation to be independent of precise density balancing.

The experiments are performed in cylindrical glass cells similar to that shown in Figure 1. The curvature of the cell results in a distorted image i.e. a sphere appears flattened in the vertical dimension. Prior to an experiment a polycrystalline cylinder of ice, previously formed in a glass tube, is frozen into the socket at the bottom of the cell. The solution is cooled to below 0°C and then poured into the cell until the end of the ice cylinder is covered.

The cells are used in two arrangements which provide different thermal geometries. In one case, the cell is placed in a constant temperature bath maintained below 0°C. Heat flow is radial in this arrangement; the ice cylinder and solution are isothermal. In these isothermal experiments, the ice cylinders are generally not melted to produce a liquid zone. Instead, a drop of water is formed in the oil and brought into contact with the ice. In the other case, the sides of the cell are insulated, its bottom is placed in a very cold bath, and a heat leak is introduced at the top by inserting a metal rod into the cell and touching the surface of the solution. The heat flow is approximately along the axis of the cell and a thermal gradient can be established. This gradient is about 10°C/cm. in most experiments.

Experimental and Theoretical Results

The major experimental effort this year has used the semi-infinite cylinder geometry shown in Figure 1. We have examined what happens at the free end of the ice cylinder when a drop of water is brought into contact with it or when it melts. We have also made some studies of the freezing of the liquid zones.

Figure 2 is a sequence of pictures taken during the addition of water to the end of an ice cylinder in an isothermal immiscible liquid of density slightly greater than 1. A small drop of water was injected into the solution through a teflon tube as shown in 2a. The tube was then slowly lowered until the drop touched the end of the ice cylinder. Upon contact, the drop immediately ran down the cylinder and formed a liquid zone about its end as seen in 2b. Pictures 2c and 2d show the ice cylinder after adding several larger water drops. Note the detached drops which have floated upward in the cell. This demonstrates that the solution density was higher than that of the water and, therefore, would exert a buoyant force on the water which would be in the direction opposite to that of the observed motion. Thus, the distribution of water around the cylinder rather than in a "pendant" drop is attributed to surface tension forces rather than inexact density balancing.

In Figure 3, we show a similar experiment in which drops of water are added to the side of the cylinder at two points. Again, the solution density was slightly greater than that of water. The stability of the liquid zones suggests that the small buoyant forces acting on the water are insignificant in comparison with the surface forces.

The distribution of the water about the cylinder seen in Figures 2 and 3 is not a new observation; Plateau obtained the same results in the last

century using olive oil, water, and an iron wire. From the perspective of containerless crystal growth in space, however, this behavior suggests possible difficulties in controlling the distribution of the melt when in contact with crystal because of capillary run-off.

The shapes of liquid zones in temperature gradients can be significantly different from those found in isothermal experiments. Figure 4 shows the successive changes in the distribution of the water when an ice cylinder is slowly melted from its end in a temperature gradient. The ice and supporting liquid are initially below the melting point (4a). The temperature at the top of the cell is then increased by lowering the heat leak. As the temperature rises at the cylinder end, the ice melts and a cap shaped water zone develops (4b). This zone slowly grows as melting continues. However, it retains its cap shape with a slightly convex liquid-solid interface (4c). Capillary run off and rapid freezing occurred shortly after 4c, leaving a smaller liquid zone and an irregular, distorted ice cylinder (4d).

A somewhat different process is seen when an ice cylinder is rapidly melted at the free end. In this case, the water cannot form a stable cap at the cylinder end like that seen in (4b, 4c). Rather the large volume of water moves down the cylinder and stabilizes in a shape like those found in the isothermal experiments (see Fig. 3). This process is shown in Figure 5. An originally cylindrical ice cylinder was very rapidly melted at its end by a thermal impulse. The mass of water produced by this process flowed down the shank and stabilized at a point where the temperature was significantly below the melting point as indicated by rapid freezing at the base of the drop (5a). Melting of the end of the cylinder and freezing at the base of the water drop continued simultaneously producing a swelling of the ice

cylinder and a cap of water (5b, 5c). A planar ice-water interface developed which then moved upward as the cell continued to cool. Eventually, a spherical cap of ice on a cylindrical shank was produced. This was the result anticipated for Walter's space experiment.[7]

The most striking difference between the isothermal and temperature gradient observations is the apparently stable cap of water formed at the cylinder end in the latter experiments. This phenomenon is seen for solution densities both greater and less than 1 at 0°C indicating that it is not attributable to buoyancy. The stabilization of the cap may be due to changes in the shape of the solid or to variations in surface tension because of the temperature gradient. Quantitative experiments will be necessary to isolate the stabilizing factor.

In addition to the experimental observations described above, calculations have been carried out on the shape and stability of a vertical rotating liquid zone subject to a weak vertical gravitational field. A discussion and the details of these calculations are given in the Appendix. Here, we briefly summarize the most important results. As illustrated in Figure 6, we consider a liquid zone between two solid disks of radius R separated by a distance L; in cylindrical coordinates (r,z) the boundary conditions on the liquid zone are $r(-L/2) = r(L/2) = R$. The volume of liquid in the zone is $\pi R^2 L$ so that in the absence of gravity the shape of the zone is cylindrical, $r(z) = R$. We assume that in a coordinate system rotating with constant angular velocity Ω about the z-axis the liquid is stationary. We find that the zone is stable if

$$L/2\alpha < \pi\{1 - [(\varepsilon^2/2)\, h(\alpha/R)]^{\frac{1}{3}} + \ldots\}$$

where $\alpha = R/[1 + \rho\Omega^2 R^3/\gamma]^{\frac{1}{2}}$, $\varepsilon = \rho g \alpha^2/\gamma$,

$$h(\alpha/R) = (9/8)\,[1 - (\alpha/R)^2 + 3(\alpha/R)^4 + (\alpha/R)^6],$$

ρ is the density difference between the liquid and surrounding medium, γ is the liquid-medium surface tension, and g is the gravitational field. This equation gives the leading correction to the zero gravity stability result; the equation should be valid as long as $[(\varepsilon^2/2)\, h(\alpha/R)]^{\frac{1}{3}} << 1$. Since $h(\alpha/R) > 0$ for all (α/R), it is clear that a weak gravitational field always destabilizes the liquid zone. For no rotation the stability criterion becomes

$$(L/2R) < \pi\{1 - [9\varepsilon^2/4]^{\frac{1}{3}}\}$$

with $\varepsilon = \rho g R^2/\gamma$. In order for the correction to the zero gravity result to be less than 10%, $\varepsilon < 0.02$. For water in the earth's gravitational field, $R \cong 0.04$ cm corresponds to $\varepsilon \cong 0.02$; in 10^{-4} gravity R can be 100 times larger.

Several lines of research for the future are indicated by the experimental and theoretical work of the past year. The determination of what stabilizes a drop of water at the end of an ice cylinder in a thermal gradient is of high priority. This will require quantitative experiments and possibly theoretical calculations. In addition, measurements of liquid zone stability between circular plates in simulated low gravitational fields would be relevant in order to determine the dynamics of instability and to delineate the stability criterion for geometries not readily amenable to theoretical treatment. For example, in general the gravitational field will not be parallel to the rotation axis of the liquid; one must then solve partial differential equations instead of the ordinary differential equations described in the Appendix. The complexities of such calculations suggest that an experimental simulation of the situation may be a better approach to the problem.

References

1. Plateau, J.A.F., Experimental and Theoretical Researches on the Figures of Equilibrium of a liquid mass ..., translated in Annual Reports of the Smithsonian Institution, 1863-1866.

2. Bolza, O., Lectures on the Calculus of Variations, Dover, New York, 1961.

3. Princen, H.M., Surface and colloid science, 2 (eds. Matijevic and Eirich) Wiley-Interscience, New York, 1969.

4. Carruthers, J.R. and Grasso, M., J. Crystal Growth 13/14, 611 (1972).

5. Carruthers, J.R. and Grasso, M., J. Appl. Phys. 43, 436 (1972).

6. Carruthers, J.R., Proceedings Third Space Processing Symposium Skylab Results, Volume 2, 837 (1974).

7. Walter, H.U., Proceedings Third Space Processing Symposium Skylab Results, Volume 1, 257 (1974).

8. Pitts, E., J. Fluid Mech. 63, 487 (1974).

9. Heywang, W., Z. Naturforsch. 11a, 238 (1956).

10. Padday, J.F., Phil. Trans. Roy. Soc. (London) 269, 265 (1971).

11. Padday, J.F. and Pitt, A.R., Phil. Trans. Roy. Soc. (London) 275, 489 (1973).

12. Gillette, R.D. and Dyson, D.C., Chemical Engineering 2, 44 (1971).

13. Howe, W., Ph.D. Dissertation, Friedrich-Wilhelms Universität zu Berlin (1887).

14. Hocking, L.M., Mathematika 7, 1 (1960).

Appendix I

Stability of a Liquid Zone

We apply the calculus of variations to study the stability of a liquid zone (bridge) between two solid circular surfaces (plates). We assume that the two circular plates are perpendicular to a line joining their centers and to the direction of the gravitational force and that the liquid remains at the edges of the plates. The distance between the plates is L and the radii of the upper and lower plates are R_u and R, respectively. We define a cylindrical coordinate system (r,ϕ,z) with origin at the center of the plates and midway between them. This is illustrated in Figure 6 for $R_u = R$. We will assume that the liquid shape $r = r(z)$ is independent of ϕ. The boundary conditions on $r(z)$ are $r(-L/2) = R$ and $r(L/2) = R_u$. Further, the volume V of liquid in the zone is fixed (strictly, the mass is fixed, but we assume the density is constant), i.e.,

$$V = \int_{-L/2}^{L/2} \pi r^2 dz \equiv \int_{-L/2}^{L/2} G(r)\, dz = \text{constant}$$

In our coordinate system which may be rotating with constant angular velocity Ω about the z-axis, we assume that the liquid is stationary, i.e., we are carrying out a static calculation in which the energy of the system is completely determined by $r(z)$, the shape of the liquid-vapor interface (although we use the word vapor, the calculation is applicable to any fluid). The calculus of variations[2] enables us to determine $r(z)$ such that the energy is stationary and further to determine whether the energy is a minimum and the shape stable. The energy can be written as a sum of surface, gravitational, and rotational energies, i.e.,

$$E' = \int_{-L/2}^{L/2} F(r,z,r_z)\, dz \quad ,$$

where

$$F(r,z,r_z) = \gamma 2\pi r(1 + r_z^2)^{\frac{1}{2}} + g\rho\pi r^2 z - \frac{1}{4}\rho\Omega^2\pi\, r^4.$$

Here γ is the liquid-vapor surface energy, the subscript z indicates differentiation, i.e., $r_z = (dr/dz)$, g is the magnitude of the gravitational acceleration which is in the negative z direction, and ρ is the density difference between the liquid and vapor. Since the volume is fixed, we introduce the Lagrange multiplier p and define $H(r,z,r_z) = F(r,z,r_z) - pG(r)$. If the integral

$$E = \int_{-L/2}^{L/2} H(r,z,r_z)\, dz$$

is a minimum, then E' is also a minimum since the integral of G(r) is a constant. We now consider variations in r, i.e. $r \to r + \delta r$ and $r_z \to r_z + \delta r_z$. Defining

$$\Delta E = \int_{-L/2}^{L/2} \{H(r + \delta r, z, r + \delta r_z) - H(r,z,r_z)\}\, dz,$$

expanding $H(r + \delta r, z, r + \delta r_z)$ to second order in δr and δr_z, and performing some partial integrations in which the boundary terms vanish since $\delta r(\pm L/2) = 0$, we obtain

$$\Delta E = \int_{-L/2}^{L/2} dz\, \{[\partial H/\partial r - (d/dz)\,(\partial H/\partial r_z)]\,[\delta r]\}$$

$$+ \frac{1}{2}\int_{-L/2}^{L/2} dz\, \{[\partial^2 H/\partial r^2 - (d/dz)(\partial^2 H/\partial r \partial r_z)][(\delta r)^2] + [\partial^2 H/\partial r_z^2][(\delta r_z)^2]\}$$

For E to be stationary requires that ΔE vanish to first order in δr, i.e.,

$$(\partial H/\partial r) - (d/dz)\,(\partial H/\partial r_z) = 0.$$

Evaluating this expression yields

$$\gamma \{r^{-1}(1 + r_z^2)^{-\frac{1}{2}} - r_{zz}(1 + r_z^2)^{-\frac{3}{2}}\} + \rho g z - \tfrac{1}{2}\rho\Omega^2 r^2 - p = 0.$$

This equation is called the Euler equation for the variational problem being considered. The coefficient of γ is the curvature of the interface and the above equation can also be derived by considering the pressure balance across the liquid-vapor interface. The pressures in the liquid and vapor are $\rho_\ell(\frac{1}{2}\Omega^2 r^2 - gz) + p'_\ell$ and $\rho_v(\frac{1}{2}\Omega^2 r^2 - gz) + p'_v$, respectively, where p'_ℓ and p'_v are constants. Then, using the Laplace equation which states that the pressure jump across the interface is the product of γ and the curvature, we obtain the Euler equation with $p = p'_\ell - p'_v$.

An expression for the volume[8] in the zone can be obtained by writing the Euler equation in the form

$$\{d/dz\}\{\gamma r/(1 + r_z^2)^{\frac{1}{2}} + (\rho g/2)zr^2 - (\rho/8)\Omega^2 r^4 - pr^2/2\} = (\rho g/2)r^2$$

and integrating with respect to z from (-L/2) to (L/2). This yields

$$\{\gamma r/(1+r_z^2) + (\rho g/2)zr^2 - (\rho/8)\Omega^2 r^4 - pr^2/2\}\Big|_{z=-L/2}^{z=\frac{L}{2}} = (\rho g/2\pi)V$$

For $R_u = R = r(\pm L/2)$, this reduces to

$$\gamma R \{(1+r_z^2)^{-\frac{1}{2}}\Big|_{-L/2}^{L/2}\} = (\rho g/2\pi)(V - \pi R^2 L).$$

Later, we will discuss solutions of the Euler equation; temporarily we assume we have found a solution of the Euler equation satisfying the boundary conditions and the volume constraint (the volume constraint specifies a particular value of p). Assuming that r(z) satisfies the Euler equation, our expression for ΔE can be written

$$\Delta E = \pi \int_{-L/2}^{L/2} dz \{-[\rho\Omega^2 r^2 + \gamma/r(1+r_z^2)^{\frac{1}{2}}][(\delta r)^2] + [\gamma r/(1+r_z^2)^{\frac{3}{2}}][(\delta r_z)^2]\}$$

For stability, we want E to be a minimum and consequently $\Delta E > 0$ for all possible variations $\delta r(z)$. The conditions under which $\Delta E > 0$ are well known from the calculus of variations; we will simply state these conditions. First, the coefficient, $\gamma r/(1 + r_z^2)^{\frac{3}{2}}$, of $(\delta r_z)^2$ must be non-negative (Legendre's condition). This condition is obviously satisfied, and the strengthened Legendre condition (coefficient of $(\delta r_z)^2$ positive) is satisfied except when $r = 0$ or r_z is infinite. On physical grounds, it is obvious that the liquid zone is not stable if $r = 0$; therefore in the remaining treatment, we will assume that the strengthened Legendre condition holds. It is interesting that Heywang[9] in his calculation for vertical zone pulling (identical rod radii) used the condition r_z infinite as a criterion for instability.

The second condition for $\Delta E > 0$ is the conjugate point condition and can be stated as follows. We first define a second differential equation, the Jacobi equation, which is the Euler equation of the quadratic functional ΔE. Since (δr) must satisfy the constraint

$$\int_{-L/2}^{L/2} r(\delta r)\, dz = 0$$

we introduce the Lagrange multiplier μ and write

$$\Delta E = \Delta E - \pi\mu \int_{-L/2}^{L/2} dz\, r(\delta r)$$

The Euler equation for ΔE (r is fixed and we consider variations in δr) is $[d/dz][\gamma r W_z/(1+r_z^2)^{\frac{3}{2}}] + [\rho\Omega^2 r^2 + \gamma/r(1+r_z^2)^{\frac{1}{2}}]\, W = -\mu r/2$, where $W = \delta r$ and $W_z = \delta r_z$; this is the Jacobi equation of the original variational problem for E. Let $u(z)$ and $v(z)$ be solutions of the homogeneous ($\mu = 0$) and inhomogeneous ($\mu \neq 0$) Jacobi equation, respectively, such that $u(-L/2) = v(-L/2) = 0$.

Define

$$m = \int_{-L/2}^{z} r\, u\, dz,$$

$$n = \int_{-L/2}^{z} r\, v\, dz,$$

and

$$D(z, -L/2) = mv - nu.$$

For stability, it is necessary that $D(z, -L/2) \neq 0$ for $-L/2 < z \leq L/2$. Obviously $D(-L/2, -L/2) = 0$; defining z^* as the next greater zero of $D(z, -L/2)$, i.e. $D(z^*, -L/2) = 0$, the stability criterion can also be written as

$$L/2 < z^*.$$

The point z^* is called the conjugate of the point $(-L/2)$.

We will now give a brief discussion of solutions of the Euler equation. For $g \neq 0$, it is not possible to solve the equation analytically, and approximations or numerical techniques are required. Extensive tables of numerical solutions of the Euler equation (for $\Omega = 0$) are available from J.F. Padday.[10-11] When $g = 0$, the solution of the Euler equation can be reduced to a simple quadrature. Writing the Euler equation in the form $(\gamma/r)\ (d/dr)\ [r/(1 + r_z^2)^{\frac{1}{2}}] - \frac{1}{2}\ \rho\Omega^2 r^2 - p = 0$, and integrating yields $r/(1 + r_z^2)^{\frac{1}{2}} = (\rho/8\gamma)\ \Omega^2 r^4 + pr^2/2\gamma + C_1 = A(r)$ where C_1 is an integration constant and $A(r)$ is defined by the second equality. Solving for r_z and integrating again gives

$$z = C_2 + \int dr\ \{A/(r^2 - A^2)^{\frac{1}{2}}\},$$

where C_2 is an integration constant. For $\Omega = 0$, the above integral can be written in terms of elliptic integrals. To show this we define two constants

ν and θ such that

$$p = 2\gamma/[\nu(1 + \cos\theta)]$$

and

$$C_1 = \nu \cos\theta/(1 + \cos\theta).$$

We then have

$$z = C_2 + \int dr\{[r^2+\nu^2\cos\theta]/[(r^2-\nu^2\cos^2\theta)(\nu^2-r^2)]^{\frac{1}{2}}\}.$$

Introducting the substitution $r = \nu\Delta(t,\theta) \equiv \nu[1-\sin^2\theta\ \sin^2 t]^{\frac{1}{2}}$ (provided ν is positive), the above equation becomes

$$z = C_2-\nu\int dt\ \{\Delta(t,\theta) + \cos\theta/\Delta(t,\theta)\}$$

or

$$z = C_2 - \nu\ \{E(t/\theta) + \cos\theta\ F(t/\theta)\},$$

where $F(t/\theta)$ and $E(t/\theta)$ are elliptic integrals of the first and second kind, respectively. The above equation and the equation $r = \nu\Delta(t,\theta)$ give a parametric representation (with t as the parameter) for the solution of the Euler equation in the absence of gravity and rotation. The solution contains three constants C_2, ν and θ which allows one to satisfy the two boundary conditions and the volume constraint. The properties of the solutions have been discussed by Gillette and Dyson.[12] These authors, making use of earlier results of Howe,[13] have determined the stability of the solutions from the conjugate point criterion for the case $R_u = R$. Their basic result is that for a given (L/R), there is a unique stable solution provided the volume V in the liquid zone lies in a specified range, i.e., defining V_A and V_B as the minimum and maximum volume, respectively, for which a stable liquid bridge exists, the bridge is unstable if $V < V_A$ or if $V > V_B$ and is stable if $V_A \leq V \leq V_B$. For $L < 2\pi R$, the solution corresponding to V_A is constricted in the middle and the one corresponding to V_B bulges out; for $L > 2\pi R$, both solutions bulge outward.

The values of V_A and V_B are given graphically by Gillette and Dyson. As pointed out by these authors, the extension of the stability calculation to the case $R_u \neq R$ should be straightforward.

We will now consider the stability of a liquid cylinder. Initially, we consider the zero gravity case. It is well known that the cylinder is unstable when $L > 2\pi R$; we will derive this result. It is clear that $r(z) = R$ is a solution of the Euler equation with $p = (\gamma/R) - \frac{1}{2} \rho \Omega^2 R^2$ and the zone volume $V = \pi R^2 L$. It is convenient to define $\alpha = R/[1 + \rho \Omega^2 R^3/\gamma]^{\frac{1}{2}}$ and $\eta = z/\alpha$. In terms of η and for $r(z) = R$, the Jacobi equation is

$$W_{\eta\eta} + W = -\mu\alpha^2/2\gamma.$$

Since we are only interested in when $D(z, -L/2) = 0$, we are free to choose any non-zero value for μ; we choose μ such that $(-\mu\alpha^2/2\gamma) = 1$. Solving the differential equation, we take

$$u(\eta) = \sin(\eta + \beta)$$

and

$$v(\eta) = 1 - \cos(\eta + \beta)$$

where $\beta = L/2\alpha$ and both u and v vanish at $\eta = -\beta(z = -L/2)$. The integrals m and n are then

$$m = R\,\alpha\,\{1 - \cos(\eta + \beta)\}$$

$$n = R\,\alpha\,\{\eta + \beta - \sin(\eta + \beta)\}$$

The equation $D(z^*, -L/2) = 0$ can be written as $\sin\xi\,\{\sin\xi - \xi\cos\xi\} = 0$, where $\xi = (\beta + \eta^*)/2$ and $\eta^* = z^*/\alpha$. The root $\xi = 0$ of this equation corresponds to $z^* = -L/2$; the next larger root is $\xi = \pi$ or $z^* = 2\pi\alpha - L/2$. The stability condition $(L/2 < z^*)$ is then

$$L < (2\pi R)/(1 + \rho \Omega^2 R^3/\gamma)^{\frac{1}{2}}.$$

For $\Omega = 0$, this is the well known result $L < 2\pi R$. The above equation has been derived by Hocking[14] by considering the dynamics of axisymmetric perturbations of an infinite cylindrical column of liquid.

We now consider the effect of a weak gravitational field upon the preceding stability result by carrying out a perturbation treatment. We take the liquid volume $V = \pi R^2 L$ so that in the absence of gravity the liquid shape is cylindrical. We expand all functions in a series in powers of g; the zeroth order terms are the zero gravity results given in the preceding paragraph. It is convenient to write the Euler and Jacobi equations in dimensionless form; we define the dimensionless variables $\eta = z/\alpha$, $\Psi = r/\alpha$, $\Phi = W/\alpha$, $\varepsilon = \rho g \alpha^2/\gamma$, $\omega = \rho\Omega^2\alpha^3/2\gamma$, $P = \alpha p/\gamma$, and $M = (-\mu\alpha/2\gamma)$, where $\alpha = R/[1 + \rho\Omega^2 R^3/\gamma]^{\frac{1}{2}}$. The Euler and Jacobi equations are now

$$[\Psi(1 + \Psi_\eta^2)^{\frac{1}{2}}]^{-1} - \Psi_{\eta\eta}/(1 + \Psi_\eta^2)^{\frac{3}{2}} + \varepsilon\eta - \omega\Psi^2 - P = 0$$

and

$$[\Psi\Phi_\eta/(1 + \Psi_\eta^2)^{\frac{3}{2}}]_\eta + \{[\Psi(1 + \Psi_\eta^2)^{\frac{1}{2}}]^{-1} + 2\omega\Psi^2\}\ \Phi = \Psi M$$

We expand Ψ, Φ, P, and M in powers of ε, i.e.

$$\Psi = \Psi_0(\eta) + \varepsilon\Psi_1(\eta) + \varepsilon^2\Psi_2(\eta) + \ldots$$

$$\Phi = \Phi_0(\eta) + \varepsilon\Phi_1(\eta) + \varepsilon^2\Phi_2(\eta) + \ldots$$

$$P = P_0 + \varepsilon P_1 + \varepsilon^2 P_2 + \ldots$$

$$M = M_0 + \varepsilon M_1 + \varepsilon^2 M_2 + \ldots \quad .$$

Recall that $\Psi_0(\eta) = R/\alpha$. Substituting these expressions into the differential equations, expanding all quantities in powers of ε, and then equating coefficients of ε^0, ε, ε^2, ..., we obtain

$$(\alpha/R) - \omega(R/\alpha)^2 = P_0$$

$$\Psi_{1_{\eta\eta}} + \Psi_1 = \eta - P_1$$

$$\Psi_{2_{\eta\eta}} + \Psi_2 = (\Psi_1^2\alpha/2R)[3(\alpha/R)^2 - 1] - (\alpha\Psi_{1_\eta}^2/2R) - P_2$$

$$\Phi_{0_{\eta\eta}} + \Phi_0 = M_0$$

$$\Phi_{1_{\eta\eta}} + \Phi_1 = \Phi_0\Psi_1[(3/\Psi_0^3) - \Psi_0^{-1}] - \Phi_{0_\eta}\Psi_{1_\eta}/\Psi_0 + M_1$$

$$\Phi_{2_{\eta\eta}} + \Phi_2 = (3/2)\,\Phi_{0_{\eta\eta}}\Psi_{1_\eta}^2 + \Phi_{0_\eta}[3\Psi_{1_\eta}\Psi_{1_{\eta\eta}} + (\Psi_1\Psi_{1_\eta}/\Psi_0^2) - (\Psi_{2_\eta}/\Psi_0)]$$
$$+ \Phi_0[(3\Psi_2/\Psi_0^3) - (\Psi_2/\Psi_0) - (3\Psi_1^2/\Psi_0^4) + (\Psi_{1_\eta}^2/2\Psi_0^2)]$$
$$- \Phi_{1_\eta}(\Psi_{1_\eta}/\Psi_0) + \Phi_1(\Psi_1/\Psi_0)[(3/\Psi_0^2) - 1] + M_2\ ,$$

where we have used the identity $2\omega = \Psi_0^{-1} - \Psi_0^{-3}$. These equations can be solved analytically by a straightforward but tedious method. The boundary conditions on Ψ are $\Psi(\pm\beta) = \Psi_0$ and

$$V = \int_{-\beta}^{\beta} \Psi^2\ d\eta = 2\beta\Psi_0^2\ .$$

The conditions on Ψ_1 and Ψ_2 are then

$$\Psi_1(\pm\beta) = \Psi_2(\pm\beta) = 0\ ,$$

$$\int_{-\beta}^{\beta}\Psi_1\ d\eta = 0\ ,$$

and

$$\int_{-\beta}^{\beta}\{2\Psi_0\Psi_2 + \Psi_1^2\}\ d\eta = 0\ .$$

The solutions for Ψ_1 and Ψ_2 which satisfy the boundary conditions are

$$\Psi_1(\eta) = \eta - \beta\sin\eta/\sin\beta$$

$$\Psi_2(\eta) = \{(\alpha/2R)(3\alpha^2/R^2 - 1)\}\{\eta^2 - (\beta^2/3)(1 + \sin^2\eta/\sin^2\beta)$$
$$- (\beta\eta\sin\eta/2\sin\beta) + (\beta^2/6\sin^2\beta)(1 - \cos\beta\cos\eta)$$
$$+ [\beta/\sin\beta][(\eta^2 - \beta^2)(\cos\eta)/2 + (3/2)(\cos\eta - \cos\beta)]\}$$
$$- \{\alpha/2R\}\{\beta^2/3 - \beta\eta\sin\eta/\sin\beta + [\beta^2/3\sin^2\beta][2 - \cos^2\eta - \cos\beta\cos\eta]$$
$$- (\beta/\sin\beta)(\cos\eta - \cos\beta)\}$$

We note that $\Psi_{1_\eta}(\beta) = \Psi_{1_\eta}(-\beta)$ and $\Psi_{2_\eta}(\beta) = \Psi_{2_\eta}(-\beta) = 0$; these values satisfy the previously derived equation (for the volume in the zone) which for $V = \pi R^2 L$ requires that $\Psi(\beta) = \pm\Psi(-\beta)$.

It is desirable to express the conjugate point equation, $D(z^*, -L/2) = 0$, as a power series in ε. We write

$$u(\eta) = u_0(\eta) + \varepsilon u_1(\eta) + \varepsilon^2 u_2(\eta) + \ldots$$

$$v(\eta) = v_0(\eta) + \varepsilon\, v_1(\eta) + \varepsilon^2\, v_2(\eta) + \ldots$$

$$\eta^* = \eta_0^* + \varepsilon\, \eta_1^* + \varepsilon^2\, \eta_2^* + \ldots$$

The conjugate point equation requires evaluation of functions at η^*; it is more convenient to evaluate these functions at η_0^*. To do this we expand in a Taylor series about η_0^*; thus for any function $f = f_0 + \varepsilon f_1 + \varepsilon^2 f_2$, we have

$$f(\eta^*) = f_0 + \varepsilon[f_1 + \eta_1^*\, f_{0_\eta}] + \varepsilon^2[f_2 + \eta_1^*\, f_{1_\eta} + \eta_2^*\, f_{0_\eta} + (\eta_1^*)^2\, f_{0_{\eta\eta}}/2] + \ldots,$$

where all quantities on the right hand side of the equation are evaluated at $\eta = \eta_0^*$. Expanding the conjugate point equation in powers of ε, and equating coefficients of ε and ε^2 we obtain the following equations for η_1^* and η_2^*

$$\eta_1^* = -(u_1/\alpha)$$

$$\eta_2^* = -(u_2/\alpha) - (\eta_1^* u_{1_\eta}/\alpha) + (v_1/2\pi\alpha^2 M_0 \Psi_0)[I(u_0\Psi_1) + I(u_1\Psi_0)].$$

All quantities on the right are to be evaluated at $\eta = \eta_0^* = 2\pi - \beta$; we have introduced the notation

$$I(f) = \int_{-\beta}^{\eta_0^*} f\, d\eta\ .$$

In obtaining the above results, we made use of the zeroth order solutions which we take as $(u_0/\alpha) = \sin(\eta + \beta)$ and $(v_0/\alpha) = M_0[1 - \cos(\eta + \beta)]$; evaluation at η_0^* yields $u_0 = 0$, $u_{0_\eta} = \alpha$, $u_{0_{\eta\eta}} = 0$, $I(\Psi_0 u_0) = 0$, $v_0 = 0$, $v_{0_\eta} = 0$, $v_{0_{\eta\eta}} = \alpha M_0$, and $I(\Psi_0 v_0) = 2\pi\alpha M_0 \Psi_0$.

A lengthy but straightforward calculation yields

$$\eta_1^* = (\alpha/R)\, a_2\, \pi(\pi - \beta)$$

$$\eta_2^* = -\pi\{(3/2) + a_1/4 + a_1 a_2 + (27/16)\, a_1 a_2^2 - (3/2)\, a_1^2\}$$
$$- \pi^3\{-2a_1 a_2^2 + 4a_1^2\} - \pi^2\beta\{3a_1 a_2^2 - 6a_1^2\}$$
$$- \beta^2\pi\{(3/8) - (5/24)\, a_1 + (3/8)\, a_1 a_2 - (25/24)\, a_1 a_2^2 + (15/4)\, a_1^2\}$$
$$- \{\pi\beta\cos\beta/\sin\beta\}\{-a_1 + (7/3)\, a_1 a_2 + (7/12)\, a_1 a_2^2 + 8a_1^2\}$$

$$- \{\pi\beta^2\cos^2\beta/\sin^2\beta\}\ h(\alpha/R),$$

where $a_1 = (\alpha/R)^2$, $a_2 = [(3\alpha^2/R^2) - 1]$, and $h(\alpha/R) = (9/8)\ [1 - a_1 + 3a_1^2 + a_1^3]$. The stability criterion is

$$\beta < \eta^* = \eta_0^* + \varepsilon\eta_1^* + \varepsilon^2\eta_2^* + \ldots$$

This can be simplified since we know that instability occurs when $\beta \tilde{=} \pi$. Letting $s = \pi - \beta$ and recognizing that $s << 1$, it is clear that the dominant term in η_2^* is the coefficient of $(1/\sin^2\beta)$. The stability criterion can then be written as $s^3 > (\varepsilon^2/2)\ \pi^3\ h(\alpha/R)$ or

$$(L/2\alpha) < \pi\ \{1 - [(\varepsilon^2/2)\ h(\alpha/R)]^{\frac{1}{3}}\}.$$

This equation gives the leading correction to the zero gravity stability result; the equation should be valid as long as $[(\varepsilon^2/2)\ h(\alpha/R)]^{\frac{1}{3}} << 1$.

We note that it was necessary to carry out the calculation to second order in ε^2 in order to obtain corrections to the zeroth order result, i.e., the term $\varepsilon\eta_1^*$ does not affect the stability criterion. Physically, this was expected since a change in the sign of g (and consequently ε) should not change the stability.

It should be possible to extend these results to arbitrary values of ε by numerically solving the Euler and Jacobi equations. We wish to acknowledge helpful discussions with R. F. Sekerka.

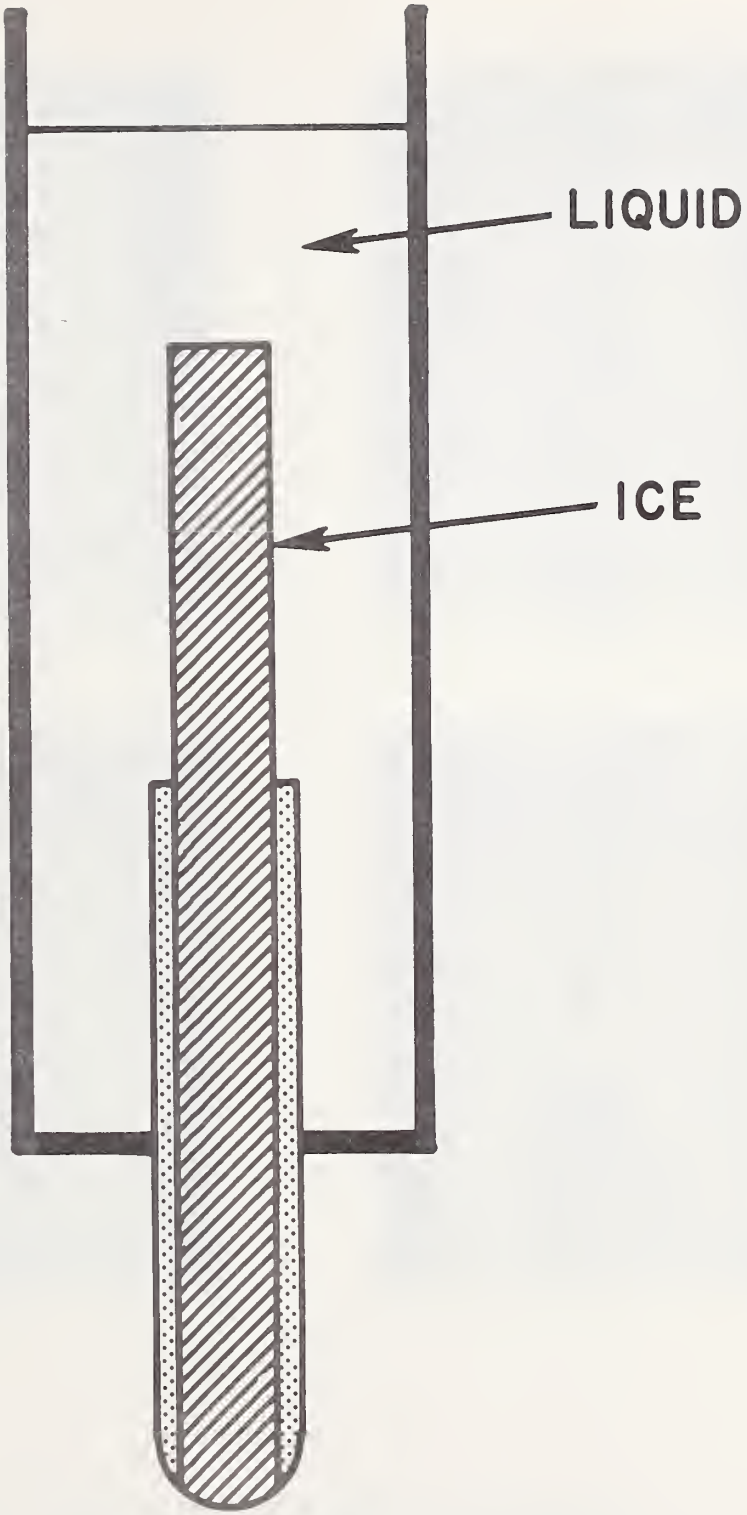

Fig. 1 Schematic diagram of experimental cell

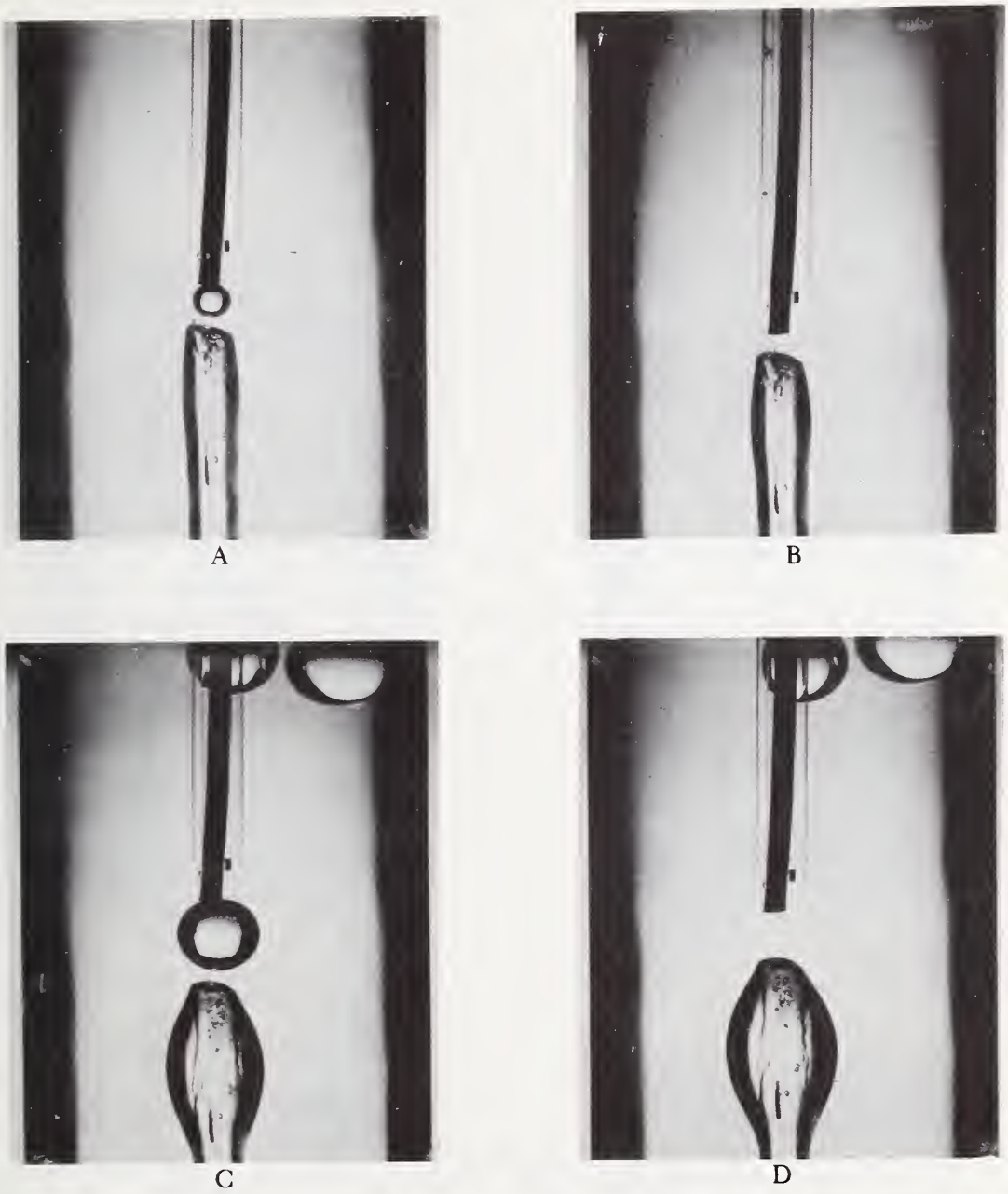

Fig. 2 The addition of water to the end of an isothermal ice cylinder. The temperature is approximately -0.2°C

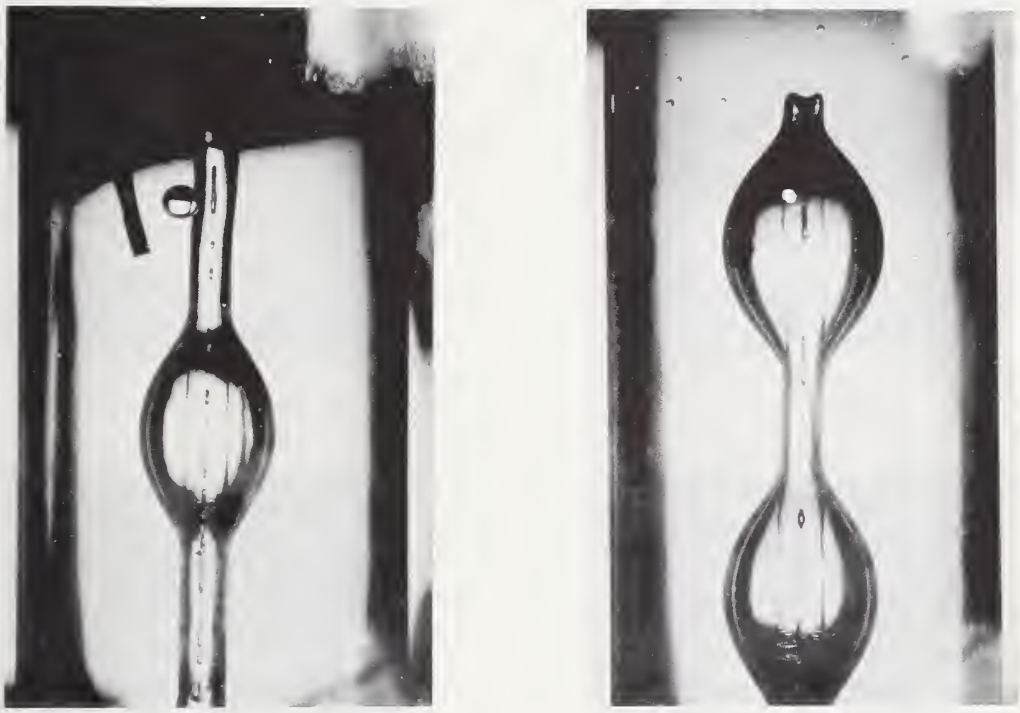

A B

Fig. 3 The addition of water to the side of an isothermal ice cylinder. The temperature is -0.2°C

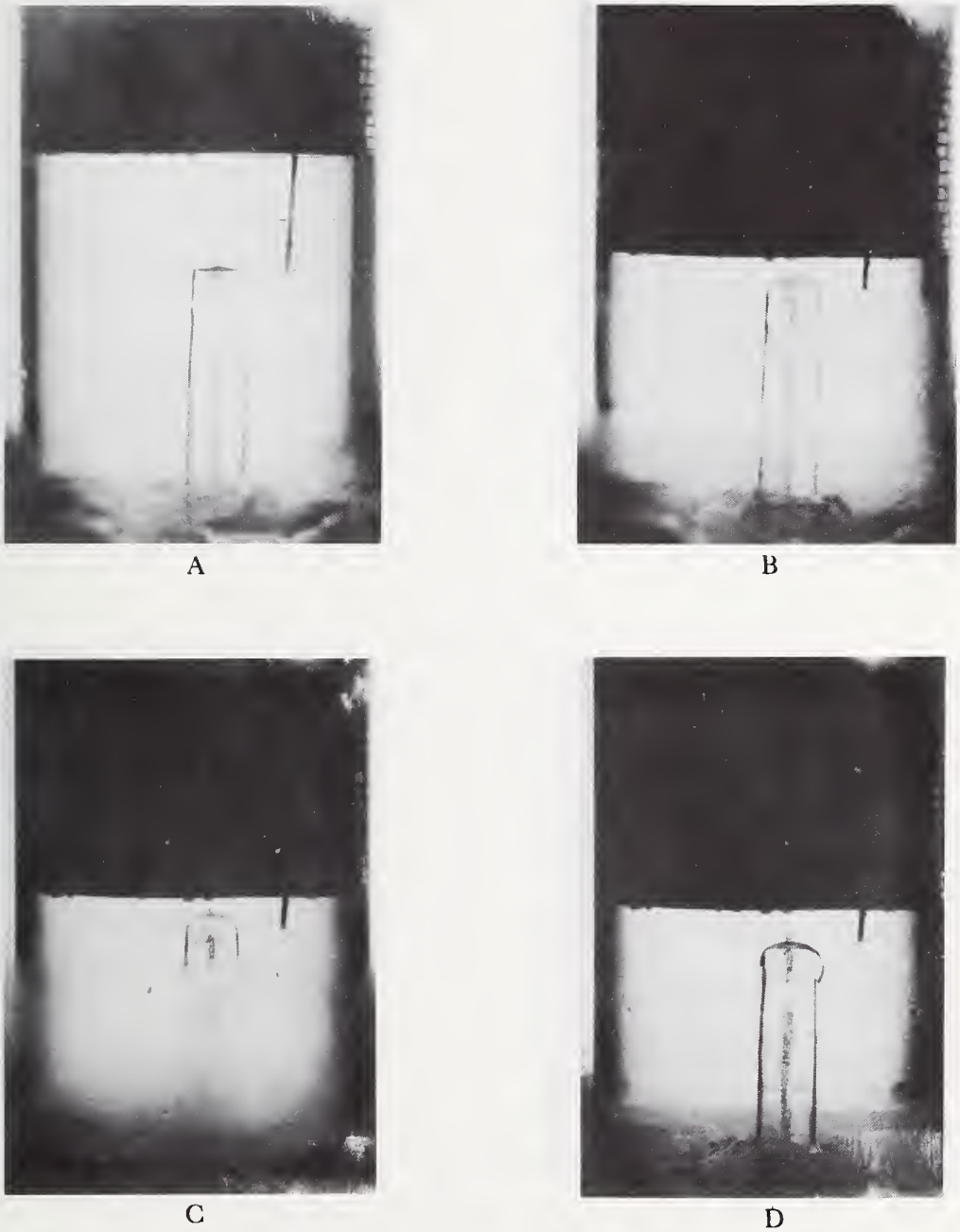

Fig. 4 The melting of an ice cylinder
in a linear temperature gradient

A

B

C

D

Fig. 5 The rapid melting of an ice cylinder in a linear temperature gradient

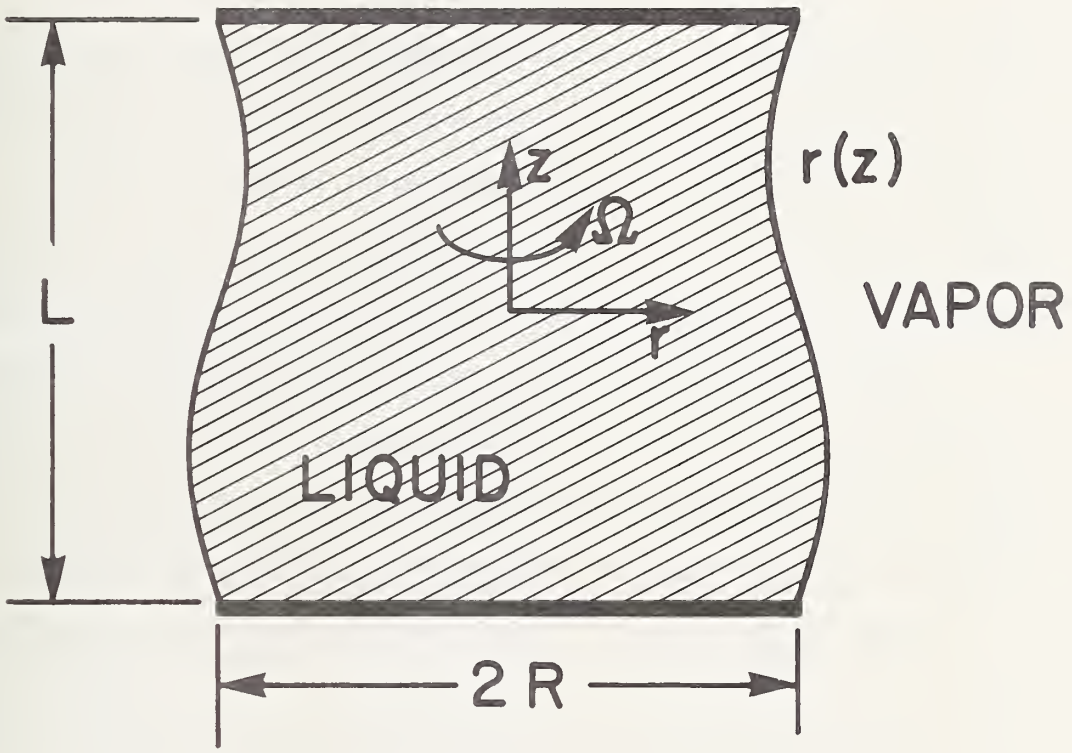

Fig. 6 Rotating zone between circular plates

Task 5

Vapor Transport Synthesis and Crystal Growth of Oxides

H. S. Parker

Inorganic Materials Division
Institute for Materials Research

Summary

The use of closed tube transport techniques is often advantageous in crystal growth where the desired material has a very high melting point, a destructive phase inversion or high vapor pressure. Transport is generally achieved in a temperature gradient by either chemical means through the addition of a suitable transporting agent or by evaporation-condensation of materials with vapor pressures sufficiently high.

This section of the report discusses further efforts to determine a suitable transporting agent for the chemical transport of ZrO_2 alone and in combination with Ta_2O_5. No successful agent was found within the limitations of temperature and pressure imposed by the quartz reaction tubes.

The results of transport rate measurements on the transport of mercurous chloride by an evaporation-condensation mechanism are presented. Experimental conditions were chosen to enhance and minimize the convective effect. Because of the relatively simple transport mechanism involved and the satisfactorily large rates obtainable, a proposal was submitted to NASA for participation in the Apollo-Soyuz Test Program.

Introduction

The major objective of this study is to investigate the effects of convective and diffusive flow in vapor transport crystal growth utilizing a closed tube system. Mass transport in the presence of a temperature gradient can be achieved either by the addition of a suitable transporting agent, generally a halide, or by a simple evaporation-condensation mechanism. The general applications of this technique have been described by Schafer [1] and Laudise [2]. Chemical transport can be of particular advantage, if a suitable transporting agent can be found, in cases where a high melting point or destructive phase transitions make more conventional techniques difficult or impossible. In more favorable cases, where the material of interest has a vapor pressure sufficiently high, the choice of an evaporation-condensation technique has the advantage of a simpler reaction mechanism. In both cases, however, convective and diffusive effects are intimately interrelated in a gravity environment. Independent control of parameters such as temperature, temperature gradient and pressure can seldom be achieved without influencing the relative contributions of convection and diffusion to the observed transport.

The initial material chosen for investigation by the chemical transport technique during the previous year was a potentially superior type of stabilized ZrO_2, using Ta_2O_5 to produce an orthorhombic, oxygen-excess form as detailed in the previous report [3]. These experiments involved selection of a suitable transport reaction for the simultaneous transport of ZrO_2 and Ta_2O_5 in a molar ratios of approximately 6:1 and 8:1.

A second material was also chosen for investigation during the present year as representative of an evaporation-condensation transport process. Mercurous chloride was selected both from the standpoint of its adaptability to this technique as well as its important optical properties.

The extremely large birefringence of mercurous chloride, approximately four times that of calcite, was first measured by Dufet [4] in the late 1890's. The possibility of utilizing this material for construction of polarizing prisms or other optical components has been neglected, with the exception of one paper by Barta [5] on the growth of Hg_2Cl_2 crystals from the melt and from the vapor although no characterization of the crystals is given. Preliminary work at NBS on Bridgman vapor growth and optical properties has indicated that the material is transparent from 0.4 μm to ∿16 μm and the birefringence is in excess of 0.5 at 10.6 μm.

Mercurous chloride has a high vapor pressure [5] at moderate temperatures, ranging from about 0.4 atmospheres at 350 °C to 44 atmospheres at the triple point, approximately 540 °C. See Figure 1, also [5,6]. The vapor species in equilibrium with $Hg_2Cl_2(s)$ has been shown to be $Hg_2Cl_2(g)$ at temperatures below about 375-400° and $Hg(g) + HgCl_2(g)$ at higher temperatures [7,8]. The vapor pressure in the temperature range of interest, 350-460 °C, ranges from about 0.5 to 10 atmospheres.

Extremely high transport rates in the absence of convection were observed by Prof. Wiedemeier in his experiments on Skylab involving chemical transport of GeSe with GeI_4. The physical perfection and size

was also markedly better as compared to crystals grown in ground-based experiments. This suggests that a series of crystal growth experiments by a simple evaporation-condensation mechanism might be of value in further understanding the phenomena of mass transport under convection-free conditions. In this case, the transport agent and the chemical reaction between transport agent and the material at the source and sink end are eliminated. However, in the case of evaporation-condensation, independent control of the total pressure in the system is lost, since the vapor pressure of the material is fixed solely by the operating temperature. The supersaturation and growth rate are, in part, determined by the choice of ΔT and thus Δp.

Experimental Procedures

Work on establishing a chemical transport reaction for the simultaneous transport of ZrO_2 and Ta_2O_5 was undertaken during the previous year of this contract and the experimental details are described in the first annual report [3].

Efforts to establish a suitable transport reaction for ZrO_2 and $8ZrO_2{:}Ta_2O_5$ or $6ZrO_2{:}Ta_2O_5$ were continued using halogens and halogens plus sulfur as transporting agents. An additional problem was the severe corrosion of the quartz tube wall when simultaneous transport of ZrO_2 and Ta_2O_5 was attempted. Transport experiments up to the practical working limits of temperature and pressure for quartz tubes, 1100-1200 °C and estimated pressures of 7 atmospheres failed to produce any significant increase in mass transport above the milligram quantities obtained in 168 hour runs at lower temperatures and pressures. In view of these extremely low rates, further attempts to transport ZrO_2 were abandoned.

For transport of Hg_2Cl_2, three different furnace configurations were used. In the initial experiments, a horizontal three zone furnace was utilized. In order to provide greater flexibility in adjustment of temperature gradients and to enable experiments to be done with the transport tube vertical a multi-tapped furnace was constructed. By the use of suitable baffles and shunt taps, it was possible to either maximize the convective effect by having the hotter (source) end of the transport tube at the bottom, or to minimize the effect by reversing the gradient. Temperature was monitored by eight thermocouples positioned along the transport tube. The tube holder was designed to allow insertion of the ampoule into the furnace at temperature. Approximately 30 minutes were required for the tube and charge to establish equilibrium with the temperature of the furnace. A blank sample tube was used to adjust the thermal profile of the furnace prior to a run. An isothermal zone at least 5 cm in length was established at the higher temperature end with a linear gradient to the colder end where a second isothermal zone was established.

All transport experiments were carried out in fused quartz tubes. Prior to filling, the tubes were cleaned and evacuated to pressures lower than 2×10^{-6} torr and baked out at 500-700 °C while under vacuum. The initial horizontal transport experiments were done in tubing of 1.8 cm inside diameter. The vertical transport experiments with the hotter end at the bottom (maximum convection) were done in 1.1 cm inside diameter tubes. In experiments with the hotter (source) end at the top, it was necessary to provide a support to hold the charge. By careful selection, it was possible to choose 1.1 cm outside

diameter (0.8 cm inside diameter) quartz tubes which fit tightly within a 1.1 cm inside diameter tube. An open fused quartz grid across the upper end provided a support for the charge. This method also provided a convenient adjustment of the transport path length.

The mercurous chloride was obtained from a commercial source in powder form and spectroscopic analysis indicated the following impurities in weight percent: Ti:0.003-0.03 percent, Fe:0.001-0.01 percent, Si, Cu, Mg:0.001-0.0001 percent. In order to provide a dense charge for the transport experiments, the as-received powder was isostatically pressed into cylinders of appropriate diameter. A few experiments were performed using once-transported material (Bridgman furnace) but no difference in results were noted. In all cases, the tube and charge were thoroughly dried at 100 °C at pressures of less than 5×10^{-6} torr before sealing off. The presence of water vapor has been shown by Gucker and Munch [8] to enhance the dissociation of Hg_2Cl_2 vapor.

Experimental Results

Horizontal transport experiments were primarily qualitative in nature for the purpose of observing the magnitude of the transport rates to be expected. At a source temperature of 450 °C and a ΔT of 100 °C, corresponding to a Δp of 8.4 atm., an entire charge of 54.1 grams was transported in less than 68 hours over a distance of 13 cm. Over the same transport distance, a source temperature of 390 °C and a 20° ΔT, corresponding to a Δp of 0.5 atm, resulted in the transport of 15.2 grams during a 48 hour period. This corresponds to a transport rate of 0.32 grams/hr.

The results of transport experiments with the ampoule in a vertical position are summarized in Table 1. With one exception, all runs were made at temperatures in the region where the dissociation of Hg_2Cl_2 vapor would be minimized. This imposes a maximum experimental temperature of about 400-410 °C. Because the primary objective was the observation of transport rates under different conditions, no attempt was made to obtain large single crystals.

Runs made with the bottom of the transport tube hottest to maximize the effects of convection were chosen to cover a wide range of temperatures and differential pressures. Unfortunately, the times chosen for the two highest pressure runs were too long and the entire charge was transported, making an accurate rate determination impossible.

In the opposite configuration, top of the tube hottest to mimimize convection, all experiments were done in the 325° - 410 °C range and the duration of the runs was drastically shortened. As expected, transport rates were much lower. A marked increase in rate was noted when the $\Delta\rho$ was increased from 0.9 to 1.6 atmospheres by lowering the temperature at the deposition end of the tube. Reduction of the transport distance to 7 cm resulted in an increase of the rate to 0.660 g/hr which corresponds to a volume deposition rate of about 0.09 cubic centimeters per hour, based on a density of 7.15 grams per cubic centimeter for Hg_2Cl_2. This would be sufficient to produce crystals large enough for property measurements and characterization in relatively short experiments of 6-8 hours duration.

In both sets of experiments, the transported product was coarsely polycrystalline, with the largest crystals 3-4 mm in size. The largest

Table 1. Summary of Hg_2Cl_2 Transport Experiments in Vertical Tube

Temperature[a] Top °C	Temperature[a] Bottom °C	Pressure[b] atm.	Time hr	Amount Transported g	Path Length cm	Transport Rate g/hr	Flux moles/cm^2·sec	Δρ atm.
				MAXIMUM CONVECTION				
240	310	0.01	96	2.0	13	0.021	1.3×10^{-8}	0.12
380	400	1.0	48	20.0[c]	13	>>0.4[c]	>>2.5×10^{-7}	0.5[d]
410	470	3.8	69	22.2[c]	13	>>0.3[c]	>>1.8×10^{-7}	8.8
				MINIMUM CONVECTION				
392	350	0.44	4.5	0.27	12	0.059	6.9×10^{-8}	0.9
405	325	0.20	7.0	3.31	12	0.473	5.6×10^{-7}	1.6[d]
410	350	0.44	7.0	2.83	10	0.404	4.8×10^{-7}	1.5[d]
410	350	0.44	7.5	4.95	7	0.660	7.8×10^{-7}	1.5[d]

[a] Temperature at source (hotter) and deposition (colder) end of transport tube.

[b] Equilibrium vapor pressure at lower temperature.

[c] Entire charge transported, actual rate not known.

[d] Assuming no dissociation of vapor. See Figure 1.

crystals were produced in the lowest temperature and lowest Δp run, at a deposition rate of 0.021 grams per hour. Several attempts at seeded growth were unsuccessful. In every case, the seed evaporated before deposition occurred.

Conclusion and Discussion

In view of the extremely low rates obtained in attempts to transport ZrO_2 with halogens or halogens plus sulfur, no further efforts to determine a suitable reaction were made. It is suggested that, if transport of ZrO_2 were essential, it would be necessary to utilize a flowing rather than a closed transport system and to utilize suitable refractory tubes to allow the use of higher temperatures than is possible in fused quartz ampoules.

Measurements of the transport rate of Hg_2Cl_2 by evaporation-condensation under conditions of minimum convection have indicated that 0.4 to 0.660 grams per hour can be transported in the 350° - 400 °C temperature range. These rates are sufficiently high so that specimens of reasonable size can be obtained in experiments of relatively short duration. The problem of preventing seed evaporation before steady-state transport and growth occurs is being investigated further.

Because of the high transport rates obtainable and the relatively simple evaporation-condensation mechanism involved, a proposal for growth of Hg_2Cl_2 crystal was submitted to NASA for participation in the Apollo-Soyuz Test Program.

References

1. a) H. Schafer, "Chemical Transport Reactions", Academic Press, New York, 1964.

   b) H. Schafer, "Preparative Methods in Solid State Chemistry", P. Hagenmuller, Ed., 251-277, Academic Press, New York, 1972.

2. R. A. Laudise, "The Growth of Single Crystals", 225-256, Prentice-Hall Inc., New Jersey, 1970.

3. E. Passaglia and R. L. Parker, "NBS Materials Science and Manufacturing in Space Research", NBS Report No. NBSIR 73-402, 25-32, November 1973.

4. M. H. Dufet, Bull. Soc. Franc de Mineral. Crist. 21, 90 (1898).

5. C. Barta, Kristall und Technik 5, 541 (1970).

6. Gmelins Handbuch der anorg. Chemie, System No. 34, Vol. B, 438-440, Velag Chemie, Bergstrasse (1967).

7. J. Weland, Helv. Phys. Acta 11, 46 (1929); 11, 77 (1929); Z. Physik 77, 157 (1932).

8. Gucker, Jr. and Munch, J. Am. Chem. Soc. 59, 1275 (1937).

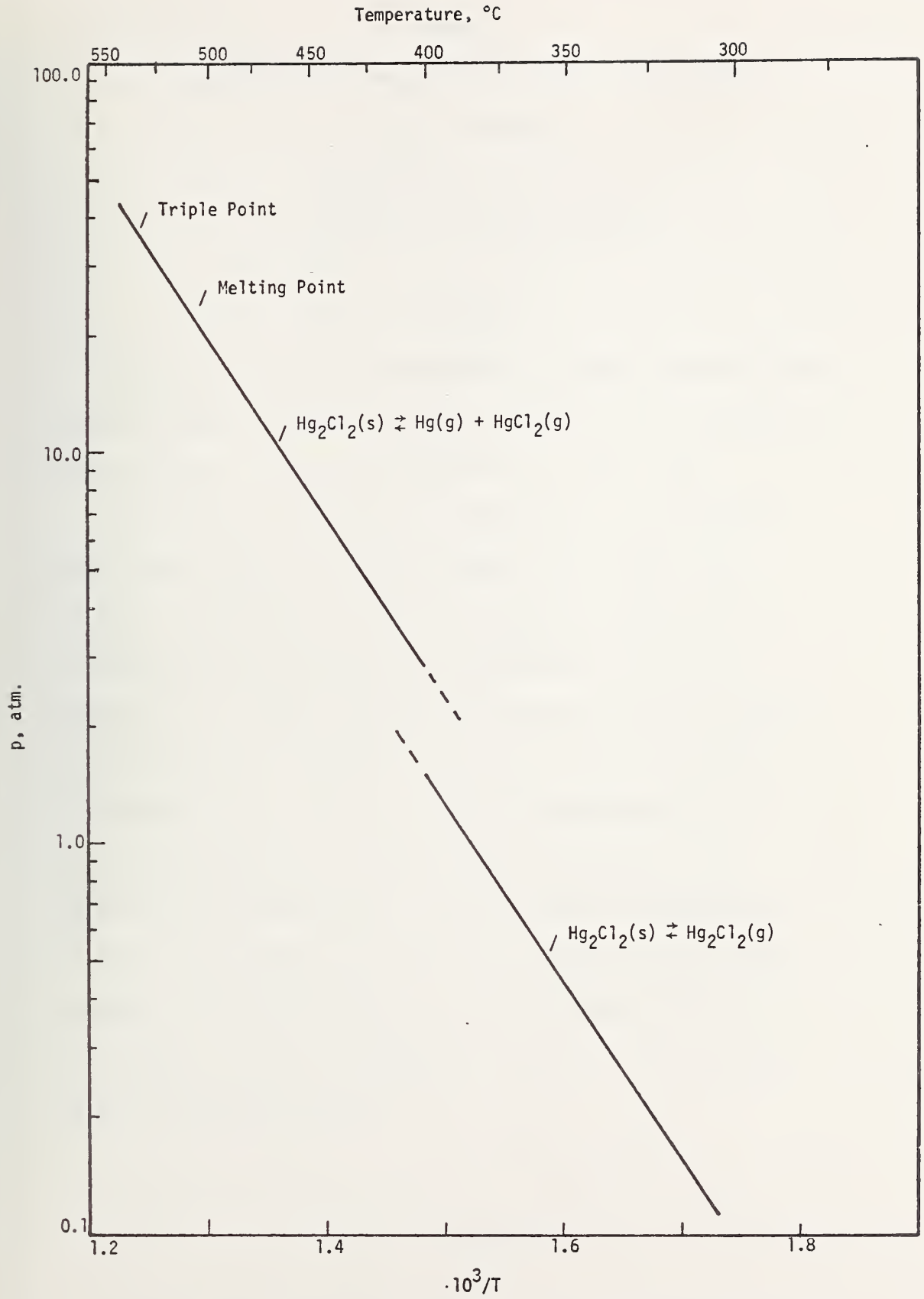

Figure 1. Vapor Pressure of Hg_2Cl_2. Data from references [5,6].

Task 6

Surface Traction and Other Surface Phenomena

Alan L. Dragoo

Inorganic Materials Division

Institute for Materials Research

Summary

Work was continued on the problem of steady thermo-capillary convection cells in nearly spherical drops. Computer programs were completed to plot the streamlines for such cells.

Regarding the problem of the enhancement of evaporation purification rates by capillary convection, a convective diffusion problem was solved by the Green's function method. The concentration was found to be expressible as a simple diffusional term plus a term for the effect of the non-uniform rate of evaporation upon diffusion plus a term for the effect of convection upon diffusion. The very complicated forms for non-uniform evaporation term and for the convective term required the development of a very approximate expression for the rate of evaporative purification in order to make simple estimates. An estimate of the convective enhancement of the purification rate was performed for the removal of CaO-trace impurity from molten alumina.

Introduction

This study of surface traction and other surface phenomena during the past year has continued both the work on the analysis of steady thermocapillary convection in liquid drops and the work on evaporative purification of the previous year. Most of the results of these two areas of work are presented in the two preprints which are attached to this report:

Alan L. Dragoo, "Steady Thermocapillary Convection Cells in Liquid Drops," presented at the International Colloquium on Drops and Bubbles, Pasadena, California, August 28-30, 1974. (See Appendix III)

Alan L. Dragoo and Robert C. Paule, "Ultrapure Materials: Containerless Evaporation and the Roles of Diffusion and Marangoni Convection," presented at the AIAA 12th Aerospace Sciences Meeting, Washington, D. C., January 30 - February 1, 1974. (See Appendix I, Task 2)

These two papers will be summarized briefly in the next section. Appendix I to this report contains the details of the solution of the convective diffusion-evaporation problem, the solution of which was treated approximately in the paper on "Ultrapure Materials."

Theoretical Results

The question of how much surface tension-gradient driven convective flow might enhance mass transport in a nearly spherical, levitated melt at zero-g can be divided into two parts:

1) How rapid is the convective flow under steady-state conditions?
2) For the most-rapid convective mode, how much does capillary convection enhance the rate of evaporative purification?

In answering both questions, creeping flow was assumed, so that all equations could be linearized with respect to the velocity. More important, thermal gradients along the surface of the melt were considered to be the sole cause of the surface tension gradients and the presence of a single condensed phase was assumed. The effect of these two assumptions, in the case of most liquids, is probably to overestimate the convective enhancement of the purification rate.

Regarding the assumption of surface thermal gradients as the sole cause of the capillary convection, surface concentration gradients were considered to be insignificant. For many liquids undergoing the loss of an impurity by non-uniform evaporation, the change in surface tension

due to thermal gradients and the change due to concentration gradients may tend to cancel each other out. However, since the surface concentration of an impurity is likely to be reduced greatly soon after evaporation begins, the concentration effect is expected to diminish quickly. The thermal gradients then would be left as the predominant source of the long-term capillary convection.

The second assumption, that of a single condensed phase, is probably the more critical one in practice. The drag upon the rise of a bubble due to contaminants at the interface has been recognized for many years [1,2]. A similar "problem" would occur if a solid phase were present on the surface of a melt. However, this problem is more likely to be troublesome in the case of an oxide scum on the surface of a molten metal than in the case of a molten oxide such as alumina which was considered in "Ultrapure Materials." In addition, the problem of a surface contaminant requires the consideration of a specific chemical system and of concentration distributions about which there is little information and which unnecessarily complicate the answer to our question at this point. To answer the initial question in as general a way as possible, the answer can be given by setting an upper limit on what is likely to be observed in practice. Such an answer can show which materials require further consideration with respect to evaporative purification and which ones can be ruled out.

The answer to the question of how rapid the thermal capillary

convection might be was worked out mostly during the previous contract year. This work was re-examined this year in the course of preparing a paper for the International Colloquium on Drops and Bubbles. This year, computer programs for plotting the streamlines were completed; examples are given in the paper on "Steady Thermocapillary Convection Cells." The circulation time was redefined to be the reciprocal of the average vorticity of a convection cell. The circulation time provides a means of comparing the rate of circulation in different liquids under similar thermal conditions and between different convective modes--different thermal conditions--for the same liquid.

In addition to capillary convection, a liquid can respond to non-uniform surface tension by deformation of its surface. In general, both will occur. In the paper on "Steady Thermocapillary Convection Cells" both were included--in fact, both must be included to satisfy both the normal and the tangential stress balance conditions at the surface of the liquid. However, in the paper, the emphasis was placed on the convective phenomenon. For completeness, the surface deformation will be compared here with the rate of convective flow. For the (n,m,σ)-mode, this comparison can be made by calculating the ratio of the radial strain E_{mn}^{σ} to the characteristic speed U_{mn}^{σ},

$$E_{mn}^{\sigma} / U_{mn}^{\sigma} = -2\mu / n(n+1)(n+2)\gamma_0 , \tag{1}$$

where μ is the coefficient of viscosity and γ_0 is the coefficient of surface tension. The significance of the deformation of the surface

decreases as the order n of the mode increases--that is, as the number of hot and cold spots on the surface of the drop increases.

The second question--how much does convection enhance the rate of evaporative purification--was examined in the paper on "ULtrapure Materials" for the ease of thermocapillary convection and for the purification of molten alumina.

To find an expression for the evaporation rate, a convective diffusion problem was solved in which the convection cell was that for the lowest order mode--the (1,0,e)-mode--obtained from the solution of the steady flow problem. This mode also has the most rapid circulation rate. The solution of the differential equation for convective diffusion, the boundary conditions and the initial condition was achieved by the Green's function method.[3] In general, the concentration can be written as

$$c(r,\theta,t) = c_0(r,t) + \sum_{n=1}' (-1)^n c_n(r,t) P_n(\cos\theta) \quad , \qquad (2)$$

where $P_n(\cos\theta)$ is a Legendre polynomial. The coefficient $c_n(r,t)$ can be expanded as

$$c_n(r,t) = c_0(r,t)\delta_{n0} + c_{nD}'(r,t) + c_{nU}(r,t) \quad , \qquad (3)$$

where $c_0(r,t)$ is a diffusional term, $c_{nD}'(r,t)$ contains the effect of non-uniform evaporation upon the diffusion process and $c_{nU}(r,t)$ contains the effect of convection on the diffusion process. Due to the natures of the non-uniform evaporation terms in the boundary condition and of the convective term in the convective diffusion equation, $c_n(r,t)$ is coupled directly or indirectly to all the coefficients in the set $\{c_m(r,t)\}$. An exact solution for (3) requires

the solution of an infinite hierarchy of equations--an impossible task. However, useful approximations can be obtained by considering the problem as a perturbation problem. Then, after deciding first what the most important mass transport process is, the integrals can be evaluated to find the first-order corrections to the concentration terms and to the expression for the evaporation rate.

A glance at the flow pattern for the (1, 0, e)-mode--Fig. 1 in "Steady Thermocapillary Convection Cells"--will show that diffusion must be the most important step in bringing the majority of impurity molecules to the surface in most instances. In this work, isotropic, radial diffusion was taken as the most important mass transport process--the solution of which was obtained by Berthier[4] and was summarized by Crank[5]. The solution for diffusion in a sphere of radius R with uniform evaporation from the surface is

$$c_{00}(r,t) = 2\mathrm{L}\, C_0 \sum_{\sigma=1}' \frac{\exp(-\beta_\sigma^2 Dt/R^2)}{\beta_\sigma^2 + \mathrm{L}(\mathrm{L}-1)} \frac{j_0(\beta_\sigma r/R)}{j_0(\beta_\sigma)} , \qquad (4)$$

where

$$\mathrm{L} = \alpha_0 D/R = Sc$$

is the Sherwood number, α_o is the evaporation rate parameter, D is the diffusion coefficient,, C_o is the initial concentration, $j_o(x)$ is the zero-order spherical Bessel function and the "wave-numbers" $\{\beta_\sigma\}$ are given by the root equation

$$\mathrm{L}\, j_0(\beta_\sigma) = \beta_\sigma j_1(\beta_\sigma) . \qquad (5)$$

Using the solution to this diffusion problem, the integral expressions for c'_{nD} (r, t) and for c_{nU} (r, t) were evaluated to

find the first-order corrections due to non-uniform evaporation and to convection.

Since the evaporation rate parameter $\alpha(T)$ was expanded only to first-order in the temperature T, as

$$\alpha(T) = \alpha_0 + \alpha_1 T_1 R\cos\theta \,, \tag{6}$$

where the temperature is given by

$$T = T_0 + T_1 r\cos\theta \,, \tag{7}$$

the rate of evaporation was expressed as

$$\begin{aligned} V(t) &= \int \alpha(T)\, c(R,\theta,t)\, d\Omega \\ &\simeq 4\pi\left[\alpha_0 c_0(R,t) - \tfrac{1}{3}\alpha_1 R T_1 c_1(R,t)\right], \end{aligned} \tag{8}$$

where the integral was over solid angle. Assuming that c_0 (R, t) $\simeq c_{0D}$ (R, t), approximate solutions were found for c'_{1D} (R, t) and for c_{1U} (R, t), namely

$$c'_{1D}(R,t) \simeq 4L L_1 C_0 \sum_{\sigma=1}^{\prime}\sum_{\omega=1}^{\prime} \frac{\beta_\omega^{(1)2}\left[\exp(-\beta_\sigma^2 Dt/R^2) - \exp(-\beta_\omega^{(1)2} Dt/R^2)\right]}{(\beta_\omega^{(1)2} - \beta_\sigma^2)\left[\beta_\sigma^2 + L(L-1)\right]\left[\beta_\omega^{(1)2} + L(L-1) - 2\right]}$$

and

$$\begin{aligned} c_{1U}(R,t) \simeq \frac{4L L_1 T R C_0}{D} \sum_{\sigma=1}^{\prime}\sum_{\omega=1}^{\prime} & \frac{\exp(-\beta_\sigma^2 Dt/R^2) - \exp(-\beta_\omega^{(1)2} Dt/R^2)}{(\beta_\omega^{(1)2} - \beta_\sigma^2)\left[\beta_\sigma^2 + L(L-1)\right]\left[\beta_\omega^{(1)2} + L(L-1) - 2\right]} \\ & \cdot \Bigg\{ \frac{(L-2)(L-1)}{\beta_\sigma^2}\left[(L+3)(L+2)(L+\beta_\sigma) - \beta_\sigma(L+1) - 1\right. \\ & \left. + \frac{2L\beta_\sigma^2}{\beta_\omega^{(1)2} - \beta_\sigma^2} - \frac{8\beta_\omega^{(1)2}\beta_\sigma^2(L+\beta_\sigma)}{(\beta_\omega^{(1)2} - \beta_\sigma^2)^2}\right] - L(L+\beta_\sigma)\beta_\omega^{(1)2} \Bigg\} \,, \end{aligned}$$

where $L_1 = T_1 R^2/D$, (10)

$U^T = -(\gamma_T T_1 R/3\mu)$ is the characteristic speed for the (1, 0, e)-mode, γ_T is the temperature coefficient of the surface tension, $\{\beta_\sigma\}$ is given by Eqn. (5) and $\{\beta_\nu^{(1)}\}$ is given by

$$(L+1)\, j_1(\beta_\nu^{(1)}) = \beta_\nu^{(1)}\, j_2(\beta_\nu^{(1)}) \tag{11}$$

Eqns. (9) and (10) were too complicated for estimating the evaporation rates, so an attempt was made to identify the most important terms in the summations to factors multiplying the isotropic rate $V_o(t) = 4\pi a_o c_{OD}(R, t)$. The approximation which was obtained is

$$V(t) \simeq V_o(t)\left[1 - (L_1^2/6\pi L)(Dt/R^2) + (LL_1 N_{Pe_m}/6\pi^4)(Dt/R^2)\right] \tag{12}$$

where the Péclet number (mass)

$$N_{Pe_m} = U^T R/D = -(\gamma_T T_1 R^2/3\mu D)$$

can also be viewed as a Marangoni number (mass), N_{Ma_m}.

REFERENCES

1. V. G. Levich, Physicochemical Hydrodynamics, Prentice-Hall Englewood Cliffs, N. J. (1962), Chapters 7 and 8.

2. J. F. Harper and D. W. Moore, J. Fluid Mech. 32, 367 (1968).

3. P. M. Morse and H. Feshbach, Methods of Mathematical Physics, McGraw-Hill Book Co., Inc., New York (1935), Chapter 7.

4. G. Berthier, J. Chim. Phys. 49, 527 (1952).

5. J. Crank, The Mathematics of Diffusion, Oxford University Press, London (1956), 6.34.

6. N. D. Young, J. S. Goldstein and M. J. Block, J. Fluid Mech. 6, 350 (1959).

7. G. Arfken, Mathematical Methods for Physicists, Academic Press, New York (1966), Chapter 12.

8. Handbook of Mathematical Functions, edited by M. Abramowitz and I. A. Stegun, National Bureau of Standards, Applied Mathematical Series, No. 55, U. S. Department of Commerce, Washington, (1964).

Appendix I: Solution of a Convective Diffusion Problem for Thermocapillary-Driven Convection in a Drop and Evaporative Removal of an Impurity

We imagine that a nearly spherical drop of radius R has a temperature field described by

$$T = T_o + T_1 r\cos\theta \tag{I.1}$$

where T_o is the average temperature <T> of the drop and T_1 is the "vertical" temperature gradient $(\partial T/\partial z)$ along the axis of the drop. The thermocapillary velocity field in the drop according to the result of Young, et. al.[6], has the components

$$u_r = (U^T/R^2)(R^2-r^2)\cos\theta \tag{I.2a}$$

$$u_o = -(U^T/R^2)(R^2-2r^2)\sin\theta \tag{I.2b}$$

$$u_\phi = 0, \tag{I.2c}$$

where the characteristic speed

$$U^T = -\gamma_T T_1 R/3\mu \tag{I.3}$$

is a function of the temperature coefficient of the surface tension $\gamma_T = (\partial\gamma/\partial T)$, of the coefficient of viscosity, μ. Further, we assume that the evaporation coefficient α can be expanded as a power series in the temperature and, to first-order, is

$$\alpha(T) = \alpha_o + \alpha_1 T_1 R\cos\theta \tag{I.4}$$

To find the concentration c as a function of position $\vec{r}$ in the drop and of time t, the convective diffusion equation

$$\frac{\partial c}{\partial t} + \vec{u}\cdot\nabla c = D\nabla^2 C, \tag{I.5}$$

where D is the diffusion coefficient, the boundary conditions

$$-D\left.\frac{\partial c}{\partial r}\right|_R = \alpha(T)c(R,t) \tag{I.6a}$$

$$\left.\frac{\partial c}{\partial r}\right|_o = 0 \tag{I.6b}$$

and the initial condition $c = C_o$, $0 \leq r \leq R$ must be solved. Having found $c(\vec{r}, t)$, the concentration distribution $c(\vec{R}, t)$ can be readily obtained, and the rate of evaporation from the drop

$$V = \int \alpha(T) c(\vec{R}, t) d\Omega \tag{I.7}$$

where $d\Omega$ is an element of solid angle, can be calculated.

Since the problem has axial symmetry--that is, the temperature, the velocity components and the boundary conditions are independent of the angle ϕ--we anticipate that the solution can expanded in a series of Legendre polynomials $P_n(x)$, $x = \cos\theta$, as

$$c(r, x, t) = c_o(r, t) + \sum_{n=1} (-1)^n c_n(r, t) P_n(x) \tag{I.8}$$

Substituting (I.8) into (I.5) and using the integrals evaluated in Appendix II, we obtain for the coefficient $c_n(r, t)$ the inhomogeneous differential equation

$$\mathcal{R} c_n - \frac{n(n+1)}{r^2} \cdot c_n - \frac{1}{D} \cdot \frac{\partial c_n}{\partial t} = \frac{(-1)^n}{D} \mathcal{F}_n c \tag{I.9}$$

where $\mathcal{R}$ is the operator

$$\frac{1}{r^2} \frac{d}{dr} \left(r^2 \frac{d}{dr} \right)$$

The details of the source term which is written formally as the operator-operand relation $\mathcal{F}_n c$ are

$$\mathcal{F}_n c = \mathcal{F}_n^{(r)} c + \mathcal{F}_n^{(\theta)} c, \tag{I.10}$$

where

$$\mathcal{F}_n^{(r)} c = f_r \cdot \delta_{ni} \frac{\partial c_o}{\partial r} - f_r \left[\frac{n}{2n-1} \cdot \frac{\partial c_{n-1}}{\partial r} \bigg|_{n \geq 2} + \frac{n+1}{2n+3} \cdot \frac{\partial c_{n+1}}{\partial r} \right] \tag{I.11a}$$

$$\mathcal{F}_n^{(\theta)} c = f_\theta \left[\frac{n(n-1)}{2n-1} \cdot \frac{c_{n-1}}{r} \bigg|_{n \geq 2} + \frac{(n+1)(n+2)}{2n+3} \cdot \frac{c_{n+1}}{r} \right] \tag{I.11b}$$

The factors f_r and f appearing in (I.11a) and (I.11b), respectively, are given by

$$f_r = (U^T/R^2)(R^2-r^2) \tag{I.12a}$$

$$f_\theta = -(U^T/R^2)(R^2-2r^2) \tag{I.12b}$$

The homogeneous part of equation (I.9) is merely the radial part of the diffusion equation in which the concentration has a θ-dependence. The source term on the righthand side of (I.9) contains the effects of convection.

Substituting (I.8) into the boundary condition (I.6a), we obtain

$$-D \left.\frac{\partial c_n}{\partial r}\right|_R = \alpha_o \delta_{no} c_o(R, t) - \alpha_1 T_1 R \delta_{n1} c_n(R, t) + \alpha_o c_n(R, t)\Big|_{n\geq 1} - \alpha_1 T_1 R\left[\frac{n}{2n-1} \cdot c_{n-1}(R, t)\Big|_{n\geq 2} + \frac{n+1}{2n+3} \cdot c_{n+1}(R, t)\right] \tag{I.13}$$

Assuming the convective effects to have been absent prior to $t = 0$, the initial condition becomes

$$c_n(r, t) = \delta_{no} C_o, \quad 0 \leq r \leq R \tag{I.14}$$

Equations (I.9) and (I.13) may be integrated by the method of Green's function[3]. The Green's function $G_n(r, t|r_o, t_o)$ which is required to find the coefficeint $c_n(r, t)$ must satisfy the inhomogeneous differential equation

$$\nabla G_n - \frac{n(n+1)}{r^2} \cdot G_n - \frac{1}{D} \frac{\partial G_n}{\partial t} = \delta(r - r_o)\,\delta(t - t_o) \tag{I.15}$$

and the boundary conditions

$$\frac{d}{dr} G_n\Big|_R + \frac{\alpha_o}{D} G_n\Big|_R = 0 \qquad \text{(I.16a)}$$

$$\frac{dG_n}{dr}\Big|_o = 0 \qquad \text{(I.16b)}$$

The required Green's function is

$$G_n(r,t\ r_o,t_o) = \frac{2Du(t-t_o)}{R^3} \sum_{\sigma=1} \exp\left[-\beta_\sigma^2 D(t-t_o)/R^2\right] \frac{\beta_\sigma^2 j_n(\beta_\sigma r/R)\ j_n(\beta_\sigma r_o/R)}{[\beta_\sigma^2 + L(L-1)-n(n+1)][j_n(\beta_\sigma)]^2} \qquad \text{(I.17)}$$

where $u(t-t_o)$ is the unit step function--$u(t-t_o) = 1$ if $t_o < t$ and $= 0$ if $t_o > t$, $j_n(x)$ is a spherical Bessel Function, the coefficient β_σ is defined by the root equation

$$Lj_n(\beta_\sigma) = -\beta_\sigma j_n'(\beta_\sigma) \qquad \text{(I.18a)}$$

or

$$(L+n)j_n(\beta_\sigma) = \beta_\sigma j_{n+1}(\beta_\sigma) \qquad \text{(I.18b)}$$

and

$$L = \alpha_o R/D = S_c \qquad \text{(I.19)}$$

is the Sherwood number. The set of coefficients $\{\beta_\sigma\}$ depends on the order n of the spherical Bessel function; however, to simplify notation, this dependence will be indicated by a superscript "(n)" only when a superscript is needed to avoid confusion.

Writing (I.9) and (.15) in terms of the variables r_o, t_o, multiplying (I.9)by the Green's function and (I.15) by $c_n(r_o, t_o)$, the two equations are combined and then integrated using Green's theorem to obtain

$$c_n(r, t) = c_{OD}(r, t)\,\delta_{no} + R^2 \int_o^t dt_o \left[G_n \frac{d}{dr_o} C_n\Big|_R - C_n \frac{d}{dr_o} G_n\Big|_R\right] - \frac{(-1)^n}{D} \int_o^t dt_o \int_o^R dr_o\, r_o^2\, G_n(r, t|r_o, t_o)\, \mathcal{F}_n c(r_o, t_o) \qquad (I.20)$$

where

$$c_{OD}(r, t) = 2LC_o \sum_{\sigma=1} \frac{\exp[-\beta_\sigma^2 Dt/R^2]}{[\beta_\sigma^2 + L(L-1)]} \frac{j_o(\beta_\sigma r/R)}{j_o(\beta_\sigma)} \qquad (I.21)$$

is the solution to the problem of diffusion in a sphere without convection and with uniform surface evaporation[5]. Formula (I.21) can be obtained from (I.9), (I.13) and (I.17) by taking n = 0 and by ignoring the convective and the non-uniform evaporation terms.

Writing (I.20) as

$$c_n(r, t) = c_{OD}(r, t)\,\delta_{no} + c'_{nD}(r, t) + c_{nU}(r, t) \qquad (I.22)$$

we can identify, in addition to the diffusional term c_{OD}, the non-uniform evaporation term c'_{nD} and the convective term c_{nU}. We see from (I.22) that the zero order coefficient $c_0(r, t)$ is not necessarily equal to $c_{OD}(r, t)$; c_{OD} is only the diffusional part of c_o. The non-uniform evaporation term can be written out using (I.13), (I.16a) and (I.17) as

$$c'_{nO}(r,t) = 2\alpha_1 T_1 \int_0^t dt_0 \sum_{\sigma=1} \exp[-\beta_\sigma^2 D(t-t_0)/R^2]$$
$$\cdot \frac{\beta_\sigma^2 j_n(\beta_\sigma r/R)}{[\beta_\sigma^2 + L(L-1) - n(n+1)] j_n(\beta_\sigma)}$$
$$\cdot [c_0(R,t_0)\delta_{n1} + \frac{n}{2n-1} c_{n-1}(R,t_0)|_{n\geq 2}$$
$$+ \frac{n+1}{2n+3} c_{n+3}(R,t_0)] . \qquad \text{(I.23)}$$

Since the factor $\mathcal{F}_n c$ in the integrand of c_{nU} is complicated, the details of c_{nU} will not be given here.

To find the rate of evaporation from the surface, we first set r = R --but we do not set r_o = R --to obtain the concentration at the surface. This introduces a little simplification into (I.20), (I.21) and (I.23) by removing the ratios of spherical Bessel functions $j_o(\beta_\sigma r/R)/j_o(\beta_\sigma)$ and $j_n(\beta_\sigma r/R)/j_n(\beta_\sigma)$. The rate of evaporation can be obtained by substituting $c_n(R,t)$ into (I.8) and then by using (I.4) and (I.8) in the integrand of (I.7). Ignoring the small deformations of the surface which sould bring in the higher order terms, the rate of evaporation is

$$V = 4\pi R^2 [\alpha_0 c_0(R,t) - \tfrac{1}{3}\alpha_1 T_1 R c_1(R,t)] \qquad \text{(I.24)}$$

Although the rate of evaporation only depends explicitly on the concentration terms $c_0(R,t)$ and $c_1(R,t)$, we must bear in m nd that $c_0(R,t)$ and $c_1(R,t)$ are found by solving a hierarchy of equations which couple all of the concentration terms out to an indefinite order.

An apparent weakness of the Green's function method is that we are ultimately required to know a priori what we have set out to find. In this instance, we must know the complete set of concentration terms to solve the hierarchy of equations. However, this paradox can be circumvented by making a physical guess as to which concentration terms are the most important ones in the set. Here, we will assume that the pure isotropic diffusion term predominates, that $c_{0D}(r,t) \simeq c_0(r,t) > c_n(r,t)\big|_{n>0}$, and we will use $c_{0D}(r,t)$ as given by (1.21) to estimate the perturbations caused by non-uniform evaporation and by convection. Further, we will only use this approximation to obtain as approximation for the evaporation rate.

Solving (I.23) for the non-uniform evaporation term, we find

$$c_{1D}'(R,t) \simeq 2\alpha_1 T_1 \int_0^t dt_0 \sum_{\sigma=1}' \exp\left[-\beta_\sigma^{(1)2} D(t-t_0)/R^2\right] \frac{\beta_\sigma^{(1)2} c_{0D}(R,t_0)}{\left[\beta_\sigma^{(1)2} + L(L-1) - 2\right]}$$

$$= 4LL_1 C_0 \sum_{\omega=1}' \sum_{\sigma=1}' \frac{\beta_\sigma^{(1)2}}{(\beta_\sigma^{(1)2} - \beta_\omega^2)} \frac{\exp(-\beta_\omega^2 Dt/R^2) - \exp(-\beta_\sigma^{(1)2} Dt/R^2)}{\left[\beta_\omega^2 + L(L-1)\right]\left[\beta_\sigma^{(1)2} + L(L-1) - 2\right]} \tag{I.25}$$

where

$$L j_0(\beta_\omega) = \beta_\omega j_1(\beta_\omega) \tag{I.26a}$$

$$(L+1) j_1(\beta_\sigma^{(1)}) = \beta_\sigma^{(1)} j_2(\beta_\sigma^{(1)}) \tag{I.26b}$$

and

$$L_1 = \alpha_1 T_1 R^2/D \tag{I.27}$$

Turning to the convective term, we find

$$c_{1u}(R,t) \simeq \frac{1}{D}\int_0^t dt_0 \int_0^R dr_0\, r_0^2\, G_1(R,t\,|\,r_0,t_0)\, f_r(r_0)\, \frac{\partial c_{0D}}{\partial r_0}$$

$$= \frac{4L\mathcal{U}_t R C_0}{D} \sum_{\sigma=1}^{\infty} \sum_{\omega=1}^{\infty} \frac{\exp(-\beta_\sigma^{(1)2} Dt/R^2) - \exp(-\beta_\omega^2 Dt/R^2)}{(\beta_\sigma^{(1)2} - \beta_\omega^2)\, j_1(\beta_\sigma^{(1)})\, j_0(\beta_\omega)}$$

$$\cdot \left\{ \int_0^1 d\xi\, \xi^2 j_1(\beta_\sigma^{(1)}\xi)\, j_1(\beta_\omega \xi) - \int_0^1 d\xi\, \xi^4 j_1(\beta_\sigma^{(1)}\xi)\, j_0(\beta_\omega \xi) \right\}$$

(I.28)

The integrals

$$I_1 = \int_0^1 d\xi\, \xi^2 j_1(\beta_\sigma^{(1)}\xi)\, j_1(\beta_\omega \xi)$$

$$I_1^{(2)} = \int_0^1 d\xi\, \xi^4 j_1(\beta_\sigma^{(1)}\xi)\, j_1(\beta_\omega \xi)$$

are evaluated in Appendix II.

Appendix II: Some Definite Integrals of Legendre Polynomials and of Spherical Bessel Functions

Legendre Polynomials

The orthogonality condition for Legendre polynomials is [7,8]

$$\langle P_n P_\ell \rangle_\theta = \frac{1}{2}\int_{-1}^{1} P_n(x)\, P_\ell(x)\, dx = \frac{\delta_{n\ell}}{2n+1}\,, \qquad \text{(II.L.1)}$$

where $x = \cos\theta$.

The integral over the product of three Legendre polynomials

$$\langle P_n P_1 P_\ell \rangle_\theta = \frac{1}{2}\int_{-1}^{1} P_n(x)\, P_1(x)\, P_\ell(x)\, dx$$

can be obtained from the more general integral over the product of three spherical harmonics [7] . The integral is found to be

$$\langle P_n P_1 P_\ell \rangle_\theta = \frac{n\,\delta_{\ell,n-1}}{(2n-1)(2n+1)} + \frac{(n+1)\,\delta_{\ell,n+1}}{(2n+1)(2n+3)} \qquad \text{(II.L.2)}$$

Similarly,

$$\left\langle P_n P_1' \frac{\partial P_\ell}{\partial\theta} \right\rangle_\theta = -\langle P_n P_1' P_1' \rangle_\theta$$

$$= -\frac{n(n-1)\,\delta_{\ell,n-1}}{(2n-1)(2n+1)} - \frac{(n+1)(n+2)\,\delta_{\ell,n+1}}{(2n+1)(2n+3)} \qquad \text{(II.L.3)}$$

Spherical Bessel Functions

The orthogonality condition for spherical Bessel functions defined over the range $0 \leq x \leq 1$ can be obtained from the orthogonality condition for ordinary Bessel functions [8] since the spherical Bessel function

$$j_n(x) = \sqrt{\frac{\pi}{2x}}\, J_{n+\frac{1}{2}}(x) \quad .$$

From formula (11.45) in the Handbook of Mathemetical Functions, the orthogonality condition is found to be

$$\int_0^1 x^2 j_n(\beta_\nu x) j_n(\beta_\sigma x)\, dx = 0, \quad \text{if } \nu \neq \sigma,\ n > -1;$$

$$= \frac{1}{2\beta_\nu}\left[\frac{d}{du}\left(u^{1/2} j_n(u)\right)\Big|_{u=\beta_\nu}\right]^2,$$

$$\text{if } \nu = \sigma,\ n > -1,\ b = 0;$$

$$= \frac{1}{2\beta_\nu^2}\left[\frac{a^2}{b^2} + \beta_\nu^2 - \left(n+\tfrac{1}{2}\right)^2\right]\left[j_n(\beta_\nu)\right]^2,$$

$$\text{if } \nu = \sigma,\ n > -1,\ b \neq 0; \tag{II.S.1}$$

where $\beta_1, \beta_2, \ldots$ are positive roots of

$$\left(a + \tfrac{1}{2}b\right) j_n(\beta_\nu) + b\,\beta_\nu\, j_n'(\beta_\nu) = 0 \tag{II.S.2}$$

The symbol "$j_n'(x)$" denotes the derivative

$$dj_n(x)/dx.$$

The orthogonality condition (II.S.1) applies when both spherical Bessel functions have wavenumbers, β_ν, which satisfy the same root equation. We will now evaluate two integrals in which the wavenumbers satisfy different root equations. Let $\{\beta\}$ satisfy the equation

$$(L+n)\, j_n(\beta) = \beta\, j_{n+1}(\beta) \tag{II.S.3a}$$

and $\{\lambda\}$ satisfy .

$$(L+n-1)\, j_{n-1}(\lambda) = \lambda\, j_n(\lambda) \tag{II.S.3b}$$

These two conditions can also be written as

$$L\, j_n(\beta) = -\beta\, j_n'(\beta) \tag{II.S.4a}$$

$$L\, j_{n-1}(\lambda) = -\lambda\, j_{n-1}'(\lambda), \tag{II.S.4b}$$

respectively.

The integral

$$I_n = \int_0^1 x^2 j_n(\beta x)\, j_n(\lambda x)\, dx \qquad \text{(II.S.5)}$$

can be evaluated by using the differential equation

$$x^2 j_n''(x) + x j_n'(x) + [x^2 - n(n+1)]\, j_n(x) = 0 \qquad \text{(II.S.6)}$$

to obtain

$$I_n = \frac{1}{\beta^2-\lambda^2} \int_0^1 \frac{d}{dx}\left[x^2\left(\beta j_n(\beta x) j_n'(\lambda x) - \beta j_n(\lambda x) j_n'(\beta x)\right)\right] dx$$

This integration can be performed immediately and

$$I_n = \frac{1}{\beta^2-\lambda^2}\left[\lambda j_n(\beta) j_n'(\lambda) - \beta j_n'(\beta) j_n(\lambda)\right]$$

$$= \frac{(L+n-1)(L+\lambda)}{\lambda(\beta^2-\lambda^2)}\, j_n(\beta)\, j_{n-1}(\lambda) \,. \qquad \text{(II.S.7)}$$

The final equality is obtained by using the root equations (II.S.4a) and (II.S.4b).

The second integral to be evaluated is

$$I_n^{(2)} = \int_0^1 x^4 j_n(\beta x)\, j_n(\lambda x)\, dx \qquad \text{(II.S.8)}$$

The integrand of (II.S.8) can be obtained by operating on the integrand of (II.S.5), n→n-1, with

$$(\beta\lambda)^{n-1} \frac{\partial^2}{\partial\beta\partial\lambda} (\beta\lambda)^{-n+1}$$

Thus, $I_n^{(2)}$ can be found by applying the same operator to the result for I_{n-1}, (II.S.7):

$$I_n^{(2)} = (\beta\lambda)^{n-1} \frac{\partial^2}{\partial\beta\partial\lambda}\left[(\beta\lambda)^{-n+1} I_{n-1}\right]$$

$$= (\beta\lambda)^{n-1} \frac{\partial^2}{\partial\beta\partial\lambda}\left[(\beta\lambda)^{-n+1} \frac{(L+n-2)(L+\lambda)}{\lambda(\beta^2-\lambda^2)}\, j_{n-1}(\beta) j_{n-2}(\lambda)\right]$$

$$= (\beta\lambda)^{n-1} \frac{\partial^2}{\partial\beta\partial\lambda}\left[(\beta\lambda)^{-n}(L+n-2)(L-n-1)(L-n)(L+\lambda)\, \frac{j_n(\beta) j_{n-1}(\lambda)}{\lambda(\beta^2-\lambda^2)}\right]$$

(II.S.9)

The differentiation of (II.S.9) is straightforward, but tedious.

The derivative of the spherical Bessel functions,

$$\frac{d}{dx}\left[x^{-n} j_n(x)\right] = (-1)\, x^{-n} j_{n+1}(x) \qquad \text{(II.S.10)}$$

the recurrence relation

$$j_{n-1}(x) + j_{n+1}(x) = (2n+1)\,\frac{j_n(x)}{x} \qquad \text{(II.S.11)}$$

and the root equations are used. The integral $I_n^{(2)}$ is

$$I_n^{(2)} = (L-n-1)(L-n)(L+n-2)\,\frac{j_n(\beta)\, j_{n-1}(\lambda)}{\beta^2\lambda^3(\beta^2-\lambda^2)}$$
$$\cdot\left[(L+n+2)(L+n+1)(L+\lambda) - \lambda(L+n) - 1\right.$$
$$\left. + \frac{2L\lambda^2}{\beta^2-\lambda^2} - \frac{8\beta^2\lambda^2(L+\lambda)}{(\beta^2-\lambda^2)^2}\right] \qquad \text{(II.S.12)}$$

Appendix III

STEADY THERMOCAPILLARY CONVECTION CELLS IN LIQUID DROPS

Alan L. Dragoo*
Institute for Materials Research, National Bureau of Standards
Washington, D. C. 20234

ABSTRACT

A nominally spherical drop is used as a model for a theoretical analysis of thermocapillary convection and for estimates of convective flow rates in "levitated" melts at zero-g. Since in practice temperature fields and the resulting convective flow can be more complicated than the simple vertical temperature gradient and the single vortex ring, respectively, the convective flow arising from a general steady-state temperature field is analyzed. Expressions for the components of a steady velocity field are obtained by adapting the analytical method of Miller and Scriven. The vortex rings are illustrated by means of typical streamlines for the simpler, more symmetric, temperature fields. The circulation time is introduced as a measure of the rate of circulation in a convection cell and typical values are given for several materials.

INTRODUCTION

When buoyant forces are negligible, such as in a space laboratory, convective flows may still occur in a liquid as the result of gradients in the surface--or interfacial tension. These convective flows are commonly called the Marangoni effect although the Marangoni effect includes both this phenomenon of convection and the phenomenon of the deformation of a free liquid surface (Ref. 1). Among the causes of gradients in the surface tension are gradients in the concentration and in the temperature along the surface of a liquid.

Concentration and temperature gradients may not be completely eliminated in many processes, and in some instances, their presence may be necessary to produce the convection which is desired. The growth of crystals from a melt is a process in which the elimination of convection in the melt is desireable because convection produces non-uniform growth conditions, and, thereby, an increase in the number of dislocations in the crystal. The evaporative purification of a levitated melt is a process in which the opposite result is desired: rapid convection is important here because it increases the rate of purification by replenishing the impurity concentration at the surface and because it tends to maintain an unifcrm composition throughout the melt.

*Financial support was provided by NASA under contract W-13,475 #1.

The question of how much surface tension driven flows might enhance the rate of purification of a levitated melt at zero-g is the motivation for the work reported here. As a model which will begin to supply part of the answer to this question, we will consider thermocapillary convection--that is, convection resulting from a temperature gradient along the surface (Ref. 2)--in nearly spherical drops. The temperature field at the surface of the drop will be treated in a general way by writing it as an expansion in spherical harmonics. The model will examine one of the convective modes corresponding to one of the terms in the expansion of the surface temperature field. The equations of motion--the Navier-Stokes equations--will be solved within the assumptions of a steady-state and of creeping flow--terms which are nonlinear in the velocity will be ignored. The mathematical analysis will proceed along the lines of the method which Miller and Scriven (3) applied to the oscillations of a fluid droplet although here we will not retain the time-dependence of their problem. The physical boundary conditions will account for both the convective flow and for the deformation of the surface so that both aspects of the Marangoni effect will appear in the problem. The velocity field components which are obtained from the Miller-Scriven analysis will be used to derive the circulation time τ whose inverse characterizes the rate of circulation within a convection cell. An expression for τ will be worked out in detail for convection cells having axial symmetry. Estimates of τ will be given for a variety of materials when the convection pattern is a single, axially symmetric vortex ring. Also, relative circulation times will be calculated for several higher order, axially symmetric convective modes. Illustrations of these convective modes will be given.

THE TEMPERATURE FIELD

The temperature field responsible for the convection is considered to be a general, non-uniform, but steady, field which can be written as:

$$T(r,\theta,\phi) = T_o + \sum_{n=1} \sum_{m=0}^{n} \sum_{\sigma} T^{\sigma}_{mn} \, r^n Y^{\sigma}_{mn}(\theta,\phi) \quad (\sigma=e,o), \tag{1}$$

where,

$$Y^{e}_{mn} = P^{m}_{n}(\cos\theta) \cos m\phi \tag{2a}$$

$$Y^{o}_{mn} = P^{m}_{n}(\cos\theta) \sin m\phi \tag{2b}$$

are spherical harmonics as defined by Morse and Feshbach (4). The function $P^{m}_{n}(\cos\theta)$ is an associated Legendre polynominal. The simple case of a constant vertical temperature gradient through the drop--$Y^{e}_{mn} = P_1(\cos\theta) = \cos\theta$-- is a special case of the solution of Young, Goldstein and Block (5) who derived the velocity field in a bubble rising in a vertical temperature gradient.

SOLUTION OF THE NAVIER-STOKES EQUATIONS

To obtain the velocity field $u(r,\theta,\phi)$ and the hydrodynamic pressure field $p(r,\theta,\phi)$ within a drop of radius R, we solve the linearized Navier-Stokes equations

$$\mu\nabla^2\vec{u} = \nabla p \tag{3a}$$

$$\nabla\cdot\vec{u} = 0, \tag{3b}$$

where μ is the coefficient of viscosity. We impose the requirements

1) of a finite solution at $r = 0$;

2) of the kinematic condition $u_r(R) = 0$, where u_r is the radial component of the velocity; and

3) of the physical boundary conditions which will be examined in the next section.

Since Eqns. (3a,b) are linear, a general solution can be written as a superposition of all the modes. Thus, it is sufficient to find a solution for one of the modes (n,m,σ).

Eqns. (3a,b) can be integrated according to the method of Miller and Scriven. This method integrates (3a,b) in terms of u_r and the radial component of the vorticity, where the vorticity is defined by

$$\vec{\zeta} \equiv \nabla \times \vec{u}. \tag{4}$$

The results of the Miller-Scriven method which satisfy requirements "1" and "2" are

$$u_r(r,\theta,\phi) = -A^{\sigma}_{mn} r^{n-1} (R^2-r^2) Y^{\sigma}_{mn}(\theta,\phi) \tag{5a}$$

$$\zeta_r(r,\theta,\phi) = B^{\sigma}_{mn} r^{n-1} Y^{\sigma}_{mn}(\theta,\phi). \tag{5b}$$

The remaining integration constants A^{σ}_{mn} and B^{σ}_{mn} will be obtained from the physical boundary conditions in the next section.

The velocity components--u_θ and u_ϕ--can be obtained from u_r and ζ_r by a relation due to Sani (6);

$$\vec{u} = \hat{e}_r u_r + [r^2/n(n+1)]\ [\nabla_{II} R u_r - \hat{e}_r \times \nabla_{II} \zeta_r], \tag{6}$$

where $\hat{e}_r$ is the radial unit vector,

$$\nabla_{II} = \nabla - \hat{e}_r \frac{\partial}{\partial r} \tag{7}$$

is the surface gradient operator and R is the operator

$$\frac{1}{r^2} \frac{\partial}{\partial r} r^2. \tag{8}$$

Eqn. (4) and the results for u_r, u_θ, u_ϕ can be used to derived ζ_θ and ζ_ϕ.

The hydrodynamic part $p(r,\theta,\phi)$ of the pressure can be found by taking the divergence of (3a) which yields $\nabla^2 p = 0$.

Thus,

$$p(r,\theta,\phi) = F^{\sigma}_{mn} r^n Y^{\sigma}_{mn}(\theta,\phi). \tag{9}$$

The coefficient F^{σ}_{mn} can also be obtained from (3a) by

$$\vec{r} \cdot \nabla^2 \vec{u} = \nabla^2 (r u_r) = (r/\mu)(\partial p/\partial r), \tag{10}$$

from which it can be shown that

$$F^{\sigma}_{mn} = 2(2n+3)\mu A^{\sigma}_{mn}/n. \tag{11}$$

PHYSICAL BOUNDARY CONDITIONS

The balance of stresses at the surface requires:

1) that the normal stress on the surface due to the hydrostatic pressure and to the motion of the fluid is balanced by the surface tension; and

2) that the shear stresses due to the variation of the surface tension are balanced by the fluid motion.

The deformation of the surface must be included in these conditions. The deformation is assumed to be small, so that

$$R + \Delta R = R\,[1 + \varepsilon(\theta,\phi)], \tag{12}$$

where ΔR is the displacement of the surface and

$$\varepsilon(\theta,\phi) = E^{\sigma}_{mn} Y^{\sigma}_{mn}(\theta,\phi) \tag{13}$$

is a radial strain. The coefficient E^{σ}_{mn} also must be obtained from the boundary conditions.

The normal stress due to the fluid

$$-p_{rr} = p_o + F^{\sigma}_{mn} R^n Y^{\sigma}_{mn} - 2\mu(\partial u_r/\partial r)\big/_{r+R^*} \tag{14}$$

is balanced by the surface tension produced stress

$$\gamma\left(\frac{1}{R_1} + \frac{1}{R_2}\right), \tag{15}$$

*A simplification of the surface conditions is introduced at this point by neglecting the interfacial dilational elasticity and the interfacial shear elasticity which contribute an interfacial viscosity term to the normal stress equations--see Scriven (7) and Miller and Scriven (5) for discussions of these properties.

where γ is the local value of the surface tension and R_1 and R_2 are the principal radii of curvature. For small deformations of the surface of a spherical drop, Lamb (8) has shown that

$$\frac{1}{R_1} + \frac{1}{R_2} = \frac{1}{R}\,[2 + (n-1)(n+2)\,E^{\sigma}_{mn} Y^{\sigma}_{mn}]. \tag{16}$$

The surface tersion coefficient is expanded in terms of the mean value γ_o and the temperature coefficient γ_T as

$$\gamma = \gamma_o + \gamma_T[T^{\sigma}_{mn} + L^{\sigma}_{mn} E^{\sigma}_{mn}]R^n Y^{\sigma}_{mn}, \tag{17}$$

where L^{σ}_{mn} is the coefficient obtained in the expansion of $T(R+\Delta R)$ of the deformed surface about the temperature $T(R)$ of the undeformed surface and $T^{\sigma}_{mn} R^n Y^{\sigma}_{mn}$ is the (n,m,σ)-term in the expansion of the surface temperature field.

Setting the hydrostatic pressure $p_o = 2\gamma_o/R$, and considering terms to first order in Y^{σ}_{mn} in the normal stress condition, we obtain the first equation for A^{σ}_{mn} and E^{σ}_{mn},

$$6\mu R^{n+1} A^{\sigma}_{mn}/n = [\gamma_o(n-1)(n+2) + 2\gamma_T L^{\sigma}_{mn} R^n]E^{\sigma}_{mn} = 2\gamma_T T^{\sigma}_{mn} R^n. \tag{18}$$

Instead of solving the shear stress conditions directly, it is more convenient to take the surface divergence and the surface curl of the force on an element of surface. The surface divergence equation is

$$\nabla^2_{II}\,\gamma = \mu[\frac{\partial}{\partial r}\,(Ru_r) - \nabla^2_{II} u_r]_{r=R}. \tag{19}$$

Eqn. (19) can be simplified since $\nabla^2_{II} u_r\Big|_{r=R} = 0$. The divergence condition, then, yields a second equation for A^{σ}_{mn} and E^{σ}_{mn},

$$2(2n+1)\mu R^{n+1} A^{\sigma}_{mn}/n - (n+1)\,\gamma_T L^{\sigma}_{mn} R^n E^{\sigma}_{mn} = (n+1)\gamma_T T^{\sigma}_{mn} R^n. \tag{20}$$

The radial part of the surface curl equation yields the result that $B^{\sigma}_{mn} = 0$, or $\zeta_r = 0$.

Eqns. (18) and (20) can be solved simultaneously for A^{σ}_{mn} and E^{σ}_{mn},

$$A^{\sigma}_{mn} = n(n+1)(n+2)\gamma_o\gamma_T T^{\sigma}_{mn}/2\mu R\, D^{\sigma}_{mn} \tag{21}$$

$$E^{\sigma}_{mn} = \gamma_T T^{\sigma}_{mn} R^n/D^{\sigma}_{mn}, \tag{22}$$

where $D^{\sigma}_{mn} = (2n+1)(n+2)\gamma_o + \gamma_T L^{\sigma}_{mn} R^n$. (23)

THE VELOCITY FIELD AND THE VORTICITY FIELD

Defining a characteristic rate of flow

$$U^{\sigma}_{mn} = -n(n+1)(n+2)\gamma_o\gamma_T T^{\sigma}_{mn} R^n/2\mu D^{\sigma}_{mn}, \tag{24}$$

the components of the velocity $\vec{u}$ can be written as

$$u_r(r,\theta,\phi) = U^{\sigma}_{mn}\tilde{r}^{n-1}(1-\tilde{r}^2)Y^{\sigma}_{mn}(\theta,\phi) \tag{25a}$$

$$u_\theta(r,\theta,\phi) = U^{\sigma}_{mn}(\tilde{r}^{n-1}/n)\left[1-\left(\frac{n+3}{n+1}\right)\tilde{r}^2\right]\cdot(\partial Y^{\sigma}_{mn}/\partial\theta) \tag{25b}$$

$$u_\phi(r,\theta,\phi) = U^{\sigma}_{mn}(\tilde{r}^{n-1}/n)\left[1-\left(\frac{n+3}{n+1}\right)\tilde{r}^2\right](1/\sin\theta)\cdot(\partial Y^{\sigma}_{mn}/\partial\theta), \tag{25c}$$

where $\tilde{r} = r/R$.

Although $\zeta_r = 0$ within the drop, ζ_θ and ζ_ϕ generally do not vanish. Using the definition of the vorticity, Eqn. (4), and Eqns. (25a,b,c),

$$\zeta_\theta = Z^{\sigma}_{mn} r^n (1/\sin\theta)(\partial Y^{\sigma}_{mn}/\partial\phi) \tag{26a}$$

$$\zeta_\phi = -Z^{\sigma}_{mn} r^n (\partial Y^{\sigma}_{mn}/\partial\theta), \tag{26b}$$

where

$$Z^{\sigma}_{mn} = 2(U^{\sigma}_{mn}/R)(2n+3)/n(n+3). \tag{27}$$

The rate of flow, or speed, is

$$v = [u_r^2+u_\theta^2+u_\phi^2]^{1/2}, \tag{28}$$

where in general,

$$u_r = \sum_{n=1}\sum_{m=0}^{n}\sum_{\sigma} u_r(n,m,\sigma) \tag{29a}$$

$$u_\theta = \sum_{n=1}\sum_{m=0}^{n}\sum_{\sigma} u_\theta(n,m,\sigma) \tag{29b}$$

$$u_\phi = \sum_{n=1}\sum_{m=0}^{n}\sum_{\sigma} u\phi(n,m,\sigma). \tag{29c}$$

Thus, the general expression for v can be very complicated. Only expressions for the pure modes will be investigated here.

For the special case of the lowest order mode $(n,m,\sigma) = (1,0,e)$ and where $L^e_{01} = 0$, we obtain equations for a levitated drop in a constant vertical temperature gradient. In this case, the temperature in the drop is

$$T = T_o + T_1 R\tilde{r}\cos\theta, \tag{30}$$

which results in the velocity components

$$u_r = -(\gamma_T T_1 R/3\mu)(1-\tilde{r}^2)\cos\theta \tag{31a}$$

$$u_\theta = (\gamma_T T_1 R/3\mu)(1-2\tilde{r}^2)\sin\theta \tag{31b}$$

$$u_\phi = 0.$$

These results can be obtained from the solutions of Young, et. al (5), as mentioned in the Introduction. In addition, we find that

$$E^e_{mn} = \gamma_T T_1 R/9\gamma_o, \tag{32}$$

so that the drop is spherical in the limit $\gamma_T/\gamma_o \to 0$.

SOME CHARACTERISTICS OF AXIALLY SYMMETRIC MODES

For an axially symmetric mode (n,0,e), the expression for the rate of flow, Eqn. (28), is

$$\tilde{v} = (\tilde{r}^{n-1}/n)[n^2(1-\tilde{r}^2)^2(P_n)^2+(1-\frac{n+3}{n+1}\tilde{r}^2)^2(P_n^1)^2]^{1/2} \tag{33}$$

where $\tilde{v} = v/U^e_{on}$, P_n is the nth order Legendre polynomial and P_n^1 is the associated Legendre polynomial of first degree. Eqn. (33) can be used to identify the stagnation points since $\tilde{v} = 0$ at these points.

Within the drop, n rings of stagnation points about the axis of the drop can be readily identified: take $\tilde{r}^2 = (n+1/(n+3)$ and $P_n = 0$; since P_n has n nodes and $0 \leq \phi \leq 2\pi$, n rings have been identified. On the surface of the drop ($\tilde{r} = 1$), the rate of flow $\tilde{v} = 0$ if $P_n^1 = 0$. The associated Legendre polynomial P_n^1 has (n+1) nodes, including one at each pole. These two stagnation points at the poles and the (n-1) stagnation rings on the surface coincide with the hot and cold spots of the temperature field and define the boundaries of the convection cells in the drop. If $n > 1$, $v = 0$ when $r = 0$. That is, flow does not occur through the center of the drop when $n > 1$. Finally, we must consider the possibility of other internal stagnation points. That is, are there other points such that

$$n^2(1-\tilde{r}^2)^2(P_n)^2 + (1-\frac{n+3}{n+1}\tilde{r}^2)^2\ (P_n^1)^2 = 0\ ?$$

The answer is no. Since each term is either positive or zero, and since neither $(1-\tilde{r}^2)$ and $(1-(n+3/n+1)\tilde{r}^2)$ nor P_n and P_n^1 vanish at identical values of $\tilde{r}$ and $\cos\theta$, respectively, there are no other internal stagnation points.

For an axially symmetric problem, a streamfunction $\psi(\tilde{r},\theta)$ can be obtained from

$$\tilde{u}_r = -\frac{1}{r^2\sin^\theta}\ \frac{\partial\psi}{\partial\theta} \tag{34a}$$

$$\tilde{u}_\theta = \frac{1}{\tilde{r}\sin\theta}\ \frac{\partial\psi}{\partial r} \tag{34b}$$

where $\tilde{u}_a = u_a/U^{\sigma}_{mn}$ $(a = r,\theta)$. For the (n,0,e)-mode, the streamfunction is

$$\psi = -r^{n+1}(1-r^2)\ \sin\theta P_n^1(x)/n(n+1), \tag{35}$$

where $x = \cos\theta$. For the mode (1,0,e), the streamfunction is that for Hill's spherical vortex (9). Stagnation points, indicated by "N", and typical streamlines for Hill's spherical vortex are illustrated in Fig. 1 and for the modes n = 2,3,4,5 in Figs. 2-5, respectively. The drops are seen in vertical cross-sections. The model rings lie in planes perpendicular to the axis in each illustration. The straight lines within the circles represent the boundaries of the convection cells, and here $\psi = 0$. The positions of the stagnation points are listed in Table 1 for these five modes.

Table 1. Stagnation "Points" for Axially Symmetric Convection Cells in Nominally Spherical Drops

Mode n	$\tilde{r}$	Interior θ	Type	Surface ($\tilde{r}$ = 1) θ	Type
1	$1/\sqrt{2}$		ring	0°	point
				180°	point
2	0	--	point	0°	point
	$\sqrt{3}/5$	54° 44' 8"	ring	90°	ring
		125° 15' 52"	ring	180°	point
3	0	--	point	0°	point
	$\sqrt{2}/3$	39° 13' 54"	ring	63° 26' 6"	ring
	"	90°	ring	116° 33' 54"	ring
	"	140° 46' 6"	ring	180°	point
4	0	--	point	0°	point
	$\sqrt{5}/7$	30° 33' 20"	ring	49° 6' 24"	ring
	"	70° 7' 28"	ring	90°	ring
	"	109° 52' 32"	ring	130° 53' 36"	ring
	"	149° 26' 40"	ring	180°	point
5	0	--	point	0°	point
	$1/2\sqrt{3}$	25° 1' 2"	ring	40° 5' 17"	ring
	"	57° 25' 14"	ring	73° 25' 38"	ring
	"	90°	ring	106° 34' 22"	ring
	"	122° 34' 46"	ring	139° 54' 43"	ring
	"	154° 58' 58"	ring	180°	point

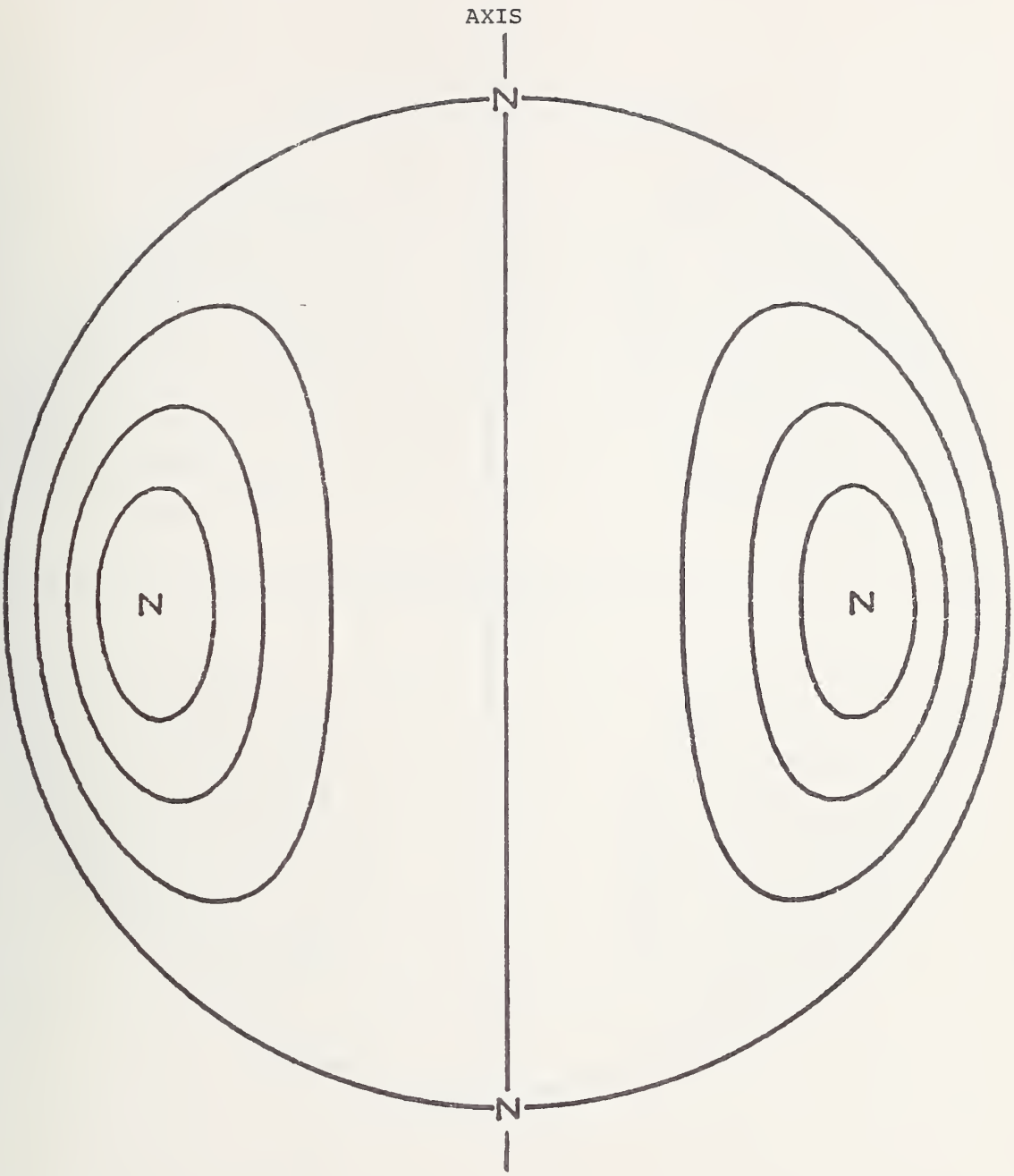

Figure 1. Streamlines and Stagnation Points ("N") for the (1,0,e)-Mode: Hills' Spherical Vortex.

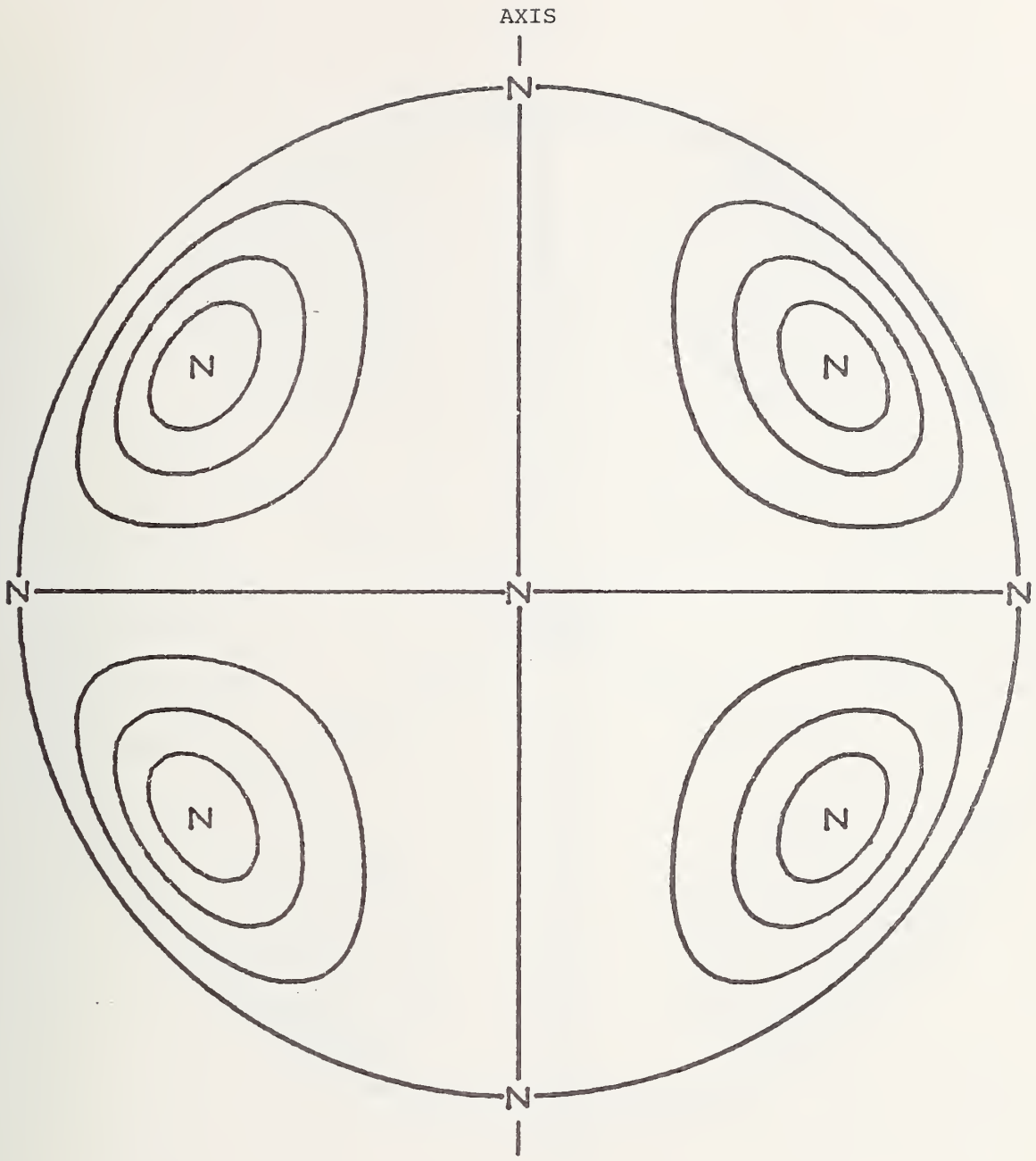

Figure 2. Streamlines and Stagnation Points for the (2,0,e)-Mode

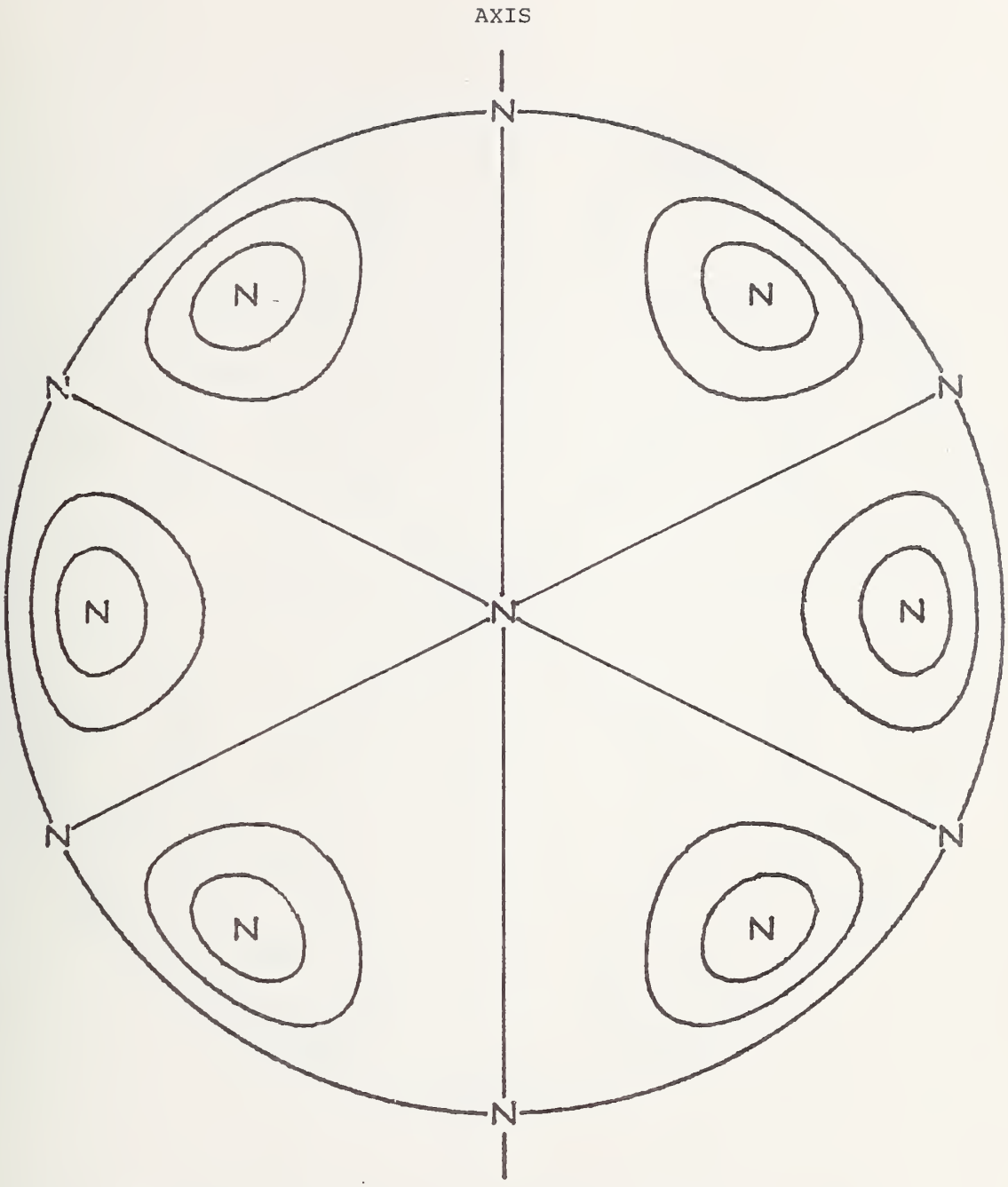

Figure 3. Streamlines and Stagnation Points for the (3,0,e)-Mode

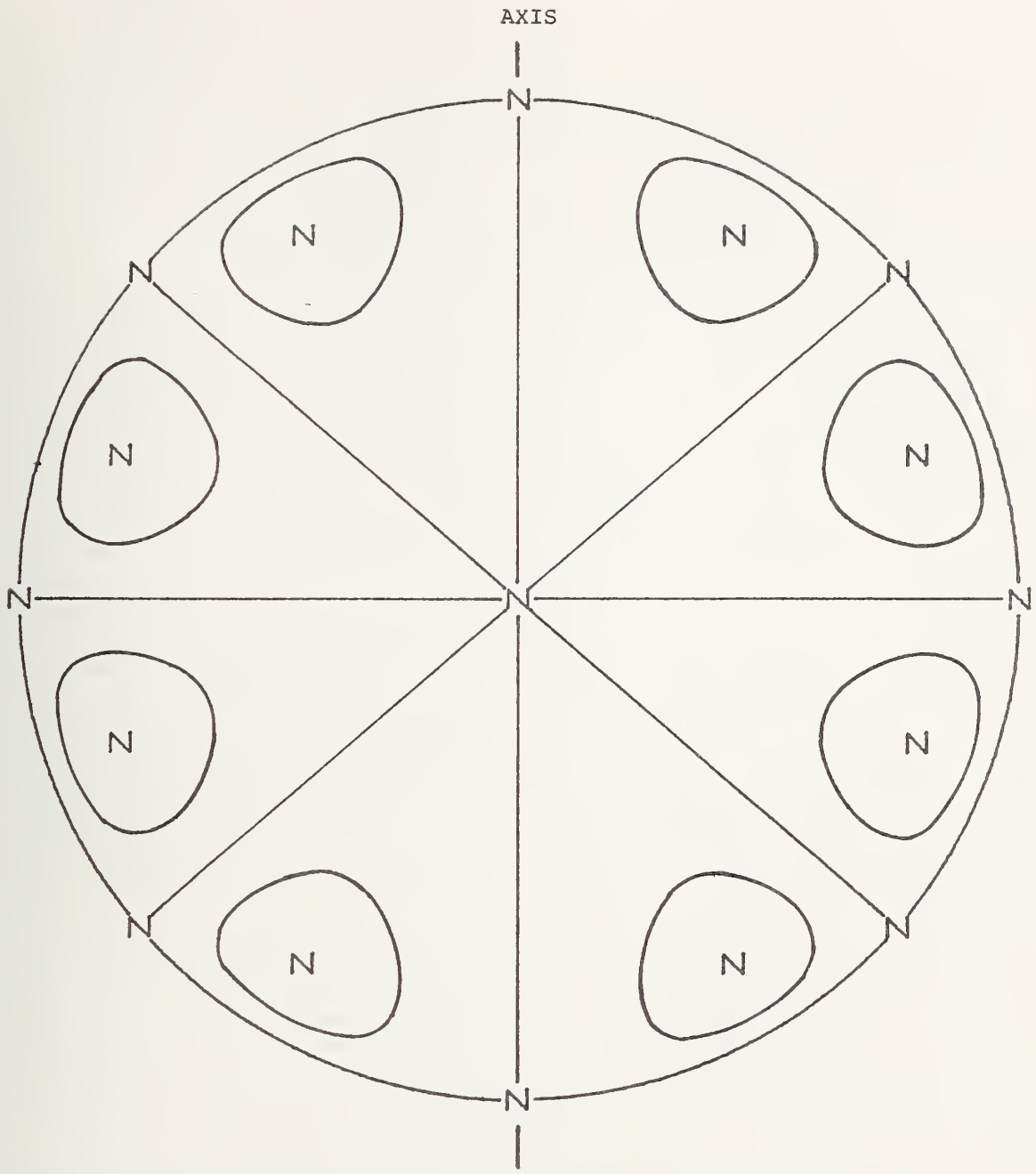

Figure 4. Streamlines and Stagnation Points for the (4, 0, e)-Mode

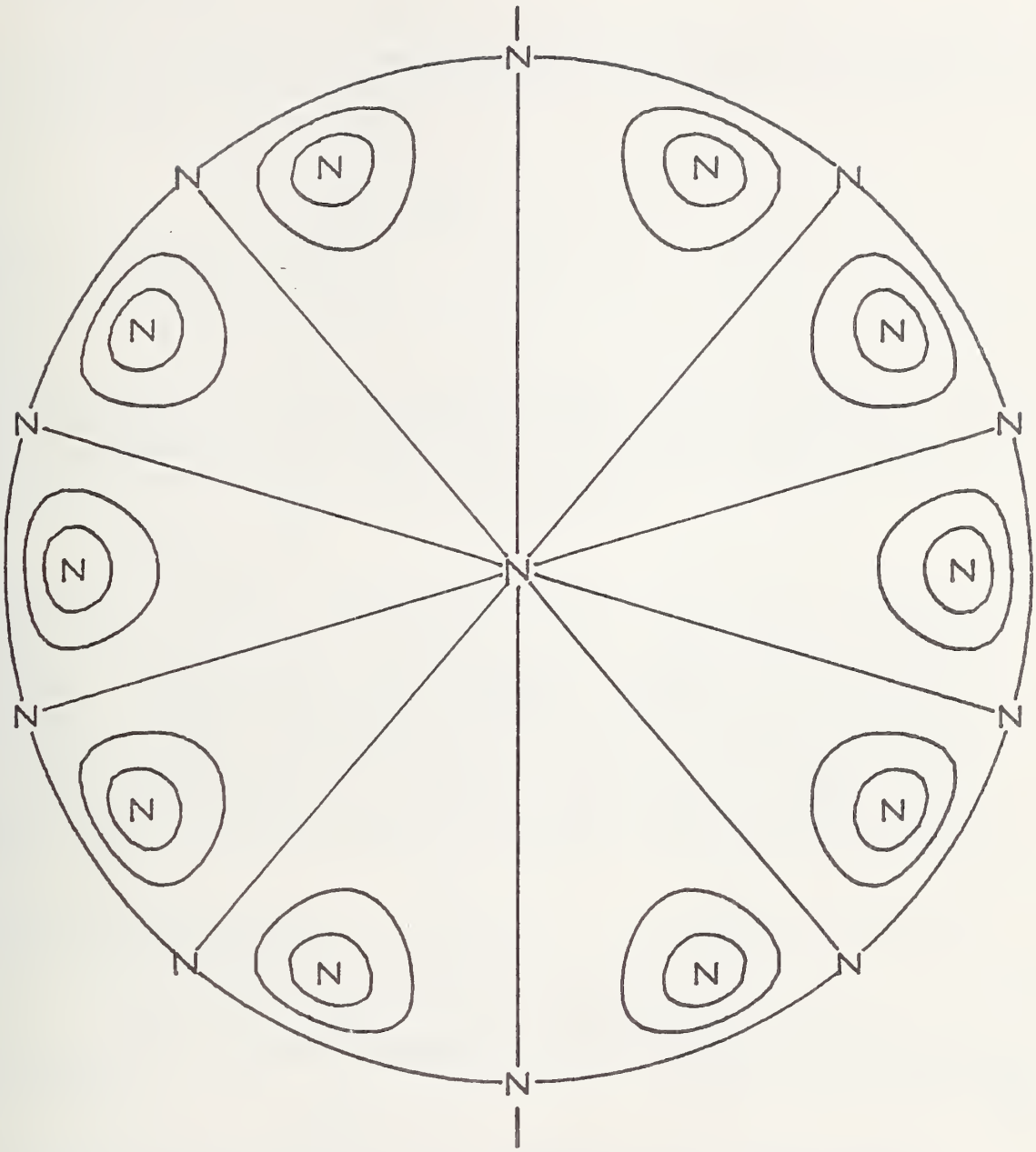

Figure 5. Streamlines and Stagnation Points For the (5,0,e)-Mode

THE CIRCULATION TIME

The circulation time τ will be introduced in this section as a means of characterizing the rate of convective mass transfer from the interior of the convection cell to the vicinity of the surface of the drop. The reciprocal circulation time τ^{-1} is defined by

$$\tau^{-1} = \oint \vec{u}\cdot d\vec{\ell}/\int dS$$
$$= \oint \vec{\zeta}\cdot\vec{n}dS/\iint dS, \tag{36}$$

where the circulation integral

$$\oint \vec{u}\cdot d\vec{\ell}$$

is taken around the boundary of the cell formed by the intersection of the cell with a vertical plane containing the axis of the drop, such as any of the cell boundaries shown in Figures 1-5. The second equality follows from Stokes's theorem, where the surface integrals

$$\int\vec{\zeta}\cdot\vec{n}dS \text{ and } \int dS$$

are taken over the region bounded by the circuit of the line integral; $\vec{n}$ is the unit normal vector to the surface and here is equal to $\hat{e}_\phi$. According to Eqn. (36), the reciprocal circulation time is the average vorticity of the cell. The circulation time resembles the period of rotation of a rigid body. Indeed, if the fluid circulated about the vortical center as a rigid body, Eqn. (36) would yield 4π times the frequency of rotation and τ would be the period of the rotation reduced by 4π. Unfortunately, such a simple interpretation of thermocapillary convection cells is not possible, but τ can still be used to characterize the rate of circulation within the cell.

For the axially symmetric mode (n,0,e), the integrals in Eqn. (36) can be performed yielding

$$\tau_{ns} = (n+2)[P_n(x'_s)-P_n(x'_{s+1})]/2Z^e_{on}(\theta'_{s+1}-\theta'_s) \tag{37}$$

for the circulation time for the s-cell, where $1 \leq s \leq n+1$, and x'_s and x'_{s+1} are roots of

$$P^1_n(x) = 0. \tag{38}$$

Cell-s has its vortical center at the stagnation point whose angular position θ_s is given by the root x_s of

$$P_n(x) = 0; \tag{39}$$

θ_s lies within the range whose lower bound is θ'_s and whose upper bound is θ'_{s+1}. The circulation time may be either positive or negative, the sign depending upon the direction of circulation in the cell. Using Eqns. (1), (24) and (27), we can show that, apart from the geometric factor, the circulation time τ_{ns} depends only on the material parameters μ and γ_T and on the temperature gradient at the surface.

The circulation times for the mode n = 1 are given in Tables 2-5 for a variety of liquids. Here, we assume "unit conditions": $L^e_{01} = 0$, and a unit temperature gradient, $T^e_{01} = -1°/cm$. The assumption of unit conditions is indicated for the circulation time by $\tau°$, where the superscript "o" designates unit conditions. Table 2 lists circulation times for some liquids at room temperature; Table 3, for five liquid metals; Table 4, for four molten oxides; and Table 5 for three molten sodium halide salts.

Table 2. Circulation Times* for Some Liquids at Room Temperature (298.15 K)

Material	γ_T mN/m/K**	Viscosity mPa.s**	$\|\tau\|$, s
Acetone	-0.112 (11)	0.316 (10)	0.0323
DC 200, 20 cs+	-0.062 (5)	19 (5)	3.5
200 cs	-0.065 (5)	193 (5)	34
1000 cs	-0.061 (5)	793 (5)	180
Ethanol	-0.9832 (11)	1.092 (10)	0.150
n-Hexadecane	-0.106 (5)	3.086 (12)	0.334
Krytox 143 AZ++	-0.1 (13)	32.4 (13)	4
Water	-0.1477 (11)	0.8904 (13)	0.06908

*temperature gradient at the poles has a magnitude of 1°/cm.
**1 mN/m = 1 dyn/cm; 1 mPa.s = 1 cp = 10^{-2} dyn.s/cm^2.
+Dow Corning silicone oils of the DC 200 series.
++A perfluoroalkylpolyether.

Table 3. Circulation Times*--Metals

Materials	γ_T mN/m/K	Temp. T_o K	Viscosity mPa.s	$\|\tau\|$,s
Aluminum	-0.356 (10)	930	4.5 (15)	0.14
		1070	2.5	0.08
Copper	-0.06 (10)	1370	4.5 (15)	0.9
		1470	3.9	0.7
Mercury	-0.2049 (11)	290	1.554 (15)	0.0869
		470	1.052	0.0588
Sodium	-0.09833 (14)	470	0.450 (15)	0.00524
		670	0.284	0.00331
Tin	-0.0706 (13)	500	1.97 (13)	0.320
		870	1.05 (13)	0.170

*The temperature gradient at the poles has a magnitude of 1°/cm.

Table 4. Circulation Times*--Oxides

Material	γ_T mN/m/K	Temp. T_o K	Viscosity Pa.s	$\|\tau\|$,s
Al_2O_3	(0.1)+	2400	0.11 (16)	13
		2600	0.062	7
B_2O_3	0.0354 (18)	1410	5.02 (17)	1620
	at 720 K	1670	2.01	651
GeO_2	0.056	1750	12.2 (17)	2500
	at 1390 K	1930	0.787	160
SiO_2	0.031	2280	717 (17)	8×10^5
	at 2000 K	2680	102	1×10^5
		2820	46.4	5×10^4

*Temperature gradient at the poles has a magnitude of 1°/cm.
+Estimated.

Table 5. Circulation Times*--Sodium Halides

Material	γ_T (18) mN/m/K	Temp. T_o K	Viscosity (17) mPa.s	$\lvert\tau\rvert$, s
NaCl	-0.0719	1090	1.38	0.220
		1150	1.08	0.172
NaBr	-0.0809	1060	1.28	0.181
		1170	1.00_6	0.142
NaI	-0.129	1030	1.15	0.102
		1100	0.96	0.085

*Temperature gradient at the poles has a magnitude of 1°/cm.

The steady-state temperature gradient is obtained by balancing the conductivie heat flux through the drop against the radiant heat flux away from the drop in the cooler hemisphere. Sufficient heat is applied to the hotter hemisphere to maintain the steady-state gradient. Since the radiant heat flux $\propto T^4$, liquids such as molten metals which have high thermal conductivities will only have steep steady-state gradients at high temperatures. Although copper has the highest thermal conductivity of the liquid metals considered in Table 3, it is the only one of the five metals which is considered at temperatures high enough for a rate of radiant heat loss to be attained which could produce a steady-state gradient of 1°/cm. Thus, the circulation times given for copper in the table are the only ones which are physically attainable under steady-state conditions. For the other metals, the physcially attainable value of τ_1 will be longer than τ_1°: the attainable steady convective rates will be less than the rates produced by a gradient of 1°/cm.

The long circulation times estimated for the oxides, B_2O_3, GeO_2 and SiO_2 show the importance of the viscosity in determining whether thermocapillary convection can occur in the liquid. For these three oxides, thermocapillary convection is expected to be negligible. However, Al_2O_3 has a lower viscosity than these other three oxides and, thus, a shorter circulation time. Since temperature gradients much larger than 1°/cm can be attained in molten oxides, significant thermocapillary convection might be observed in molten alumina.

The n = 1 mode has been demonstrated on earth by the work of Young, Goldstein and Block (5) who observed the balancing of the thermocapillary and buoyancy forces on small bubbles in a vertical temperature gradient. The low-g of a space laboratory in addition to facilating the levitation of a drop would allow the observation of the higher convective modes, in particular, the n = 2 mode. The circulation could be observed by the movement of a dye or of a radiotracer.

Relative circulation times for the axially symmetric modes n=2,3,4,5 are given in Table 6. These times are calculated relative to the single vortex (n = 1) time τ_1°. The sign of the circulation time for a particular cell indicates the direction of circulation with respect to that in the single vortex drop. Since the convective rate decreases as n increases, the higher modes appear to be less desirable than the n = 1 mode for obtaining rapid purification. However, the convective rates for some of these higher modes still can be large enough for the convective pattern to be studied and for these modes to have some utility for the purification of levitated melts in space.

SUMMARY

Equations describing the convective flow velocities in thermocapillary convection cells in drops have been derived. When the thermal conditions approximate a pure, symmetric mode--that is, when the temperature field can be described by a single Legendre polynomial, the streamlines of the vortex and the positions of the stagnation points in each cell can be calculated. The circulation time, which is the reciprocal of the average vorticity of the cell and which characterizes the rate of circulation, also can be calculated for these high symmetry cells. An estimate of the circulation time for a liquid drop is an indicator of the probable significance of thermocapillary convection in the drop when a temperature gradient is imposed across it.

Table 6. Relative Circulation Times, $\tau_{ns}^\circ/\tau_1^\circ$, for Axially Symmetric Modes with n > 1

Mode n	Cells s	$\tau_{ns}^\circ/\tau_1^\circ$*
2	1	3.968
	2	-3.968
3	1	9.981
	2	-7.365
	3	9.981
4	1	19.994
	2	-13.505
	3	13.505
	4	-19.994
5	1	34.960
	2	-22.691
	3	20.647
	4	-22.691
	5	34.960

*τ_{ns}° is the circulation time for the s-cell of the nth mode, τ_1° is the circulation time for mode n = 1; a temperature gradient with a magnitude of 1°/cm is assumed at the poles. The sign indicates the direction of circulation with respect to the n = 1 mode.

REFERENCES

1. L. E. Scriven and G. V. Sternling, Nature 187, 186 (1960).

2. V. G. Levich, Physicochemical Hydrodynamics, Prentice-Hall, Englewood Cliffs, N. J., (1962), Chapters 7 and 8.

3. C. A. Miller and L. E. Scriven, J. Fluid Mech. 32, 417 (1968).

4. P. M. Morse and H. Feshbach, Methods of Theoretical Physics, McGraw-Hill, New York (1953), Chapter 10.

5. N. O. Young, J. S. Goldstein and M. J. Block, J. Fluid Mech. 6, 350 (1959).

6. R. L. Sani, "Convective Instability", Ph.D. Thesis, Department of Chemical Engineering, University of Minnesota, 1963.

7. L. E. Scriven, Chem. Engineering Sci. 12, 98 (1960).

8. H. Lamb, Hydrodynamics, Sixth Ed., Cambridge University Press, London (1932), p. 475.

9. L. M. Milne-Thomson, Theoretical Hydrodynamics, Fifth Ed., Macmillan, New York (1968), Section 19.51.

10. Handbook of Chemistry and Physics, 47th Ed., R. C. Weast, ed. Chemical and Rubber Company, Cleveland, Ohio, (1966).

11. J. J. Jasper, J. Phys. Chem. Ref. Data 1, 841 (1972).

12. R. S. Marvin and D. L. Hogenboom, "Viscosity of Liquids," in the American Institute of Physics Handbook, Third Ed., D. E. Gray, ed., McGraw-Hill, New York (1972).

13. P. G. Grodzka and T. C. Bannister, Sci. 176, 506 (1972).

14. Liquid Metals Handbook, Sodium (NaK) Supplement, C. B. Jackson, ed., U. S. Atomic Energy Commission and the Bureau of Ships, U. S. Department of the Navy, Washington (1955).

15. C. J. Smithells, Metals Reference Book, 4th Ed., Vol. 3 Plenum, New York (1967)

16. J. L. Bates, C. E. McNeilly and J. J. Rasmussen, "Properties of Molten Ceramics", Ceramics in Severe Environments, W. W. Kriegel and H. Palmour III, ed., Plenum, New York (1971).

17. G. J. Janz, F. W. Dampier, G. R. Lakshminarayanan, P. K. Lorenz and R. P. T. Tomkins, Molten Salts, Vol. 1, NSRDS-NBS 15, National Bureau of Standards, U. S. Department of Commerce, Washington (1968).

18. G. J. Janz, G. R. Lakshminarayanan, R. P. T. Tomkins, and J. Wong, Molten Salts, Vol. 2, NSRDS-NBS 28.

Task 7

Consulting Support

NBS personnel have consulted with other groups engaged in the Space Processing Program, including Marshall S.F.C., General Electric (Valley Forge), State University of New York at Stony Brook, Grumman Aerospace, Jet Propulsion Laboratory and others. We have shared computer programs and data with SUNY. We have assisted in the evaluation of proposals. We have attended technical meetings in San Francisco, California; Huntsville, Alabama; Washington, D. C.; Pasadena, California, and others. We have provided advice and consultation with NASA Headquarters as required. We have organized a Space Processing Seminar Series with invited speakers from Bell Laboratories, J. T. Baker Company, Renssalaer Polytechnic Institute, General Electric Corporation and others.

Distribution:

National Aeronautics and Space Administration
Washington, D. C. 20546

Mr. F. L. Williams	Code ES	1 copy
Dr. J. H. Bredt	Code ES	4 copies

National Aeronautics and Space Administration
Johnson Space Center
Houston, Texas 77058

Mr. W. E. Rice	Code EA	2 copies
Mr. J. P. Loftus	Code AT	1 copy
Mr. J. A. Mason	Code DA	1 copy
Mr. E. J. Svreek	Code FM5	1 copy

National Aeronautics and Space Administration
George C. Marshall Space Flight Center
Marshall Space Flight Center, Alabama 35812

Mr. H. P. Gierow	Code PD-MP-DIR	1 copy
Mr. K. R. Taylor	Code PD-MP-T	2 copies
Mr. B. O. Montgomery	Code S&E-DIR	1 copy
Dr. W. G. Johnson	Code S&E-R-DIR	1 copy
Mr. R. E. Lake	Code S&E-R	1 copy
Mr. R. Schwinghamer	Code S&E-ASTN-M	1 copy
Dr. R. S. Snyder	Code S&E-ASTN-MTE	1 copy
Mr. E. C. McKannan	Code S&E-ASTN-MM	1 copy
Mr. R. C. Ruff	Code S&E-ASTN-MEV	1 copy
Miss M. H. Johnston	Code S&E-ASTN-MEV	1 copy
Mr. H. Wuenscher	Code S&E-PE-DIR	1 copy
Mr. I. C. Yates, Jr.	Code S&E-PE-A	1 copy
Mr. L. H. Berge	Code S&E-PE-A	1 copy
Mr. G. M. Arnett	Code S&E-SSL-TR	1 copy
Mr. T. C. Bannister	Code S&E-SSL-T	1 copy
Mr. M. C. Davidson	Code S&E-SSL-TR	1 copy
Mr. A. C. Krupnick	Code S&E-ASTN-MT	1 copy
Mr. W. B. McPherson	Code S&E-ASTN-MMM	1 copy
Mr. J. H. Hess	Code S&E-ASTN-MM	1 copy
Mr. L. L. Lacy	Code S&E-SSL-NP	1 copy
Mr. M. F. Nowakowski	Code S&E-QUAL-QT	1 copy
Dr. R. E. Allen	Code S&E-ASTN-MTM	1 copy
Mr. P. H. Rhodes	Code S&E-ASTN-MTE	1 copy
Mr. J. Bond	Code S&E-ASTN-MTE	1 copy
Mrs. B. R. Facemire	Code S&E-SSL-TR	1 copy
Mr. C. F. Schafer	Code S&E-SSL-TR	1 copy
Mr. B. R. Aldrich	Code S&E-PE-MXX	1 copy
Mr. A. Boese	Code S&E-PE-A	1 copy
Mr. R. A. Taylor	Code S&E-PE-MEI	1 copy
Mr. J. R. Williams	Code S&E-PE-M	1 copy
Mr. V. H. Yost	Code S&E-PE-MW	1 copy
Dr. M. P. L. Siebel	Code S&E-PE-DIR	1 copy

Jet Propulsion Laboratory
California Institute of Technology
4800 Oak Grove Drive
Pasadena, California 91103

Dr. C. H. Savage	Code 158-235	1 copy
Dr. M. M. Saffren	Code 183-301	1 copy
Dr. T. G. Wang	Code 183-401	1 copy
Dr. D. D. Elleman	Code 183-401	1 copy
Dr. J. W. Lucas	Code 180-700	1 copy

National Aeronautics and Space Administration
Langley Research Center
Hampton, Virginia 23665

Dr. L. T. Melfi, Jr.	Code 401A	1 copy
Mr. B. W. Cocke, Jr.	Code 401A	1 copy
Dr. R. A. Outlaw	Code 234	1 copy
Dr. J. P. Mugler	Code 215B	1 copy
Mr. J. D. DiBattista	Code 215B	1 copy
Mr. W. C. Ayers	Code 418	1 copy

National Aeronautics and Space Administration
Ames Research Center
Moffett Field, California 91103

Dr. J. A. Parker	Code SC	1 copy

Grumman Aerospace Corporation
Bethpage, New York 11714

Dr. C. H. Li 1 copy

General Electric Company
Space Sciences Laboratory
P.O. Box 8555
Philadelphia, Pennsylvania 19101

Dr. R. T. Frost 1 copy

European Space Research Organization
114 Avenue Charles de Gaulle
92 Neuilly, France

Dr. G. Seibert 1 copy

Gesellschaft fur Weltraumforschung mbH
505 Porz-Wahn
Linder Hohe
German Federal Republic

Dr. A. Bewersdorff 1 copy

NBS-114A (REV. 7-73)

U.S. DEPT. OF COMM. BIBLIOGRAPHIC DATA SHEET	1. PUBLICATION OR REPORT NO. NBSIR 74-611	2. Gov't Accession No.	3. Recipient's Accession No.

4. TITLE AND SUBTITLE

NBS Space Processing Research

5. Publication Date: November 1974

6. Performing Organization Code

7. AUTHOR(S)
E. Passaglia, R. L. Parker

8. Performing Organ. Report No. NBSIR 74-611

9. PERFORMING ORGANIZATION NAME AND ADDRESS

NATIONAL BUREAU OF STANDARDS
DEPARTMENT OF COMMERCE
WASHINGTON, D.C. 20234

10. Project/Task/Work Unit No.

11. Contract/Grant No. W-13,475 Mod 3

12. Sponsoring Organization Name and Complete Address *(Street, City, State, ZIP)*
NASA - Advanced Missions Program
600 Independence Avenue S.W.
Washington, D.C. 20546

13. Type of Report & Period Covered
Annual Report
11/73-11/74

14. Sponsoring Agency Code

15. SUPPLEMENTARY NOTES

Annual Report

16. ABSTRACT *(A 200-word or less factual summary of most significant information. If document includes a significant bibliography or literature survey, mention it here.)*

This report describes NBS work for NASA in support of NASA's Space Processing Program covering the period November 1, 1973 to October 31, 1974. The objectives of the NBS program are to perform ground-based studies (and, where appropriate, space-based studies) of those aspects of space that could possibly provide a unique environment for making materials more perfect or more pure. The approach taken deals primarily with experimental and theoretical studies of the possible effects of the absence of gravitational forces on those materials preparation processes where the presence of gravity may be important in reducing perfection or purity. The materials preparation processes studied comprise six tasks in the areas of crystal growth, purification and chemical processing, and the preparation of composites. There is an additional seventh task on consulting support.

17. KEY WORDS *(six to twelve entries; alphabetical order; capitalize only the first letter of the first key word unless a proper name; separated by semicolons)*

Crystal growth; crystal perfection; gravitational effects; purification; space processing; zero-g.

18. AVAILABILITY

☐ Unlimited

☒ For Official Distribution. Do Not Release to NTIS

☐ Order From Sup. of Doc., U.S. Government Printing Office Washington, D.C. 20402, SD Cat. No. C13

☐ Order From National Technical Information Service (NTIS) Springfield, Virginia 22151

19. SECURITY CLASS (THIS REPORT)	21. NO. OF PAGES
Unclassified UNCLASSIFIED	224
20. SECURITY CLASS (THIS PAGE)	**22. Price**
UNCLASSIFIED	